ATOMISTIC CHARACTERIZATION OF METAL-ORGANIC FRAMEWORKS FOR SUB-AMBIENT PRESSURE SWING ADSORPTION OF POST-COMBUSTION CO_2 CAPTURE AND SEPARATION

A Dissertation
Presented to
The Academic Faculty

by

Jongwoo Park

In Partial Fulfillment
of the Requirements for the Degree
Doctor of Philosophy in the
School of Chemical and Biomolecular Engineering

Georgia Institute of Technology
December 2019

ATOMISTIC CHARACTERIZATION OF METAL-ORGANIC FRAMEWORKS FOR SUB-AMBIENT PRESSURE SWING ADSORPTION OF POST-COMBUSTION CO_2 CAPTURE AND SEPARATION

Approved by:

Dr. David S. Sholl, Advisor
School of Chemical and Biomolecular Engineering
Georgia Institute of Technology

Dr. Matthew J. Realff
School of Chemical and Biomolecular Engineering
Georgia Institute of Technology

Dr. Ryan P. Lively
School of Chemical and Biomolecular Engineering
Georgia Institute of Technology

Dr. James C. Gumbart
School of Physics
Georgia Institute of Technology

Dr. Krista S. Walton
School of Chemical and Biomolecular Engineering
Georgia Institute of Technology

Date Approved: October 21st, 2019

To my fellow friends and family.

“If you can’t explain it simply, you don’t understand it well enough.”

Albert Einstein

ACKNOWLEDGEMENTS

It was a long and arduous journey to complete my Ph.D. I could enjoy this journey though due to great supports from many people I have met at Georgia Tech. All their helps both in academic and personal perspectives made Dr. Park possible.

I wish to express gratitude to Prof. David Sholl for his guidance throughout my Ph.D. When I first joined the ChBE program at Georgia Tech, I did not have a clear idea about the computational modeling. By the time for an advisor selection (after my first choice did not go well), Prof. Sholl suggested to join his group. Prof. Sholl told me on the day when I finally decided to study the modeling; let's make today's decision not regrettable after 4-5 years for both of us. As of this point, I feel it was one of my best decisions I have ever made within 5 years – I wish somewhat similar for him as well.

Many thanks to committee members too; Profs. Lively, Walton, Realff, and Prof. Gumbart. Especially ChBE faculties were beyond committee members; they were all super helpful "collaborative" advisors during my study. I greatly appreciate simulating discussions with them. It was my pleasure to work with their students and post-doctoral member as well, Stephen, Eli, and Héctor, as a team for past years. I wish to thank all of Sholl group members for sure. There were a lot of changes in members during past 4 years, but I want to emphasize that I will never forget their warm supports both in academic and personal perspectives. I look forward to meeting with you in the future in better places.

I have had two supportive groups during my time at Georgia Tech – Korean graduate students at ChBE and Dokdo United which is a Korean graduate student soccer team at Georgia Tech. With friends in ChBE, I could have lots of fruitful and memorable talks (sometimes regarding research, but not often to be honest) and activities – thanks a million times. Without friends in Dokdo United, I could not have any positive interactions with friends outside ChBE and/or Georgia Tech, and could not stay healthy as I am now – thanks a lot for the times they shared with me.

I am now heading to the National Energy Technology Laboratory as a post-doctoral researcher at Computational Materials Engineering Team. I always had wished to have post-doctoral experience as my last step towards the real world, no matter what I do later on. I hope I can achieve higher goals at NETL as I dreamed, and wish to make good scientific contributions based on what I have learned during Ph.D. Again I appreciate Drs. Sholl and Lively for their recommendations for this position.

Last of all and most importantly, I owe the best appreciation to my family – father, mother, and a little sister – in Korea. Without all of their loves and encouragements, over the Pacific Ocean, none of my journeys were possible. I cannot think of any excellent words in any languages, to describe how much I love them and how pleasant I am to have them as my dad, mom, and sister. Writing few words here would never ever be enough to describe my appreciation for them, but I want to highlight that this thesis is also heavily dedicated to my family – thank you.

Please note below information for financial supports and work contributions:

The contents of Chapters 2, 3, and 4 in this dissertation were financially supported by the U.S. Department of Energy through grant DE-FE0026433 through a project titled "Enabling 10 mol/kg swing capacity via heat integrated sub-ambient pressure swing adsorption". Any options, findings, conclusions or recommendations expressed here do not necessarily reflect the views of the Department of Energy. Special thanks to Dr. Héctor Octavio Rubiera Landa for providing the process optimization modeling results as the partial contents in Chapter 4.

The content of Chapter 5 in this dissertation was financially supported by the Sandia National Laboratories. Sandia National Laboratories is a multimission laboratory managed and operated by National Technology and Engineering Solutions of Sandia, LLC., a wholly owned subsidiary of Honeywell International, Inc., for the U.S. Department of Energy's National Nuclear Security Administration under contract DE-NA-0003525. Special thanks to Mayank Agrawal for supporting with the generation of MD structure snapshots as the resources in Chapter 5.

TABLE OF CONTENTS

LIST OF TABLES

LIST OF FIGURES

SUMMARY

Developing cost-effective and less energy-intensive carbon capture processes for dilute CO_2 sources is of high interest. Adsorption-based CO_2 capture such as pressure swing adsorption (PSA) is one promising approach to this challenge. PSA and other cyclic adsorption processes are materials-enabled separations that use porous adsorbents, including metal-organic frameworks (MOFs). This thesis examines post-combustion carbon capture in sub-ambient PSA, a potential route to an effective adsorption process, using MOF materials *via* molecular modeling.

We first estimated the reproducibility of CO_2 adsorption isotherm measurements in MOFs *via* literature meta-analysis. This chapter provides a comprehensive summary of the state of knowledge regarding CO_2 adsorption in MOFs and its implications for molecular modeling of adsorption in MOFs. We then examined the upper bounds on CO_2 swing capacity in sub-ambient PSA by Grand Canonical Monte Carlo (GCMC) simulation of an extensive collection of MOFs. A wide variety of MOFs was found to have swing capacity exceeding 10 mol/kg at sub-ambient temperatures provided that MOFs are appropriately selected based on their physical properties. We also assessed the capability of simple proxies for adsorbent performance and approximate models of cyclic adsorption to predict the outcomes of detailed process models of adsorption-based CO_2 capture processes. To this end, we discuss the correlations between predictions from the simpler models and detailed process models.

As a separate contribution, molecular modeling of chemical warfare agents (CWAs) adsorption in MOFs was analyzed. Molecular models of adsorption of CO_2, CWAs or other molecules typically employ a rigid framework approximation for computational convenience. All real frameworks including MOFs, however, have intrinsic flexibility due to thermal vibrations. We examine the implications of this simple observation for quantitative predictions of the properties of adsorbed CWAs.

CHAPTER 1. INTRODUCTION

1.1 POST-COMBUSTION CO_2 CAPTURE AND SEPARATION

Developing efficient methods to separate chemical mixtures into pure or purer forms are of interest for many engineers both in academia and industry.[1] Physical and chemical separation processes currently account for 10–15% of the world-wide energy consumption.[1-3] In this context, the improvement of the separation process of greenhouse gases such as CO_2 from dilute emissions would gain significant global benefits.

Anthropogenic CO_2 emissions are one of the main drivers of global climate change. It is, however, challenging and expensive to capture CO_2 from dilute sources such as power plants, refinery exhausts, and air.[1,4] Stationary point sources, like power plants, are practical locations to implement CO_2 capture technology.[5] There are three scenarios where CO_2 can be captured and separated in power plants: pre-combustion, oxy-fuel combustion, and post-combustion. Figure 1.1 lays out these general options of CO_2 capture methods and frequently used materials for each option.[6] The selection of CO_2 capture technology is based on the fuel composition, the heat, the influence of water, the resulting partial pressure of the gas mixture, and the configuration of the power plant.[7] Post-combustion CO_2 capture and separation is the main scenario where substantial efforts have been undertaken to develop more cost-effective and less energy-intensive processes. The major challenge in the post-combustion process is in separating the low concentration of CO_2 out of the high concentration of N_2. The processes of absorption, adsorption, cryogenic distillation, membranes, and gas hydrates have been found to be potential candidates for post-combustion CO_2 capture.[8]

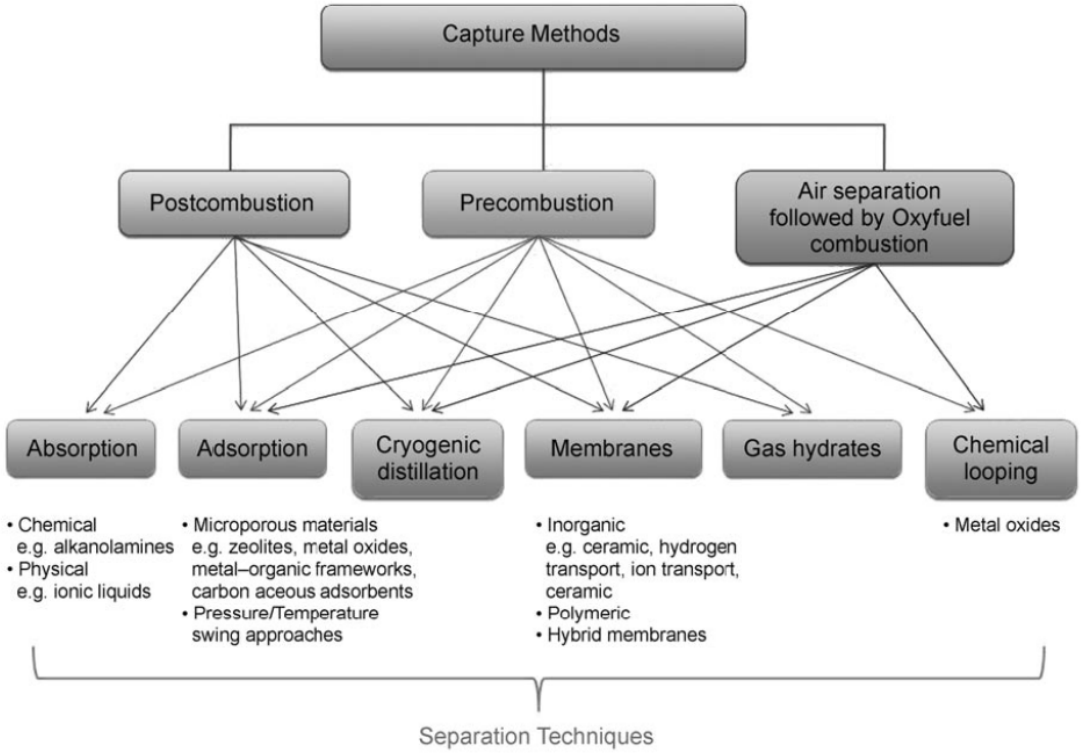

Figure 1.1. Methods and materials for CO_2 capture and separation possible for each combustion process. Post-combustion CO_2 capture can play a key role in addressing CO_2 emission concerns. Figure adapted from D'Alessandro et al.[6]

One promising separations process is *via* adsorption of desired gas molecules using solid physical adsorbents in packed or fluidized adsorbent beds.[9] CO_2 adsorption involves either physisorption derived by van der Waals interaction or chemisorption derived by covalent bonding between the CO_2 molecules and the surface of a material. Cyclic adsorption processes include the processes in which desorption is induced by pressure swing (pressure swing adsorption, PSA), temperature swing (temperature swing adsorption, TSA), or vacuum swing (vacuum swing adsorption, VSA).[4,9-12] Because of its low energy requirement and fast regeneration, PSA is used as a commercial technology for a number of applications.[11] In a PSA process, the feed gas flows through a packed bed of adsorbent at elevated pressure until the concentration of the desired gas approaches equilibrium, which is then regenerated by reducing the pressure. VSA has a similar

operating principle with PSA, but regeneration is accomplished using pressures below 1.0 bar.[11,12]

1.1.1 Metal-Organic Frameworks

Cyclic adsorption processes are materials-enabled separations that use porous adsorbents. Porous solid adsorbents such as activated carbon, zeolites, and metal-organic frameworks (MOFs) have been considered as efficient materials for adsorptive CO_2 capture and separation.[4,13-15] MOFs, also known as porous coordination polymers, are an emerging class of crystalline porous materials that consist of metal or metal-oxide corners connected by organic linkers. They have attracted considerable attention due to their structural properties including high surface area, high porosity and low crystal density.[4-6,14-20] The major advantages of MOFs over traditional porous materials are the greater scope for tailoring these materials for specific applications because of their modular synthesis.[16,17] Investigation of these materials for CO_2 capture and separation has become very active in the past years[4-6,15] both experimentally and computationally.[21-26]

For the purpose of computational examination of MOF materials, Chung et al. developed a computation-ready, experimental (CoRE) MOF database.[27] The CoRE MOF database (Figure 1.2) contains over 5,000 crystal structures that are made up of experimentally reported existing structures. This database allows high-throughput computational screening of MOFs for adsorption and/or diffusion modeling in these materials. The frameworks are optimized *via* density functional theory (DFT) calculation with the PBE functional[28,29] that allows reliable adsorption modeling of CO_2 and other gas species.

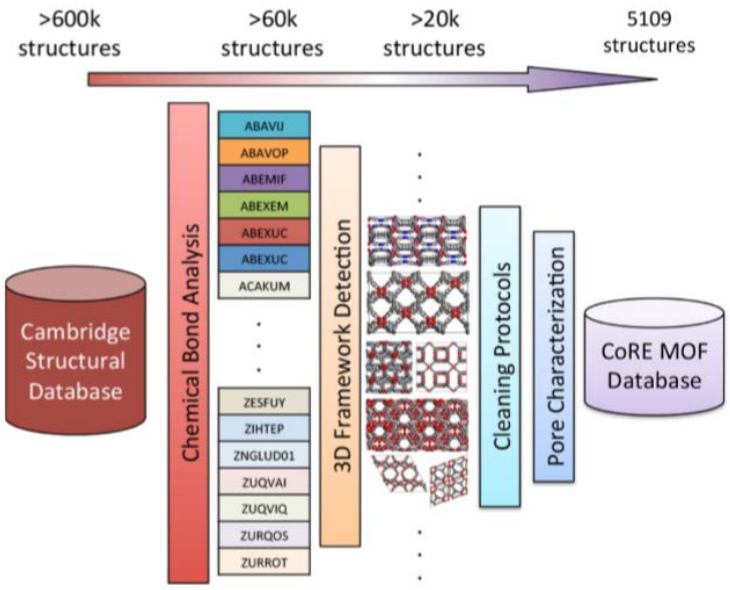

Figure 1.2. Schematic illustration for construction of CoRE MOF database as adapted from Chung et al.[27] All structures in the CoRE MOF database have pore limiting diameters larger than 2.4 Å.

1.2 SUB-AMBIENT GAS PROCESSING FOR CO_2 CAPTURE

Besides the development of porous adsorbent materials, designing a proper process strategy is another key in an attempt to create a productive CO_2 capture route. To evaluate the feasibility of processes and adsorbent materials, adsorbent evaluation criteria have been proposed.[21-26] The criteria that are typically used to assess a large number of adsorbent candidates for capturing gas species of interest (i) include swing capacity (ΔN_i), adsorption selectivity ($S_{ads,i/j}$), and the regenerability of adsorbent.[11,21]

The concept of sub-ambient operation has been widely discussed as a route to improve H_2 capacity in applications of porous materials for H_2 storage.[30] A general strategy for increasing PSA swing capacity for weakly adsorbing species like H_2 and CO_2 is to lower the operation temperature. It is widely assumed, however, that the cooling cost associated with sub-ambient processes make these conditions impractical for large-scale

CO_2 capture from flue gases. Recently, however, Air Liquide had developed a prospective technology for cost and energy effective post-combustion CO_2 capture from power plant flue gas *via* an energy integrated cold membrane process.[31-34] They designed a hybrid CO_2 capture process based on sub-ambient temperature operation of a hollow fiber membrane in combination with cryogenic distillation. The pre-treated flue gas is compressed and dried before being fed into the low-temperature membrane system. A highly selective cold membrane provides pre-concentration of CO_2 prior to partial condensation in the CO_2 liquefier. Liquid CO_2 is pumped from the phase separator to provide a sequestration-ready product, and vent from the CO_2 liquefier is recycled to the low-temperature membrane system. The cryogenic heat exchanger provides energy integration between the low temperature membrane and CO_2 liquefier. These developments suggest that large-scale selective adsorption of CO_2 with sub-ambient operation may be viable when coupled with heat integration and power recovery.[12,31-34] A schematic diagram of this sub-ambient membrane process is shown in Figure 1.3.

Air Liquide had also performed an extensive techno-economic analysis of a process for compressing and cooling flue gas to conditions giving 14 bar in total pressure, i.e. partial pressure of around 2.0 bar of CO_2, at 240 K.[31-33] It suggests that the pressure swing range within moderate CO_2 partial pressures up to 2.0 bar is feasible to deliver cold, compressed flue gas to a sub-ambient gas processing system. In this thesis, a PSA process which combines sub-ambient gas processing and adopting low regeneration pressure to avoid a cost-prohibitive pressurization step[35] is the target system for adsorptive CO_2 capture from post-combustion flue gas.

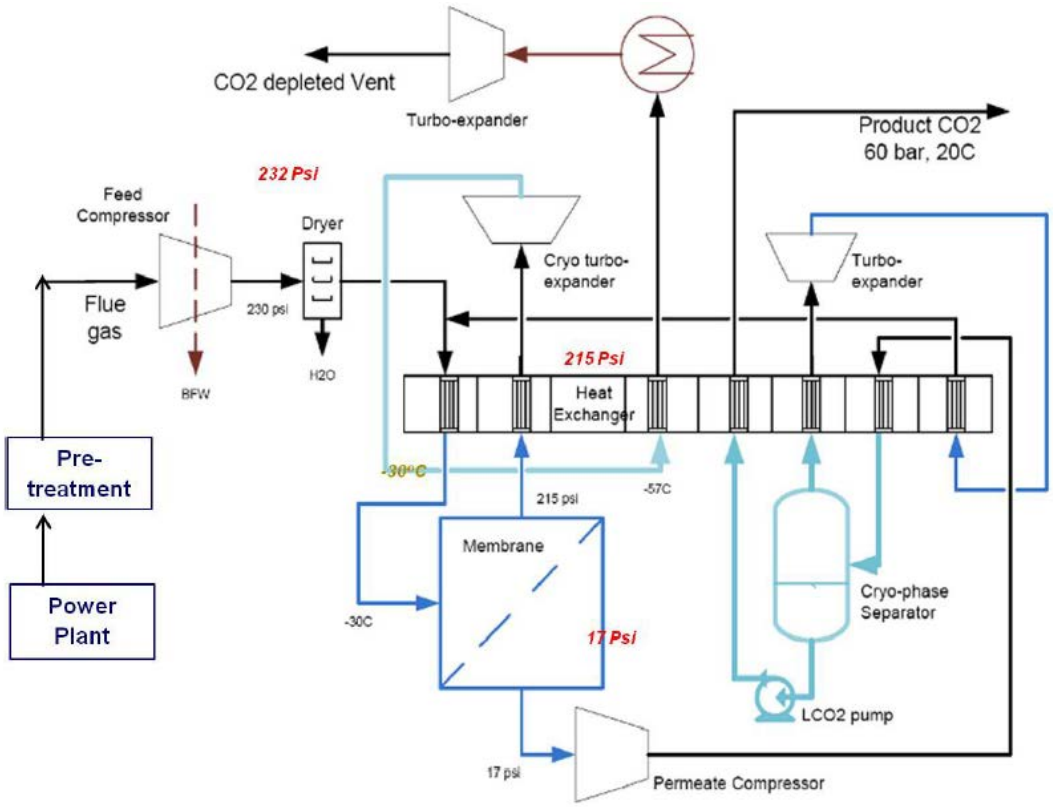

Figure 1.3. Schematic diagram of sub-ambient membrane-based CO_2 cryogenic purification unit process as adapted from Hasse et al.[33] Sub-ambient gas processing can be adopted in energy-intensive rapidly cycled PSA process for adsorptive CO_2 capture and separation applications by utilizing MOFs.

1.3 MOLECULAR SIMULATION FOR ADSORPTION MODELING

Computational chemistry methods can provide a detailed picture on the molecular scale that is not easily accessible from experimental methods for a variety of applications.[36-38] They offer an additional dimension to the characterization and understanding of systems in the fields of physical, chemical, and materials sciences. The computational approaches that are commonly used to investigate systems at atomistic level are quantum mechanical calculations and force field-based simulations.[39,40] The former category is required when examining the electronic nature of material properties such as bond breakage and formation. The latter method is applicable when studying larger systems and when investigating a wide variety of thermodynamic and dynamic properties. Force

field-based classical simulations typically include energy minimization of structures, molecular dynamics simulations, and Monte Carlo simulations.

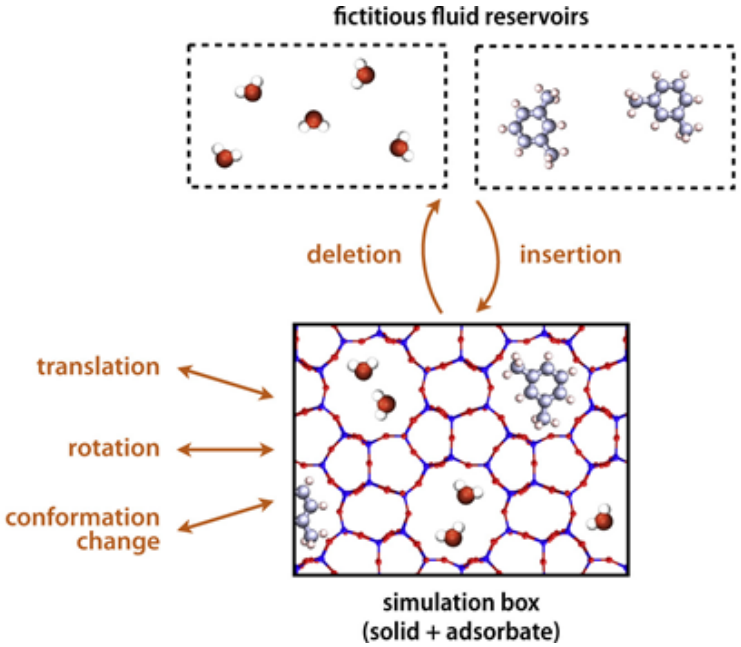

Figure 1.4. Schematic diagram of the Monte Carlo simulation of adsorption in a porous material in the Grand Canonical thermodynamic ensemble, Ξ (μ, V, T), as adapted from Coudert et al.[37]

Force field-based classical molecular simulations are a useful tool to quantitatively predict adsorption behavior and to gain insight into the corresponding molecular level phenomena.[36] They also provide an efficient method that can be used to screen existing and/or hypothetical crystal structures for specific applications which allow narrowing down the search to a subset of promising structures.[25,36,39] Furthermore, the molecular level insights can be combined to develop design principles for specific applications.[25,36] The standard force field-based molecular simulation to predict adsorption equilibrium is Grand Canonical Monte Carlo (GCMC) simulation (illustrated in Figure 1.4). GCMC holds the chemical potential (μ), volume (V), and temperature (T) constant while allowing the number of adsorbate molecules (N) to fluctuate. Fugacity needs to be imposed, which determines the chemical potential; fugacity can be converted from pressure using the Peng-

Robinson equation of state (or another appropriate equation of state).[39,40] GCMC mimics the experimental equilibrium conditions where the chemical potential and the temperature between solid reservoir and external gas fluid must be equal.

To model adsorption equilibrium by such a systematic computational approach, van der Waals interactions and electrostatic interactions are taken into account.[41] Appropriate force fields are required to describe van der Waals interactions for adsorbate-adsorbent interactions and adsorbate-adsorbate interactions.[42] The van der Waals interactions are modeled by the conventional Lennard-Jones potential:

$$V_{ij}(r_{ij}) = 4\varepsilon_{ij}\left[\left(\frac{\sigma_{ij}}{r_{ij}}\right)^{12} - \left(\frac{\sigma_{ij}}{r_{ij}}\right)^{6}\right]$$

where i and j stand for interacting atoms, and r_{ij} is the distance between interacting atoms. ε_{ij} and σ_{ij} refer to Lennard-Jones energy and length parameter, respectively. The use of generic force fields such as the universal force field (UFF)[43] and the transferable potentials for phase equilibria (TraPPE) force field[44] for material screening purpose is reasonably well justified.[42] Therefore, Lennard-Jones parameters for framework atoms and adsorbate molecules can be taken from UFF and TraPPE force field, respectively, in general. The van der Waals interactions between adsorbate-adsorbent are typically defined with the Lorentz-Berthelot mixing rules[45]:

$$\sigma_{ij} = \frac{\sigma_i + \sigma_j}{2} \qquad \varepsilon_{ij} = \sqrt{\varepsilon_i \varepsilon_j}$$

Electrostatic interactions are typically modeled pairwise with a long-range Ewald summation scheme[46] by employing charges for framework atoms and adsorbate molecules. One of multiple methods to assign electrostatic charges to framework atoms is the density

derived electrostatic and chemical (DDEC) method.[47-49] It is based on the electron density partitioning in periodic structures. The point charges are found by minimizing an optimization functional to reproduce both the charge distribution and local electrostatic potential.[47-49]

Isosteric heats of adsorption (Q_{ads}) are another thermodynamic quantity that can be computed during GCMC simulations based on the fluctuation method.[39,40] These calculations use the expression

$$Q_{ads} = RT - \frac{< NV > - < N >< V >}{< N^2 > - < N >^2}$$

where *R*, *T*, and *N* refers to the ideal gas constant, temperature, and the number of adsorbed molecules, respectively. *V* means the sum of the interactions of all adsorbed molecules among themselves and with adsorbent. < > is an ensemble average over the Monte Carlo steps.

Typically, GCMC simulations assume that the adsorbents are rigid, that is, relaxation of the framework atoms due to the presence of adsorbed molecules is neglected. Chapter 5 of this thesis examines some implications of this common assumption. Periodic boundary conditions are defined in all dimensions allowing simulations to occur in an infinite, perfect crystal structure.[41] In general, GCMC simulation procedure includes initialization cycles followed by production cycles, where each cycle consists of *N* steps.[41] This is to ensure well converged results for adsorption amount of gas molecules at desired pressure points. Random Monte Carlo moves, either accepted or rejected according to Boltzmann-type weighting criteria, allow translation, rotation, regrowth, reinsertion, deletion and insertion moves of gas molecules at certain probabilities.[41]

1.4 REFERENCES

(1) Sholl, D. S.; Lively, R. P. Seven chemical separations to change the world. *Nature* **2016,** *532*, 435-437.

(2) Oak Ridge National Laboratory. *Materials for Separation Technologies: Energy and Emission Reduction Opportunities*, Oak Ridge National Laboratory, **2005**.

(3) Humphrey, J.; Keller, G. E. *Separation Process Technology*, McGraw-Hill: New York, **1997**.

(4) Choi, S.; Drese, J. H.; Jones, C. W. Adsorbent Materials for Carbon Dioxide Capture from Large Anthropogenic Point Sources. *ChemSusChem* **2009,** *2*, 796-854.

(5) Sumida, K.; Rogow, D. L.; Mason, J. A.; McDonald, T. M.; Bloch, E. D.; Herm, Z. R.; Bae, T. H.; Long, J. R. Carbon Dioxide Capture in Metal-Organic Frameworks. *Chem. Rev.* **2012,** *112*, 724-781.

(6) D'Alessandro, D. M.; Smit, B.; Long, J. R. Carbon Dioxide Capture: Prospects for New Materials. *Angew. Chem. Int. Ed.* **2010,** *49*, 6058-6082.

(7) Rao, A. B.; Rubin, E. S. A technical, economic, and environmental assessment of amine-based CO_2 capture technology for power plant greenhouse gas control. *Environ. Sci. Technol.* **2002,** *36*, 4467-4475.

(8) Wilcox, J. *Carbon capture*, Springer: New York, **2012**.

(9) Ruthven, D. *Principles of Adsorption & Adsorption Processes*, Wiley: New York, **1984**.

(10) Yang, R. T. *Gas Separation by Adsorption Processes*, Imperial College Press: London, **1987**.

(11) Bae, Y. S.; Snurr, R. Q. Development and Evaluation of Porous Materials for Carbon Dioxide Separation and Capture. *Angew. Chem. Int. Ed.* **2011,** *50*, 11586-11596.

(12) Hedin, N.; Andersson, L.; Bergstrom, L.; Yan, J. Y. Adsorbents for the post-combustion capture of CO_2 using rapid temperature swing or vacuum swing adsorption. *Appl. Energy* **2013,** *104*, 418-433.

(13) Ferey, G.; Mellot-Draznieks, C.; Serre, C.; Millange, F. Crystallized frameworks with giant pores: Are there limits to the possible? *Acc. Chem. Res.* **2005,** *38*, 217-225.

(14) Meek, S. T.; Greathouse, J. A.; Allendorf, M. D. Metal-Organic Frameworks: A Rapidly Growing Class of Versatile Nanoporous Materials. *Adv. Mater.* **2011,** *23*, 249-267.

(15) Keskin, S.; van Heest, T. M.; Sholl, D. S. Can Metal-Organic Framework Materials Play a Useful Role in Large-Scale Carbon Dioxide Separations? *ChemSusChem* **2010,** *3*, 879-891.

(16) Ferey, G. Hybrid porous solids: past, present, future. *Chem. Soc. Rev.* **2008,** *37*, 191-214.

(17) Yaghi, O. M.; O'Keeffe, M.; Ockwig, N. W.; Chae, H. K.; Eddaoudi, M.; Kim, J. Reticular synthesis and the design of new materials. *Nature* **2003,** *423*, 705-714.

(18) Furukawa, H.; Cordova, K. E.; O'Keeffe, M.; Yaghi, O. M. The Chemistry and Applications of Metal-Organic Frameworks. *Science* **2013,** *341*, 974-985.

(19) Furukawa, H.; Ko, N.; Go, Y. B.; Aratani, N.; Choi, S. B.; Choi, E.; Yazaydin, A. O.; Snurr, R. Q.; O'Keeffe, M.; Kim, J.; Yaghi, O. M. Ultrahigh Porosity in Metal-Organic Frameworks. *Science* **2010,** *329*, 424-428.

(20) Farha, O. K.; Yazaydin, A. O.; Eryazici, I.; Malliakas, C. D.; Hauser, B. G.; Kanatzidis, M. G.; Nguyen, S. T.; Snurr, R. Q.; Hupp, J. T. *De novo* synthesis of a metal-organic framework material featuring ultrahigh surface area and gas storage capacities. *Nat. Chem.* **2010,** *2*, 944-948.

(21) Wilmer, C. E.; Farha, O. K.; Bae, Y. S.; Hupp, J. T.; Snurr, R. Q. Structure-property relationships of porous materials for carbon dioxide separation and capture. *Energ. Environ. Sci.* **2012,** *5*, 9849-9856.

(22) Simmons, J. M.; Wu, H.; Zhou, W.; Yildirim, T. Carbon capture in metal-organic frameworks-a comparative study. *Energ. Environ. Sci.* **2011,** *4*, 2177-2185.

(23) Lin, L. C.; Berger, A. H.; Martin, R. L.; Kim, J.; Swisher, J. A.; Jariwala, K.; Rycroft, C. H.; Bhown, A. S.; Deem, M. W.; Haranczyk, M.; Smit, B. *In silico* screening of carbon-capture materials. *Nat. Mater.* **2012,** *11*, 633-641.

(24) Wu, D.; Yang, Q. Y.; Zhong, C. L.; Liu, D. H.; Huang, H. L.; Zhang, W. J.; Maurin, G. Revealing the Structure-Property Relationships of Metal-Organic Frameworks for CO_2 Capture from Flue Gas. *Langmuir* **2012,** *28*, 12094-12099.

(25) Colon, Y. J.; Snurr, R. Q. High-throughput computational screening of metal-organic frameworks. *Chem. Soc. Rev.* **2014,** *43*, 5735-5749.

(26) Yazaydin, A. O.; Snurr, R. Q.; Park, T. H.; Koh, K.; Liu, J.; LeVan, M. D.; Benin, A. I.; Jakubczak, P.; Lanuza, M.; Galloway, D. B.; Low, J. J.; Willis, R. R. Screening of Metal-Organic Frameworks for Carbon Dioxide Capture from Flue Gas Using a Combined Experimental and Modeling Approach. *J. Am. Chem. Soc.* **2009,** *131*, 18198-18199.

(27) Chung, Y. G.; Camp, J.; Haranczyk, M.; Sikora, B. J.; Bury, W.; Krungleviciute, V.; Yildirim, T.; Farha, O. K.; Sholl, D. S.; Snurr, R. Q. Computation-Ready, Experimental Metal-Organic Frameworks: A Tool To Enable High-Throughput Screening of Nanoporous Crystals. *Chem. Mater.* **2014,** *26*, 6185-6192.

(28) Nazarian, D.; Camp, J. S.; Chung, Y. G.; Snurr, R. Q.; Sholl, D. S. Large-Scale Refinement of Metal-Organic Framework Structures Using Density Functional Theory. *Chem. Mater.* **2017,** *29*, 2521-2528.

(29) Nazarian, D.; Camp, J. S.; Sholl, D. S. A Comprehensive Set of High-Quality Point Charges for Simulations of Metal-Organic Frameworks. *Chem. Mater.* **2016,** *28*, 785-793.

(30) Tedds, S.; Walton, A.; Broom, D. P.; Book, D. Characterisation of porous hydrogen storage materials: carbons, zeolites, MOFs and PIMs. *Faraday Discuss.* **2011,** *151*, 75-94.

(31) Hasse, D. J.; Kulkarni, S. S.; Sanders Jr., E. S.; Tranier, J. P.; Terrien, P. Method of Obtaining Carbon Dioxide From a Carbon Dioxide-Containing Gas Mixture. EP Patent 2,512,634, **2012**.

(32) Hasse, D.; Kulkarni, S.; Sanders, E.; Corson, E.; Tranier, J. P. CO_2 capture by sub-ambient membrane operation. *Energy Procedia* **2013,** *37*, 993-1003.

(33) Hasse, D.; Ma, J.; Kulkarni, S.; Terrien, P.; Tranier, J. P.; Sanders, E.; Chaubey, T.; Brumback, J. CO_2 Capture by Cold Membrane Operation. *Energy Procedia* **2014,** *63*, 186-193.

(34) Liu, L.; Sanders, E. S.; Kulkarni, S. S.; Hasse, D. J.; Koros, W. J. Sub-ambient temperature flue gas carbon dioxide capture via Matrimid® hollow fiber membranes. *J. Membrane Sci.* **2014,** *465*, 49-55.

(35) Chaffee, A. L.; Knowles, G. P.; Liang, Z. J.; Zhang, J.; Xiao, P.; Webley, P. A. CO_2 capture by adsorption: Materials and process development. *Int. J. Greenh. Gas Con.* **2011,** *5*, 1368-1368.

(36) Duren, T.; Bae, Y. S.; Snurr, R. Q. Using molecular simulation to characterise metal-organic frameworks for adsorption applications. *Chem. Soc. Rev.* **2009,** *38*, 1237-1247.

(37) Coudert, F. X.; Fuchs, A. H. Computational characterization and prediction of metal-organic framework properties. *Coord. Chem. Rev.* **2016,** *307*, 211-236.

(38) Li, J. R.; Ma, Y. G.; McCarthy, M. C.; Sculley, J.; Yu, J. M.; Jeong, H. K.; Balbuena, P. B.; Zhou, H. C. Carbon dioxide capture-related gas adsorption and separation in metal-organic frameworks. *Coord. Chem. Rev.* **2011,** *255*, 1791-1823.

(39) Dubbeldam, D.; Calero, S.; Ellis, D. E.; Snurr, R. Q. RASPA: molecular simulation software for adsorption and diffusion in flexible nanoporous materials. *Mol. Simulat.* **2016,** *42*, 81-101.

(40) Dubbeldam, D.; Torres-Knoop, A.; Walton, K. S. On the inner workings of Monte Carlo codes. *Mol. Simulat.* **2013,** *39*, 1253-1292.

(41) Frenkel, D.; Smit, B. *Understanding of Molecular Simulation: from Algorithms to Applications*, Academic Press: San Diego, **2002**.

(42) Addicoat, M. A.; Vankova, N.; Akter, I. F.; Heine, T. Extension of the Universal Force Field to Metal-Organic Frameworks. *J. Chem, Theory Comput.* **2014,** *10*, 880-891.

(43) Rappe, A. K.; Casewit, C. J.; Colwell, K. S.; Goddard, W. A.; Skiff, W. M. UFF, A Full Periodic-Table Force-Field for Molecular Mechanics and Molecuar Dynamics Simulations. *J. Am. Chem. Soc.* **1992,** *114*, 10024-10035.

(44) Martin, M. G.; Siepmann, J. I. Transferable potentials for phase equilibria. 1. United-atom description of n-alkanes. *J. Phys. Chem. B* **1998,** *102*, 2569-2577.

(45) Allen, M. P.; Tildesley, D. J. *Computer Simulation of Liquids*, Oxford University Press: New York, **1987**.

(46) Wells, B. A.; Chaffee, A. L. Ewald Summation for Molecular Simulations. *J. Chem, Theory Comput.* **2015,** *11*, 3684-3695.

(47) Manz, T. A.; Sholl, D. S. Chemically Meaningful Atomic Charges That Reproduce the Electrostatic Potential in Periodic and Nonperiodic Materials. *J. Chem, Theory Comput.* **2010,** *6*, 2455-2468.

(48) Manz, T. A.; Sholl, D. S. Improved Atoms-in-Molecule Charge Partitioning Functional for Simultaneously Reproducing the Electrostatic Potential and Chemical States in Periodic and Nonperiodic Materials. *J. Chem, Theory Comput.* **2012,** *8*, 2844-2867.

(49) Watanabe, T.; Manz, T. A.; Sholl, D. S. Accurate Treatment of Electrostatics during Molecular Adsorption in Nanoporous Crystals without Assigning Point Charges to Framework Atoms. *J. Phys. Chem. C* **2011,** *115*, 4824-4836.

CHAPTER 2. HOW REPRODUCIBLE ARE ISOTHERM MEASUREMENTS IN METAL-ORGANIC FRAMEWORKS?

Scientific progress is severely impeded if experimental measurements are not reproducible. Materials chemistry and related fields commonly report new materials with limited attention paid to reproducibility. In this chapter, we describe methods that are well suited for assessing reproducibility in these fields *via* retrospective analysis of reported data. This concept is illustrated by an exhaustive analysis of a topic that has been the focus of thousands of published studies, gas adsorption in metal-organic framework (MOF) materials. We show that for the well-studied case of CO_2 adsorption there are only 15 of the thousands of known MOFs for which enough experiments have been reported to allow strong conclusions to be drawn about the reproducibility of these measurements. Our results have immediate implications for the characterization of gas adsorption in porous materials, but more importantly, demonstrate an approach to assessing reproducibility that will be widely applicable in materials chemistry.

* Contents of this chapter have been reproduced from the previously published article

Jongwoo Park, Joshua D. Howe, David S. Sholl, ″How Reproducible Are Isotherm Measurements in Metal-Organic Frameworks?″, ***Chemistry of Materials***, 29 (2017) 10487-10495.

2.1 INTRODUCTION

Substantial efforts have been undertaken recently to examine reproducibility in fields including psychology[1,2] and biomedical science[3,4]. In this chapter, we examine the reproducibility of experimental measurements in a subfield of materials chemistry that has generated tens of thousands of publications, namely the properties of metal-organic frameworks (MOFs).[5,6] Specifically, we consider the measurement of equilibrium single-component adsorption isotherms in these materials. Adsorption isotherms are a fundamental property for considering MOFs and similar materials in applications involving chemical separations,[7] and thousands of papers have been published related to these applications.[8,9] We examine the issue of reproducibility by a meta-analysis of an exhaustive compilation of adsorption isotherms in MOFs.

Single-component adsorption isotherms quantify the amount of an adsorbing species (the sorbate) on the internal and external surfaces of a material (the sorbent) in equilibrium with a bulk phase of the species at a well-defined pressure. These isotherms can be routinely measured using widely available commercial instruments, provided hundreds of milligrams of the sorbent of interest are available. Assuming proper equilibration and preparation of the system, this implies that differences, if they exist, between measured isotherms for the same material will typically be related to variations in the underlying material's properties. Thousands of distinct MOFs have been synthesized and characterized,[10] and adsorption isotherms have been reported for many of these materials. Recently, NIST has developed a publicly available database that systematically collects single-component adsorption data reported for MOFs (and other sorbents) from the peer-reviewed literature.[11] Although no data set of this type can be truly complete, this

database captures the vast majority of extant experimental adsorption data for MOFs. In this chapter, we analyze this data set to examine what can be concluded about the reproducibility of CO_2 adsorption isotherms in MOFs.

Reproducibility in adsorption and materials chemistry has previously drawn interest and been discussed with regards to H_2 storage.[12,13] These works have discussed sources of irreproducibility, highlighting concerns such as methodological errors, sample contamination, and even the "publish or perish" academic culture.[12,13] H_2 adsorption is a particularly challenging case because the adsorbed amounts are typically low. For more strongly adsorbing molecules, however, measurements of adsorption isotherms are typically regarded as "routine" experiments that can be performed with widely available commercial instruments. Researchers must evaluate reports of material properties and consider them with respect to one another, so it is important to have a sense of what bounds may exist on uncertainty in material property measurements. To this end, we aim to establish uncertainty bounds across reports of adsorption isotherms when those reports purport to have measured the same material properties under comparable conditions. It is important to note that this approach does not seek to assign causes to underlying variations between experimental measurements.

We have established simple statistical metrics for and provided a comprehensive analysis of what is known about the reproducibility of adsorption isotherms in MOF materials. As examples, we have cataloged all materials for which repeat measurements of CO_2 adsorption have been reported. We also report a long list of molecules for which no repeat measurements have been reported in any MOFs. In addition to the immediate relevance to measurements of this large class of materials, the methods we have used here

could be applied with only minor modifications to a very wide class of materials chemistry problems. Widespread adoption of this kind of analysis could aid the reproducibility and, ultimately, the assessment of utility of new materials in many applications.

2.2 METHODS

2.2.1 A Taxonomy for Describing Reproducibility of Adsorption Isotherms

All adsorption data were obtained from the NIST/ARPA-E Adsorption Database[11] cataloged as NIST Standard Reference Database (SRD) 205, which reproduces data from peer-reviewed literature reports. This source includes experimental and modeling results, but only experimental data were used in our analysis. Many published reports do not distinguish between absolute and excess adsorbed amounts. The differences between these two quantities are small at all conditions we considered. In addition, the hysteresis between adsorption and desorption branches was negligible in all cases we considered, if any desorption branches were reported.

We consider a situation where the adsorbed amount of a specific molecule in a given sorbent is available over a range of pressures, P, from N independently measured isotherms measured at a temperature $T \pm 5$ K. Using this range of temperatures increases the number of replicate experiments than can be identified by grouping experiments that most practitioners would consider to have "similar" temperatures into a single class. Examples for adsorption of CO_2 at 298 ± 5 K in HKUST-1 (a material first reported by Chui *et al.*[14] and also frequently known as Cu-BTC) with $N = 18$ and UiO-66 (a material first reported by Cavka *et al.*[15]) with $N = 9$ are shown in Figures 2.1a and 2.2a. Visual inspection of these figures indicates that both sets of data include isotherms that are likely

to be outliers and the variation between measurements is much smaller for UiO-66 than for HKUST-1. It is important, however, to use well-defined metrics that do not rely on qualitative judgments about the underlying data to assess these features. We define metrics for this purpose below.

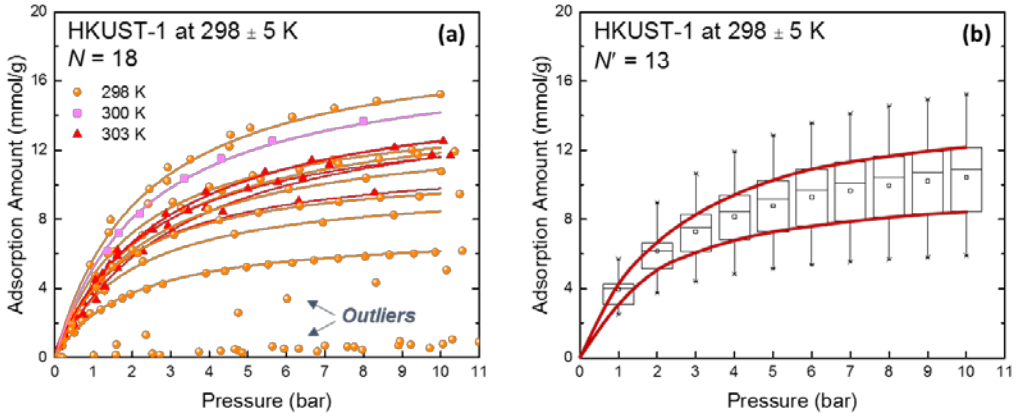

Figure 2.1. (a) Experimental data from 18 independent measurements of CO_2 adsorption in HKUST-1 at 298 ± 5 K listed in the NIST/ARPA-E Adsorption Database, with temperatures indicated by color and symbol type. Outliers identified by the methods defined in the text are indicated. Solid curves show the fitted functions used in analysis of the data. (b) Box and whisker plot for 13 independent measurements of CO_2 adsorption in HKUST-1 at 298 ± 5 K obtained after rejecting outliers. In each box and whisker plot the top and bottom of the box indicate the upper quartile (Q_U) and lower quartile (Q_L), respectively, the center line denotes the median, the square corresponding to the mean, and the whiskers indicate Q_L – 1.5IQR and Q_U + 1.5IQR, where the interquartile range IQR = $Q_U - Q_L$.

To allow direct comparison among all N measurements at the same values of P, continuous adsorption isotherms were fitted to each experiment, choosing functional forms that give fits with a high value of R^2 without accounting for the small variations in the number of fitting parameters between functional forms. The functional forms adopted here include Langmuir, Freundlich, and Langmuir-Freundlich isotherm models. The solid curves in Figures 2.1a and 2.2a show examples of this procedure. All further analysis is performed using adsorbed amounts defined by these fitted isotherms. When $N > 4$, outliers

are identified by Tukey's method[16] as values lying outside the range of a standard box and whisker plot. This approach designates 5 isotherms for HKUST-1 (Figure 2.1a) and 1 isotherm for UiO-66 (Figure 2.2a) as outliers (data shown without fitted curves). We denote the number of independent experiments in a given pressure range after removing outliers as N'. We designate sets of data for which outliers have been removed in this way as having outlier level O1.

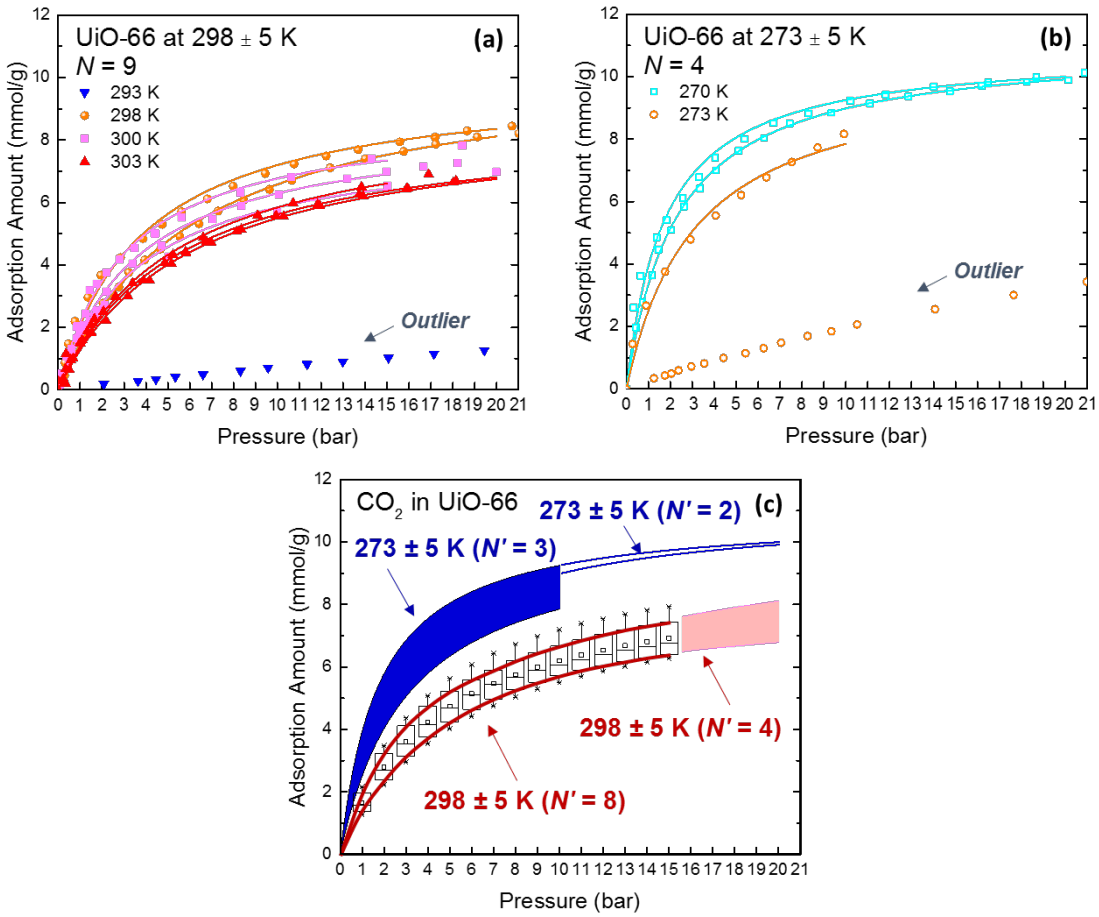

Figure 2.2. Experimental data from (a) 9 independent measurements of CO_2 adsorption in UiO-66 at 298 ± 5 K and (b) 4 independent measurements of CO_2 adsorption in UiO-66 at 273 ± 5 K listed in the NIST/ARPA-E Adsorption Database, with temperatures indicated by color and symbol type. Outliers identified by the methods defined in the text are indicated. Solid curves show the fitted functions used in analysis of the data. (c) Summary of adsorption data for CO_2 in UiO-66 at 298 ± 5 K and 273 ± 5 K showing preferred representations of data with $N' > 4$, $N' = 3$ or 4, and $N' = 2$.

When N = 3 or 4, a box and whisker plot is not appropriate. In this case, outliers are defined as measurements where the root mean square error (RMSE) relative to the set of N measurements is larger than $\sigma/2$, where σ is the standard deviation of a comparison measurement.[17] Although it is commonly accepted that a lower RMSE indicates better agreement between two measurements, this criterion was suggested as a guideline to qualify what is considered as a low RMSE.[17] We describe this procedure in more detail in Appendix 2.A. Figure 2.2b shows an example for CO_2 adsorption in UiO-66 at 273 ± 5 K, where N = 4 and N' = 3 after identifying 1 isotherm as an outlier. Data sets with outliers removed in this way are designated as having outlier level O2. A final case that is relatively common with experimental data is when N = 2. In this case it is not possible to identify outliers in a reliable manner, so N' = 2. We designate this situation was having outlier level O3.

In addition to designating how outliers were determined, it is useful to succinctly describe how many outliers were found, a factor we will refer to as consistency. We denote the consistency rating as either high, moderate, or low (see Table 2.1 for definitions). Isotherms are said to have high consistency when $N > 2$ and the fraction of measurements labeled as outliers (f) is ≤ 0.25. Isotherms are said to have moderate consistency when $0.25 < f \leq 0.4$ and low consistency when $f > 0.4$. When N = 2, isotherms can have at most moderate consistency (when RMSE < $\sigma/2$) and otherwise have low consistency.

Table 2.1. Outlier isotherm detection and consistency rating for adsorption isotherms in MOFs.

Outlier Level	Outlier Detection Criteria and Methods	Consistency Rating	Consistency Rating Criteria and Methods
O1	Tukey's method: $N > 4$ *Label outlier for adsorption amount outside the bounds defined by box and whisker plot*	High	Fraction of outliers, f $f \leq 0.25$
		Moderate	Fraction of outliers, f $0.25 < f \leq 0.4$
		Low	Fraction of outliers, f $f > 0.4$
O2	Error index statistics: $N = 3$ or 4 *Label outlier for isotherm curves with RMSE larger than σ/2 relative to a comparison measurement*	High	Fraction of outliers, f $f \leq 0.25$
		Moderate	Fraction of outliers, f $0.25 < f \leq 0.4$
		Low	Fraction of outliers, f $f > 0.4$
O3	$N = 2$ *Inadequate N to label outlier*	Moderate	RMSE < $\sigma/2$

It is useful to plot the conclusions from the analysis above in a way that represents the different levels of information available depending on the value of N'. Our suggested approach to this issue is illustrated in Figures 2.1b and 2.2c. When $N' > 4$, a box and whisker plot is appropriate. We refer to examples of this kind as having a reproducibility level of R1. In these cases the solid curves in Figures 2.1b and 2.2c show the interquartile range, which can be thought of as the "consensus" bounds to the measurement of the adsorbed amount as a function of P. It is important to note, however, that reported measurements can in some cases lie well outside this range, as shown for HKUST-1 in Figure 2.1b. When $N' = 3$ or 4, isotherms are plotted using a shaded region that encompasses all of the measured data, outliers excluded. Examples are shown in Figure 2.2c for CO_2 in UiO-66 at $P > 15$ bar at $T = 298 \pm 5$ K and $P < 10$ bar at $T = 273 \pm 5$ K. We refer to the reproducibility level of data of this kind as R2. Finally, when $N' = 2$, the pair of fitted isotherms is plotted, as for $P > 10$ bar at 273 ± 5 K in Figure 2.2c. We denote the

reproducibility level of examples of this kind as R3 or R4, depending on the variation between the two isotherms (see Table 2.2 for definitions). In addition to encapsulating the state of experimental knowledge in a convenient way, the information in these kinds of figures will be useful for process models that explicitly seek to incorporate parametric uncertainty.[18]

Table 2.2. Isotherm reproducibility assessment for adsorption isotherms in MOFs.

Reproducibility Level	Criteria and Methods
R1	Box isotherm: $N' > 4$ *Isotherm bounds assigned by interquartile range of adsorbed amount as a function of pressure*
R2	Region isotherm: $N' = 3$ or 4 *Isotherm bounds assigned by the upper and lower measurement over a common pressure range*
R3	$N' = 2$: *Pair of fitted isotherms with RMSE* $< \sigma/2$
R4	$N' = 2$: *Pair of fitted isotherms with RMSE* $> \sigma/2$

The discussion above has introduced three complementary characteristics of a collection of experimental isotherms, namely the outlier level (O1-O3), the consistency rating (high, moderate, low), and the reproducibility level (R1-R4). We illustrate this analysis in Appendix 2.A (Figure 2.A.1). We feel that each of these characteristics represents a different and useful facet of the overall reliability of a set of experimental measurements and considering them together provides a more nuanced view than attempting to give a simplistic binary answer to the question of whether a particular experiment is reproducible. All of the definitions above have been given in terms of data for adsorption isotherms, but they could readily be adapted to describe repeated measurements of any well-defined property of a material or chemical.

2.2.2 Molecular Simulations

Molecular simulations of CO_2 adsorption were performed in the materials for which there exist enough data in the literature to yield firm conclusions about the reproducibility of measured isotherms. Grand Canonical Monte Carlo (GCMC) simulations were conducted to study adsorption properties using RASPA.[19-21] "Standard" force fields were used to describe van der Waals interactions between sorbate/sorbent and sorbate/sorbate.[22] Lennard-Jones parameters for MOF atoms and quadrupolar CO_2 molecules were taken from the universal force field (UFF)[23] and TraPPE[24] force field, respectively. Interactions between CO_2 molecules and MOFs were defined with Lorentz-Berthelot mixing rules.[25] Electrostatic interactions were modeled by employing point charges for MOF atoms and CO_2 molecules. Point charges were assigned to MOF atoms using an extended charge equilibration method for EQeq charges[26] and TraPPE charges[24] were used for CO_2 molecules. The extended charge equilibration method for EQeq charges is a semiempirical method that is much less computationally expensive than charge assignments on the basis of electronic structure calculations.[26] Random Monte Carlo moves, either accepted or rejected according to Boltzmann-type weighting criteria, allowed translation, rotation, regrowth, reinsertion, and deletion and insertion moves at identical probabilities. All MOF structures were assumed to be rigid in their experimentally reported crystal structures. For breathing MOFs, the narrow pore or large pore rigid structure was used depending on their observed structural transition pressure and the pressure being simulated. The simulated surface area was calculated by using N_2 as a probe molecule with overlap distance criteria set to a size parameter σ of 3.31 Å. Further details are given in Appendix 2.A.

2.3 RESULTS AND DISCUSSION

2.3.1 Surface Area Analysis Affecting Gas Adsorption in MOFs

When modeling adsorption in MOFs using atomistic methods, the predicted BET surface area of the ideal crystal structure is frequently noted to differ from the measured BET surface area of synthesized materials.[27-31] These differences are often ascribed to defects in the real material, although the identity and characteristics of these defects are rarely quantified.[32] An approach that is widely used when comparing simulated and experimental data in this situation is to scale the experimental data by the ratio of the simulated and experimental surface area.[29-31] The assumption underlying this scaling is that the "non-crystalline" portions of the real material are nonporous (or, more precisely, non-adsorbing). If this assumption was correct, using scaled experimental data could give information about the "intrinsic" adsorption properties of the defect-free material. The data in Figures 2.1 and 2.2 (Section 2.2.1) create an opportunity to examine whether this approach makes the underlying experimental data more consistent. Figures 2.A.2 and 2.A.4 show the adsorption isotherms for CO_2 in HKUST-1 and UiO-66 with and without surface area scaling. For HKUST-1, scaling increases the adsorbed amount because the measured surface areas are often substantially less than the simulated surface area. This situation is not surprising given the sensitivity of HKUST-1 to exposure to even small amounts of moisture.[33] In both cases, however, surface area scaling does not significantly reduce the consensus range of adsorbed amounts. That is, the observed variations in the adsorbed amount of CO_2 in these materials cannot be ascribed simply to variations in the surface areas of the reported materials.

Nonetheless, the surface area of porous materials is an important characteristic that affects the adsorption properties of gas molecules. The reproducibility analysis metrics described in Section 2.2.1 were applied to measured N_2 adsorption isotherms at 77 K in HKUST-1 and UiO-66 to gain an understanding of the reproducibility of the surface areas of these materials. Figures 2.3a and 2.4a show histograms of the adsorbed amount of N_2 at intermediate and low P/P^o that are taken from compiling N_2 adsorption isotherms in HKUST-1 ($N = 90$, $N' = 86$) and UiO-66 ($N = 18$, $N' = 15$), respectively. Both histograms indicate considerable variation in the reported uptake of N_2. The methods described above were applied to give bounds on the consensus N_2 isotherms by connecting the upper and lower quartiles as a function of P/P^o. These isotherms were then used for surface area analysis using BET theory. Figures 2.3b and 2.4b show the BET plots for HKUST-1 and UiO-66, respectively, which were fit over $0.05 < P/P^o < 0.15$ to calculate BET surface areas. The consensus isotherms for HKUST-1 vary between 933 and 1486 m^2/g, whereas UiO-66 varied from 845 to 1170 m^2/g. More information about this analysis is given in Appendix 2.A (Figures 2.A.3, 2.A.5 and Table 2.A.1).

As an aside, we note that analysis of adsorption isotherms from the NIST/ARPA-E Adsorption Database reveals a large number of literature reports for materials with no reported BET surface area. The value of reported isotherms to the research community would be improved if experimenters (and journal reviewers) insisted upon reporting BET surface areas for any materials in which adsorption was measured.

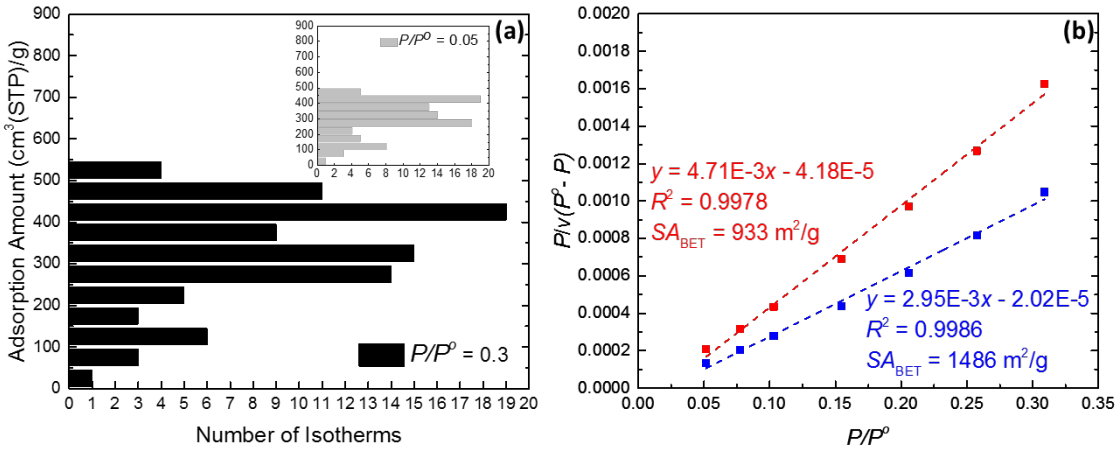

Figure 2.3. (a) Histogram of adsorption amount at intermediate P/P^o and low P/P^o (inset) taken from experimental data of 90 independent measurements for N_2 adsorption in HKUST-1 at 77 K listed in the NIST/ARPA-E Adsorption Database. (b) BET plots of the upper and lower bounds on the consensus isotherms obtained with solid curves connecting IQRs as a function of P/P^o over the linear region of P/P^o range. The lines are fit over $0.05 < P/P^o < 0.15$ to calculate BET surface areas.

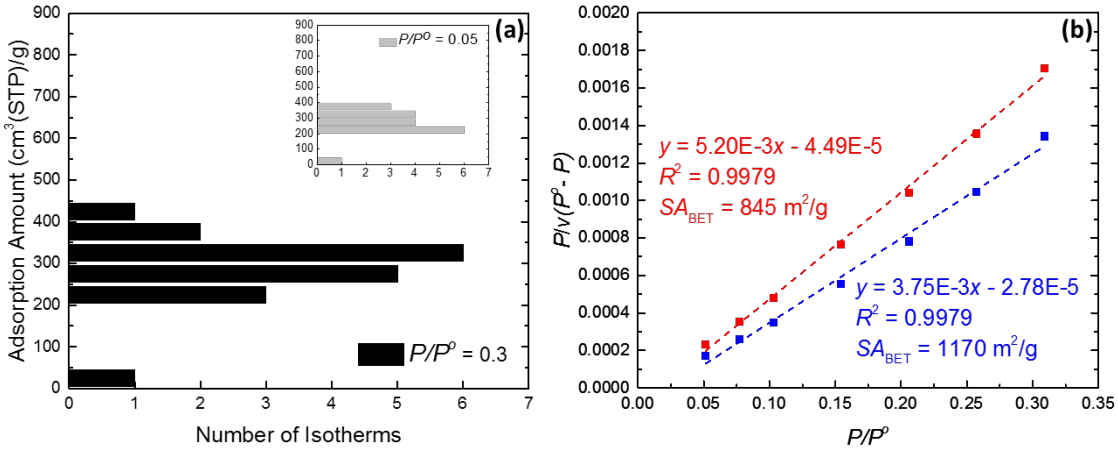

Figure 2.4. (a) Histogram of adsorption amount at intermediate P/P^o and low P/P^o (inset) taken from experimental data of 18 independent measurements for N_2 adsorption in UiO-66 at 77 K listed in the NIST/ARPA-E Adsorption Database. (b) BET plots of the upper and lower bounds on the consensus isotherms obtained with solid curves connecting IQRs as a function of P/P^o over the linear region of P/P^o range. The lines are fit over $0.05 < P/P^o < 0.15$ to calculate BET surface areas.

2.3.2 Reproducibility of CO_2 Adsorption Isotherms in MOFs

Potential applications of porous adsorbents in capturing CO_2 have led to an enormous number of experiments being performed measuring adsorption of CO_2 in MOFs and other materials.[34,35] The NIST/ARPA-E Adsorption Database lists 211 measured CO_2 isotherms in 27 different MOFs with $N > 1$. We applied the analysis described in Section 2.2.1 to all of these isotherms. Despite the large number of isotherms that have been reported, there are only 9 materials for which $N' > 4$ at any temperature $T \pm 5$ K. The results for each of these materials are shown in Figure 2.A.6 and summarized at specific pressures in Figure 2.5a.

There are an additional 8 examples for which $N' = 3$ or 4 at some temperature $T \pm 5$ K (shown in Figure 2.A.7). The range of adsorbed amounts of CO_2 at 1 bar for each of these examples is shown in Figure 2.5b. The uptake of CO_2 in MOF-74(Mg) is higher than the other 7 materials because of the strong interactions that exist between CO_2 and the large number of undercoordinated metal sites in this material.[36] The large CO_2 adsorption capacity in bio-MOF-11 has been attributed to the presence of multiple Lewis basic sites and nano-sized channels.[37] The remaining materials show a weak correlation between increasing surface area and CO_2 uptake, but it is clear that this factor alone cannot describe the results.

The results in Figures 2.5a and 2.5b show that, despite the large number of studies of CO_2 adsorption in MOFs, firm conclusions about the reproducibility of CO_2 isotherms can only be drawn for a small set of materials. In this set of MOFs, our analysis indicates that the overall fraction of CO_2 adsorption isotherms identified as outliers is 0.21 (0.22 for

MOFs with outlier level O1 where $N > 4$ and 0.19 for MOFs with outlier level O2 where $N = 3$ or 4, respectively). A more provocative way to state this observation is that around 1 in 5 of all CO_2 isotherms in this analysis cannot be used to give information that is even qualitatively reliable about the properties of the material that was putatively being characterized.

Our analysis found 10 materials for which two independent CO_2 isotherm measurements exist at some temperature $T \pm 5$ K (*i.e.* $N = N' = 2$, listed in Table 2.A.2). It is also noteworthy that even though temperature variation is a primary means of cycling materials in adsorption cycles[38] and is unavoidable in operation of realistic separation processes,[39,40] essentially nothing is currently known about the reproducibility of CO_2 adsorption isotherms at temperatures other than room temperature.

Our results have important implications for modeling of adsorption in MOFs. Simulation of adsorption isotherms requires defining force fields for sorbate/sorbent interactions, and a significant body of work exists developing these force fields.[41-45] Collections of data such as those in Figures 2.5a and 2.5b give the most reliable path forward for comparing simulation results to experiments with the purpose of testing the validity of broadly applicable force fields. Figure 2.5c compares experimental results with simulations using "standard" force fields for all of the materials with $N' \geq 3$ for CO_2 adsorption. It would be surprising if these simulations were in good agreement with experiments for materials with high densities of open metal sites (OMS) such as the MOF-74 series[46,47] or for materials that have marginal stability[33] (*e.g.* HKUST-1), and the results in Figure 2.5c bear out this general expectation. Nevertheless, the simulation results for almost all of the materials overlap with the experimental data when a 15% relative error

between simulation and experiment is allowed. Understanding the details of the differences between experiment and simulation for materials without OMS when these differences are appreciable (particularly for PCN-200 and MOF-177) is likely to spur advances in these kinds of simulations. Among other choices that must be made in molecular models, the choice of point charges on framework atoms can influence the molecular modeling for adsorption. To illustrate this effect, we compared calculations using DDEC charges[19] in addition to calculations using EQeq charges. Figure 2.A.8 in Appendix 2.A shows the sensitivity to the choice of charges in the predicted adsorption properties for the materials shown in Figure 2.5c.

A comprehensive summary of the current state of knowledge regarding CO_2 adsorption in MOFs is shown in Figure 2.6. This reproducibility map shows all known MOFs for which any conclusions can be drawn about the reproducibility of CO_2 adsorption at any temperature $T \pm 5$ K. In this map, materials where the strongest conclusions about reproducibility can be drawn lie further to the right, materials with the smallest fraction of outliers lie towards the top, and the font size of the label indicates the number of independent measurements that exist after discarding outliers (N'). A material can appear in multiple places on the map for data at different temperature ranges, as is the case for HKUST-1. It is of course possible, and indeed desirable, that the materials of significant practical interest will move towards the upper right corner of the reproducibility map in the future as additional independent measurements are made.

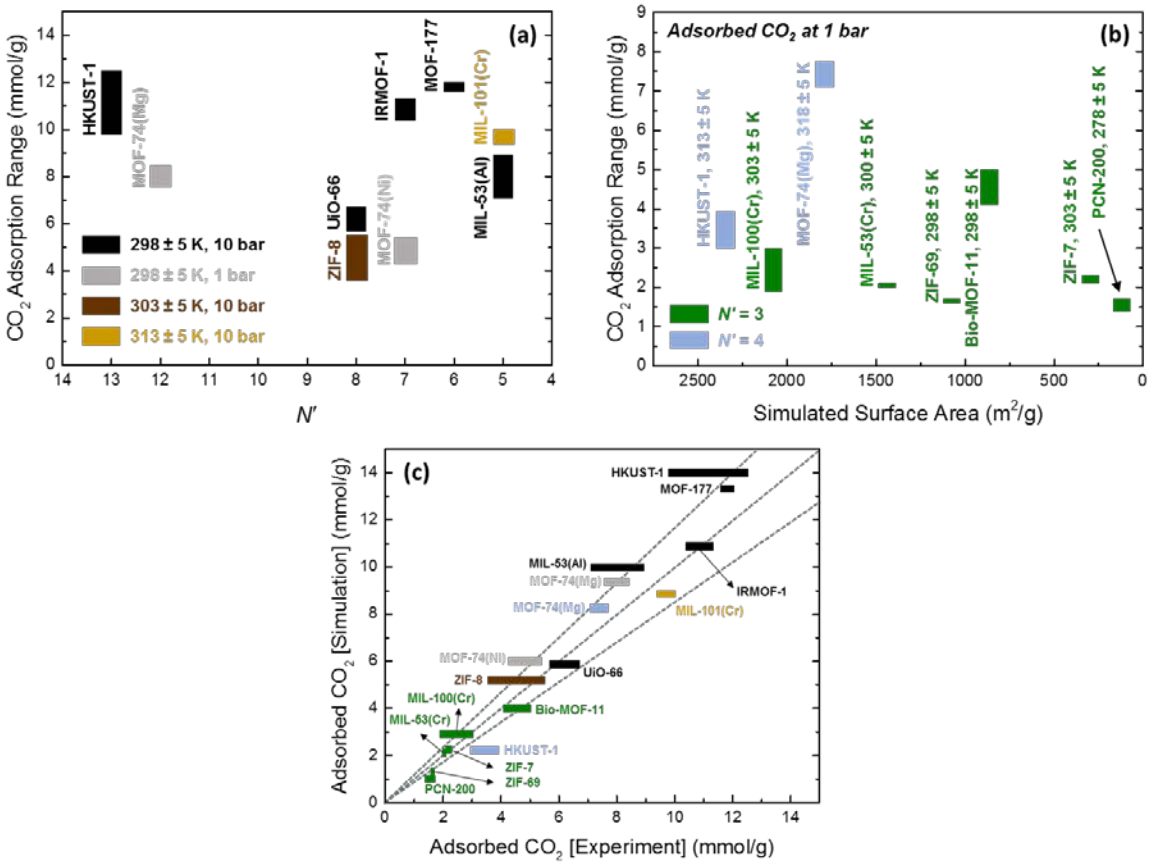

Figure 2.5. (a) Summary of interquartile range for CO_2 adsorption at 10 bar (1 bar for MOF-74) for all known MOFs with $N' > 4$. Box and whisker plots for each material as a function of pressure are shown in Figure 2.A.6. Numbers of independent measurements that exist after discarding outliers (N') were used for each material on the horizontal axis. (b) Summary of range for CO_2 adsorption at 1 bar for all known MOFs with $N' = 3$ or 4. Further detail for each material as a function of pressure is shown in Figure 2.A.7. Simulated surface areas were used for each material on the horizontal axis. (c) Comparison of CO_2 adsorbed amounts from experiments in materials with $N' \geq 3$ (horizontal axis) and predictions from molecular simulations using "standard" force fields (vertical axis) using the same color scheme and labels as in (a) and (b). Molecular simulations were conducted at the median temperature, T K, within the temperature range $T \pm 5$ K that was applied for analysis of experiments. The diagonal lines have slopes of 1.15, 1, and 0.85 from top to bottom to illustrate the variation from parity between the simulated and experimental results.

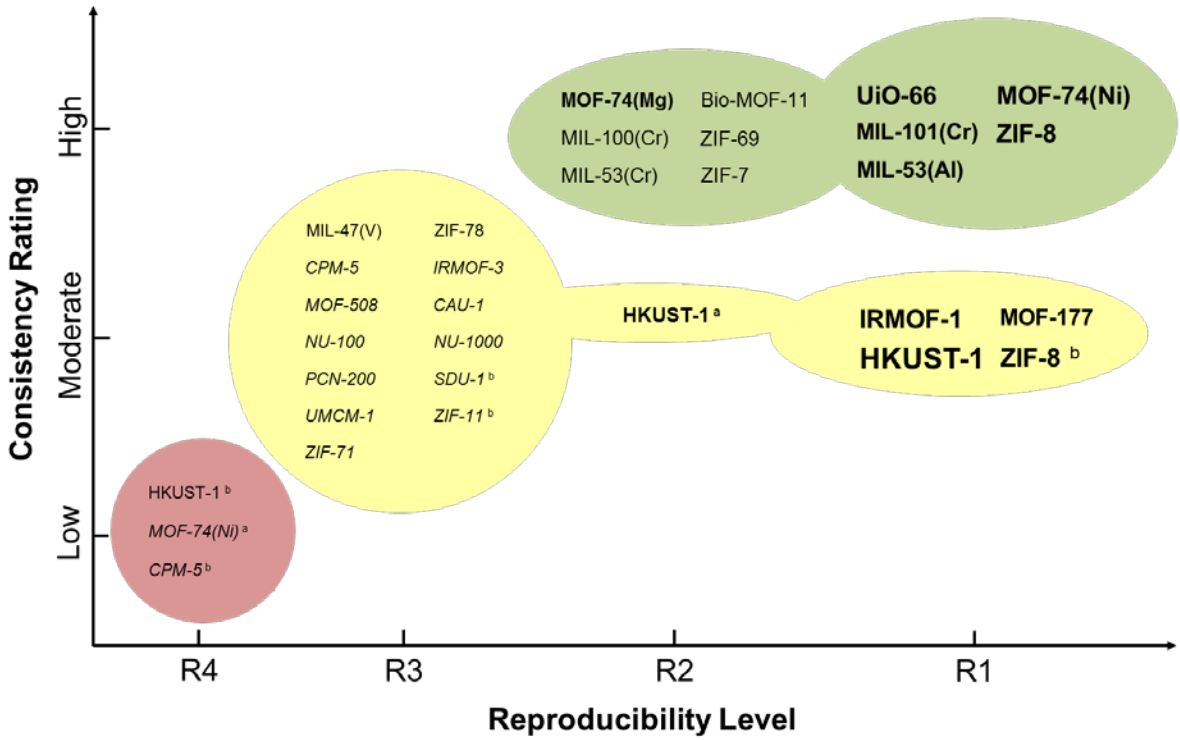

Figure 2.6. Reproducibility map for a comprehensive summary of reproducibility, consistency, and outlier levels for CO_2 isotherms in MOFs that were analyzed using our metrics in this chapter. The definitions of reproducibility level (horizontal axis) and consistency rating (vertical axis and colored regions) are given in Table 2.2 and Table 2.1, respectively. Outlier levels are indicated by font in the form *O3*, O2, and **O1**. Font sizes are scaled to *N'*. The majority of data are for isotherms at 298 ± 5 K except for data at 313 ± 5 K ([a]) and at 273 ± 5 K ([b]). Further details for other temperatures are given in Table 2.A.3.

2.3.3 Molecules for Which No Conclusions Can Be Drawn About Reproducibility of Adsorption in MOFs

The analysis above focused on CO_2 adsorption in MOFs, a situation that has been measured in many materials. We now turn to what might be considered the other end of the reproducibility spectrum by asking whether there are adsorbing molecules for which no conclusions can currently be drawn about the reproducibility of experimental data. To this end, we analyzed all of the data listed in the NIST/ARPA-E Adsorption Database. The database includes information on adsorption of 295 distinct sorbates. For 223 (76%) of

these species, no experimentally measured adsorption isotherms for MOF materials have been reported, although there may be adsorption data for other porous materials, such as zeolites. There are 72 sorbates for which at least one adsorption isotherm in one or more MOFs has been reported. In order to find cases where $N > 1$ where the reproducibility of adsorption data could be analyzed, we required that there be experimentally measured adsorption isotherms for a specific sorbate/sorbent pair from independent research groups at temperatures within $T \pm 5$ K. For 47 of these 72 species, there is no MOF for which $N > 1$ with this approach. This means that there are only 25 molecules (8% of the sorbates listed in the NIST/ARPA-E Adsorption Database) for which any information about reproducibility is currently available for adsorption in MOFs. For most of these molecules this information is only available in one or two materials and at the lowest level of confidence (*i.e.* $N = N' = 2$). In fact, only 12 of the sorbates have a material and temperature range ($T \pm 5$ K) pair for which there are three or more independent measurements ($N > 2$). The methods applied above for CO_2 could also be applied to these sorbates, although doing so is beyond the scope of this chapter. The three groups of sorbates that have just been described are listed in Tables 2.A.4-2.A.6. Given the huge number of distinct molecules that exist and the thousands of MOFs that have been synthesized, the number of molecule/MOF pairs for which any information about reproducibility is available is sparse in the extreme.

2.4 CONCLUSIONS

In this chapter we have established metrics for assessing the reproducibility of adsorption isotherms in MOFs. These metrics rely on comparing independent measurements of the adsorption isotherm from the open literature and make no pre-

judgments about which experiments are “better” or “correct”. We applied these methods to a comprehensive set of CO_2 isotherm measurements in MOFs. Despite the widespread interest in CO_2 adsorption in these materials, there are only a small number of MOFs for which firm conclusions can be drawn about the reproducibility of these measurements. In the examples where enough data exists to assess the existence of outliers, approximately 20% of isotherms in the literature were classified as outliers. This value should cause anyone who makes use of single isotherms from the literature for any purpose (validating a force field for molecular simulations, commenting on whether a material “improves” on previous properties *etc.*) to pause. In the absence of direct evidence, we feel that it would be unwise to assume that the occurrence of outliers is lower than 20% for adsorption of other gases in MOFs. We want to emphasize that the meta-analysis we have described does not provide direct physical insight into why a particular measurement is an outlier or why a material may have a smaller or larger fraction of outliers. Since the actual measurement of adsorption for gases such as CO_2 is relatively routine, it is reasonable to assume that most outliers occur because of variations in the properties of the materials used in experiments stemming from materials synthesis, post-synthesis steps such as activation, or degradation of materials during storage and/or measurement.

The results in this chapter have several implications for experimenters developing MOFs or related materials for chemical separations applications. First, the amount of effort needed to move a molecule/material pair into the group with what we have classed as the highest level of reproducibility is not large. A concerted effort by a small number of experimental groups could quickly improve the current paucity of examples in this class. In this context, we note that simply measuring multiple samples from a single synthesized

batch of a material in multiple locations has less value than having multiple groups independently synthesize the material of interest, although both approaches are better than not assessing reproducibility at all. Second, any report that a new material is "interesting" or "promising" because its adsorption properties differ from existing materials by, say, 15-20% should be treated with skepticism. There are many examples in the literature where several functionalized versions of a material are measured and one material is declared the "best" by some metric. Unless the differences between the materials are large compared to the typical ranges seen for reliably reproducible examples at similar conditions, there are limited grounds to conclude that the observed differences are real. Third, we have deliberately focused on a physical property, single-component adsorption, that has been very widely measured. Single-component adsorption is far from the only property that matters in developing sorbents for real applications,[40,48] and our results point to challenges that should be considered associated with establishing the reproducibility of other physical properties that are relevant in this context.

The analysis in this chapter relied on the availability of a comprehensive database of adsorption isotherms from the open literature. Our methods could be adapted with minimal changes to many areas of materials chemistry provided that similar collections of experimental data are available. It is quite likely that the isotherms available in the literature represent only a fraction, perhaps only a small fraction, of the isotherms that have actually been measured by investigators around the world. Finding avenues to encourage sharing of previously unreported data, particularly for materials where the result has been previously published and is therefore regarded for purposes of publication as "already known", would have long-lasting value to the community. Our results suggest one path

towards this goal, namely identifying materials that can be moved to a firmer set of conclusions about reproducibility by reporting and analyzing additional measurements, thus justifying publication of these measurements.

2.5 REFERENCES

(1) Open Science Collaboration. Estimating the reproducibility of psychological science. *Science* **2015,** *349*, aac4716-1-aac4716-8.

(2) Klein, R. A.; Ratliff, K. A.; Vianello, M.; Adams, R. B.; Bahnik, S.; Bernstein, M. J.; Bocian, K.; Brandt, M. J.; Brooks, B.; Brumbaugh, C. C.; Cemalcilar, Z.; Chandler, J.; Cheong, W.; Davis, W. E.; Devos, T.; Eisner, M.; Frankowska, N.; Furrow, D.; Galliani, E. M.; Hasselman, F.; Hicks, J. A.; Hovermale, J. F.; Hunt, S. J.; Huntsinger, J. R.; Ijzerman, H.; John, M. S.; Joy-Gaba, J. A.; Kappes, H. B.; Krueger, L. E.; Kurtz, J.; Levitan, C. A.; Mallett, R. K.; Morris, W. L.; Nelson, A. J.; Nier, J. A.; Packard, G.; Pilati, R.; Rutchick, A. M.; Schmidt, K.; Skorinko, J. L.; Smith, R.; Steiner, T. G.; Storbeck, J.; Van Swol, L. M.; Thompson, D.; van 't Veer, A. E.; Vaughn, L. A.; Vranka, M.; Wichman, A. L.; Woodzicka, J. A.; Nosek, B. A. Investigating Variation in Replicability A "Many Labs" Replication Project. *Soc. Psychol.* **2014,** *45*, 142-152.

(3) Begley, C. G.; Ellis, L. M. Raise standards for preclinical cancer research. *Nature* **2012,** *483*, 531-533.

(4) Ioannidis, J. P. A.; Greenland, S.; Hlatky, M. A.; Khoury, M. J.; Macleod, M. R.; Moher, D.; Schulz, K. F.; Tibshirani, R. Increasing value and reducing waste in research design, conduct, and analysis. *Lancet* **2014,** *383*, 166-175.

(5) Yaghi, O. M.; O'Keeffe, M.; Ockwig, N. W.; Chae, H. K.; Eddaoudi, M.; Kim, J. Reticular synthesis and the design of new materials. *Nature* **2003,** *423*, 705-714.

(6) Ferey, G. Hybrid porous solids: past, present, future. *Chem. Soc. Rev.* **2008,** *37*, 191-214.

(7) Sholl, D. S.; Lively, R. P. Seven chemical separations to change the world. *Nature* **2016,** *532*, 435-437.

(8) Li, J. R.; Kuppler, R. J.; Zhou, H. C. Selective gas adsorption and separation in metal-organic frameworks. *Chem. Soc. Rev.* **2009,** *38*, 1477-1504.

(9) Furukawa, H.; Ko, N.; Go, Y. B.; Aratani, N.; Choi, S. B.; Choi, E.; Yazaydin, A. O.; Snurr, R. Q.; O'Keeffe, M.; Kim, J.; Yaghi, O. M. Ultrahigh Porosity in Metal-Organic Frameworks. *Science* **2010,** *329*, 424-428.

(10) Chung, Y. G.; Camp, J.; Haranczyk, M.; Sikora, B. J.; Bury, W.; Krungleviciute, V.; Yildirim, T.; Farha, O. K.; Sholl, D. S.; Snurr, R. Q. Computation-Ready, Experimental

Metal-Organic Frameworks: A Tool To Enable High-Throughput Screening of Nanoporous Crystals. *Chem. Mater.* **2014,** *26*, 6185-6192.

(11) Siderius, D. W.; Shen, V. K.; Johnson III, R. D.; van Zee, R. D. *NIST/ARPA-E Datab ase of Novel and Emerging Adsorbent Materials, NIST Standard Reference Database Number 205*; National Institute of Standards and Technology: Gaithersburg MD 208 99; http://adsorbents.nist.gov, (retrieved June 30, 2017).

(12) Zlotea, C.; Moretto, P.; Steriotis, T. A Round Robin characterisation of the hydrogen sorption properties of a carbon based material. *Int. J. Hydrogen Energy* **2009,** *34*, 3044-3057.

(13) Broom, D. P.; Hirscher, M. Irreproducibility in hydrogen storage material research. *Energy Environ. Sci.* **2016,** *9*, 3368-3380.

(14) Chui, S. S. Y.; Lo, S. M. F.; Charmant, J. P. H.; Orpen, A. G.; Williams, I. D. A chemically functionalizable nanoporous material $[Cu_3(TMA)_2(H_2O)_3]_n$. *Science* **1999,** *283*, 1148-1150.

(15) Cavka, J. H.; Jakobsen, S.; Olsbye, U.; Guillou, N.; Lamberti, C.; Bordiga, S.; Lillerud, K. P. A new zirconium inorganic building brick forming metal organic frameworks with exceptional stability. *J. Am. Chem. Soc.* **2008,** *130*, 13850-13851.

(16) Tukey, J. W. *Exploratory Data Analysis*; Addison-Wesley: MA, 1977.

(17) Moriasi, D. N.; Arnold, J. G.; Van Liew, M. W.; Bingner, R. L.; Harmel, R. D.; Veith, T. L. Model evaluation guidelines for systematic quantification of accuracy in watershed simulations. *T. ASABE* **2007,** *50*, 885-900.

(18) Kalyanaraman, J.; Kawajiri, Y.; Lively, R. P.; Realff, M. J. Uncertainty Quantification *via* Bayesian Inference Using Sequential Monte Carlo Methods for CO_2 Adsorption Process. *AIChE J.* **2016,** *62*, 3352-3368.

(19) Park, J.; Lively, R. P.; Sholl, D. S. Establishing upper bounds on CO_2 swing capacity in sub-ambient pressure swing adsorption *via* molecular simulation of metal-organic frameworks. *J. Mater. Chem. A* **2017,** *5*, 12258-12265.

(20) Dubbeldam, D.; Calero, S.; Ellis, D. E.; Snurr, R. Q. RASPA: molecular simulation software for adsorption and diffusion in flexible nanoporous materials. *Mol. Simul.* **2016,** *42*, 81-101.

(21) Dubbeldam, D.; Torres-Knoop, A.; Walton, K. S. On the inner workings of Monte Carlo codes. *Mol. Simul.* **2013,** *39*, 1253-1292.

(22) Addicoat, M. A.; Vankova, N.; Akter, I. F.; Heine, T. Extension of the Universal Force Field to Metal-Organic Frameworks. *J. Chem. Theory Comput.* **2014,** *10*, 880-891.

(23) Rappe, A. K.; Casewit, C. J.; Colwell, K. S.; Goddard, W. A.; Skiff, W. M. UFF, a Full Periodic Table Force Field for Molecular Mechanics and Molecular Dynamics Simulations. *J. Am. Chem. Soc.* **1992,** *114*, 10024-10035.

(24) Martin, M. G.; Siepmann, J. I. Transferable potentials for phase equilibria. 1. United-atom description of n-alkanes. *J. Phys. Chem. B* **1998,** *102*, 2569-2577.

(25) Allen, M. P.; Tildesley, D. J. *Computer Simulation of Liquids*; Oxford University Press: New York, 1987.

(26) Wilmer, C. E.; Kim, K. C.; Snurr, R. Q. An Extended Charge Equilibration Method. *J. Phys. Chem. Lett.* **2012,** *3*, 2506-2511.

(27) Walton, K. S.; Snurr, R. Q. Applicability of the BET method for determining surface areas of microporous metal-organic frameworks. *J. Am. Chem. Soc.* **2007,** *129*, 8552-8556.

(28) Duren, T.; Millange, F.; Ferey, G.; Walton, K. S.; Snurr, R. Q. Calculating geometric surface areas as a characterization tool for metal-organic frameworks. *J. Phys. Chem. C* **2007,** *111*, 15350-15356.

(29) Demir, H.; Greathouse, J. A.; Staiger, C. L.; Perry, J. J.; Allendorf, M. D.; Sholl, D. S. DFT-based force field development for noble gas adsorption in metal organic frameworks. *J. Mater. Chem. A* **2015,** *3*, 23539-23548.

(30) Dubbeldam, D.; Frost, H.; Walton, K. S.; Snurr, R. Q. Molecular simulation of adsorption sites of light gases in the metal-organic framework IRMOF-1. *Fluid Phase Equilib.* **2007,** *261*, 152-161.

(31) Surble, S.; Millange, F.; Serre, C.; Duren, T.; Latroche, M.; Bourrelly, S.; Llewellyn, P. L.; Ferey, G. Synthesis of MIL-102, a chromium carboxylate metal-organic framework, with gas sorption analysis. *J. Am. Chem. Soc.* **2006,** *128*, 14889-14896.

(32) Sholl, D. S.; Lively, R. P. Defects in Metal-Organic Frameworks: Challenge or Opportunity? *J. Phys. Chem. Lett.* **2015,** *6*, 3437-3444.

(33) Burtch, N. C.; Jasuja, H.; Walton, K. S. Water Stability and Adsorption in Metal-Organic Frameworks. *Chem. Rev.* **2014,** *114*, 10575-10612.

(34) D'Alessandro, D. M.; Smit, B.; Long, J. R. Carbon Dioxide Capture: Prospects for New Materials. *Angew. Chem., Int. Ed.* **2010,** *49*, 6058-6082.

(35) Keskin, S.; van Heest, T. M.; Sholl, D. S. Can Metal-Organic Framework Materials Play a Useful Role in Large-Scale Carbon Dioxide Separations? *ChemSusChem* **2010,** *3*, 879-891.

(36) Britt, D.; Furukawa, H.; Wang, B.; Glover, T. G.; Yaghi, O. M. Highly efficient separation of carbon dioxide by a metal-organic framework replete with open metal sites. *Proc. Natl. Acad. Sci. U.S.A.* **2009,** *106*, 20637-20640.

(37) Chen, Y. F.; Jiang, J. W. A Bio-Metal-Organic Framework for Highly Selective CO_2 Capture: A Molecular Simulation Study. *ChemSusChem* **2010,** *3*, 982-988.

(38) Mason, J. A.; Sumida, K.; Herm, Z. R.; Krishna, R.; Long, J. R. Evaluating metal-

organic frameworks for post-combustion carbon dioxide capture *via* temperature swing adsorption. *Energy Environ. Sci.* **2011,** *4*, 3030-3040.

(39) Lively, R. P.; Realff, M. J. On Thermodynamic Separation Efficiency: Adsorption Processes. *AIChE J.* **2016,** *62*, 3699-3705.

(40) Maring, B. J.; Webley, P. A. A new simplified pressure/vacuum swing adsorption model for rapid adsorbent screening for CO_2 capture applications. *Int. J. Greenhouse Gas Control* **2013,** *15*, 16-31.

(41) Fang, H. J.; Demir, H.; Kamakoti, P.; Sholl, D. S. Recent developments in first-principles force fields for molecules in nanoporous materials. *J. Mater. Chem. A* **2014,** *2*, 274-291.

(42) Dzubak, A. L.; Lin, L. C.; Kim, J.; Swisher, J. A.; Poloni, R.; Maximoff, S. N.; Smit, B.; Gagliardi, L. *Ab initio* carbon capture in open-site metal-organic frameworks. *Nat. Chem.* **2012,** *4*, 810-816.

(43) McDaniel, J. G.; Li, S.; Tylianakis, E.; Snurr, R. Q.; Schmidt, J. R. Evaluation of Force Field Performance for High-Throughput Screening of Gas Uptake in Metal-Organic Frameworks. *J. Phys. Chem. C* **2015,** *119*, 3143-3152.

(44) Schmidt, J. R.; Yu, K.; McDaniel, J. G. Transferable Next-Generation Force Fields from Simple Liquids to Complex Materials. *Acc. Chem. Res.* **2015,** *48*, 548-556.

(45) Mercado, R.; Vlaisavljevich, B.; Lin, L. C.; Lee, K.; Lee, Y.; Mason, J. A.; Xiao, D. J.; Gonzalez, M. I.; Kapelewski, M. T.; Neaton, J. B.; Smit, B. Force Field Development from Periodic Density Functional Theory Calculations for Gas Separation Applications Using Metal-Organic Frameworks. *J. Phys. Chem. C* **2016,** *120*, 12590-12604.

(46) Poloni, R.; Lee, K.; Berger, R. F.; Smit, B.; Neaton, J. B. Understanding Trends in CO_2 Adsorption in Metal-Organic Frameworks with Open-Metal Sites. *J. Phys. Chem. Lett.* **2014,** *5*, 861-865.

(47) Kulkarni, A. R.; Sholl, D. S. Screening of Copper Open Metal Site MOFs for Olefin/Paraffin Separations Using DFT-Derived Force Fields. *J. Phys. Chem. C* **2016,** *120*, 23044-23054.

(48) Walton, K. S.; Sholl, D. S. Research Challenges in Avoiding "Showstoppers" in Developing Materials for Large-scale Energy Applications. *Joule* **2017,** *1*, 208-211.

APPENDIX 2.A. SUPPORTING INFORMATION – CHAPTER 2

2.A.1 Taxonomy for Outlier Level, Consistency Rating, and Reproducibility Level

We have introduced three complementary characteristics of a collection of experimental adsorption isotherms. The definitions for these characteristics are summarized in Section 2.A.1.

The detection of outliers in data sets is an essential part of data analysis. We use several different outlier labeling methods to narrow down our attention to a normal range of data for meaningful statistical comparison. Outlier level O1 (employing Tukey's method[1]) is used when $N > 4$ to label outliers. Tukey's method, constructing a box and whisker plot, is a well-known graphical tool to display statistical information about data set (*i.e.* the median, lower quartile, upper quartile, lower extreme, upper extreme, and the mean). An outlier is defined as a value more than 1.5IQR (IQR = interquartile range) from either end of the box. Hence, any isotherms having adsorption amount lying outside the range of a standard box and whisker plot at any pressure point are designated as outliers. Once outliers are identified, they are excluded from further analysis.

Outlier level O2 uses the root mean square error (RMSE) when $N = 3$ or 4 to label outliers. RMSE is commonly used in model evaluation.[2,3] In this case, we calculate RMSE between two existing measurements to determine the agreement between the measurements. For a set of 3 or 4 isotherms, we analyze these data in terms of the standardized RMSE, which allows a comparison between two sets of data. Singh *et al.*[4] recommended a guideline to qualify what is considered a low RMSE based on the standard

deviation (σ) of observations. According to the recommendation, an RMSE smaller than $\sigma/2$ is accepted as a low RMSE. Therefore, the O2 level labels and rejects outliers when RMSE is larger than $\sigma/2$ of a comparison isotherm. When $N = 3$, we designate as the comparison isotherm the isotherm with the second-largest uptake of adsorbate at the greatest pressure common to all three isotherms, essentially comparing against the "middle" isotherm. When $N = 4$, we repeat this procedure, assigning the second-largest uptake at the highest common pressure to be the comparison isotherm for the two isotherms with the largest and third-largest uptakes, not considering initially the isotherm with the smallest uptake. If the isotherm with the third-largest uptake is identified as an outlier, the isotherm with the smallest uptake will also automatically be identified as an outlier. Otherwise, this procedure will be repeated, designating the isotherm with the third-largest uptake as the comparison isotherm and comparing the isotherm with the smallest uptake against it. We note that this analysis procedure biases toward keeping greater uptakes in the case that $N = 4$ has highly disparate data.

Lastly, outlier level O3 describes the situation when $N = 2$. In this case it is not possible to label outliers in a reliable manner, so we do not label outliers and do not reject any measurements.

Consistency refers to how many outliers were found among a set of isotherms. The consistency rating is labeled as high, moderate, or low when $N > 2$ and as moderate or low when $N = 2$, since we do not think it is appropriate to label a set of two isotherms as having "high" consistency. When $N > 2$, the rating is defined by the fraction of measurements labeled as outliers (f). When $N = 2$, the consistency rating is determined by RMSE criteria that was used for outlier level O2; two isotherms are defined as having moderate

consistency when they have RMSE < $\sigma/2$. The criteria and methods to detect outlier isotherms and to rate consistency are summarized in Table 2.1.

Once outliers have been rejected, we denote the number of independent experiments in a given pressure range as N'. We represent the remaining isotherms graphically using different methods depending on the value of N'. A key aspect of this approach is to assign consensus bounds to the isotherm quantities that are consistent with the underlying experimental data. Reproducibility level R1 applies box and whisker plots as a function of pressure when $N' > 4$. For R1 level materials, the isotherm bounds are assigned for interquartile range (IQR) of adsorption amount at each pressure point. Reproducibility level R2 uses a shaded region that encompasses all of the measured data after rejecting outlier(s) when $N' = 3$ or 4. In this case, the region or isotherm bounds are given by the upper measurement (the isotherm with the largest uptakes) and lower measurement (the isotherm with the smallest uptakes) over a common pressure range. With reproducibility level R3 and R4 when $N' = 2$, the isotherm bounds cannot be made due to lack of information about the isotherm reproducibility. Only the pair of fitted isotherms can be plotted, if desired, and the different levels depend on the variation between the two isotherms.

Isotherm models used to fit experimental measurements include the Langmuir, Freundlich, and Langmuir-Freundlich models that are available in the NIST/ARPA-E Adsorption Database:

$$\Gamma(P) = \Gamma_{\infty} \frac{KP}{1+KP} \quad \ldots \text{Langmuir model}$$

$$\Gamma(P) = kP^{1/n} \quad \ldots \text{Freundlich model}$$

$$\Gamma(P) = \Gamma_{\infty} \frac{(KP)^n}{1+(KP)^n} \quad \ldots \text{Langmuir-Freundlich model}$$

where $\Gamma(P)$ is the adsorbed amount as a function of pressure (P). We chose a functional form that give fits with a high value of R^2 (*i.e.* $R^2 \geq 0.99$) without accounting the variations in the number of fitting parameters between forms. A simpler isotherm model of fewer parameters was chosen if multiple models had similar levels of R^2.

The criteria and methods to assess isotherm reproducibility and graphical representations are described in Table 2.2. Figure 2.A.1 illustrates the overall analysis platform performed for a set of isotherms to develop of the complementary characteristics discussed above.

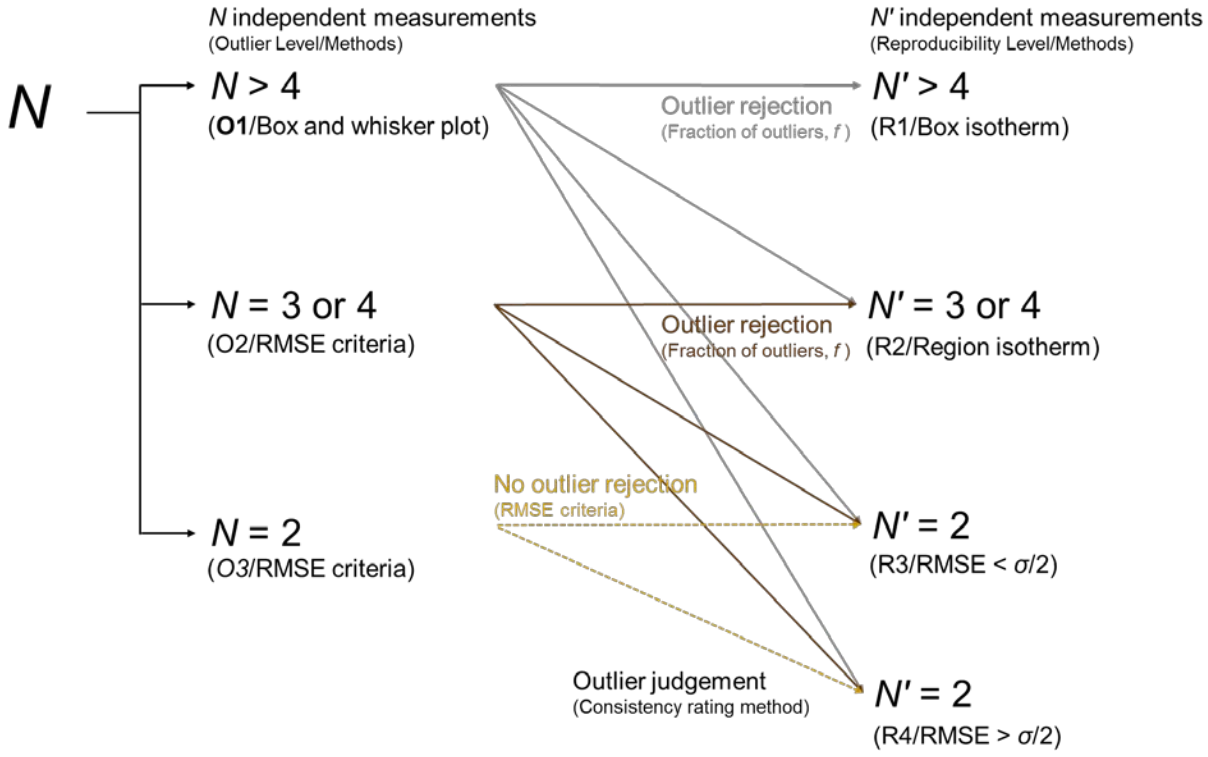

Figure 2.A.1. Reproducibility analysis flow used in this chapter. The scheme illustrates that materials with sufficient measurements starting from outlier level O1 can be characterized with any reproducibility level from R1 to R4, depending on how many outliers exist. Similarly, materials starting from outlier level O2 can be characterized with reproducibility level from R2 to R4, but not with R1. The materials with few measurements starting from outlier level O3 can only be characterized with reproducibility level R3 and R4, which are the lowest levels of confidence.

2.A.2 Reproducibility Analysis of CO_2 Adsorption Isotherms in MOFs

2.A.2.1 Surface Area Scaling and Analysis of N_2 Adsorption Isotherms

The quality of MOFs can vary depending on details of their synthesis, activation, and stability.[5] These variations affect the measured BET surface areas of MOFs. An approach that has been widely used when comparing isotherm data with different surface areas is to scale the experimental isotherms by the ratio of the simulated and experimental surface area.[6-8] We applied this method to examine whether it makes the underlying experimental data more consistent for HKUST-1 and UiO-66. For the surface area scaling in this chapter, the ratio of simulated to experimental surface area was used as follows:

$$q_{exp} \cdot \frac{SA_{simulated}}{SA_{experimental}} = q_{exp,scaled}$$

In addition, the reproducibility analysis metrics were applied for N_2 adsorption isotherms at 77 K that were complied from the NIST/ARPA-E Adsorption Database for HKUST-1 and UiO-66. This procedure reveals the utility of our established metrics to assess the reproducibility of gas adsorption isotherms, and hence results in the consensus bounds to N_2 adsorption amount measurements as for the case of CO_2 analysis. In general, N_2 adsorption isotherms measured at 77 K are used to yield porous materials' surface area by applying the Brunauer, Emmett, and Teller (BET) theory.[9-11] Therefore analysis of N_2 adsorption range, more importantly, creates a chance to identify the statistically quantified consensus bounds in BET surface area. The BET analysis is conducted by using BET plot, $P/v(P^o - P)$ as a function of P/P^o, as follows:

$$\frac{P}{v(P^0 - P)} = \frac{c-1}{v_m c}\frac{P}{P^o} + \frac{1}{v_m c}$$

In the BET equation, P^o is the pressure of the vapor in equilibrium with its non-vapor phase (P^o = 0.971 bar for N_2 at 77 K) and v is the volume of N_2 adsorbed per gram of MOF at STP (cm^3(STP)/g). The BET theory to calculate surface area is valid over the pressure range where the BET plot is linear with the assumption that monolayer formation occurs within this region.[9-11] The slope ($[c-1]/v_m c$) and intercept ($1/v_m c$) of from the linear region give the c value that is related to the heat of adsorption and v_m which is referred to the monolayer capacity. The BET surface area, SA_{BET}, is then calculated by $SA_{BET} = v_m \sigma_o N_{AV}$, where σ_o is the cross-sectional area of the adsorbate at liquid density (σ_o = 16.2 $Å^2$ for N_2) and N_{AV} is the Avogadro's number.

For HKUST-1, the simulated surface area is 2340.7 m^2/g (see Section 2.A.4 for details of simulation) and reported experimental surface areas range from as small as 921 m^2/g to as large as 2211 m^2/g for the isotherms that are included in box and whisker plot. The substantial difference in simulated and experimental surface areas is typically ascribed to intrinsic instability of HKUST-1.[12] Figure 2.A.2a is a box isotherm (reproduced from Figure 2.1b) at 298 ± 5 K with N' = 13 that does not take account of surface area scaling. Among these 13 measurements, 11 measurements had reported BET surface area (denoted as N'') whereas 2 had not. Figure 2.A.2b is a box isotherm constructed with 13 measurements using 11 scaled isotherms along with 2 non-scaled isotherms. Figure 2.A.2c is a box isotherm made from 11 scaled isotherms (*i.e.* eliminating the data for which no surface area was available). With both treatments of the data, surface area scaling leads to an increase in the apparent adsorbed amount but, critically, to a larger IQR. At least in this case, therefore, applying surface area scaling does not make the underlying data more self-consistent.

Figure 2.A.3 shows that our analysis metrics enable the assessment to BET surface area range of HKUST-1. Figure 2.A.3a exhibits compiled experimental data of N_2 adsorption isotherms in HKUST-1 at 77 K with $N = 90$. For this specific purpose, BET adsorption isotherm model was used in fitting and analysis of the data that allow direct comparison among all N measurements at the same values of P/P^o. Outliers are detected and removed by outlier level O1. Box isotherm by applying the reproducibility level R1 is shown in Figure 2.A.3b. The solid curves connecting IQRs were defined as the consensus bounds to the measurements of the adsorbed amount as a function of P/P^o. These are now used as pseudo-experimental isotherms to give upper and lower limits to N_2 isotherms with $N' = 86$. Note that the solid curves are drawn by conneting Q_U and Q_L labels at higher P/P^o resolution where boxes at low P/P^o are not shown. Ultimately, Figure 2.A.3c (reproduced from Figure 2.3b) shows the BET plots to determine the upper and lower bounds of BET surface areas using the pseudo-experimental isotherms. Each BET surface area was calculated with the fits given in the figure and the methods described above, *i.e.* $SA_{BET} = \nu_m \sigma_o N_{AV}$.

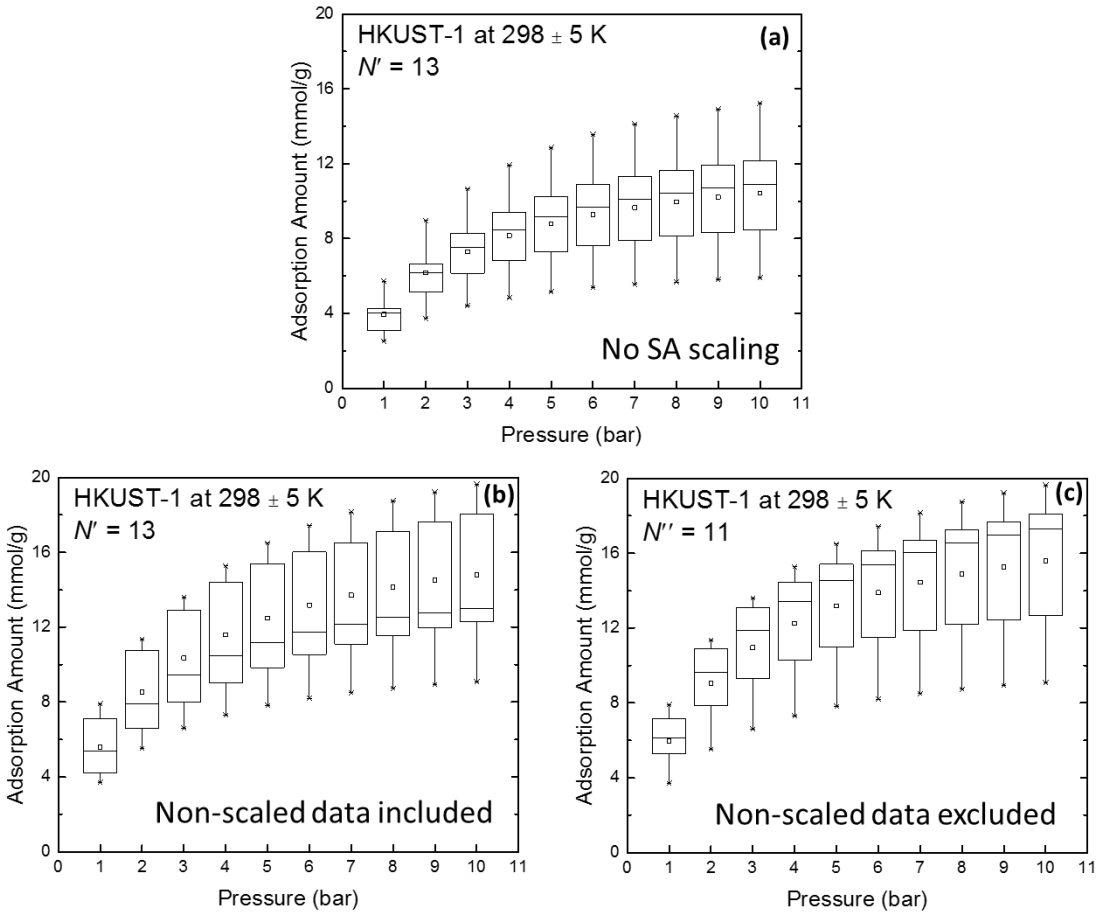

Figure 2.A.2. (a) Box isotherm for CO_2 adsorption in HKUST-1 at 298 ± 5 K without surface area scaling. (b) Box isotherm for CO_2 adsorption in HKUST-1 at 298 ± 5 K with surface area scaling which includes non-scaled measurements. (c) Box isotherm for CO_2 adsorption in HKUST-1 at 298 ± 5 K with surface area scaling which excludes non-scaled measurements with no reported BET surface area. The solid curves connecting IQRs are omitted.

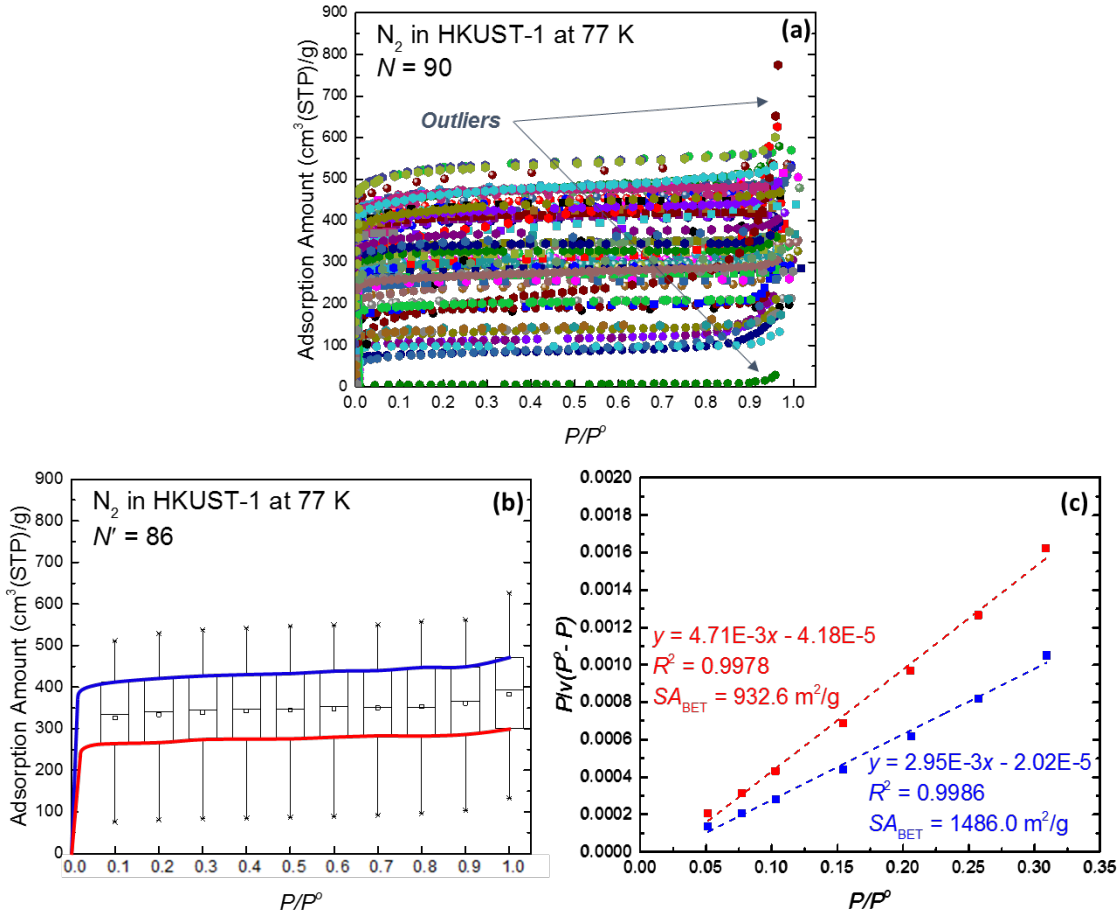

Figure 2.A.3. (a) Experimental data from 90 independent measurements of N_2 adsorption in HKUST-1 at 77 K listed in the NIST/ARPA-E Adsorption Database. Outliers identified by the methods defined in the text are indicated. BET adsorption isotherm model was used in fitting and analysis of the data (solid curves being omitted). (b) Box isotherm for N_2 adsorption in HKUST-1 at 77 K with the solid curves connecting IQRs which can be thought of as the consensus bounds to the measurements of the adsorbed amount as a function of P/P^o. These curves connecting Q_L's and Q_U's are used as pseudo-experimental isotherms for surface area analysis using BET theory. (c) BET plots over the standard BET pressure range using pseudo-experimental isotherms with the same color index as in (b). Notice that the lines are fit over $0.05 < P/P^o < 0.15$ which is the most commonly used BET pressure range for porous materials.

UiO-66 has widely been investigated as a CO_2 adsorbent, in part due to its water stability.[13,14] The simulated surface area is 1165.0 m^2/g and experimental surface area ranges from 998 m^2/g to 1160 m^2/g for the isotherms that are involved in box and whisker plot, so unlike the situation for HKUST-1, the simulated and experimental surface areas are in fair agreement. Figure 2.A.4a is a box isotherm (reproduced from Figure 2.2c) at 298 ± 5 K below 15 bar for UiO-66 with $N' = 8$ that does not take account of surface area scaling. Among these 8 measurements, 7 measurements had reported BET surface area (denoted as N'') whereas 1 had not. Figure 2.A.4b is a box isotherm constructed with 8 measurements using 7 scaled isotherms along with 1 non-scaled isotherm. Figure 2.A.4c is a box isotherm made from 7 scaled isotherms (*i.e.* eliminating the data for which no surface area is available). Because of the small discrepancies between the simulated and reported experimental surface areas, only marginal changes in IQRs are observed with surface area scaling, so surface area scaling does not tighten the consensus range of adsorbed CO_2 amounts.

Figure 2.A.5 demonstrates the procedure of assessing BET surface area range of UiO-66. Figure 2.A.5a shows compiled experimental data of N_2 adsorption isotherms in UiO-66 at 77 K with $N = 18$. Outliers are detected and removed by outlier level O1. Figure 2.A.5b shows a box isotherm by applying the reproducibility level R1. The pseudo-experimental isotherms, as defined for HKUST-1 example, can be obtained to give upper and lower limits to N_2 isotherms with $N' = 15$. Finally, Figure 2.A.5c (reproduced from Figure 2.4b) shows the BET plots to determine the upper and lower bounds of BET surface areas using the pseudo-experimental isotherms.

Table 2.A.1 summarizes the results of surface area analysis using simulated and statistically quantified experimental N_2 adsorption isotherms at 77 K in HKUST-1 and UiO-66. Simulated N_2 adsorption isotherms at 77 K in both materials were obtained by Grand Canonical Monte Carlo simulation (data not shown), and the simulation details can be found in Section 2.A.4. Choosing an appropriate linear P/P^o region in a BET plot is generally known to be somewhat subjective since often several regions give a roughly linear BET plot.[9,10] BET surface areas of each material were calculated over different P/P^o ranges, where their BET plots showed linearity within both P/P^o ranges, using the simulated N_2 adsorption isotherms. Note that the variation between BET surface areas calculated over different P/P^o ranges are about 10% for both materials indicating only a minor effect in the selection of P/P^o range for these materials. It grants our choice of BET analysis over $0.05 < P/P^o < 0.15$ that enabled the statistical quantification of BET surface area ranges for HKUST-1 and UiO-66 that have been built up from our reproducibility analysis metrics (curated in the last column of the table). A take-home message at the end of this analysis is that larger discrepancy in surface area range would result in larger deviation in CO_2 adsorption range (HKUST-1) and smaller difference in surface area would lead to smaller variation in CO_2 adsorption range (UiO-66).

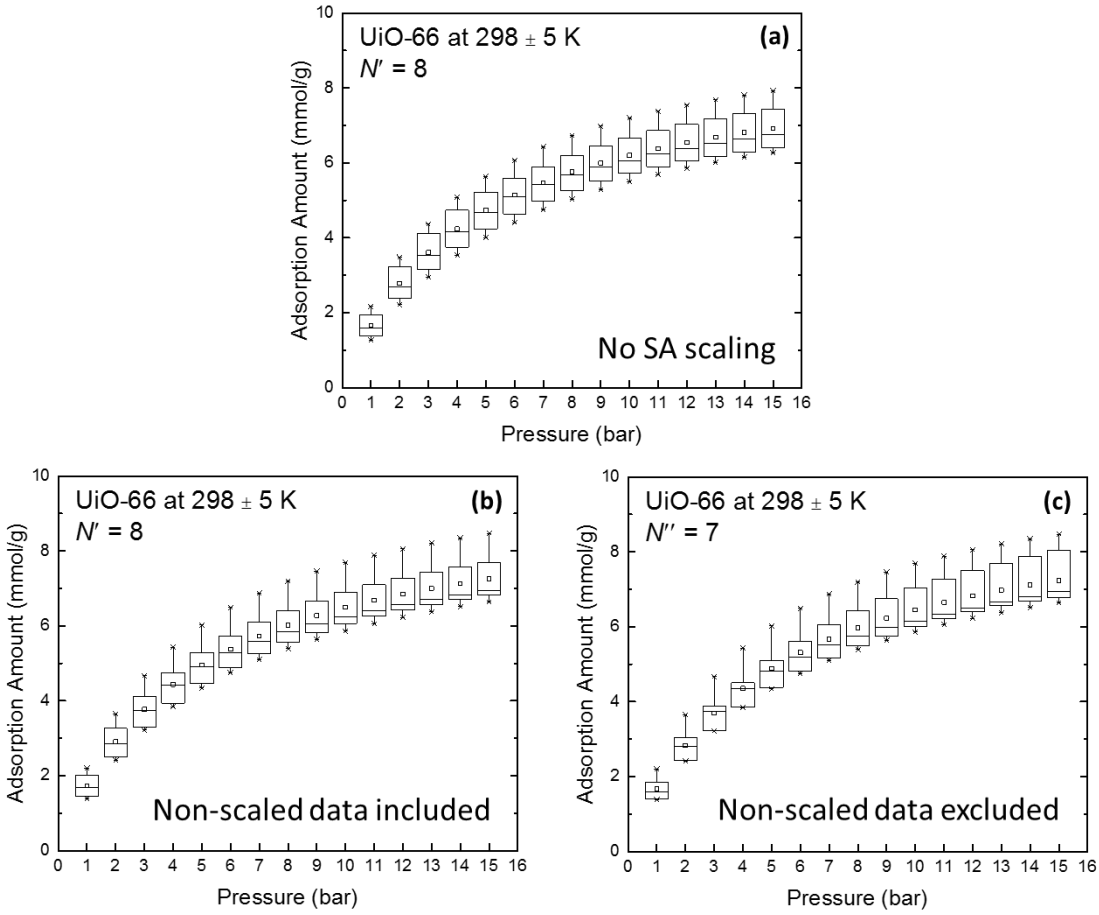

Figure 2.A.4. (a) Box isotherm for CO_2 adsorption in UiO-66 at 298 ± 5 K without surface area scaling. (b) Box isotherm for CO_2 adsorption in UiO-66 at 298 ± 5 K with surface area scaling which includes non-scaled measurements. (c) Box isotherm for CO_2 adsorption in UiO-66 at 298 ± 5 K with surface area scaling which excludes non-scaled measurements with no reported BET surface area. The solid curves connecting IQRs are omitted.

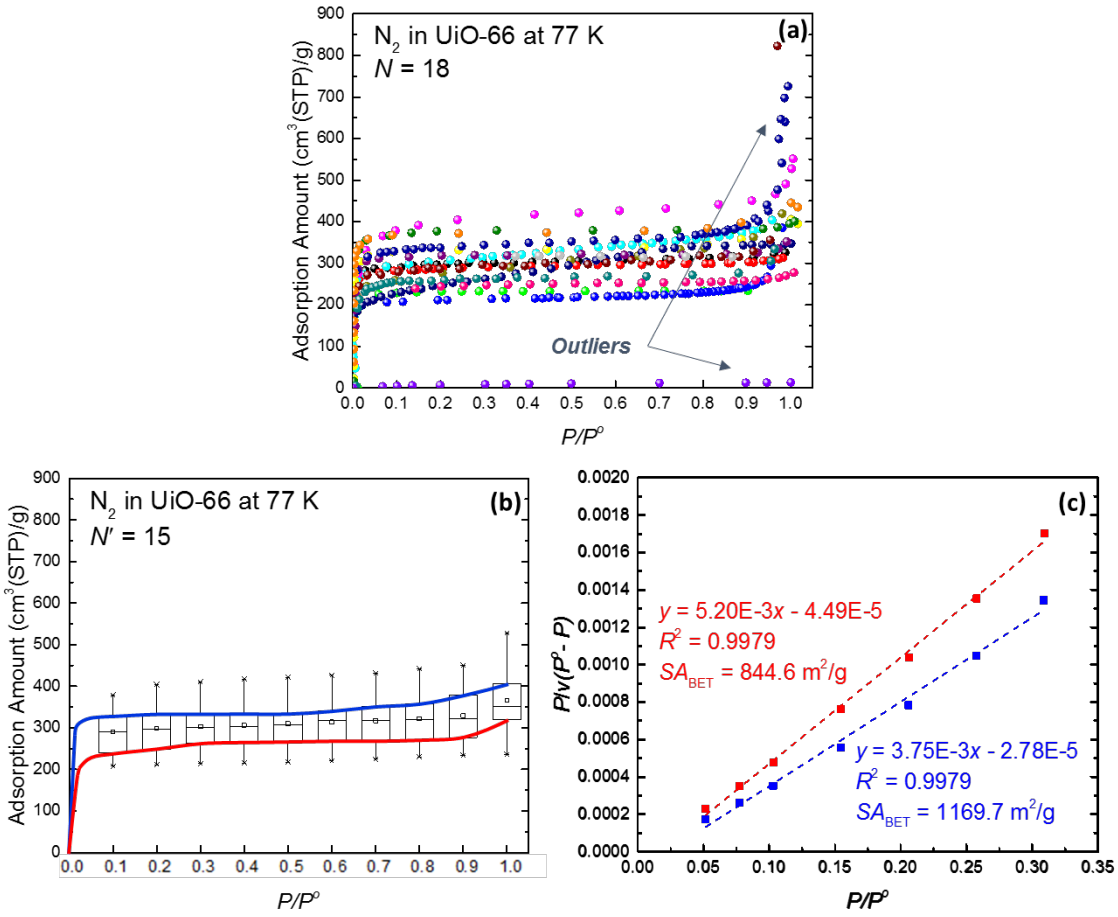

Figure 2.A.5. (a) Experimental data from 18 independent measurements of N_2 adsorption in UiO-66 at 77 K listed in the NIST/ARPA-E Adsorption Database. Outliers identified by the methods defined in the text are indicated. BET adsorption isotherm model was used in fitting and analysis of the data (solid curves being omitted). (b) Box isotherm for N_2 adsorption in UiO-66 at 77 K with the solid curves connecting IQRs which can be thought of as the consensus bounds to the measurements of the adsorbed amount as a function of P/P^o. These curves connecting Q_L's and Q_U's are used as pseudo-experimental isotherms for surface area analysis using BET theory. (c) BET plots over the standard BET pressure range using pseudo-experimental isotherms with the same color index as in (b). Notice that the lines are fit over $0.05 < P/P^o < 0.15$ which is the most commonly used BET pressure range for porous materials.

Table 2.A.1. Surface area analysis using reproducibility analysis metrics for N_2 adsorption isotherms at 77 K enabling statistical quantification of consensus bounds in BET surface area (SA_{BET}).

MOFs	SA_{BET} [a] [m^2/g]		SA_{BET} range [b] [m^2/g]
	$P/P^o \leq 0.01$	$0.05 < P/P^o < 0.15$	$0.05 < P/P^o < 0.15$
HKUST-1	1909.5	1667.1	[932.6, 1486.0]
UiO-66	1180.4	1041.7	[844.6, 1169.7]

[a] SA_{BET} calculated by using simulated N_2 adsorption isotherms at 77 K over linear region of BET plot, $P/v(P^o\text{-}P)$ *vs*. P/P^o. BET analysis were conducted over consistency criteria pressure range $P/P^o \leq 0.01$ (proposed by Rouquerol *et al*.[9] and shown for IRMOF series by Walton *et al*.[10]) and over standard pressure range $0.05 < P/P^o < 0.3$ (proposed by Brunauer[11] and $0.05 < P/P^o < 0.15$ being the most commonly used).

[b] SA_{BET} range quantified from an exhaustive compilation of experimental N_2 adsorption isotherms at 77 K from the NIST/ARPA-E Adsorption Database. SA_{BET} range results from SA_{BET}'s calculated with pseudo-experimental N_2 adsorption isotherms that are thought of as the consensus bounds to the N_2 measurements by connecting the IQRs (Figure 2.A.3b and Figure 2.A.5b for HKUST-1 and UiO-66, respectively). BET theory was applied in a same manner for treating experimental data (Figure 2.A.3c and Figure 2.A.5c for HKUST-1 and UiO-66, respectively).

2.A.2.2 Box Isotherms for R1 Reproducibility Level MOFs

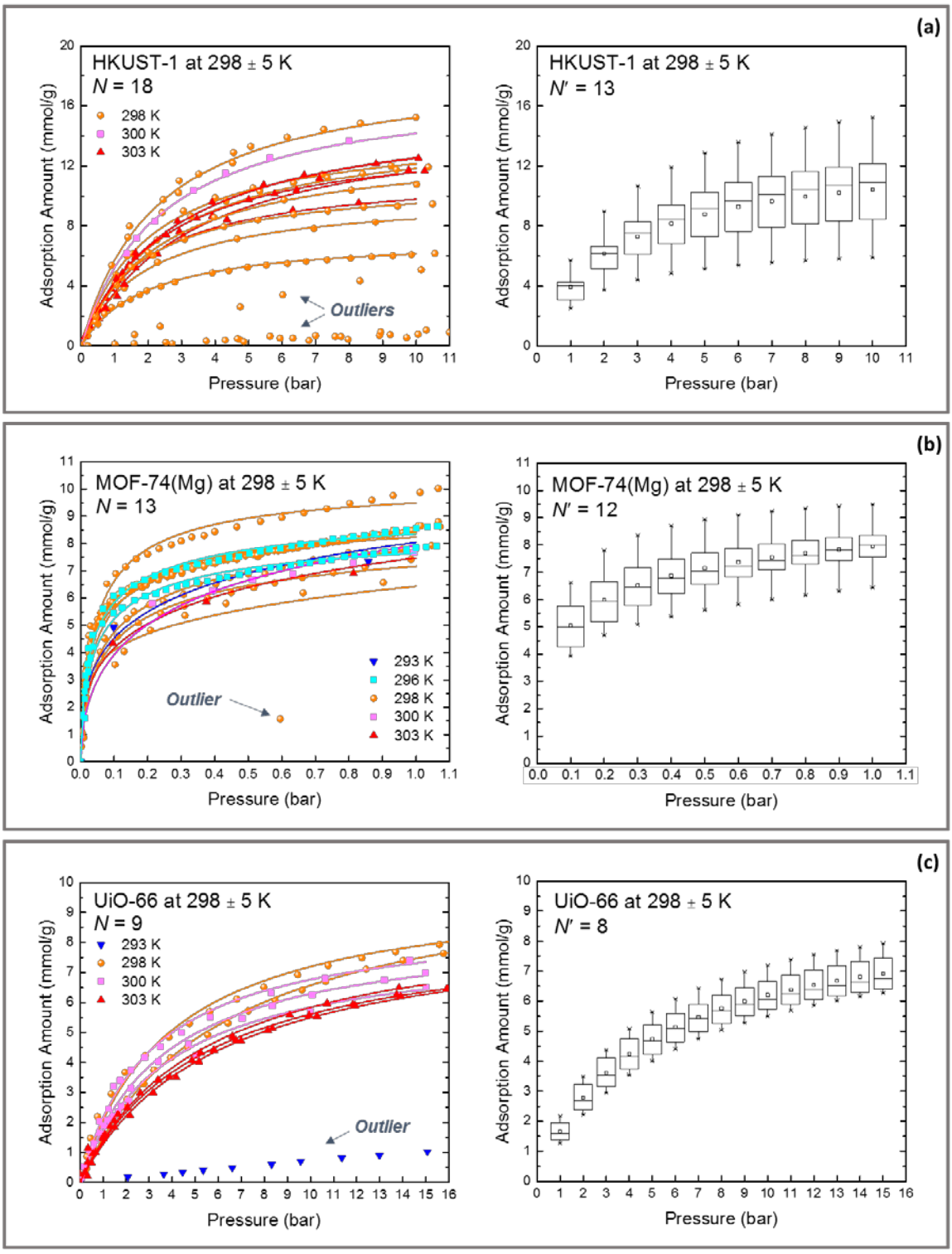

Figure 2.A.6. Box isotherms for 9 MOFs at temperatures $T \pm 5$ K ordered from the highest to lowest N'. The solid curves are omitted. (a) HKUST-1, (b) MOF-74(Mg), and (c) UiO-66.

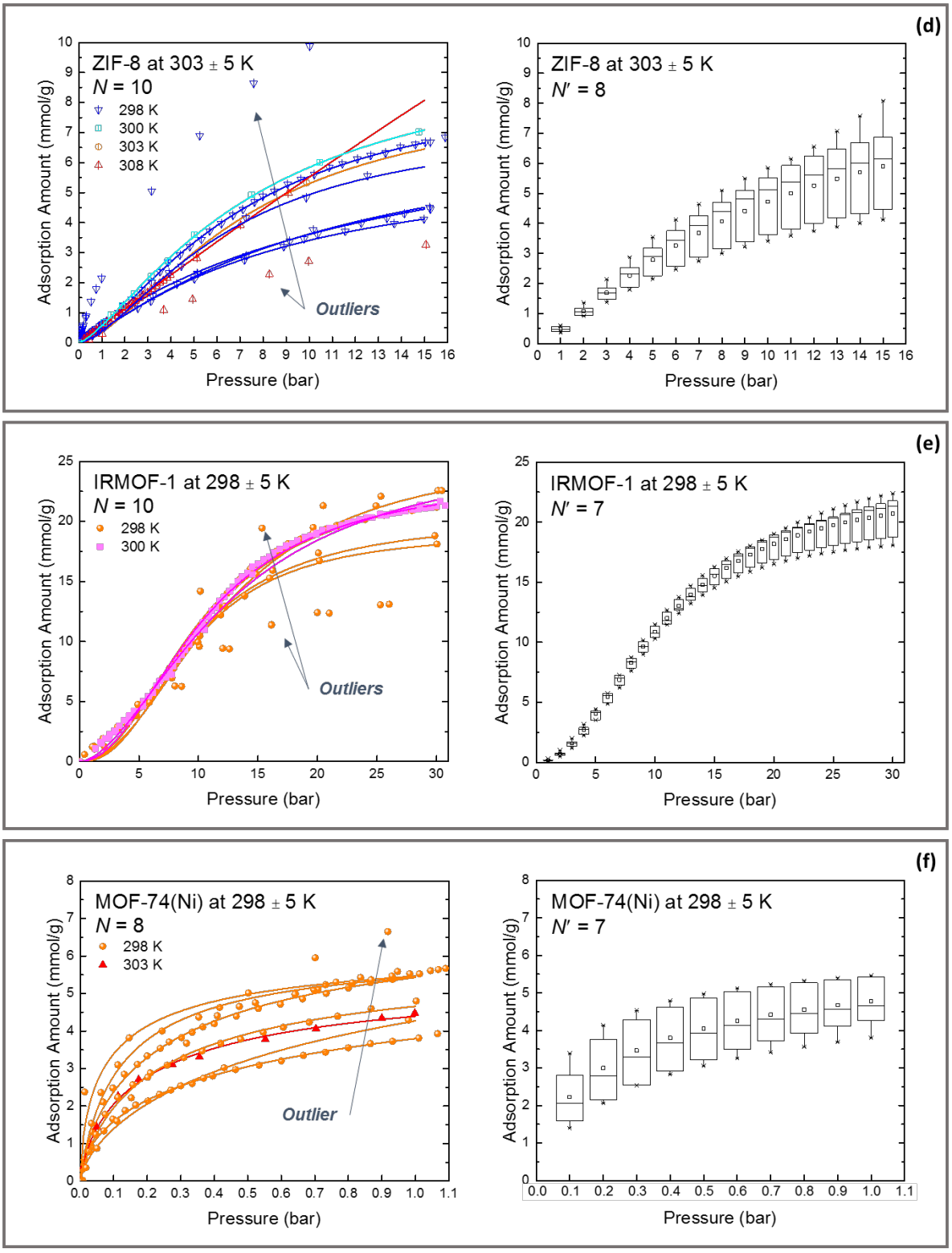

Figure 2.A.6. Continued. (d) ZIF-8, (e) IRMOF-1, and (f) MOF-74(Ni).

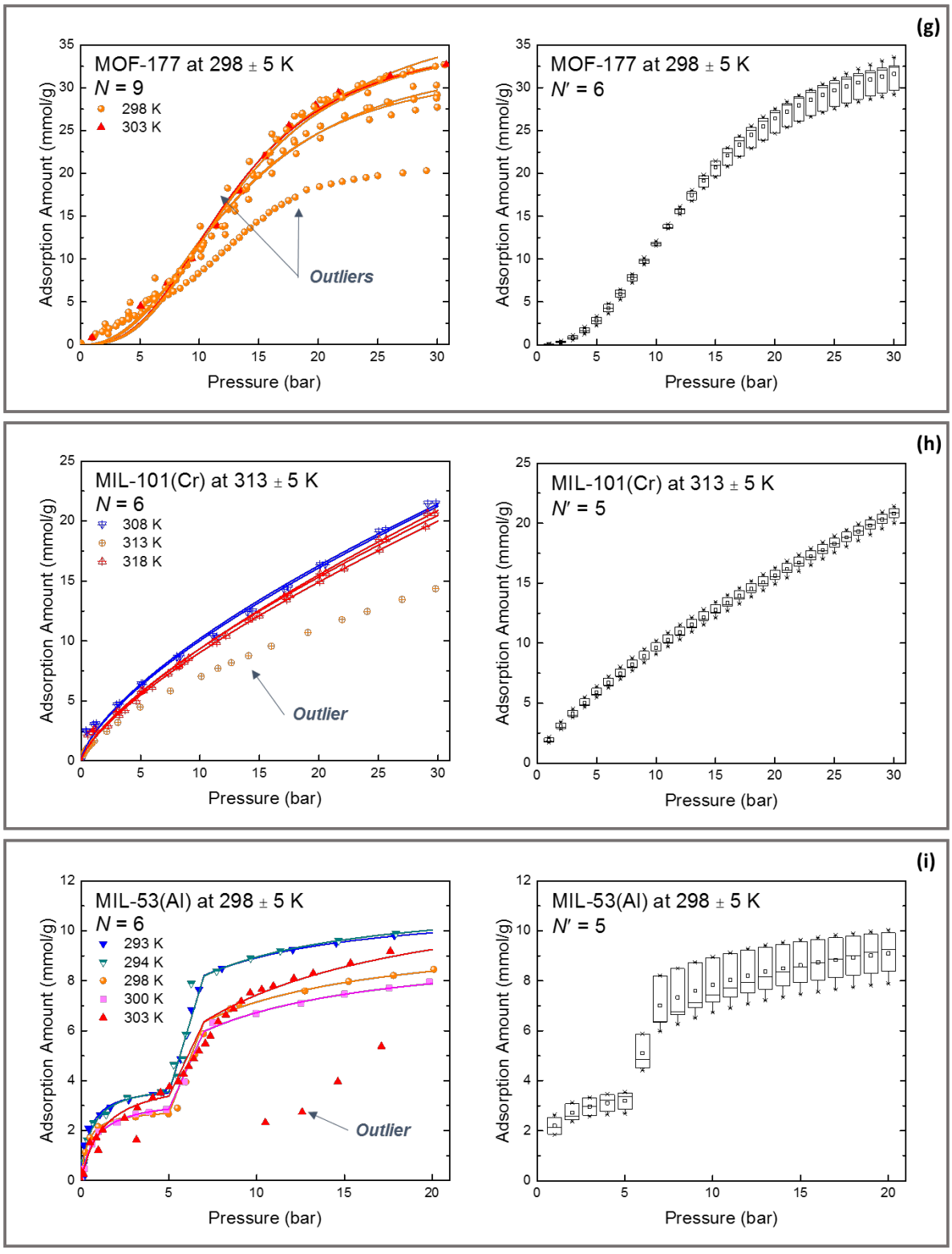

Figure 2.A.6. Continued. (g) MOF-177, (h) MIL-101(Cr), and (i) MIL-53(Al).

2.A.2.3 Region Isotherms for R2 Reproducibility Level MOFs

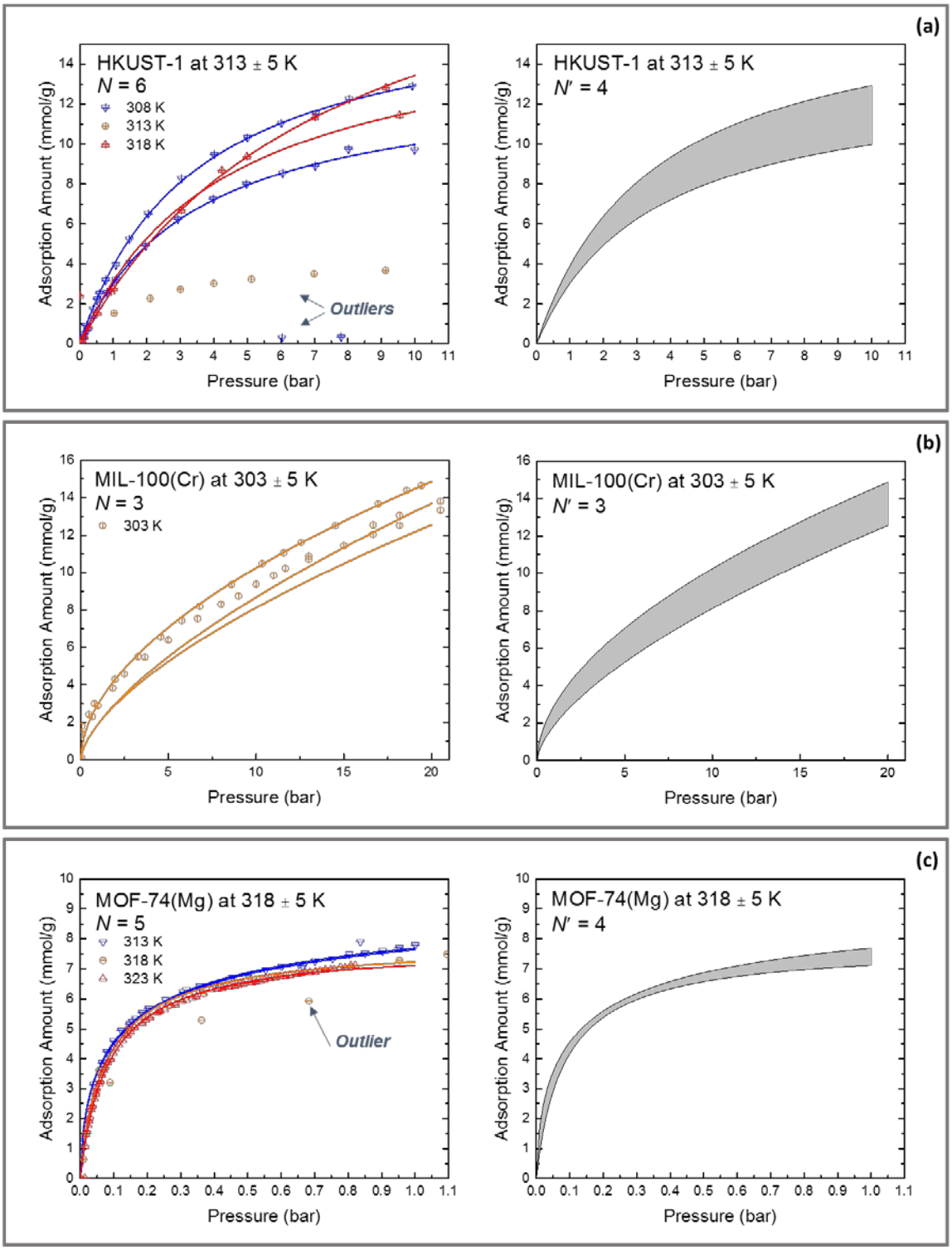

Figure 2.A.7. Region isotherms for 8 MOFs at temperatures T ± 5 K ordered from the highest to lowest simulated surface area. (a) HKUST-1, (b) MIL-100(Cr), and (c) MOF-74(Mg).

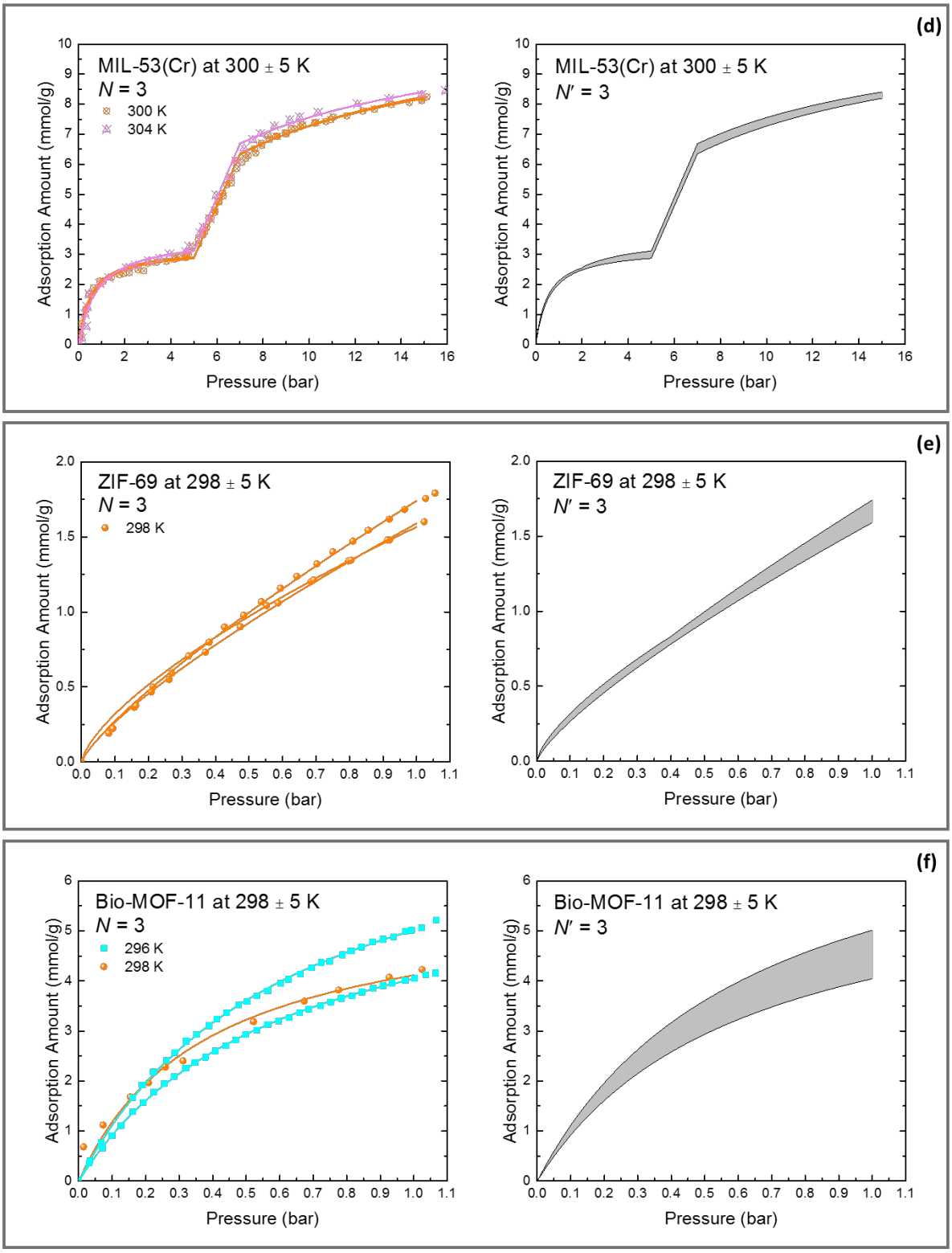

Figure 2.A.7. Continued. (d) MIL-53(Cr), (e) ZIF-69, and (f) Bio-MOF-11.

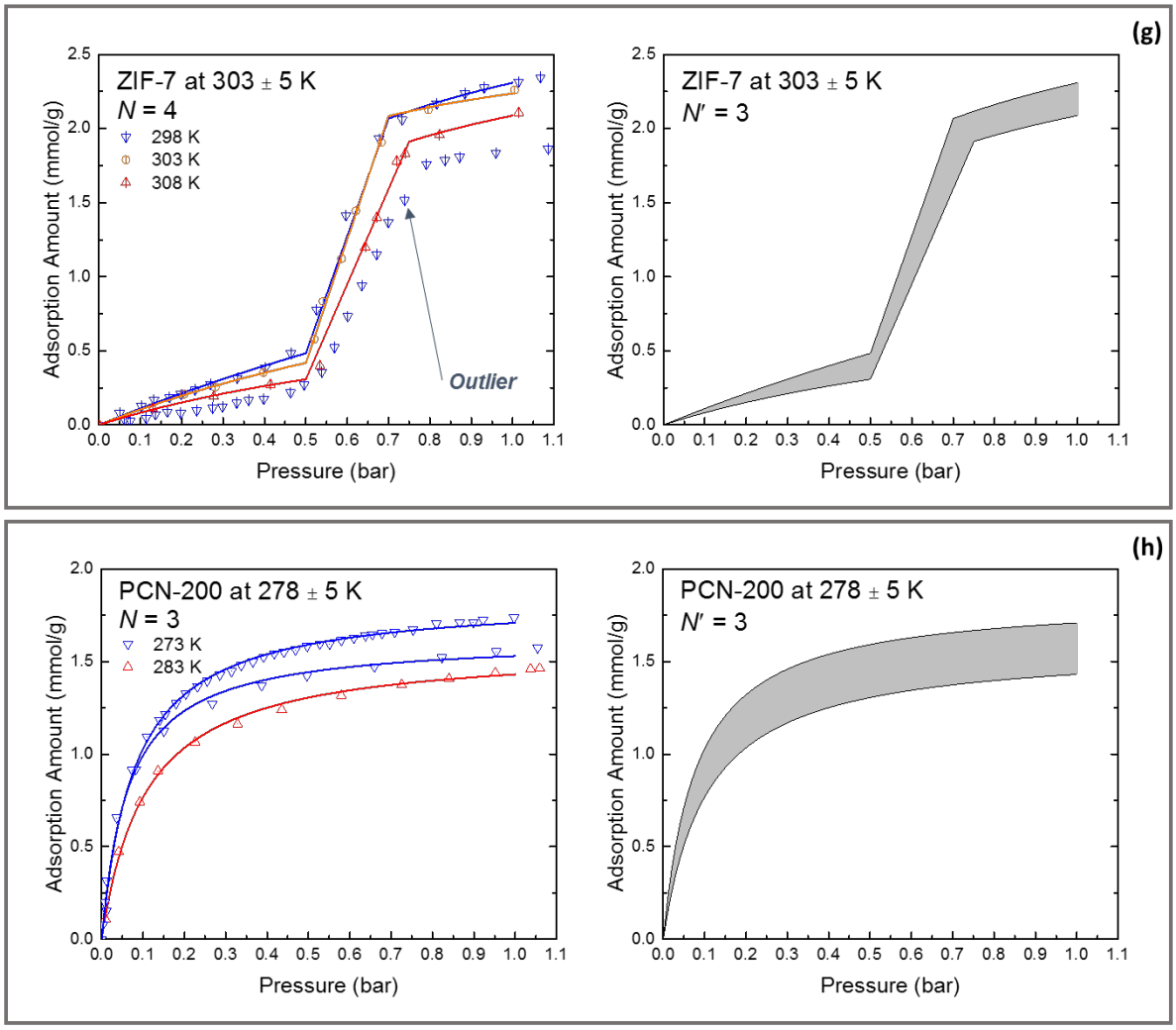

Figure 2.A.7. Continued. (g) ZIF-7 and (h) PCN-200.

2.A.2.4 List of MOFs with $N = N' = 2$ CO_2 Isotherms

By analyzing the NIST/ARPA-E Adsorption Database, we identified 15 MOFs which allow strong conclusions to be drawn about the reproducibility of single-component adsorption isotherms. Additionally, our reproducibility analysis identified 10 materials for which two independent CO_2 isotherm measurements exist at some temperature $T \pm 5$ K. Table 2.A.2 lists these MOFs having CO_2 isotherms with $N = N' = 2$ at given temperature and pressure ranges. They refer to the materials categorized from combination of outlier level O3 and reproducibility level R3 or R4 (refer to yellow arrows in Figure 2.A.1).

Table 2.A.2. List of MOFs for $N = N' = 2$ CO_2 isotherms at given temperature and pressure ranges identified from the NIST/ARPA-E Adsorption Database. MOFs are ordered alphabetically.

MOFs	*T* range	*P* range	MOFs	*T* range	*P* range
CAU-1	273 ± 5 K 298 ± 5 K	[0, 1] bar	NU-100	298 ± 5 K	[0, 1] bar
CPM-5	273 ± 5 K 298 ± 5 K	[0, 1] bar	NU-1000	273 ± 5 K 293 ± 5 K	[0, 1] bar
IRMOF-3	298 ± 5 K	[0, 30] bar	SDU-1	273 ± 5 K	[0, 1] bar
MOF-508	303 ± 5 K 323 ± 5 K 343 ± 5 K	[0, 5] bar	UMCM-1	298 ± 5 K	[0, 15] bar
			ZIF-11	273 ± 5 K	[0, 1] bar
			ZIF-71	298 ± 5 K	[0, 1] bar

2.A.2.5 Summary of CO_2 Adsorption in MOFs

Table 2.A.3 lists a comprehensive summary of the reproducibility analysis regarding CO_2 adsorption in 27 MOFs. This table curates all known MOFs for which any conclusions can be drawn about the reproducibility of CO_2 adsorption at different adsorption conditions. In this table, the isotherm models to fit the experimental measurements, consistency rating defined in Section 2.A.1, different adsorption conditions including temperature ranges and pressures, evaluation metric as a combination of outlier level and reproducibility level defined in Section 2.A.1, and quantified CO_2 adsorption range at corresponding conditions are given. A material can appear multiple times for data with different *N* and *N'* depending at different adsorption conditions.

Table 2.A.3. A comprehensive summary of the reproducibility analysis regarding CO_2 adsorption in 27 MOFs from NIST/ARPA-E Adsorption Database. Isotherm model, consistency rating, adsorption conditions, evaluation metric, and quantified CO_2 adsorption range at corresponding conditions are given. All definitions for complementary characteristics used in this table are as defined in Tables 2.1 and 2.2. List of MOFs is ordered from Section 2.A.2.2 to Section 2.A.2.4.

MOFs	Isotherm Model	Consistency Rating	Adsorption Conditions	Evaluation Metric	Adsorption Range [a]
HKUST-1	Langmuir	Low	278 ± 5 K, 1 bar	O2/R4	[7.0, 9.3]
		Moderate	298 ± 5 K, 10 bar	O1/R1	[9.8, 12.5]
		Moderate	313 ± 5 K, 10 bar	O1/R2	[10.0, 12.9]
		High	328 ± 5 K, 7.5 bar	O2/R2	[8.6, 9.6]
		High	343 ± 5 K, 10 bar	O1/R1	[7.6, 9.6]
		High	375 ± 5 K, 10 bar	O2/R2	[5.1, 5.4]
MOF-74(Mg)	Langmuir-Freundlich	High	298 ± 5 K, 1 bar	O1/R1	[7.6, 8.4]
		High	298 ± 5 K, 20 bar	O1/R2	[11.3, 12.6]
		High	318 ± 5 K, 1 bar	O1/R2	[7.1, 7.7]
UiO-66	Langmuir	High	273 ± 5 K, 1 bar	O1/R1	[2.4, 3.3]
		High	273 ± 5 K, 10 bar	O2/R2	[7.9, 9.3]
		High	298 ± 5 K, 1 bar	O1/R1	[1.4, 2.0]
		High	298 ± 5 K, 15 bar	O1/R1	[6.4, 7.4]
		Moderate	310 ± 5 K, 1 bar	O2/R3	[1.3, 1.6]

[a] Adsorption amount in *mmol CO_2/g MOF* as recommended in IUPAC manual on Reporting Physisorption Data for Gas/Solid Systems.[15]

Table 2.A.3. Continued.

MOFs	Isotherm Model	Consistency Rating	Adsorption Conditions	Evaluation Metric	Adsorption Range [a]
ZIF-8	Langmuir-Freundlich	Moderate	273 ± 5 K, 1 bar	O1/R1	[1.5, 1.6]
		High	303 ± 5 K, 15 bar	O1/R1	[4.5, 6.9]
		Moderate	323 ± 5 K, 25 bar	O3/R3	[3.9, 4.1]
IRMOF-1	Langmuir-Freundlich	Moderate	298 ± 5 K, 30 bar	O1/R1	[18.7, 21.8]
MOF-74(Ni)	Langmuir-Freundlich	High	298 ± 5 K, 1 bar	O1/R1	[4.3, 5.4]
		Low	318 ± 5 K, 1 bar	O3/R4	[3.4, 3.9]
		Moderate	348 ± 5 K, 1 bar	O2/R3	[2.2, 2.6]
MOF-177	Langmuir-Freundlich	Moderate	298 ± 5 K, 30 bar	O1/R1	[29.7, 32.6]
MIL-101(Cr)	Freundlich	Moderate	273 ± 5 K, 1 bar	O3/R3	[3.2, 3.3]
		High	313 ± 5 K, 30 bar	O1/R1	[20.0, 21.2]
		Moderate	328 ± 5 K, 30 bar	O2/R3	[20.1, 20.3]
MIL-53(Al) [b]	Langmuir	High	298 ± 5 K, 5 bar	O1/R1	[2.9, 3.5]*
		High	298 ± 5 K, 20 bar	O1/R1	[8.4, 9.9]
MIL-100(Cr)	Freundlich	High	303 ± 5 K, 20 bar	O2/R2	[12.6, 14.8]
MIL-53(Cr) [b]	Langmuir	High	300 ± 5 K, 5 bar	O2/R2	[2.8, 3.1]*
		High	300 ± 5 K, 15 bar	O2/R2	[8.2, 8.4]
ZIF-69	Freundlich	High	298 ± 5 K, 1 bar	O2/R2	[1.6, 1.7]
Bio-MOF-11	Langmuir	Moderate	273 ± 5 K, 1 bar	O3/R3	[5.8, 6.4]
		High	298 ± 5 K, 1 bar	O2/R2	[4.1, 5.0]
ZIF-7 [c]	Langmuir	Moderate	273 ± 5 K, 0.2 bar	O3/R3	[0.6, 0.8]*
		Moderate	273 ± 5 K, 1 bar	O3/R3	[2.3, 2.7]
		High	303 ± 5 K, 0.5 bar	O2/R2	[0.3, 0.5]*
		High	303 ± 5 K, 1 bar	O2/R2	[2.1, 2.3]

[a] Adsorption amount in *mmol CO_2/g MOF* as recommended in IUPAC manual on Reporting Physisorption Data for Gas/Solid Systems.[15]

[b] Breathing MOFs with asterisks (*) dictating P_{trans} for a structural transition effect. Langmuir models are used to fit measurements of both narrow and large pore structures, and connected.

[c] Gate-opening MOF with asterisk (*) dictating threshold pressure for a gate-opening effect. Langmuir models are used for measurements before and after a gate-opening, and connected.

Table 2.A.3. Continued.

MOFs	Isotherm Model	Consistency Rating	Adsorption Conditions	Evaluation Metric	Adsorption Range [a]
PCN-200	Langmuir	High	278 ± 5 K, 1 bar	O2/R2	[1.4, 1.7]
		Moderate	296 ± 5 K, 1 bar	O3/R3	[1.3, 1.5]
CAU-1	Freundlich	Moderate	273 ± 5 K, 1 bar	O3/R3	[3.3, 3.7]
		Moderate	298 ± 5 K, 1 bar	O3/R3	[1.7, 2.0]
CPM-5	Freundlich	Low	273 ± 5 K, 1 bar	O3/R4	[2.8, 3.7]
		Moderate	298 ± 5 K, 1 bar	O3/R3	[2.2, 2.5]
IRMOF-3	Langmuir-Freundlich	Moderate	298 ± 5 K, 30 bar	O3/R3	[18.3, 18.6]
MOF-508	Langmuir	Moderate	303 ± 5 K, 5 bar	O3/R3	[6.2, 6.3]
		Moderate	323 ± 5 K, 5 bar	O3/R3	[4.2, 4.3]
		Moderate	343 ± 5 K, 5 bar	O3/R3	[3.1, 3.2]
NU-100	Langmuir	Moderate	298 ± 5 K, 1 bar	O3/R3	[2.6, 2.7]
NU-1000	Langmuir	Moderate	273 ± 5 K, 1 bar	O3/R3	[2.9, 3.0]
		Moderate	293 ± 5 K, 1 bar	O3/R3	[1.6, 1.7]
SDU-1	Langmuir	Moderate	273 ± 5 K, 1 bar	O3/R3	[1.5, 1.6]
UMCM-1	Freundlich	Moderate	298 ± 5 K, 15 bar	O3/R3	[13.1, 14.4]
ZIF-11	Langmuir	Moderate	273 ± 5 K, 1 bar	O3/R3	[1.6, 1.8]
ZIF-71	Freundlich	Moderate	298 ± 5 K, 1 bar	O3/R3	[0.6, 0.7]
MIL-47(V) [d]	Langmuir-Freundlich	Moderate	303 ± 5 K, 20 bar	O2/R3	[6.9, 7.4]
ZIF-78 [d]	Langmuir	Moderate	298 ± 5 K, 1 bar	O2/R3	[2.1, 2.2]

[a] Adsorption amount in *mmol CO_2/g MOF* as recommended in IUPAC manual on Reporting Physisorption Data for Gas/Solid Systems.[15]

[d] MOFs not listed from Section 2.A.2.2 to Section 2.A.2.4 with outlier level O2 and reproducibility level R3.

2.A.3 List of Molecules with Unknown Reproducibility of Adsorption in MOFs

In Section 2.A.3, we summarize the adsorbates in the NIST/ARPA-E Adsorption Database in Tables 2.A.4-2.A.6. The adsorbates are grouped based on whether conclusions can be drawn about reproducibility (Table 2.A.4), adsorption has been measured in a MOF but no conclusions can be drawn (Table 2.A.5), or if no experimental adsorption isotherms are reported (Table 2.A.6).

Table 2.A.4. Adsorbates in the NIST/ARPA-E Adsorption Database for which a reproducibility assessment can be performed for at least one MOF material (*i.e.* $N > 1$ for at least one MOF). For adsorbates marked with an asterisk (*), the largest number of independent measurements in any MOF is two (*i.e.* $N \leq 2$ in all MOFs). Adsorbates are ordered alphabetically and are listed as reported in the NIST/ARPA-E Adsorption Database.

1-butene*	Methane
Acetone*	Methanol*
Acetylene*	n-Butane*
Ammonia*	n-Hexane*
Argon	Nitric oxide*
Benzene	Nitrogen
Carbon dioxide	n-propane
Carbon monoxide*	Oxygen
Ethane	o-Xylene*
Ethanol*	Propene
Ethene*	p-Xylene
Hydrogen	Water
Isobutane*	

Table 2.A.5. Adsorbates in the NIST/ARPA-E Adsorption Database for which an adsorption isotherm in at least one MOF has been reported, but for which no reproducibility assessment can be performed (*i.e.* $N \leq 1$ for all MOFs). Adsorbates are ordered alphabetically and are listed as reported in the NIST/ARPA-E Adsorption Database.

1,2-Dichloroethane	Dimethyl ether	Nitrous oxides (NO_X)
1-Butanol	Dimethylformamide	n-Nonane
1-hexanol	Ethenylbenzene	n-Octane
1-Octanol	Ethyl acetate	n-Pentane
1-Pentanol	Helium	Pyridine
1-Propanol	Hydrogen chloride	Sevoflurane
1-propyne	Hydrogen sulfide	Styrene
2,2-Dimethyl-Butane	Hydrogen/Deuterium mixture	Sulfur dioxide
2-Propanol	Isobutanol	Sulfur hexafluoride
Acetaldehyde	Isobutene	Tert-Butanol
Acetonitrile	Krypton	Tetrahydrofuran
Carbon tetrafluoride	Methyl ethyl ketone	Toluene
Cis-2-Butene	m-Xylene	Trans-2-Butene
Cyclohexane	Neopentane	Trichloromethane
Deuterium	m-Heptane	Xenon
Diethyl ether	Nitrous oxide (N_2O)	

Table 2.A.6. Adsorbates in the NIST/ARPA-E Adsorption Database for which no experimentally measured isotherms are reported for any MOF materials (*i.e.* $N = 0$ in all MOFs). Adsorbates are ordered alphabetically and are listed as reported in the NIST/ARPA-E Adsorption Database.

[Bu4N]4HPW11CoO39	Acenaphthene	Chlorobenzene
[CpPd(eta3-C3H5)]	Acenaphthylene	Chromate
[CpPtMe3]	Acetonitrile-D3	Chromium
[Pt(cod)Me2]	Alizarin red S	Chromium hexacarbonyl
[Ru(cod)(cot)]	Ametryn	Cis-piperylene
1,1,2-Trichloroethene	Aniline	Clofibric acid
1,1-dichloroethylene	Anthracene	Congo red
1,3-benzothiazole	Benz[a]anthracene	Copper
1-benzothiophene	Benzo[A]Pyrene	Copper cluster
1-Naphthol	Bisphenol A	Copper(II) ion
2-ethylhexyl oleate	Bromine	Cumene
2-ethylhexyl oleic estolide ester	Bromobenzene	Cyanobenzene
2-Methoxytoluene	Bromo-chloro-fluoromethane	Cyclohexene
2-Methylbutane	Buckminsterfullerene C60	Cyclopentane
2-Methylisoborneol	Buckminsterfullerene C70	D131 dye
2-Methylpyridine	Butan-1-amine	Dibenzothiophene
2-Pentanone	$C_2H_{10}Zn$	Dichlofluanid
3-Hexanol	Cadmium	Dichloromethane
3-Methoxytoluene	Cadmium(II) ion	Dichromate
4-atom palladium-4-atom gold cluster	Caffeine	Diethyl sulfide
4-Chlorophenol	Calcium	Difluorocarbene
4-ethyl-4-methyloctane	Carbon disulfide	Diisopropyl fluorophosphate
4-Methoxytoluene	Carbon tetrachloride	Dimethyl methylphosphonate
8-Atom gold cluster	Cesium	Dimethylamine
8-Atom palladium cluster	Chlorine	Dimethylcyclopentanomethylcyclohexane

Table 2.A.6. Continued.

Ethylene glycol	Lead	Molybdenum hexacarbonyl
Ethylene oxide	Lead(II) Iion	n,n-diethylformamide
Flumetralin	Lithium	N719 dye
Fluoranthene	Malachite green	$NaH_4PW_{11}TiO_{40}$
Fluorescein	m-Chlorotoluene	Naphthalen-1-amine
Fluracil	m-cymene	Naphthalene
Formaldehyde	m-dichlorobenzene	Naproxen
Furfural	m-Dinitrobenzene	n-decane
Glycerin	Mercury	n-Docosane
Glycidol	Mercury dichloride	n-Dodecane
Gold	Methyl isobutyl ketone	Neon
Hex-1-ene	Methyl laurate	n-heneicosane
Hydrogen cyanide	Methyl oleate	n-Heptadecane
Hydrogen deuteride	Methyl oleic estolide ester	n-hexadecane
Ibuprofen	Methyl orange	Nickel
Indole	Methyl palmitate	n-Icosane
Iodine	Methyl stearate	Nitric acid
Iodo-Benzene	Methyl tertiary-butyl ether	Nitrobenzene
Iron	Methyl viologen	Nitrogen dioxide
Isoamyl alcohol	Methylcyclohexane	Nitromethane
Isocetane	Methylcyclopentanodecalin	n-nonadecane
Isoheptane	Methylene blue	n-octadecane
Isooctane	Methylene green	n-Pentadecane
Isoprene	m-Ethyltoluene	n-Perfluoroethane
Kresoxim-methyl	m-nitrophenol	

Table 2.A.6. Continued.

n-Perfluorohexane	Phenol	Sulfur
n-Propanal	Phenylalanine	Sulfur trifluoride
n-Propylbenzene	p-Nitrophenol	Sulfur trioxide
n-Tetracosane	p-Nitrotoluene	Sulfuric acid
n-Tetradecane	Polycyclic aromatic hydrocarbons	Sulfurous acid
n-Tricosane	Pyrazine	Tebuconazole
n-tridecane	Pyrene	Terephthalic acid
n-undecane	Pyrimethanil	Tert-Pentanol
o-Chlorotoluene	Quinoline	Tetrachloroethene
o-Cymene	R-115	Tetrachlorogold(1-)
o-Dichlorobenzene	R-124	Tetraconazole
o-Ethyltoluene	R-125	Tetrahydrophenanthrene
Oil red O	R-134A	Tetrahydrothiophene
o-Nitrophenol	R-21	Thiophene
Palladium(II) ion	R-22	Titanium
p-Chlorotoluene	R-23	Trans-piperylene
p-Cymene	R-410A	Tribromomethane
p-Dichlorobenzene	R-507A	Trifluoroethanol
Pentafluorophenol	Radon	Triiodide
Perhydrophenanthrene	Scandium	Tris(8-hydroxyquinoline)aluminum
Permanganate	Selenium	Tritium
Perrhenate	Silver	Uranium dioxide
p-Ethyltoluene	Sodium hydroxide	Xylene (mixture of isomers)
p-Fluorotoluene	Strontium	Zinc
Phenanthrene	Sudan black B	

2.A.4 Molecular Simulation Details

Molecular simulations of CO_2 and N_2 adsorption were conducted by standard Grand Canonical Monte Carlo (GCMC) simulations[5,16-19] using RASPA[18,19]. This atomistic classical simulation for adsorption isotherms requires force fields to describe van der Waals interactions for sorbate/sorbent interactions and sorbate/sorbate interactions.[20] "Standard" force fields, namely the universal force field (UFF)[21] and the TraPPE[22] force field, were used. Lennard-Jones parameters for MOF atoms and quadrupolar CO_2, N_2 molecules were, therefore, taken from UFF and TraPPE force field, respectively, and molecule/MOF interactions were defined with standard mixing rules. In GCMC simulations associated with these force fields, truncated potentials with tail corrections are applied. Lennard-Jones interactions are truncated at 12 Å. Simulation boxes are expanded to at least 26 Å along each dimension and triclinic periodic boundary conditions were defined in all dimensions. Electrostatic interactions were modeled by employing EQeq point charges for MOF atoms[23,24] and TraPPE charges for CO_2, N_2 molecules[18,19]. The extended charge equilibration method for EQeq charges is a semiempirical method which is much less computationally expensive than charge assignments on the basis of electronic structure calculations.[23-25] All GCMC calculations included 5,000 initialization cycles followed by 50,000 production cycles, which were found in initial tests to be sufficient to achieve well converged results. Random Monte Carlo moves, either accepted or rejected according to Boltzmann-type weighting criteria, allowed translation, rotation, regrowth, reinsertion, deletion and insertion moves at identical probabilities.

The materials investigated in this chapter for computational simulations are 15 of the known MOFs where firm conclusions could be drawn about the measurement

reproducibility. The structures simulated are HKUST-1, MOF-74(Mg), UiO-66, ZIF-8, IRMOF-1, MOF-74(Ni), MOF-177, MIL-101(Cr), MIL-53(Al), MIL-100(Cr), MIL-53(Cr), ZIF-69, Bio-MOF-11, ZIF-7, and PCN-200. The MOF .cif files distributed from the RASPA molecular simulation code[18,19] were used for the crystal structures. All calculations assumed that the MOFs were rigid, that is, relaxation of the MOF atoms due to the presence of adsorbed molecules was neglected. For the breathing MOFs, the narrow pore or large pore structure was used depending on their observed structural transition pressure and the pressure being simulated. This means that the large pore structure for MIL-53(Al) and the narrow pore structure for MIL-53(Cr) were used, respectively. For ZIF-7, the open-framework structure was used.

The choice of charges on framework atoms in molecular models of MOFs can influence the predictions of these models. In addition to the EQeq charges used for the calculations in Figure 2.5, the density derived electrostatic and chemical (DDEC) method[26-28] is another method to assign high quality point charges for framework atoms. It has been observed by Nazarian *et al*.[24] and Haldoupis *et al*.[29] that on average EQeq predicts charges for metals higher than those predicted by DDEC. Watanabe *et al*.[28] pointed out the assignment of framework charges always introduces ambiguity even when the true electron density of a material is known. Figure 2.A.8 shows a comparison between simulated adsorption of CO_2 by employing EQeq and DDEC charges, with other details of the simulations held fixed. Figure 2.A.8a compares the box isotherm (reproduced from Figure 2.1b) and simulated adsorption isotherm by employing EQeq and DDEC charges in HKUST-1. Figure 2.A.8b is a parity plot for simulated adsorbed CO_2 using either EQeq and DDEC charges for the 15 MOFs where firm conclusions could be drawn about the

measurement reproducibility at the conditions shown in Figure 2.5. This information provides a useful baseline for future comparison and potential refinement of molecular models using the reproducible adsorption information from Figure 2.5.

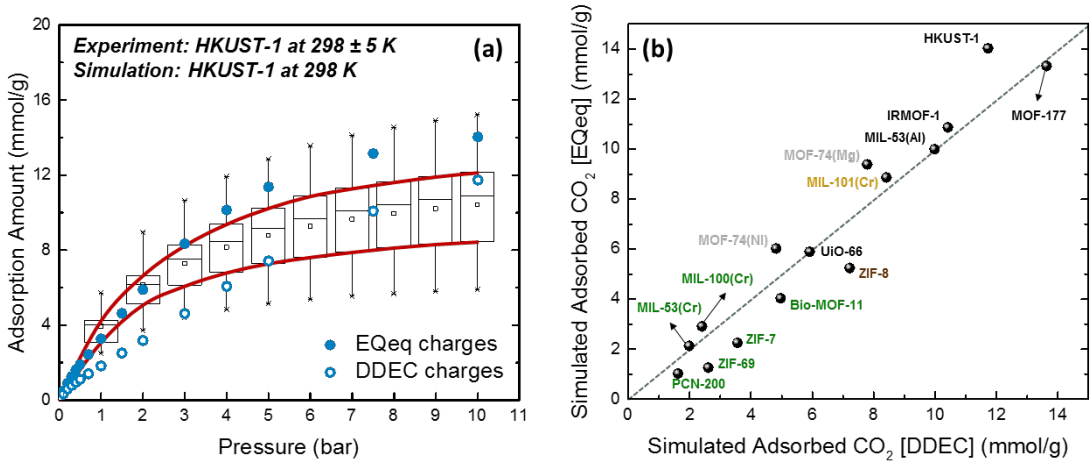

Figure 2.A.8. (a) Comparison between experimental box isotherm for CO_2 adsorption in HKUST-1 at 298 ± 5 K and simulated isotherms for CO_2 adsorption in HKUST-1 at 298 K with EQeq (filled circles) and DDEC (open circles) charges on framework atoms. (b) Comparison of simulated CO_2 adsorbed amounts using EQeq and DDEC charges for the 15 materials that were classified for reproducibility level R1 or R2. The adsorption conditions for molecular simulations are as stated in Figures 2.5a and 2.5b using the same color labels. Data is not reported for HKUST-1 at 313 K and MOF-74(Mg) at 318 K.

The simulated surface area calculated in this chapter is so-called "accessible" surface area. It corresponds to the area traced out by the center of a probe molecule as the probe is rolled across the surface of the framework atoms.[5] The probe should be chosen to correspond to the size of the adsorbate of interest[5] – CO_2 in this chapter. N_2 has similar molecular diameter compared to CO_2. Therefore, the simulated surface area was calculated by using N_2 as probe molecule with overlap distance criteria set to a size parameter σ of 3.31 Å.[18,19]

2.A.5 References for Appendix 2.A

(1) Tukey, J. W. *Exploratory Data Analysis*; Addison-Wesley: MA, 1977.

(2) Moriasi, D. N.; Arnold, J. G.; Van Liew, M. W.; Bingner, R. L.; Harmel, R. D.; Veith, T. L. Model evaluation guidelines for systematic quantification of accuracy in watershed simulations. *T. ASABE* **2007,** *50*, 885-900.

(3) Chai, T.; Draxler, R. R. Root mean square error (RMSE) or mean absolute error (MAE)? - Arguments against avoiding RMSE in the literature. *Geosci. Model Dev.* **2014,** *7*, 1247-1250.

(4) Singh, J.; Knapp, H. V.; Arnold, J. G.; Demissie, M. Hydrologic modeling of the Iroquois River watershed using HSPF and SWAT. *J. Am. Water Resour. Assoc.* **2005,** *41*, 361-375.

(5) Duren, T.; Bae, Y. S.; Snurr, R. Q. Using molecular simulation to characterise metal-organic frameworks for adsorption applications. *Chem. Soc. Rev.* **2009,** *38*, 1237-1247.

(6) Demir, H.; Greathouse, J. A.; Staiger, C. L.; Perry, J. J.; Allendorf, M. D.; Sholl, D. S. DFT-based force field development for noble gas adsorption in metal organic frameworks. *J. Mater. Chem. A* **2015,** *3*, 23539-23548.

(7) Dubbeldam, D.; Frost, H.; Walton, K. S.; Snurr, R. Q. Molecular simulation of adsorption sites of light gases in the metal-organic framework IRMOF-1. *Fluid Phase Equilib.* **2007,** *261*, 152-161.

(8) Surble, S.; Millange, F.; Serre, C.; Duren, T.; Latroche, M.; Bourrelly, S.; Llewellyn, P. L.; Ferey, G. Synthesis of MIL-102, a chromium carboxylate metal-organic framework, with gas sorption analysis. *J. Am. Chem. Soc.* **2006,** *128*, 14889-14896.

(9) Rouquerol, J.; Llewellyn, P.; Rouquerol, F. Is the BET equation applicable to microporous adsorbents? *Stud. Surf. Sci. Catal.* **2007,** *160*, 49-56.

(10) Walton, K. S.; Snurr, R. Q. Applicability of the BET method for determining surface areas of microporous metal-organic frameworks. *J. Am. Chem. Soc.* **2007,** *129*, 8552-8556.

(11) Brunauer, S. *The Adsorption of Gases and Vapours*; Oxford University Press: Oxford, 1945.

(12) Burtch, N. C.; Jasuja, H.; Walton, K. S. Water Stability and Adsorption in Metal-Organic Frameworks. *Chem. Rev.* **2014,** *114*, 10575-10612.

(13) Jasuja, H.; Zang, J.; Sholl, D. S.; Walton, K. S. Rational Tuning of Water Vapor and CO_2 Adsorption in Highly Stable Zr-Based MOFs. *J. Phys. Chem. C* **2012,** *116*, 23526-23532.

(14) Cmarik, G. E.; Kim, M.; Cohen, S. M.; Walton, K. S. Tuning the Adsorption Properties of UiO-66 *via* Ligand Functionalization. *Langmuir* **2012,** *28*, 15606-15613.

(15) Thommes, M.; Kaneko, K.; Neimark, A. V.; Olivier, J. P.; Rodriguez-Reinoso, F.; Rouquerol, J.; Sing, K. S. W. Physisorption of gases, with special reference to the evaluation of surface area and pore size distribution (IUPAC Technical Report). *Pure Appl. Chem.* **2015,** *87*, 1051-1069.

(16) Coudert, F. X.; Fuchs, A. H. Computational characterization and prediction of metal-organic framework properties. *Coord. Chem. Rev.* **2016,** *307*, 211-236.

(17) Li, J. R.; Ma, Y. G.; McCarthy, M. C.; Sculley, J.; Yu, J. M.; Jeong, H. K.; Balbuena, P. B.; Zhou, H. C. Carbon dioxide capture-related gas adsorption and separation in metal-organic frameworks. *Coord. Chem. Rev.* **2011,** *255*, 1791-1823.

(18) Dubbeldam, D.; Calero, S.; Ellis, D. E.; Snurr, R. Q. RASPA: molecular simulation software for adsorption and diffusion in flexible nanoporous materials. *Mol. Simul.* **2016,** *42*, 81-101.

(19) Dubbeldam, D.; Torres-Knoop, A.; Walton, K. S. On the inner workings of Monte Carlo codes. *Mol. Simul.* **2013,** *39*, 1253-1292.

(20) Addicoat, M. A.; Vankova, N.; Akter, I. F.; Heine, T. Extension of the Universal Force Field to Metal-Organic Frameworks. *J. Chem. Theory Comput.* **2014,** *10*, 880-891.

(21) Rappe, A. K.; Casewit, C. J.; Colwell, K. S.; Goddard, W. A.; Skiff, W. M. UFF, A Full Periodic-Table Force-Field for Molecular Mechanics and Molecuar Dynamics Simulations. *J. Am. Chem. Soc.* **1992,** *114*, 10024-10035.

(22) Martin, M. G.; Siepmann, J. I. Transferable potentials for phase equilibria. 1. United-atom description of n-alkanes. *J. Phys. Chem. B* **1998,** *102*, 2569-2577.

(23) Wilmer, C. E.; Kim, K. C.; Snurr, R. Q. An Extended Charge Equilibration Method. *J. Phys. Chem. Lett.* **2012,** *3*, 2506-2511.

(24) Nazarian, D.; Camp, J. S.; Sholl, D. S. A Comprehensive Set of High-Quality Point Charges for Simulations of Metal-Organic Frameworks. *Chem. Mater.* **2016,** *28*, 785-793.

(25) Wilmer, C. E.; Farha, O. K.; Bae, Y. S.; Hupp, J. T.; Snurr, R. Q. Structure-property relationships of porous materials for carbon dioxide separation and capture. *Energy Environ. Sci.* **2012,** *5*, 9849-9856.

(26) Manz, T. A.; Sholl, D. S. Chemically meaningful atomic charges that reproduce the electrostatic potential in periodic and nonperiodic materials. *J. Chem. Theory Comput.* **2010,** *6*, 2455-2468.

(27) Manz, T. A.; Sholl, D. S. Improved atoms-in-molecule charge partitioning functional for simultaneously reproducing the electrostatic potential and chemical states in periodic and nonperiodic materials. *J. Chem. Theory Comput.* **2012,** *8*, 2844-2867.

(28) Watanabe, T.; Manz, T. A.; Sholl, D. S. Accurate treatment of electrostatics during molecular adsorption in nanoporous crystals without assigning point charges to framework atoms. *J. Phys. Chem. C* **2011,** *115*, 4824-4836.

(29) Haldoupis, E.; Nair, S.; Sholl, D. S. Finding MOFs for highly selective CO_2/N_2 adsorption using materials screening based on efficient assignment of atomic point charges. *J. Am. Chem. Soc.* **2012,** *134*, 4313-4323.

CHAPTER 3. ESTABLISHING UPPER BOUNDS ON CO_2 SWING CAPACITY IN SUB-AMBIENT PRESSURE SWING ADSORPTION VIA MOLECULAR SIMULATION OF METAL-ORGANIC FRAMEWORKS

Swing capacity is a key performance metric for processes designed to capture CO_2 by pressure swing adsorption (PSA). Sub-ambient operation of PSA units enables large changes in CO_2 swing capacity, and can be economically viable when coupled with heat integration and power recovery. In this chapter, we examine what upper bounds on CO_2 swing capacity exist *via* molecular simulation of a large collection of metal-organic frameworks (MOFs). As has been observed previously for zeolites, the materials with the largest swing capacity at a given temperature have large pore volumes and heats of adsorption within a narrow range of optimal values. A number of materials are identified with swing capacities up to 40 mol/kg using a pressure swing from 0.1 bar to 2.0 bar.

* Contents of this chapter have been reproduced from the previously published article

Jongwoo Park, Ryan P. Lively, David S. Sholl, ″Establishing upper bounds on CO_2 swing capacity in sub-ambient pressure swing adsorption *via* molecular simulation of metal-organic frameworks″, ***Journal of Materials Chemistry A***, 5 (2017) 12258-12265.

3.1 INTRODUCTION

Anthropogenic CO_2 emissions are one of the main drivers of global climate change. Unfortunately, it is difficult and expensive to capture CO_2 from dilute sources such as power plants, refinery exhausts, and air.[1,2] As a result there is considerable interest in developing more cost effective and less energy intensive CO_2 capture technology. Porous solid adsorbents such as activated carbon, zeolites, and metal-organic frameworks (MOFs) have been considered as efficient materials for adsorptive CO_2 capture and separation.[2-5] Typically, solid adsorbents are used in cyclic adsorption processes in which desorption is induced by pressure swing (pressure swing adsorption, PSA), temperature swing (temperature swing adsorption, TSA), or vacuum swing (vacuum swing adsorption, VSA).[2,6-8] A critical performance metric that dictates the economic viability of a PSA process is the swing capacity, that is, the difference between the amount of adsorbed gas in the adsorbent at the adsorption condition and the residual adsorbed gas at the desorption condition.[6-8]

A question of broad fundamental interest is how large the CO_2 swing capacity for realistic porous adsorbents can be under practical process conditions. Fang *et al*. recently addressed this question *via* molecular simulations of a large set of cationic zeolites for several prototypical processes chosen for industrial relevance. By considering PSA cycles between 1 bar and 5 bar at 300 K, they showed that materials exist with PSA swing capacity for CO_2 as large as 7.5 mol/kg.[9]

A general strategy for increasing PSA swing capacity, particularly for weakly adsorbing species, is to lower the temperature. The concept of sub-ambient operation has

been widely discussed as a route to improve H_2 capacity in applications of porous materials for H_2 storage.[10] Sub-ambient operations are able to increase deliverable capacity and adsorption selectivity for H_2.[10] It is widely assumed, however, that the cooling cost associated with sub-ambient processes make sub-ambient temperatures impractical for large-scale CO_2 capture from flue gases. Recently, however, Air Liquide had developed a prospective technology for cost- and energy- efficient post-combustion CO_2 capture from power plant flue gas *via* an energy integrated cold membrane process.[11-13] Their developments suggest that large-scale selective adsorption of CO_2 with sub-ambient operation may be viable when coupled with heat integration and power recovery.[8,11-14] These observations make it interesting to examine what upper bounds exist on CO_2 swing capacity in sub-ambient PSA using porous adsorbents.

To search for materials that may define the upper limits for sub-ambient PSA CO_2 swing capacity, we used molecular simulations of CO_2 adsorption on the materials contained in the computation-ready, experimental (CoRE) MOF database.[15] This library of materials is made up of experimentally reported MOF crystal structures that have been prepared for computational simulations. The set of materials we screened was the frameworks optimized *via* density functional theory (DFT) calculation reported recently by Nazarian *et al*.[16,17] for which atomic point charges assigned by the density derived electrostatic and chemical (DDEC) method[18-20] are available. Our calculation strategy was driven by the observations of Fang *et al*. for CO_2 adsorption in zeolites.[9] Their calculations showed that materials with large pore volume and a CO_2 heat of adsorption in a narrow optimal range were required to achieve a large CO_2 swing capacity in typical process conditions. We adapted these criteria to efficiently screen the CoRE MOF database for CO_2

adsorption at sub-ambient conditions. Our calculations show that single component CO_2 swing capacities as high as 40 mol/kg at 213 K and 18 mol/kg at 258 K were possible over a pressure range from 0.1 to 2.0 bar.

Swing capacity is clearly not the only metric that affects the economic viability of PSA and related cyclic processes for gas capture, especially when these capacities are based on single component data. Competitive adsorption during treatment of multicomponent gas mixtures will almost always reduce swing capacities relative to single component adsorption.[6,21,22] The adsorption selectivity of the component of interest in mixture adsorption is also critical to the product purity that can be achieved.[6,21,22] Additionally, the stability of adsorbents with respect to impurities and degradation, the lifetime and cost of the adsorbents, and similar factors also influence the viability of any adsorption process.[1,6] Nevertheless, the maximum achievable swing capacity places bounds on the throughput of PSA and similar cyclic processes. It is therefore useful to consider the single component CO_2 swing capacity before any of the other performance metrics just listed are examined.

3.2 COMPUTATIONAL METHODS

3.2.1 Energy Optimized CoRE MOF DDEC Charge Database

Material selection of MOFs for prediction of gas adsorption and separation is a challenge due to large and diverse set of MOF materials that are known.[23-25] Computational analysis of molecular adsorption and diffusion in MOFs can provide atomic-level insight that is often difficult to obtain experimentally.[26-29] To enable high-throughput computational screening of MOFs, Chung *et al*. developed the CoRE MOF database.[15] The

CoRE MOF database contains over 5,000 MOF structures that are derived from experimental data but are immediately applicable for classical molecular simulations.[15,28] Nazarian *et al*. have recently shown that the DFT optimization of these structures, particularly those for which solvent was removed from the original experimental data, has a considerable impact on the prediction of gas adsorption.[16,30] Thus, we restricted our attention to structures from the CoRE MOF database that have been optimized *via* periodic DFT with the PBE functional. Modeling CO_2 adsorption requires a description of electrostatic interactions between quadrupolar CO_2 and framework atoms. We therefore only considered materials for which the atomic point charges of the framework atoms have been assigned by the DDEC method.[18-20] This approach accurately represents the electrostatic potential of the DFT-derived electron distribution inside the open pores of MOFs. The set of energy optimized CoRE MOFs with DDEC charges reported by Nazarian *et al*.[16,17] contains 477 structures.

3.2.2 Framework Characterization and Monte Carlo Simulation

Each MOF was first examined for its geometric properties.[31] Pore volume was calculated from the helium void fraction by Widom particle insertion.[26-29,32] The accessible surface area was computed using a sphere representing a nitrogen probe molecule.[26-29,32] The largest cavity diameter (LCD) and pore limiting diameter (PLD) were calculated by Zeo++ applying the high-accuracy setting with probe radius corresponding to nitrogen.[33-35] All structures described below have a PLD greater than 2.4 Å, indicating a sufficient window size to admit CO_2.[8]

Atomistic classical simulations were conducted using RASPA.[32] Adsorption isotherms and isosteric heats of adsorption were calculated by standard Grand Canonical Monte Carlo (GCMC) simulations.[28-32] All frameworks were approximated as rigid structures.[26-29,32] The use of generic force fields such as the universal force field (UFF)[36] or DREIDING[37] for material screening purposes appears to be reasonably well justified.[25-29,38] Hence, van der Waals interaction between hosts and adsorbates was described by combining Lennard-Jones parameters from the UFF for MOF atoms and from the TraPPE[39] force field for quadrupolar CO_2 molecules using the Lorentz-Berthelot mixing rule[40]. Electrostatic interactions were modeled by employing DDEC point charges for MOF atoms[18-20] and TraPPE charges for CO_2 molecules[32]. Simulation volumes were expanded to at least 26 Å along each dimension and periodic boundary conditions were defined in all dimensions. The isosteric heats of adsorption at zero loading was computed in the canonical ensemble with one gas molecule added into a simulation box.[41,42] Further details of the simulation methods can be found in Appendix 3.A.

3.2.3 Sub-Ambient PSA Process Details

We focused on single component CO_2 adsorption to estimate the viability of sub-ambient gas processing in porous materials. The pressure swing range was set between 0.1 bar and 2.0 bar for desorption (P_{des}) and adsorption (P_{ads}), respectively. Air Liquide has performed an extensive technoeconomic analysis of a process for compressing and cooling flue gas to conditions giving a partial pressure of approximately 2.0 bar of CO_2 at 240 K.[11,12] This analysis suggests that our choice of the pressure swing range is feasible to deliver cold, compressed flue gas to a sub-ambient gas processing system. The PSA swing capacity was defined as the difference between gas storage capacity at the adsorption and

desorption pressures[9,42], $\Delta N_{CO2} = N_{CO2}^{ads} - N_{CO2}^{des}$. We considered sub-ambient temperatures of 213, 228, 243, and 258 K.

3.3 RESULTS AND DISCUSSION

3.3.1 Sub-Ambient CO_2 Adsorption in UiO-66

UiO-66 and its derivatives have been widely explored as adsorbents due to their water stability.[43-49] We therefore use UiO-66 to illustrate our calculations. The molecular modeling methods used in our calculations are compared to experimental CO_2 isotherms in Figure 3.1a. Good agreement can be seen between the experimental data and model predictions. The predicted sub-ambient PSA swing capacity for CO_2 in UiO-66 is shown in Figure 3.1b. The swing capacity increases from about 3 mol/kg at 273 K to around 5.3 mol/kg at 213 K. The heat of adsorption in Figure 3.1c is weakly loading dependent, but is almost independent of temperature.[50,51] The trends in Figure 3.1 are straightforward to understand. As the temperature is reduced from 273 to 228 K, the amount of CO_2 in the MOF at the adsorption pressure (2.0 bar) increases substantially. The residual CO_2 in the MOF at the desorption pressure (0.1 bar) also increases with decreasing temperature, but not as markedly as at the adsorption pressure. As a result, the swing capacity increases significantly with decreasing temperature. This trend cannot, however, continue indefinitely. As the adsorbed amount of the adsorption pressure approaches the material's saturation loading, no further gains in swing capacity can be achieved by further lowering the temperature. This effect can be seen in the relatively modest increase in swing capacity in changing from 228 to 213 K. At temperatures lower than 200 K, the swing capacity in this material is reduced by lowering the temperature.

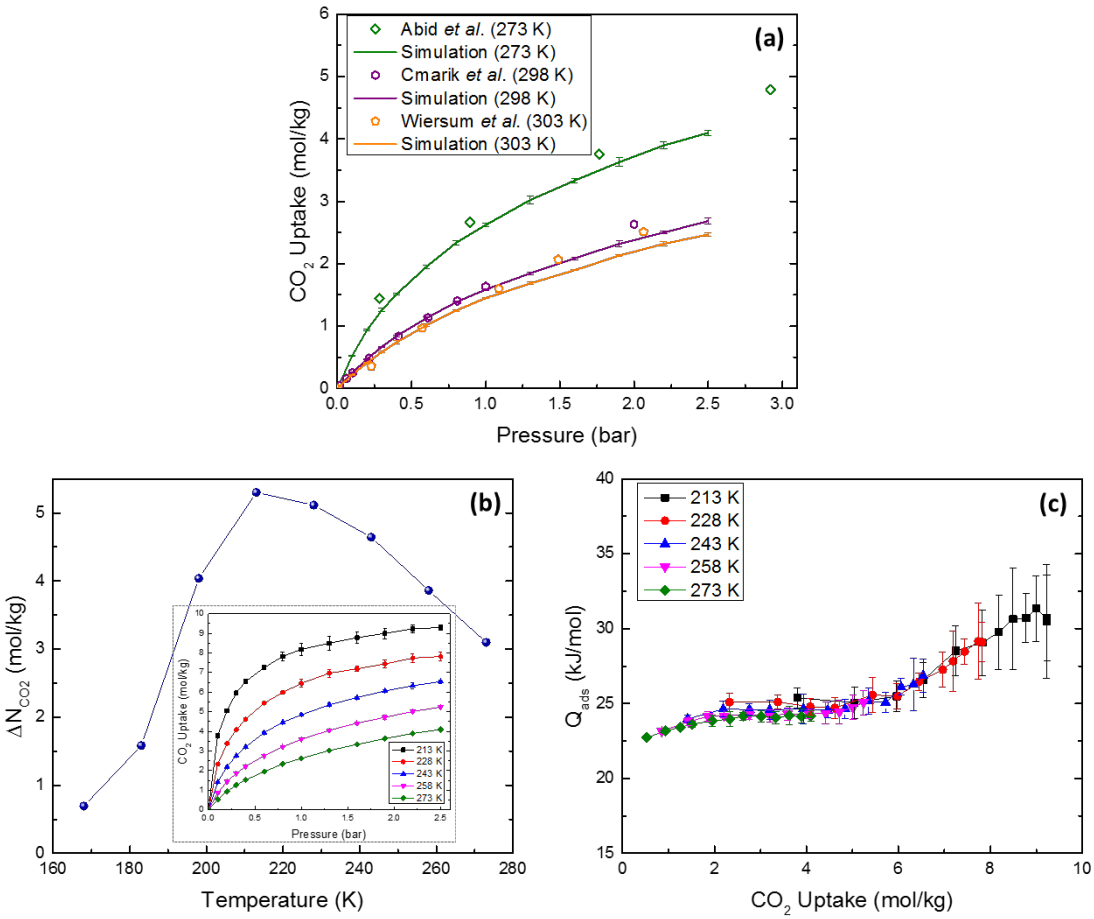

Figure 3.1. (a) Comparison between experimental and simulated adsorption isotherms for CO_2 in UiO-66 at ambient temperatures. The experimental data are from Abid *et al.*,[43] Cmarik *et al.*,[45] and Wiersum *et al.*[49] for 273, 298, and 303 K, respectively. (b) Sub-ambient PSA CO_2 swing capacity in UiO-66 with corresponding adsorption isotherms predicted by GCMC simulations (inset). (c) Heat of adsorption of CO_2 in UiO-66 as a function of CO_2 uptake, obtained from GCMC simulations.

3.3.2 Sub-Ambient PSA CO_2 Swing Capacity in MOFs

Computational screening has been conducted on various libraries of porous materials for adsorption applications including efforts to find optimal CO_2 adsorbents.[7-9,15-17,21,52-61] We calculated the CO_2 swing capacity as discussed in Section 3.3.1 for the 477 MOFs described in Section 3.2.1. The resulting swing capacities are shown in terms of each material's pore volume in Figure 3.2. A striking feature of these results is the existence

of materials with very high swing capacities, including capacities of 30 – 40 mol/kg at 213 K and 15 – 18 mol/kg at 258 K. At the lowest temperature we examined, increasing pore volume is correlated with larger swing capacity. At 258 K, however, the materials with the highest pore volume do not show the highest swing capacity. This phenomenon has been observed before and its physical origins have been explained by Fang *et al*.[9] and others[53,56], who noted that materials with extremely large pores also often have relatively low heats of adsorption. Fang *et al*. examined correlations between process dependent swing capacities and pore volumes of zeolites.[9] It is very likely that a decrease in swing capacity also occurs at 213 K for materials with sufficiently large pore volumes, but none of the materials we examined in Figure 3.2 approach that regime.

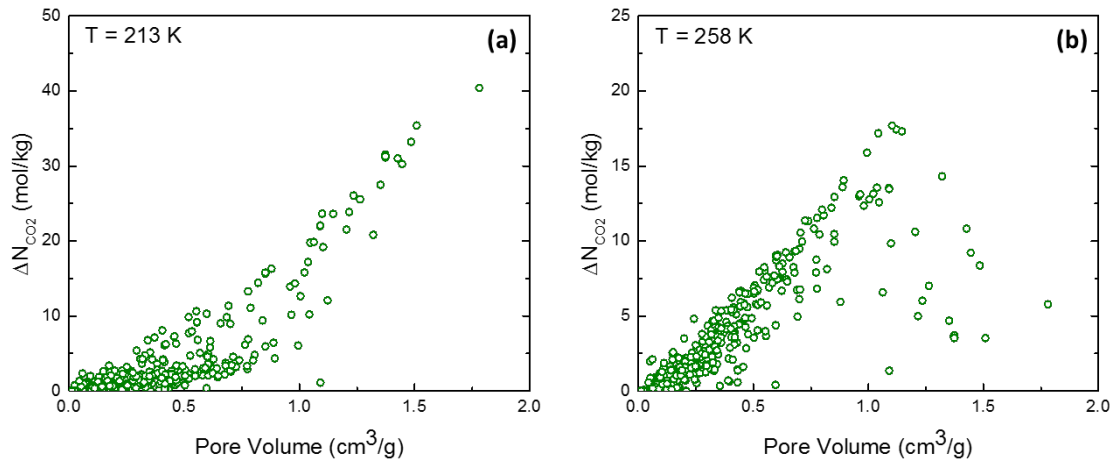

Figure 3.2. Calculated CO_2 swing capacity between 0.1 bar and 2.0 bar in 477 MOFs at (a) 213 K and (b) 258 K.

The computed swing capacities for the 477 MOFs are plotted with respect to each material's heat of adsorption at zero loading (Q_{ads}^{0}) in Figure 3.3a and the average heat of adsorption (Q_{ads}^{avg}) between the pressure swing conditions in Figure 3.3b. Both energetic quantities demonstrate the presence of the range of optimal values for the heat of adsorption. The existence of an optimal heat of adsorption for adsorptive storage of gases

has been investigated before elsewhere.[9,50,52-56] For instance, Fang *et al*. found that the optimal average heat of adsorption range for CO_2 capture in zeolites was 28 ± 3 kJ/mol in a PSA process that swings between 1 bar and 5 bar at 300 K.[9] Simmons *et al*. estimated the optimal average heat of adsorption range for CO_2 based on the thermodynamic methodology developed by Bhatia and Myers, which assumes Langmuir adsorption isotherms in a homogeneous adsorbent[50] to be 22 – 26 kJ/mol in PSA between 1 bar and 6 bar at room temperature.[62] The optimal average heat of adsorption for CO_2 in MOFs at sub-ambient temperatures observed in our calculations are similar to these observations.

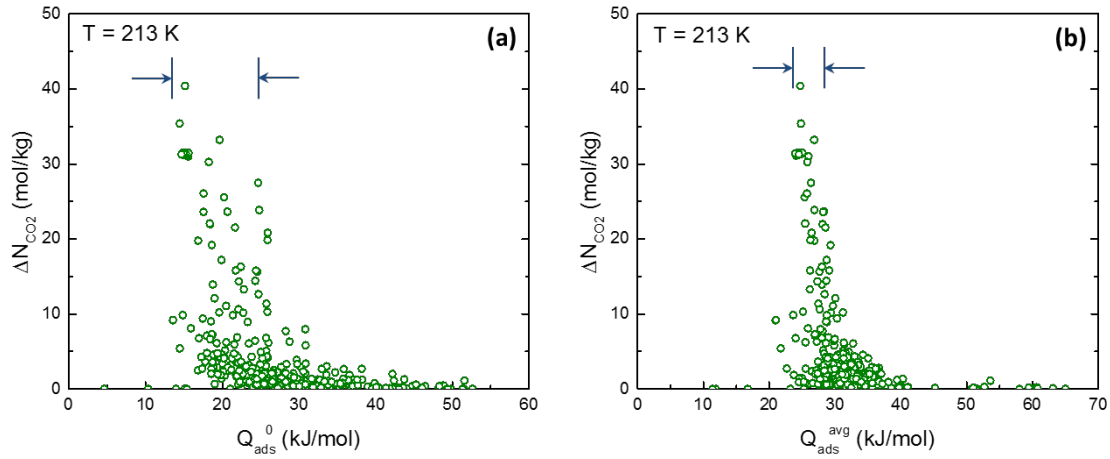

Figure 3.3. (a) Heat of adsorption at zero loading and (b) average heat of adsorption between adsorption and desorption conditions at 213 K in 477 MOFs. Arrows indicate the optimal range for the heat of adsorption.

The optimal heat range for Q_{ads}^0 and Q_{ads}^{avg} as a function of temperature are shown in Figure 3.4. The optimal values for both Q_{ads}^0 and Q_{ads}^{avg} are approximately independent of temperature within the scatter of our data. We note that the analysis of Bhatia and Myers[50] predicts that the optimal heat of adsorption is temperature dependent. Extending the calculations of Simmons *et al*.[62] with this approach, however, indicates that this variation is around 4 kJ/mol over the temperature range in Figure 3.4 for a simple model

of CO_2 adsorption based on Langmuir isotherms. The qualitative trend in our results is therefore consistent with the expectations from the Langmuir-based model of Bhatia and Myers. The optimal Q_{ads}^{avg} is about 5 kJ/mol larger than the optimal Q_{ads}^{0}. This indicates that materials in which the heat of adsorption increases with loading have favorable properties for achieving large swing capacities. The loading dependent heat of adsorption in UiO-66 shown in Figure 3.1 is one example of this behavior, albeit with only a moderate pore volume. The general connection between this trend in the heat of adsorption and the desirable features of a *S*-shaped isotherm that is not associated with a structural change in the adsorbent have been pointed out in several previous studies.[10-14,26,62-65] The overall correlation between Q_{ads}^{0} and Q_{ads}^{avg} at 213 K in 477 MOFs is shown in Appendix 3.A (Figure 3.A.3). This data shows that the heat of adsorption for CO_2 increases as a loading increases in the majority of the materials we examined.

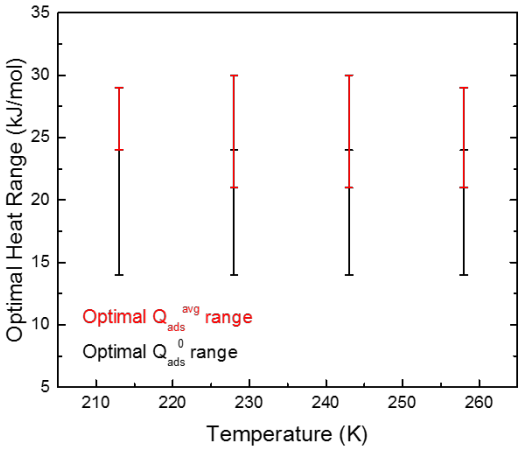

Figure 3.4. Optimal heat range for heat of adsorption at zero loading (Q_{ads}^{0}, black) and average heat of adsorption (Q_{ads}^{avg}, red) as a function of temperature.

3.3.3 Upper Bounds on Sub-Ambient PSA CO_2 Swing Capacity in MOFs

Our results above imply the adsorbent evaluation criteria reported by Fang *et al*.[9] are applicable to a large variety of porous materials. Figure 3.5 illustrates a screening process to identify MOF candidates that have a CO_2 swing capacity exceeding 10 mol/kg in sub-ambient PSA. Of the 477 structures we studied, 63 structures satisfy the geometric criteria of having pore volume above 0.75 cm^3/g. 37 structures remain after applying the energetic criteria we defined for the optimal average heat of adsorption. From this group, we identified materials that give a CO_2 swing capacity larger than 10 mol/kg at all temperatures from 213 to 258 K. We found 20 structures that satisfy this requirement. It is useful to note that the geometric and energetic criteria defined in Figure 3.5 could allow efficient analysis of larger material libraries in the future.

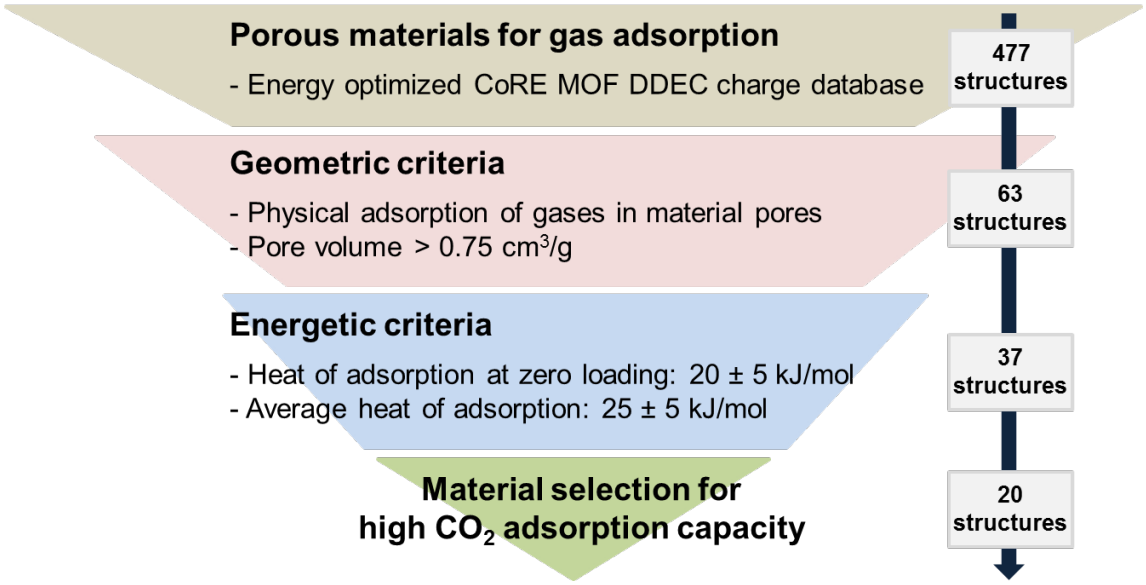

Figure 3.5. Schematic illustration of the material selection criteria to accomplish large sub-ambient PSA CO_2 swing capacities.

The MOF candidates and their predicted swing capacities that emerged from the procedure described above are listed in Table 3.1. This list contains 20 structures satisfying

the criteria defined above and one additional structure (XAWVUN) that shows the largest swing capacity of any material (40.4 mol/kg at 213 K) but does not have a swing capacity exceeding 10 mol/kg at every temperature. The material properties for each candidate are provided in Appendix 3.A (Table 3.A.1). It is highly likely that not all the materials listed in Table 3.1 are viable for practical use in sub-ambient gas processing due to the stability and lifetime concerns, the cost and ease of material synthesis, and related challenges that cannot be directly quantified in our calculations. Nevertheless, our computations reveal that a large number of real materials exist with swing capacities for CO_2 at sub-ambient temperatures that greatly exceed 10 mol/kg. In Section 3.A.3 of Appendix 3.A, several materials that reach 10 mol/kg swing capacities even at narrower pressure swing conditions are identified.

In our simulations, XAWVUN, a porous Cu-based coordination network that was reported for H_2 sorption behavior by Sun *et al*.[66], exhibits the highest overall swing capacity of 40.4 mol/kg at 213 K. The temperature dependent CO_2 adsorption and desorption isotherms for XAWVUN are shown in Figure 3.6a. The simulated isotherms show no effects of hysteresis. The material does not satisfy our overall material selection criteria because the swing capacity drops to 5.8 mol/kg at 258 K. The loading dependent heat of adsorption is shown in Figure 3.6b. Similar to the results for UiO-66 shown in Figure 3.1, the heat of adsorption increases as a function of loading. This results in the desirable *S*-shaped isotherms[14,62] at 213 and 228 K. In Figure 3.6c, the mixture adsorption selectivity for CO_2 associated with a bulk binary CO_2/N_2 mixture with molar composition 0.14/0.86 calculated by binary GCMC simulations is shown. The adsorption selectivity increases from around 5.5 at 273 K to about 15.5 at 213 K with only a marginal change as a function

of the total pressure. At the latter temperature, this adsorption selectivity corresponds to an adsorbed mixture with CO_2/N_2 composition of 0.73/0.27. In Section 3.A.3 of Appendix 3.A, the mixture adsorption selectivity of CO_2 in three other large capacity MOF candidates is identified. Two of these materials, WONZOP and SENWAL, have selectivities of around 40 at 213 K, corresponding to an adsorbed mixture with CO_2/N_2 composition 0.875/0.125. A potential trade-off between swing capacity and selectivity has been discussed elsewhere.[67-69] Understanding the generality of this trade-off and assessing its implications for practical implementation of sub-ambient CO_2 capture will be important future steps.

Table 3.1. MOF candidates from energy optimized CoRE MOF DDEC charge database with large sub-ambient PSA ΔN_{CO2}.

Metal-Organic Frameworks [a]	**ΔN_{CO2} (mol/kg)**				
	213 K	**228 K**	**243 K**	**258 K**	**273 K** [c]
XAWVUN (Cu_2(TCPPDA)) [b]	40.4	35.2	13.1	5.8	3.5
ANUGIA (UMCM-152)	31.0	28.6	22.4	10.8	5.8
WONZOP	23.7	22.9	19.2	10.0	5.3
SENWAL	23.6	23.9	21.7	17.3	9.1
YUGLES	22.1	21.4	19.0	13.5	6.5
NUTQAV (PCN-16)	22.0	21.3	19.0	13.5	6.6
WONZUV	21.5	21.7	17.6	10.6	7.3
OJICUG	20.8	22.1	19.0	14.3	10.3
NUTQEZ (PCN-16')	19.8	19.8	17.6	12.6	7.0
SENWOZ	19.2	22.7	21.2	17.7	11.0
MATVEJ	17.2	19.1	17.5	13.6	8.4
UTEWUM ($Cu_3(BTP)_2$)	15.8	16.9	15.9	13.2	8.7
XAMDUM07	15.8	15.7	13.9	10.0	5.6
FIQCEN (HKUST-1)	15.6	15.7	14.1	10.5	5.9
UTEWOG ($Ni_3(BTP)_2$)	14.3	15.3	14.6	12.4	8.5
BIBXUH	13.9	17.0	15.9	13.0	8.7
XUGSEY	12.6	16.0	15.3	12.8	9.4
KEFBEE (IZE-1)	12.1	21.1	20.3	17.4	12.1
FEFCUQ	11.1	13.2	12.7	10.4	7.1
QUQFIS	10.2	15.7	15.2	13.1	9.8
SENWIT	10.2	20.6	20.0	17.2	11.9

[a] CSD reference codes reported in the CoRE MOF database with common names in brackets (if available). [b] Material that exhibited the maximum sub-ambient PSA ΔN_{CO2} upper bound predicted by GCMC molecular simulation beside the material selection criteria. [c] Swing capacities at 273 K are computed to observe the effectiveness of sub-ambient operation.

Figures 3.A.4 – 3.A.6 (see Appendix 3.A) illustrate the variation in swing capacity for several high capacity MOFs as a function of desorption pressure. Increasing the pressure used for desorption reduces the CO_2 swing capacity and also increases the temperature at which the maximum in this swing capacity occurs. These observations, coupled with the significant temperature dependence of adsorption selectivity in these and similar materials highlight that careful process models will be required to closely examine the trade-offs between process performance and cost associated with varying the desorption pressure and operating temperature.

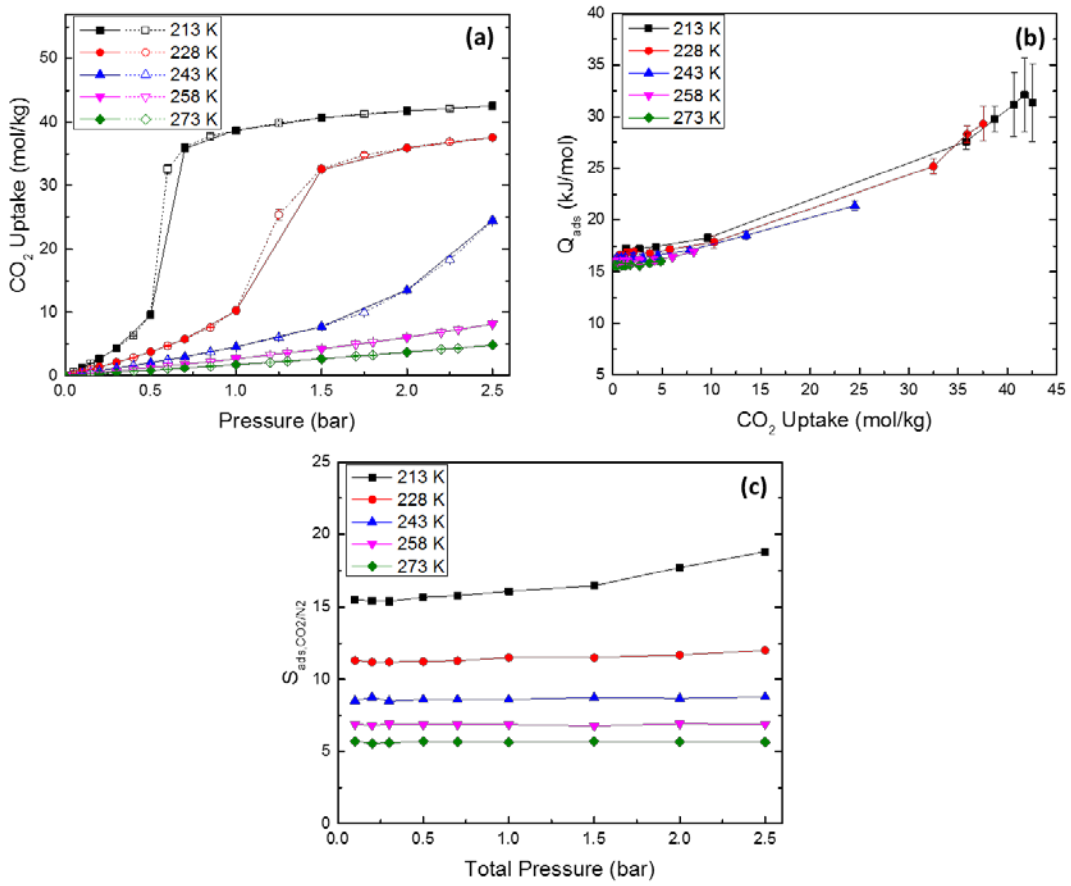

Figure 3.6. (a) Sub-ambient CO_2 adsorption (filled symbols with solid lines) and desorption (open symbols with dashed lines) in XAWVUN predicted by GCMC molecular simulations. (b) Heat of adsorption of CO_2 in XAWVUN as a function of CO_2 uptake, obtained from GCMC simulations. (c) Adsorption selectivity of CO_2 from bulk CO_2/N_2 0.14/0.86 mixture calculated by binary GCMC simulations.

3.4 CONCLUSIONS

In this chapter, we have sought upper bounds on CO_2 swing capacity in a sub-ambient PSA process, which may be viable when coupled with heat integration and power recovery, *via* molecular simulation of 477 MOF structures. Swing capacities as high as 30 – 40 mol/kg at 213 K and 15 – 18 mol/kg at 258 K are predicted for the MOFs that have large pore volume and fall into a narrow range of optimal average heats of adsorption. Our results enabled formulation of material selection criteria that allow efficient identification of materials with high CO_2 swing capacity. Ultimately, 20 MOF candidates were identified that show a swing capacity over 10 mol/kg at all the sub-ambient temperatures we considered.

Our assessment of porous materials for CO_2 capture has focused solely on single component CO_2 adsorption. The viability of a practical process clearly also relies on a host of other factors, including adsorption selectivity, material stability and cost among others. Nevertheless, establishing upper bounds on swing capacity is critical to understanding the limits on performance that are physically achievable with PSA and related cyclic adsorption processes. Our results indicate that use of high capacity MOFs and other porous materials in sub-ambient CO_2 capture processes merits more detailed examination, and this chapter point to specific materials and more general material characteristics that should be the focus of future work of this kind.

3.5 REFERENCES

(1) Sholl, D. S.; Lively, R. P. Seven Chemical Separations to Change the World, *Nature* **2016**, *532*, 435-437.

(2) Choi, S.; Drese, J. H.; Jones, C. W. Adsorbent Materials for Carbon Dioxide Capture from Large Anthropogenic Point Sources. *ChemSusChem* **2009**, *2*, 796-854.

(3) Ferey, G.; Mellot-Draznieks, C.; Serre, C.; Millange, F. Crystallized Frameworks with Giant Pores: Are There Limits to the Possible? *Acc. Chem. Res.* **2005**, *38*, 217-225.

(4) Meek, S. T.; Greathouse, J. A.; Allendorf, M. D. Metal-Organic Frameworks: A Rapidly Growing Class of Versatile Nanoporous Materials. *Adv. Mater.* **2011**, *23*, 249-267.

(5) Keskin, S.; van Heest, T. M.; Sholl, D. S. Can Metal-Organic Framework Materials Play a Useful Role in Large-Scale Carbon Dioxide Separations? *ChemSusChem* **2010**, *3*, 879-891.

(6) Yang, R. T. *Gas Separation by Adsorption Processes*; Imperial College Press: London, 1987.

(7) Bae, Y. S.; Snurr, R. Q. Development and Evaluation of Porous Materials for Carbon Dioxide Separation and Capture. *Angew. Chem. Int. Ed.* **2011**, *50*, 11586-11596.

(8) Hedin, N.; Andersson, L.; Bergstrom, L.; Yan, J. Adsorbents for the post-combustion capture of CO_2 using rapid temperature swing or vacuum swing adsorption. *Appl. Energ.* **2013**, *104*, 418-433.

(9) Fang, H.; Kulkarni, A.; Kamakoti, P.; Awati, R.; Ravikovitch, P. I.; Sholl, D. S. Identification of High-CO_2-Capacity Cationic Zeolites by Accurate Computational Screening. *Chem. Mater.* **2016**, *28*, 3887-3896.

(10) Tedds, S.; Walton, A.; Broom, D. P.; Book, D. Characterisation of porous hydrogen storage materials: carbons, zeolites, MOFs and PIMs. *Faraday Discuss.* **2011,** *151*, 75-94.

(11) Hasse, D.; Kulkarni, S.; Sanders, E.; Corson, E.; Tranier, J. P. CO_2 capture by sub-ambient membrane operation. *Energy Procedia* **2013**, *37*, 993-1003.

(12) Hasse, D.; Ma, J.; Kulkarni, S.; Terrien, P.; Tranier, J. P.; Sanders, E.; Chaubey, T.; Brumback, J. CO_2 Capture by Cold Membrane Operation. *Energy Procedia* **2014**, *63*, 186-193.

(13) Liu, L.; Sanders, E. S.; Kulkarni, S. S.; Hasse, D. J.; Koros, W. J. Sub-ambient temperature flue gas carbon dioxide capture via Matrimid® hollow fiber membranes. *J. Membrane Sci.* **2014**, *465*, 49-55.

(14) Walton, K. S.; Millward, A. R.; Dubbeldam, D.; Frost, H.; Low, J. J.; Yaghi, O. M.; Snurr, R. Q. Understanding inflections and steps in carbon dioxide adsorption

isotherms in metal-organic frameworks. *J. Am. Chem. Soc.* **2008,** *130*, 406-407.

(15) Chung, Y. G.; Camp, J.; Haranczyk, M.; Sikora, B. J.; Bury, W.; Krungleviciute, V.; Yildirim, T.; Farha, O. K.; Sholl, D. S.; Snurr, R. Q. Computation-Ready, Experimental Metal-Organic Frameworks: A Tool To Enable High-Throughput Screening of Nanoporous Crystals. *Chem. Mater.* **2014**, *26*, 6185-6192.

(16) Nazarian, D.; Camp, J. S.; Chung, Y. G.; Snurr, R. Q.; Sholl, D. S. Large-Scale Refinement of Metal-Organic Framework Structures Using Density Functional Theory. *Chem. Mater.* **2017**, *29*, 2521-2528.

(17) Nazarian, D.; Camp, J. S.; Sholl, D. S. A Comprehensive Set of High-Quality Point Charges for Simulations of Metal-Organic Frameworks. *Chem. Mater.* **2016**, *28*, 785-793.

(18) Manz, T. A.; Sholl, D. S. Chemically Meaningful Atomic Charges That Reproduce the Electrostatic Potential in Periodic and Nonperiodic Materials. *J. Chem. Theory Comput.* **2010**, *6*, 2455-2468.

(19) Manz, T. A.; Sholl, D. S. Improved Atoms-in-Molecule Charge Partitioning Functional for Simultaneously Reproducing the Electrostatic Potential and Chemical States in Periodic and Nonperiodic Materials. *J. Chem. Theory Comput.* **2012**, *8*, 2844-2867.

(20) Watanabe, T.; Manz, T. A.; Sholl, D. S. Accurate Treatment of Electrostatics during Molecular Adsorption in Nanoporous Crystals without Assigning Point Charges to Framework Atoms. *J. Phys. Chem. C* **2011**, *115*, 4824-4836.

(21) Braun, E.; Zurhelle, A. F.; Thijssen, W.; Schnell, S. K.; Lin, L. C.; Kim, J.; Thompson, J. A.; Smit, B. High-throughput computational screening of nanoporous adsorbents for CO_2 capture from natural gas. *Mol. Syst. Des. Eng.* **2016**, *1*, 175-188.

(22) Wu, D.; Yang, Q.; Zhong, C.; Liu, D.; Huang, H.; Zhang, W.; Maurin, G. Revealing the Structure-Property Relationships of Metal-Organic Frameworks for CO_2 Capture from Flue Gas. *Langmuir* **2012**, *28*, 12094-12099.

(23) Cavka, J. H.; Jakobsen, S.; Olsbye, U.; Guillou, N.; Lamberti, C.; Bordiga, S.; Lillerud, K. P. A new zirconium inorganic building brick forming metal organic frameworks with exceptional stability. *J. Am. Chem. Soc.* **2008,** *130*, 13850-13851.

(24) Ferey, G. Hybrid porous solids: past, present, future. *Chem. Soc. Rev.* **2008,** *37*, 191-214.

(25) Watanabe, T.; Sholl, D. S. Accelerating Applications of Metal-Organic Frameworks for Gas Adsorption and Separation by Computational Screening of Materials. *Langmuir* **2012**, *28*, 14114-14128.

(26) Duren, T.; Bae, Y. S.; Snurr, R. Q. Using molecular simulation to characterise metal-organic frameworks for adsorption applications. *Chem. Soc. Rev.* **2009,** *38*, 1237-1247.

(27) Keskin, S.; Liu, J.; Rankin, R. B.; Johnson, J. K.; Sholl, D. S. Progress, Opportunities, and Challenges for Applying Atomically Detailed Modeling to Molecular Adsorption and Transport in Metal-Organic Framework Materials. *Ind. Eng. Chem. Res.* **2009**, *48*, 2355-2371.

(28) Coudert, F. X.; Fuchs, A. H. Computational characterization and prediction of metal-organic framework properties. *Coord. Chem. Rev.* **2016,** *307*, 211-236.

(29) Li, J. R.; Ma, Y. G.; McCarthy, M. C.; Sculley, J.; Yu, J. M.; Jeong, H. K.; Balbuena, P. B.; Zhou, H. C. Carbon dioxide capture-related gas adsorption and separation in metal-organic frameworks. *Coord. Chem. Rev.* **2011,** *255*, 1791-1823.

(30) Nazarian, D.; Ganesh, P.; Sholl, D. S. Benchmarking density functional theory predictions of framework structures and properties in a chemically diverse test set of metal-organic frameworks. *J. Mater. Chem. A* **2015,** *3*, 22432-22440.

(31) Duren, T.; Millange, F.; Ferey, G.; Walton, K. S.; Snurr, R. Q. Calculating geometric surface areas as a characterization tool for metal-organic frameworks. *J. Phys. Chem. C* **2007,** *111*, 15350-15356.

(32) Dubbeldam, D.; Calero, S.; Ellis, D. E.; Snurr, R. Q. RASPA: molecular simulation software for adsorption and diffusion in flexible nanoporous materials. *Mol. Simulat.* **2016,** *42*, 81-101.

(33) Willems, T. F.; Rycroft, C. H.; Kazi, M.; Meza, J. C.; Haranczyk, M. Algorithms and tools for high-throughput geometry-based analysis of crystalline porous materials. *Micropor. Mesopor. Mat.* **2012**, *149*, 134-141.

(34) Pinheiro, M.; Martin, R. L.; Rycroft, C. H.; Haranczyk, M. High accuracy geometric analysis of crystalline porous materials. *CrystEngComm* **2013**, *15*, 7531-7538.

(35) Bae, Y. S.; Yazaydin, A. O.; Snurr, R. Q. Evaluation of the BET method for determining surface areas of MOFs and zeolites that contain ultra-micropores. *Langmuir* **2010,** *26*, 5475-5483.

(36) Rappe, A. K.; Casewit, C. J.; Colwell, K. S.; Goddard, W. A.; Skiff, W. M. UFF, A Full Periodic-Table Force-Field for Molecular Mechanics and Molecuar Dynamics Simulations. *J. Am. Chem. Soc.* **1992,** *114*, 10024-10035.

(37) Mayo, S. L.; Olafson, B. D.; Goddard, W. A. DREIDING: a generic force field for molecular simulations. *J. Phys. Chem.* **1990,** *94*, 8897-8909.

(38) Addicoat, M. A.; Vankova, N.; Akter, I. F.; Heine, T. Extension of the Universal Force Field to Metal-Organic Frameworks. *J. Chem. Theory Comput.* **2014,** *10*, 880-891.

(39) Martin, M. G.; Siepmann, J. I. Transferable potentials for phase equilibria. 1. United-atom description of n-alkanes. *J. Phys. Chem. B* **1998,** *102*, 2569-2577.

(40) Allen, M. P.; Tildesley, D. J. *Computer Simulation of Liquids*; Oxford University Press: New York, 1987.

(41) Do, D. D.; Nicholson, D.; Do, H.D. On the Henry constant and isosteric heat at zero loading in gas phase adsorption. *J. Colloid Interface Sci.* **2008**, *324*, 15-24.

(42) Qiao, Z. W.; Zhang, K.; Jiang, J. W. *In silico* screening of 4764 computation-ready, experimental metal-organic frameworks for CO_2 separation. *J. Mater. Chem. A* **2016,** *4*, 2105-2114.

(43) Abid, H. R.; Pham, G. H.; Ang, H. M.; Tade, M. O.; Wang, S. B. Adsorption of CH_4 and CO_2 on Zr-metal organic frameworks. *J. Colloid Interface Sci.* **2012,** *366*, 120-124.

(44) Jasuja, H.; Zang, J.; Sholl, D. S.; Walton, K. S. Rational Tuning of Water Vapor and CO_2 Adsorption in Highly Stable Zr-Based MOFs. *J. Phys. Chem. C* **2012,** *116*, 23526-23532.

(45) Cmarik, G. E.; Kim, M.; Cohen, S. M.; Walton, K. S. Tuning the adsorption properties of UiO-66 via ligand functionalization. *Langmuir* **2012,** *28*, 15606-15613.

(46) Wu, D.; Maurin, G.; Yang, Q. Y.; Serre, C.; Jobic, H.; Zhong, C. L. Computational exploration of a Zr-carboxylate based metal-organic framework as a membrane material for CO_2 capture. *J. Mater. Chem. A* **2014,** *2*, 1657-1661.

(47) Zhang, W. J.; Huang, H. L.; Zhong, C. L.; Liu, D. H. Cooperative effect of temperature and linker functionality on CO_2 capture from industrial gas mixtures in metal-organic frameworks: a combined experimental and molecular simulation study. *Phys. Chem. Chem. Phys.* **2012,** *14*, 2317-2325.

(48) Yang, Q. Y.; Wiersum, A. D.; Llewellyn, P. L.; Guillerm, V.; Serred, C.; Maurin, G. Functionalizing porous zirconium terephthalate UiO-66(Zr) for natural gas upgrading: a computational exploration. *Chem. Commun.* **2011,** *47*, 9603-9605.

(49) Wiersum, A. D.; Soubeyrand-Lenoir, E.; Yang, Q. Y.; Moulin, B.; Guillerm, V.; Ben Yahia, M.; Bourrelly, S.; Vimont, A.; Miller, S.; Vagner, C.; Daturi, M.; Clet, G.; Serre, C.; Maurin, G.; Llewellyn, P. L. An evaluation of UiO-66 for gas-based applications. *Chem. Asian J.* **2011,** *6*, 3270-3280.

(50) Bhatia, S. K.; Myers, A. L. Optimum Conditions for Adsorptive Storage. *Langmuir* **2006,** *22*, 1688-1700.

(51) Hyla, A. S.; Fang, H.; Boulfelfel, S. E.; Muraro, G.; Paur, C.; Strohmaier, K.; Ravikovitch, P. I.; Sholl, D. S. Significan Temperature Dependence of the Isosteric Heats of Adsorption of Gases in Zeolites Demonstrated by Experiments and Molecular Simulation. *J. Phys. Chem. C* **2019,** *123*, 20405-20412.

(52) Bae, Y. S.; Snurr, R. Q. Optimal isosteric heat of adsorption for hydrogen storage and delivery using metal-organic frameworks. *Micropor. Mesopor. Mat.* **2010,** *132*, 300-303.

(53) Simon, C. M.; Kim, J.; Lin, L. C.; Martin, R. L.; Haranczyk, M.; Smit, B. Optimizing nanoporous materials for gas storage. *Phys. Chem. Chem. Phys.* **2014,** *16*, 5499-5513.

(54) Lin, L. C.; Berger, A. H.; Martin, R. L.; Kim, J.; Swisher, J. A.; Jariwala, K.; Rycroft, C. H.; Bhown, A. S.; Deem, M. W.; Haranczyk, M.; Smit, B. *In silico* screening of carbon-capture materials. *Nat. Mater.* **2012,** *11*, 633-641.

(55) Fernandez, M.; Boyd, P. G.; Daff, T. D.; Aghaji, M. Z.; Woo, T. K. Rapid and Accurate Machine Learning Recognition of High Performing Metal Organic Frameworks for CO_2 Capture. *J. Phys. Chem. Lett.* **2014,** *5*, 3056-3060.

(56) Wilmer, C. E.; Farha, O. K.; Bae, Y. S.; Hupp, J. T.; Snurr, R. Q. Structure-property relationships of porous materials for carbon dioxide separation and capture. *Energy Environ. Sci.* **2012**, *5*, 9849-9856.

(57) D'Alessandro, D. M.; Smit, B.; Long, J. R. Carbon Dioxide Capture: Prospects for New Materials. *Angew. Chem., Int. Ed.* **2010,** *49*, 6058-6082.

(58) Colon, Y. J.; Snurr, R. Q. High-throughput computational screening of metal-organic frameworks. *Chem. Soc. Rev.*, **2014**, *43*, 5735-5749.

(59) Yazaydin, A. O.; Snurr, R. Q.; Park, T. H.; Koh, K.; Liu, J.; LeVan, M. D.; Benin, A. I.; Jakubczak, P.; Lanuza, M.; Galloway, D. B.; Low, J. J.; Willis, R. R. Screening of metal-organic frameworks for carbon dioxide capture from flue gas using a combined experimental and modeling approach. *J. Am. Chem. Soc.*, **2009**, *131*, 18198-18199.

(60) Garcia-Perez, E.; Parra, J. B.; Ania, C. O.; Garcia-Sanchez, A.; van Baten, J. M.; Krishna, R.; Dubbeldam, D.; Calero, S. A computational study of CO_2, N_2, and CH_4 adsorption in zeolites. *Adsorption*, **2007**, *13*, 469-476.

(61) Vicent-Luna, J. M.; Luna-Triguero, A.; Calero, S. Storage and Separation of Carbon Dioxide and Methane in Hydrated Covalent Organic Frameworks. *J. Phys. Chem. C*, **2016**, *120*, 23756-23762.

(62) Simmons, J. M.; Wu, H.; Zhou, W.; Yildirim, T. Carbon capture in metal-organic frameworks - a comparative study. *Energy Environ. Sci.* **2011,** *4*, 2177-2185.

(63) Ho, M. T.; Allinson, G. W.; Wiley, D. E. Reducing the Cost of CO_2 from Flue Gas Using Pressure Swing Adsorption. *Ind. Eng. Chem. Res.* **2008,** *47*, 1562-1568.

(64) Millward, A. R.; Yaghi, O. M. Metal-Organic Frameworks with Expectionally High Capacity for Storage of Carbon Dioxide at Room Temperature. *J. Am. Chem. Soc.* **2005,** *127*, 17998-17999.

(65) McDonald, T. M.; Mason, J. A.; Kong, X.; Bloch, E. D.; Gygi, D.; Dani, A.; Crocella, V.; Giordanino, F.; Odoh, S. O.; Drisdell, W. S.; Vlaisavljevich, B.; Dzubak, A. L.; Poloni, R.; Schnell, S. K.; Planas, N.; Lee, K.; Pascal, T.; Wan, L. F.; Prendergast, D.; Neaton, J. B.; Smit, B.; Kortright, J. B.; Gagliardi, L.; Bordiga, S.; Reimer, J. A.; Long, J. R. Cooperative insertion of CO_2 in diamine-appended metal-organic frameworks. *Nature* **2015**, *519*, 303-308.

(66) Sun, D. F.; Ke, Y. X.; Mattox, T. M.; Ooro, B. A.; Zhou, H. C. Temperature-dependent supramolecular stereoisomerism in porous copper coordination networks based on a

designed carboxylate ligand. *Chem. Commun.* **2005,** *43*, 5447-5449.

(67) Yeo, B. C.; Kim, D.; Kim, H.; Han, S. S. High-Throughput Screening to Investigate the Relationship between the Selectivity and Working Capacity of Porous Materials for Propylene/Propane Adsorptive Separation. *J. Phys. Chem. C*, **2016**, *120*, 24224-24230.

(68) Garcia, E. J.; Perez-Pellitero, J.; Pirngruber, G. D.; Jallut, C.; Palomino, M.; Rey, F.; Valencia, S. Tuning the Adsorption Properties of Zeolites as Adsorbents for CO_2 Separation: Best Compromise between the Working Capacity and Selectivity. *Ind. Eng. Chem. Res.* **2014**, *53*, 9860-9874.

(69) Garcia, E. J.; Perez-Pellitero, J.; Pirngruber, G. D.; Jallut, C. Sketching a Portrait of the Optimal Adsorbent for CO_2 Separation by Pressure Swing Adsorption. *Ind. Eng. Chem. Res.* **2017**, *56*, 4818-4829.

APPENDIX 3.A. SUPPORTING INFORMATION – CHAPTER 3

3.A.1 Molecular Simulation Details

Atomistic classical GCMC simulations of single component CO_2 adsorption and desorption, and adsorption of a binary CO_2/N_2 0.14/0.86 mixture were conducted on the energy optimized CoRE MOF DDEC charge database using RASPA[1]. Fugacity was converted from pressure using the Peng-Robinson equation of state.[1] All the MOF structures investigated are approximated by rigid model with triclinic boundary conditions applied in all dimensions. A rigid and linear model was used for both CO_2 and N_2 molecules. Lennard-Jones (LJ) parameters for framework atoms are obtained from the UFF[2] which is widely used force field for MOFs, and the parameters for CO_2 and N_2 are obtained from the TraPPE[3] force field. In Monte Carlo simulation associated with these force fields, the truncated potentials with tail corrections are applied. Simulation volumes are expanded to at least 26 Å along each dimension and LJ interactions are truncated at 12 Å. Electrostatic interactions were computed pairwise with a long range Ewald summation scheme[4] based on atomic point charges assigned *via* DDEC method. DDEC is one of multiple methods to assign electrostatic charges to framework atoms, and it is based on the electron density partitioning in periodic structures.[5] The point charges are found by minimizing an optimization functional to reproduce both the charge distribution and local electrostatic potential.[5]

All GCMC calculations included 5,000 initialization cycles to equilibrate the positions of the atoms in the system followed by 50,000 production cycles. A Monte Carlo cycle consists of N steps where N is the number of molecules in the system. Random Monte

Carlo moves, either accepted or rejected according to Boltzmann-type weighting criteria, allowed translation, rotation, regrowth, reinsertion, deletion and insertion moves at the identical probabilities. For a mixture gas adsorption simulation, a Monte Carlo move that swapped the identity of existing molecules associated with the competitive adsorption of each component was imposed in addition to above random Monte Carlo moves.

Isosteric heats of adsorption (Q_{ads}) was computed during GCMC simulations based on the fluctuation method.[1] The heat of adsorption at zero loading (Q_{ads}^0) was also computed in the canonical ensemble.[6,7] Q_{ads}^0 is an indicator for the host-adsorbate affinity under infinite dilute conditions.[6] Random Monte Carlo moves in this simulation allowed translation, rotation, regrowth, and reinsertion moves at the identical probabilities.

The void fraction of each computation-ready structure was calculated from a Widom particle insertion method using a He probe molecule (ε/k_B = 10.9 K, σ = 2.64 Å) at 298 K.[1] The pore volume was calculated by multiplying the void fraction with the unit cell volume. The accessible surface area was calculated by using N_2 as probe molecule with overlap distance criteria set to a size parameter σ of 3.31 Å.[1] The largest cavity diameter and the pore limiting diameter were calculated by Zeo++ applying the high-accuracy setting with a probe of radius 1.86 Å, corresponding to N_2.[8]

3.A.2 Sub-Ambient PSA CO_2 Swing Capacity in MOFs

3.A.2.1 Geometric Properties of MOFs for Swing Capacity

The pore volume (V_P) is one of the most critical geometric properties that governs physisorption of adsorbate molecules. There are also other geometric indicators that could

potentially be used to estimate CO_2 capture performance using porous materials. They include the accessible surface area (SA_{acc}), largest cavity diameter (LCD), and the pore limiting diameter (PLD). In this Appendix, we examine correlations between each property and sub-ambient PSA CO_2 swing capacity.

Figure 3.A.1 shows the correlation between V_P and swing capacity at 228 K and 243 K. The existence of materials with large swing capacities of 25 – 35 mol/kg at 228 K and 18 – 23 mol/kg at 243 K are observed. As discussed, the correlation between V_P and swing capacity becomes more pronounced at lower temperature.

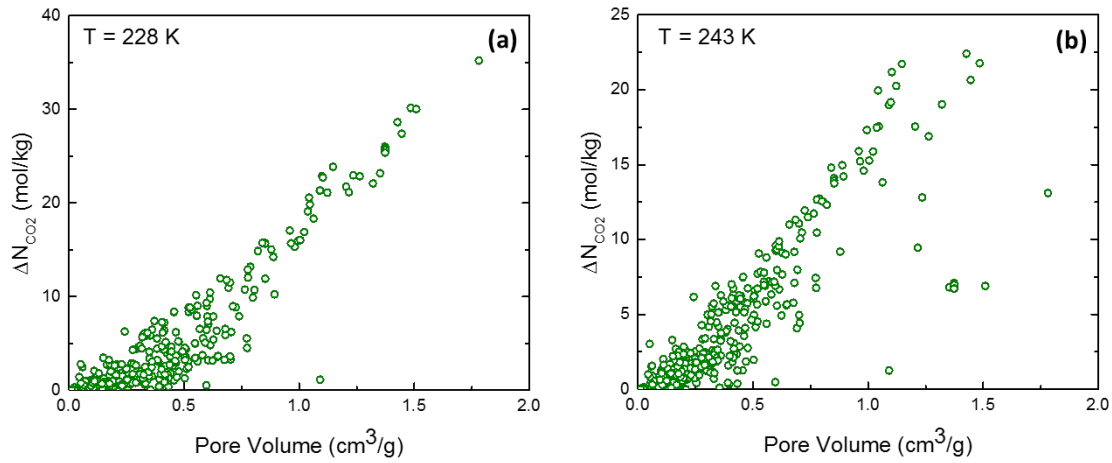

Figure 3.A.1. Calculated CO_2 swing capacity between 0.1 bar and 2.0 bar in 477 MOFs at (a) 228 K and (b) 243 K.

Figure 3.A.2 shows the computed PSA swing capacity as a function of four representative geometric MOF properties at 243 K. Large V_P and SA_{acc} show clear correlations to accomplish high swing capacities. We note that V_P and SA_{acc} are stronlgy correlated to one another. LCD and PLD exhibit poor correlation to achieve large swing capacities. Similar results were seen at other temperatures (data not shown).

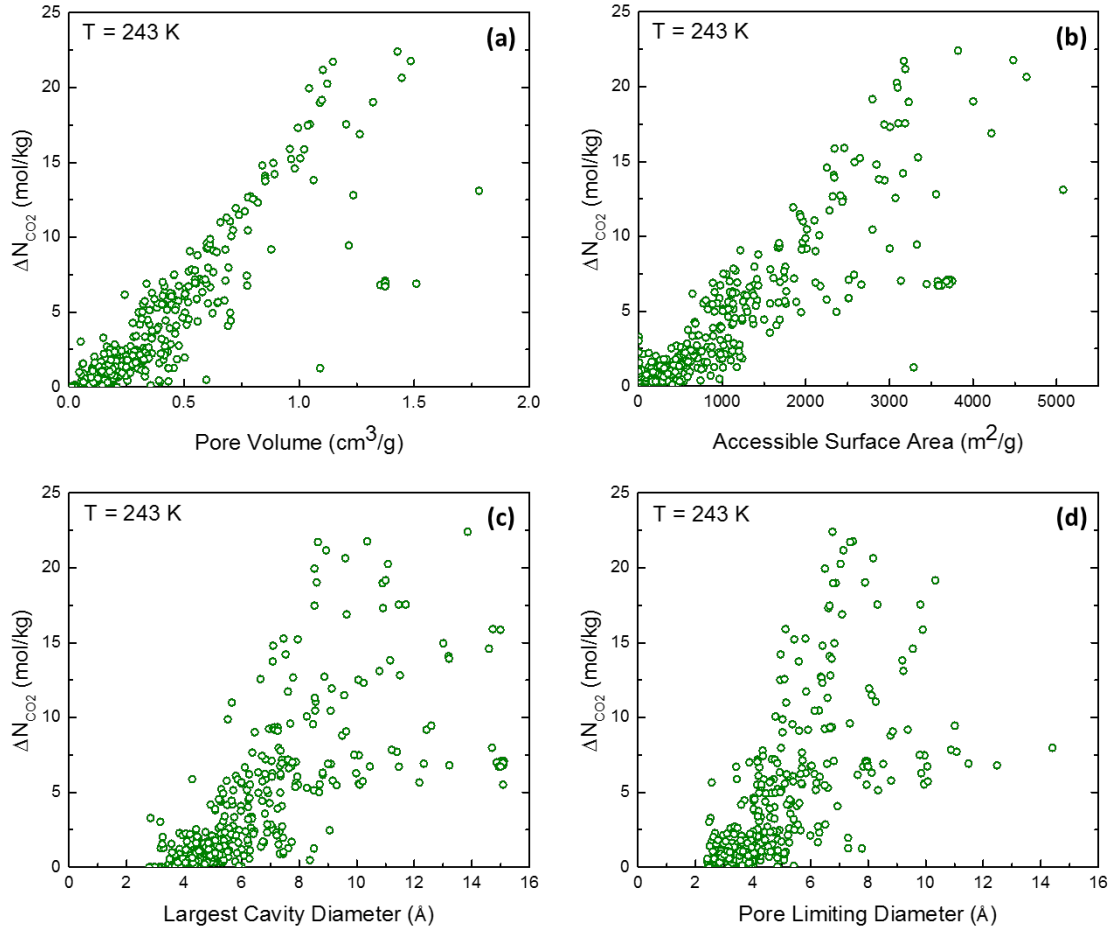

Figure 3.A.2. Calculated CO_2 swing capacity between 0.1 bar and 2.0 bar in 477 MOFs at 243 K as a function of (a) pore volume, (b) accessible surface area, (c) largest cavity diameter, and (d) pore limiting diameter.

3.A.2.2 Energetic Properties of MOFs for Swing Capacity

Once geometric criteria are satisfied, it is useful to observe how energetic properties of MOFs enable large swing capacity as discussed in Chapter 3. The predicted sub-ambient PSA CO_2 swing capacity as a function of Q_{ads}^{0} and Q_{ads}^{avg} is investigated in Figure 3.A.3a and Figure 3.A.3b, respectively. The presence of the optimal heat range at different temperatures are observed for both quantities. The optimum for both thermodynamic quantities to achieve a breakthrough improvement in a PSA process is weakly temperature

dependent. The correlation between Q_{ads}^{0} and Q_{ads}^{avg} in Figure 3.A.3c shows that the majority of the materials show the increase in Q_{ads} as loading increases with optimal Q_{ads}^{0} and Q_{ads}^{avg} for large swing capacity.

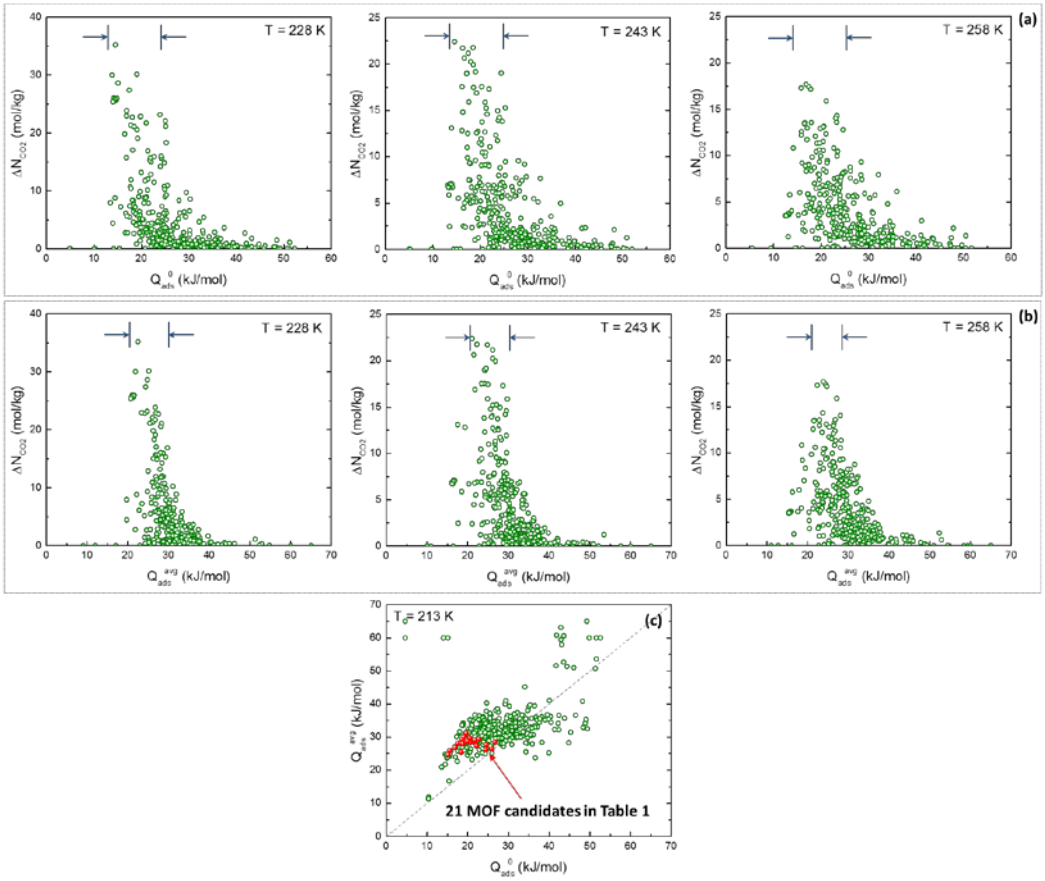

Figure 3.A.3. (a) Q_{ads}^{0} and (b) Q_{ads}^{avg} at 228 K, 243 K, and 258 K in 477 MOFs. Arrows indicate the optimal range for the heat of adsorption. (c) Correlation between Q_{ads}^{0} and Q_{ads}^{avg} at 213 K in 477 MOFs with entries of high swing capacity 21 MOF candidates noted.

3.A.2.3 MOF Candidates for Large Sub-Ambient PSA CO_2 Swing Capacity

Table 3.A.1. MOF candidates for large sub-ambient PSA ΔN_{CO2} with geometric [a] and energetic properties.

Metal-Organic Frameworks	V_P (cm^3/g)	SA_{acc} (m^2/g)	LCD (Å)	PLD (Å)	Q_{ads}^0 (kJ/mol)					Q_{ads}^{avg} (kJ/mol)				
					213 K	228 K	243 K	258 K	273 K	213 K	228 K	243 K	258 K	273 K
XAWVUN	1.8	5077	10.8	9.2	15.1	14.5	13.9	13.4	12.9	24.7	22.5	17.5	16.2	15.7
ANUGIA	1.4	3820	13.9	6.8	15.6	15.1	14.6	14.2	13.7	26.0	24.7	21.1	18.5	17.7
WONZOP	1.1	2796	11.0	10.3	20.7	19.8	19.0	18.1	17.3	28.3	26.9	24.5	20.9	19.9
SENWAL	1.2	3171	8.7	7.4	17.5	16.9	16.3	15.8	15.3	28.2	26.7	24.8	22.3	19.7
YUGLES	1.1	3231	10.9	6.8	18.4	17.8	17.1	16.5	15.9	25.5	26.1	24.2	21.5	19.2
NUTQAV	1.1	3229	10.9	6.9	18.4	17.8	17.2	16.6	16.1	28.1	26.0	24.3	21.6	19.4
WONZUV	1.2	3187	11.5	9.8	21.7	21.0	20.3	19.6	19.0	28.5	26.7	23.4	21.8	21.6
OJICUG	1.3	4001	8.6	7.9	25.9	25.0	24.4	23.3	22.6	26.4	26.1	24.1	23.6	23.4
NUTQEZ	1.1	3105	11.7	8.3	16.8	16.5	16.2	15.9	15.5	26.9	26.2	24.1	21.3	19.6
SENWOZ	1.1	3189	8.9	7.1	18.6	18.1	17.5	16.9	16.3	29.3	27.5	26.1	23.8	21.2
MATVEJ	1.0	2938	8.5	6.7	19.9	19.2	18.6	17.9	17.4	28.7	26.8	24.9	22.8	21.1
UTEWUM	1.0	2342	15.0	9.9	21.8	21.4	21.0	20.6	20.2	29.1	29.7	29.7	26.4	23.7
XAMDUM07	0.9	2338	13.2	6.7	24.4	24.1	23.8	23.4	22.9	26.2	26.8	25.8	23.8	22.4
FIQCEN	0.9	2333	13.2	6.7	24.6	24.3	23.9	23.5	23.0	27.6	27.6	26.0	24.2	22.5
UTEWOG	1.0	2251	14.6	9.6	22.2	21.8	21.4	21.0	20.6	27.3	29.3	29.5	26.7	24.1
BIBXUH	1.0	2458	14.7	5.1	18.8	18.1	17.6	17.1	16.6	28.0	26.9	24.8	22.8	21.2
XUGSEY	1.0	3342	7.5	5.8	26.7	26.1	25.2	24.6	23.8	28.4	28.0	27.1	25.2	23.9
KEFBEE	1.1	3088	11.1	7.0	19.0	18.5	17.9	17.4	16.9	30.0	28.2	26.1	24.2	22.1
FEFCUQ	0.8	2413	8.9	6.4	20.5	20.0	19.5	19.0	18.5	29.7	27.9	26.1	23.9	22.3
QUQFIS	1.0	2646	8.0	5.4	22.7	21.9	21.3	20.5	19.8	29.4	27.1	26.1	24.6	22.7
SENWIT	1.0	3098	8.5	6.5	19.6	19.0	18.5	17.8	17.3	31.2	28.1	26.8	24.7	22.5

[a] Geometric properties were adapted from CoRE MOF database developed by Chung *et al.*[9] with some properties recomputed in this chapter if needed.

3.A.3 Desorption Condition in Sub-Ambient PSA CO_2 Swing Capacity

The choice of desorption pressure in a PSA process strongly affects the energy and cost efficiency of the overall process.[10] The analysis in Chapter 3 used a desorption pressure of 0.1 bar, which may be considerably lower than is desirable in practice. Here, we examine the influence of the desorption pressure on the CO_2 swing capacities in a number of large capacity MOFs.

Figures 3.A.4 – 3.A.6 show the computed CO_2 adsorption isotherms, heat of adsorption, predicted swing capacities by varying desorption pressures from 0.1 to 1.0 bar in ANUGIA (Figure 3.A.4), WONZOP (Figure 3.A.5), and SENWAL (Figure 3.A.6). Two observations can be made from these results. First, all three materials achieve 10 mol/kg swing capacities at 243 and/or 258 K using a pressure swing between 2.0 bar for adsorption and 1.0 bar for desorption. Second, the temperature at which the maximum swing capacity is observed increases as the desorption pressure is increased. This observation, coupled with the reduced swing capacity as the desorption pressure is increased, indicate that a set of trade-offs will dictate the optimal desorption pressure and operating temperature in designing an optimal PSA process.

Figures 3.A.4 – 3.A.6 also show the mixture adsorption selectivity for CO_2 relative to a bulk binary CO_2/N_2 0.14/0.86 mixture in ANUGIA (Figure 3.A.4), WONZOP (Figure 3.A.5), and SENWAL (Figure 3.A.6). As expected, lowering the temperature increases the adsorption selectivity in every example. These materials have higher selectivities than the high capacity material shown in Figure 3.6. WONZOP (Figure 3.A.5) and SENWAL

(Figure 3.A.6) both show selectivities exceeding 40 at 213 K. All of the materials in Figures 3.A.4 – 3.A.6 and Figure 3.6 show only moderate selectivity at 258 K and 273 K.

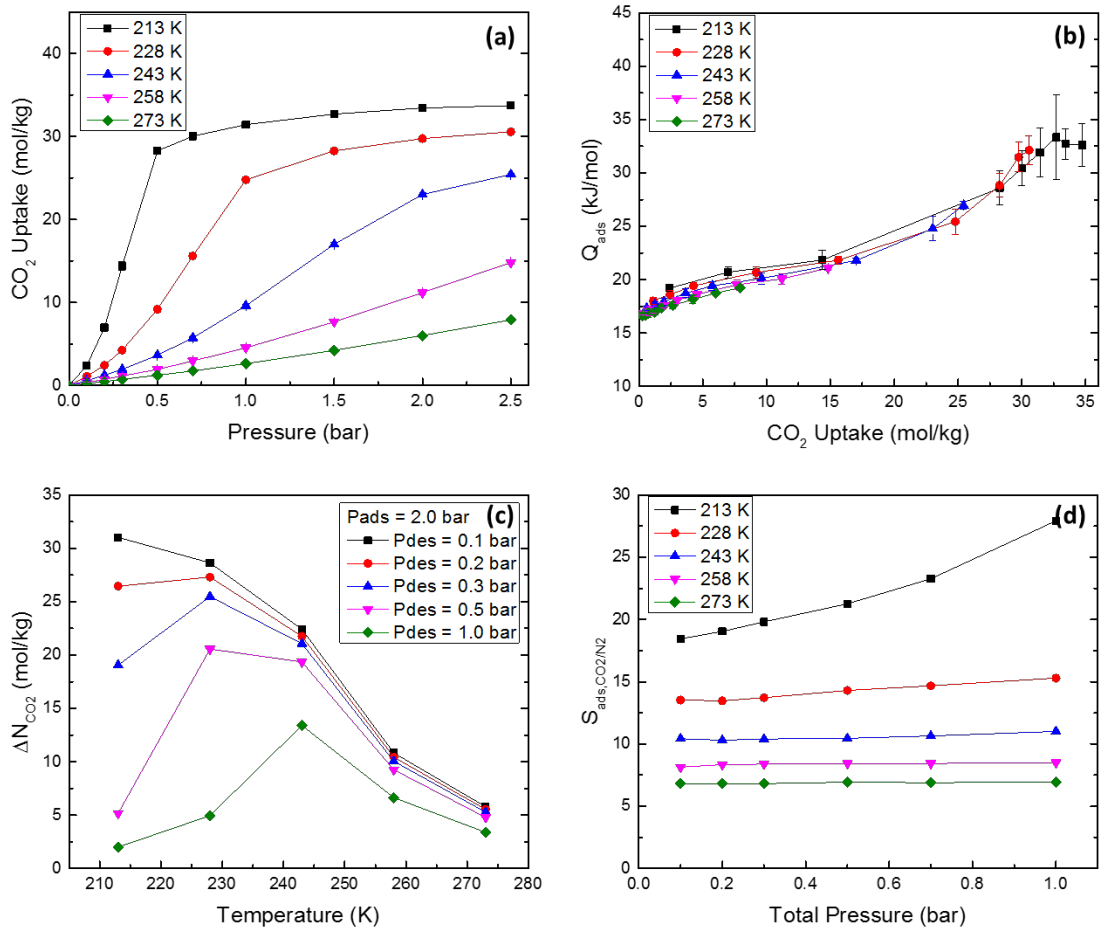

Figure 3.A.4. (a) Sub-ambient CO_2 adsorption isotherms computed by GCMC simulations, (b) heat of adsorption as a function of CO_2 uptake obtained from GCMC simulation, (c) predicted sub-ambient PSA CO_2 swing capacity as a function of desorption pressure, and (d) CO_2 adsorption selectivity from bulk CO_2/N_2 0.14/0.86 mixture calculated by binary GCMC simulations in ANUGIA.

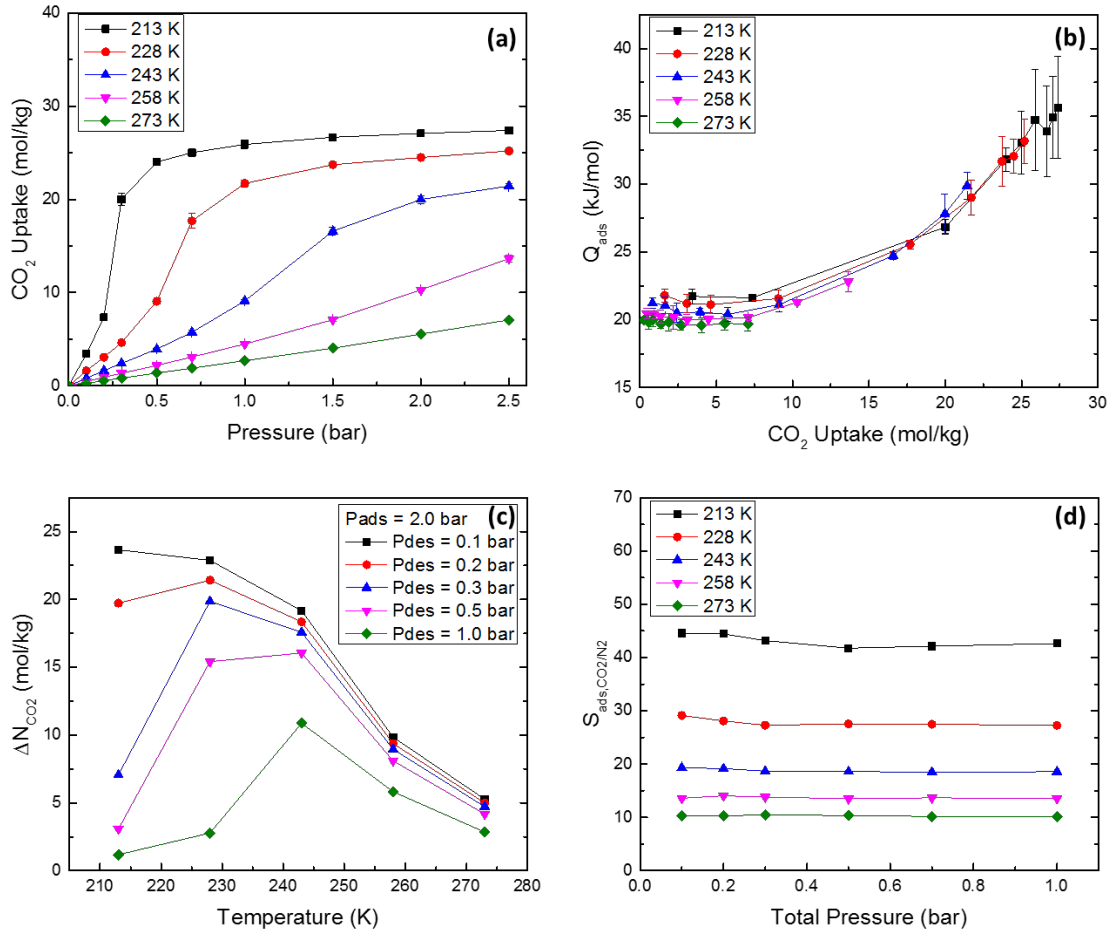

Figure 3.A.5. (a) Sub-ambient CO_2 adsorption isotherms computed by GCMC simulations, (b) heat of adsorption as a function of CO_2 uptake obtained from GCMC simulation, (c) predicted sub-ambient PSA CO_2 swing capacity as a function of desorption pressure, and (d) CO_2 adsorption selectivity from bulk CO_2/N_2 0.14/0.86 mixture calculated by binary GCMC simulations in WONZOP.

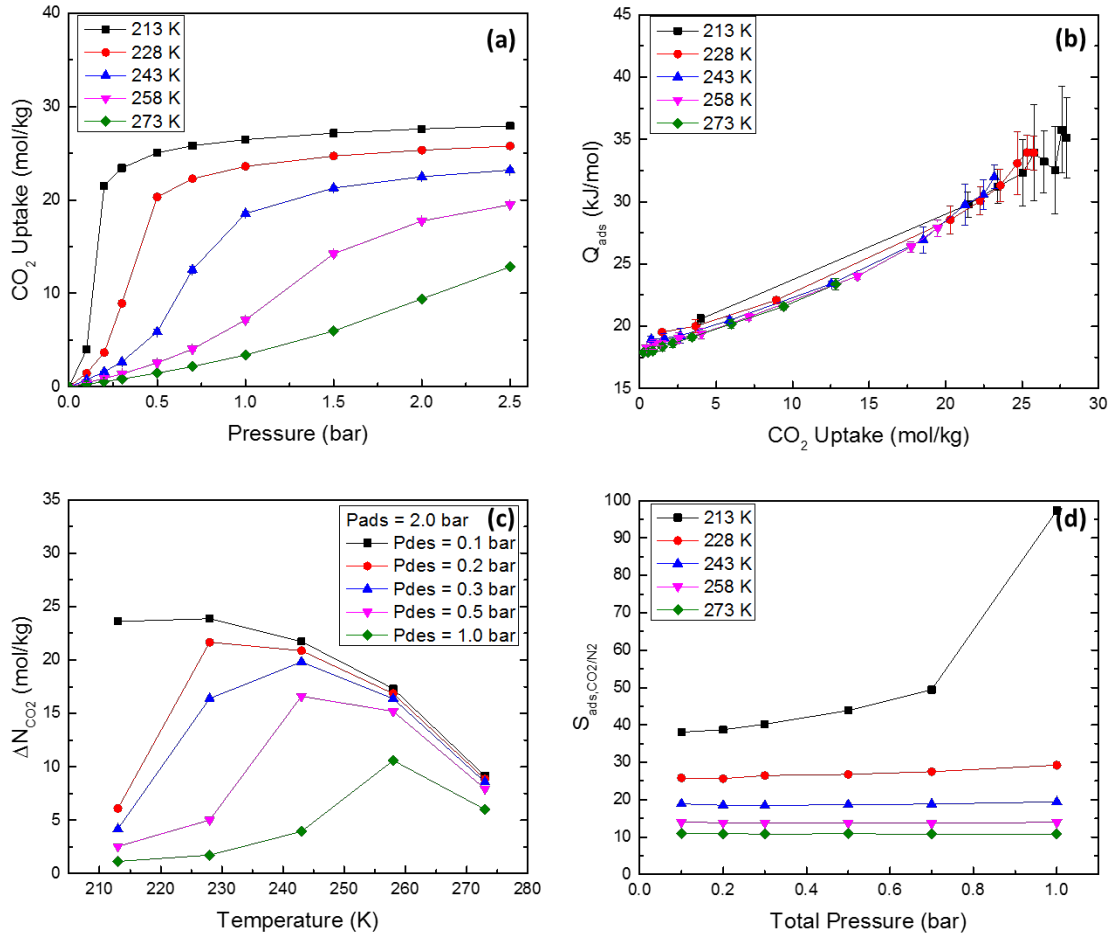

Figure 3.A.6. (a) Sub-ambient CO_2 adsorption isotherms computed by GCMC simulations, (b) heat of adsorption as a function of CO_2 uptake obtained from GCMC simulation, (c) predicted sub-ambient PSA CO_2 swing capacity as a function of desorption pressure, and (d) CO_2 adsorption selectivity from bulk CO_2/N_2 0.14/0.86 mixture calculated by binary GCMC simulations in SENWAL.

3.A.4 References for Appendix 3.A

(1) Dubbeldam, D.; Torres-Knoop, A.; Walton, K. S. On the inner workings of Monte Carlo codes. *Mol. Simulat.* **2013,** *39*, 1253-1292.

(2) Rappe, A. K.; Casewit, C. J.; Colwell, K. S.; Goddard, W. A.; Skiff, W. M. UFF, A Full Periodic-Table Force-Field for Molecular Mechanics and Molecuar Dynamics Simulations. *J. Am. Chem. Soc.* **1992,** *114*, 10024-10035.

(3) Martin, M. G.; Siepmann, J. I. Transferable potentials for phase equilibria. 1. United-atom description of n-alkanes. *J. Phys. Chem. B* **1998,** *102*, 2569-2577.

(4) Wells, B. A.; Chaffee, A. L. Ewald Summation for Molecular Simulations. *J. Chem. Theory Comput.* **2015**, *11*, 3684-3695.

(5) Manz, T. A.; Sholl, D. S. Chemically Meaningful Atomic Charges That Reproduce the Electrostatic Potential in Periodic and Nonperiodic Materials. *J. Chem. Theory Comput.* **2010**, *6*, 2455-2468.

(6) Do, D. D.; Nicholson, D.; Do, H.D. On the Henry constant and isosteric heat at zero loading in gas phase adsorption. *J. Colloid Interface Sci.* **2008**, *324*, 15-24.

(7) Dickey, A. N.;Yazaydin, A. O.; Willis, R. R.; Snurr, R. Q. Screening CO_2/N_2 selectivity in metal-organic frameworks using Monte Carlo simulations and ideal adsorbed solution theory. *Can. J. Chem. Eng.* **2012**, *90*, 825-832.

(8) Willems, T. F.; Rycroft, C. H.; Kazi, M.; Meza, J. C.; Haranczyk, M. Algorithms and tools for high-throughput geometry-based analysis of crystalline porous materials. *Micropor. Mesopor. Mat.* **2012**, *149*, 134-141.

(9) Chung, Y. G.; Camp, J.; Haranczyk, M.; Sikora, B. J.; Bury, W.; Krungleviciute, V.; Yildirim, T.; Farha, O. K.; Sholl, D. S.; Snurr, R. Q. Computation-Ready, Experimental Metal-Organic Frameworks: A Tool To Enable High-Throughput Screening of Nanoporous Crystals. *Chem. Mater.* **2014**, *26*, 6185-6192.

(10) Ho, M. T.; Allinson, G. W.; Wiley, D. E. Reducing the Cost of CO_2 from Flue Gas Using Pressure Swing Adsorption. *Ind. Eng. Chem. Res.* **2008,** *47*, 1562-1568.

CHAPTER 4. HOW WELL DO APPROXIMATE MODELS OF ADSORPTION-BASED CO_2 CAPTURE PROCESSES PREDICT RESULTS OF DETAILED PROCESS MODELS?

Appropriate selection of adsorbent materials is essential in developing adsorption-based processes such as CO_2 capture. Approximate methods to evaluate material candidates exist using adsorbent evaluation metrics or simplified process models. These approximate methods do not, of course, completely describe the performance of adsorbents in real separation processes. In this chapter, we assess the correlations between approximate predictions and detailed process models of pressure swing adsorption (PSA) at sub-ambient temperatures for post-combustion CO_2 capture using metal-organic frameworks (MOFs). Our results indicate that CO_2 swing capacity and adsorbent regenerability are useful in predicting the ranking of materials for this process. These results illustrate the opportunities and challenges in bridging approximate and detailed methods for evaluating adsorbents for cyclic separations processes.

* Contents of this chapter have been submitted for publication in a peer-reviewed journal

Jongwoo Park, Héctor Octavio Rubiera Landa, Yoshiaki Kawajiri, Matthew J. Realff, Ryan P. Lively, David S. Sholl, ″How Well Do Approximate Models of Adsorption-based CO_2 Capture Processes Predict Results of Detailed Process Models?″, submitted to and under review at ***Industrial & Engineering Chemistry Research***.

4.1 INTRODUCTION

Atmospheric CO_2 concentrations are rising due to anthropogenic emissions.[1,2] This has motivated efforts to develop cost-effective and energy-efficient carbon capture processes.[3] Cyclic adsorption-based CO_2 capture has emerged as a promising approach. Typical examples of these processes include pressure swing adsorption (PSA), vacuum swing adsorption (VSA), and temperature swing adsorption (TSA).[4-7] Adsorption-based carbon capture is a materials-enabled technology. Porous materials including activated carbon, zeolites, and metal-organic frameworks (MOFs) have been actively examined for use in CO_2 capture processes.[2,8-11] Although effective cycle configurations are important, the performance of cyclic adsorption processes depends heavily on the selection of adsorbent materials.[12] Given the large numbers of potential adsorbents that exist, finding effective means to evaluate adsorbents is a key challenge in developing cyclic adsorption-based CO_2 capture processes.

A major hurdle in adsorbent evaluation is the choice of performance descriptors. When screening a large spectrum of adsorbent materials, single component adsorption isotherms for gas species of interest are typically the only information that can be reasonably obtained.[7,11] Multiple approximate performance metrics that can readily be calculated from these isotherms have been proposed.[7,12-18] These metrics are typically based on physical intuition.[7,12] They have served as proxies to evaluate a wide spectrum of materials, especially when combined with high-throughput molecular modeling of adsorption isotherms.[17-23]

Another way to predict the performance of an adsorbent for CO_2 capture is to use simplified process models describing fully detailed PSA and/or VSA processes.[24-27] These models are designed to provide industry-relevant performance descriptors such as product purity and energy consumption without the complexity of detailed process modeling. The models avoid the complexity associated with detailed process optimization[24,25] and can be used with limited information beyond single component adsorption isotherms.[26,27] These models do not, however, include detailed cycle configurations, so there is a gap between what they can predict and the performance of real processes.

Several studies have used detailed process optimization in combination with approximate metrics to better understand the suitability of materials for adsorption-based separations.[12,28-34] These studies have primarily focused on a restricted spectrum of materials that satisfy targeted constraints of product purity and recovery. Motivated by these previous contributions, the objective of this chapter is to directly assess the capability of simple proxies for adsorbent performance and approximate models of cyclic adsorption to predict the outcomes of detailed process models of adsorption-based CO_2 capture processes. We consider the situation where a range of adsorbent materials is available and each level of modeling is used to rank the materials in terms of performance. After producing these rankings with models of multiple levels of complexity and fidelity it is possible to discuss the correlations between predictions from the simpler models and detailed process models.

We focus below on the use of MOFs as adsorbents for sub-ambient PSA for post-combustion CO_2 capture. Sub-ambient separations have been recently reported by Air Liquide for large-scale CO_2 separation from power plant flue gas via a membrane system,

which appeared feasible when implemented with appropriate heat integration and power recovery.[35-37] A potential advantage of operating a PSA process at sub-ambient temperatures is the ability to achieve large swing capacities for adsorption. We previously examined a large number of MOFs with respect to this metric and showed that many materials exist with a CO_2 swing capacity larger than 10 mol/kg.[38] Below, we use the task of ranking materials of this type for use in sub-ambient temperature CO_2 capture as an example to explore the correlation (or lack of correlation) between predictions based on simplified models and detailed process optimization.

4.2 METHODS

4.2.1 Sub-Ambient PSA Process

We focus on an adsorption-based PSA CO_2 capture process at sub-ambient temperatures using MOF materials. In Chapter 3[38], the viability of the sub-ambient PSA process using MOFs was estimated using single component CO_2 adsorption isotherms obtained from molecular modeling. Compelling evidence exists that molecular modeling can accurately predict the adsorption isotherms of CO_2 and similar species in a wide range of MOFs.[11,38,39] The large pore volumes and surface areas of MOFs, coupled with a suggested process design made them appealing materials as adsorbents.[6-11,38] In this chapter we extend our focus to a bulk mixture of CO_2/N_2 at compositions relevant to post-combustion flue gas. Real flue gas contains other contaminants including H_2O, O_2, CO, SO_x, NO_x, and Hg species.[40-43] The presence of these contaminants could impact adsorption properties of primary components and the stability of adsorbents.[44-46] Air Liquide has demonstrated that dry and clean flue gas feeds can be achieved by appropriate system

design combined with a sub-ambient heat exchanger.[47] Hence we focus on adsorptive separation of CO_2 from a dry bulk binary mixture of CO_2/N_2 with molar composition 0.14/0.86 with no other components. Typical pressures for PSA desorption and adsorption are 0.7 bar ($P_{CO2,des}$ = 0.1 bar) and 14.3 bar ($P_{CO2,ads}$ = 2.0 bar), respectively, at T = 243 K. The choice of the pressure swing range and temperature are adapted from earlier findings.[35,36,38] The adsorption and desorption pressures are treated as decision variables in our detailed process models.

4.2.2 Adsorbent Evaluation Metrics

To evaluate materials as adsorbents for gas capture, a general starting point is to obtain adsorption isotherms for the gases of interest. Multiple efforts have focused on proposing performance metrics that can be derived from adsorption isotherms to forecast their capabilities in end-use applications.[7,13-18] Table 4.1 summarizes the metrics used below to make predictions about PSA processes.[7,13,16]

The first two metrics are the swing capacity and adsorption selectivity.[7,27] Swing capacity is defined as the difference between gas storage capacities of the species targeted for capture at the adsorption (N_{CO2}^{ads}) and desorption (N_{CO2}^{des}) pressures chosen as bounds on the process. We used $P_{CO2,ads}$ = 2.0 bar and $P_{CO2,des}$ = 0.1 bar. The mixture adsorption selectivity is defined as the ratio of adsorption capacity of each component and mole fraction of each component in bulk phase (y_i) at the adsorption conditions, P_{total} = 14.3 bar ($S_{ads,CO2/N2}^{ads}$) and/or P_{total} = 0.7 bar ($S_{ads,CO2/N2}^{des}$). The other two metrics, the sorbent selection parameter and the adsorbent performance score, combine information from the swing capacity of the component of interest and of the competing species, and the

adsorption selectivity at adsorption and desorption pressures under adsorption conditions in different ways.[7,12,16] Such metrics aim to reflect the trade-off relationships that generally exist between swing capacity and adsorption selectivity.[48,49] A remaining metric, the regenerability, is the ratio of the swing capacity and the adsorbed amount of strongly adsorbed species at the adsorption pressure. This parameter estimates the fraction of the adsorption sites that are regenerated during the desorption step.[18,19] All adsorbent evaluation metrics above are calculated from mixture adsorption data (N_i).[7,13,17-19] In principle, molar composition of the bulk phase at the desorption condition completely describes the amount of adsorbing molecules at the desorption pressure (N_i^{des}). Estimating information regarding the desorption condition is, however, complicated because defining the composition of the bulk phase is not trivial.[12,50] Hence relying on adsorption conditions as described above has been a common practice.[7,13,17-21]

We obtained mixture adsorption data using molecular modeling via Grand Canonical Monte Carlo (GCMC) simulations. The MOFs of interest were taken from a subset of the CoRE MOF database[51], namely the energy optimized CoRE MOF DDEC charge database[52,53], which includes 477 DFT optimized structures to which high quality atomic point charges have been assigned. 143 MOFs were selected from this collection that showed PSA CO_2 swing capacity exceeding 4 mol/kg at 243 K between 0.1 bar and 2.0 bar.[38] Binary mixture GCMC simulations were conducted in these 143 materials to calculate adsorption properties of a CO_2/N_2 mixture at bulk pressures of 0.7 bar and 14.3 bar. The resulting mixture adsorption properties were then used to calculate the adsorbent evaluation metrics in Table 4.1 for each material. Detailed descriptions of the molecular modeling and the materials we used are given in Appendix 4.A (Sections 4.A.1 and 4.A.2).

Table 4.1. Definitions of adsorbent evaluation metrics[7,13,16] used to assess adsorbent materials[52,53] for post-combustion CO_2 separation with a sub-ambient PSA process.

Adsorbent Evaluation Metric		Metric Formula
ΔN_{CO2} (mol/kg)	Swing capacity	$\Delta N_{CO2} = {N_{CO2}}^{ads} - {N_{CO2}}^{des}$
$S_{ads,CO2/N2}{}^{ads}$	Adsorption selectivity	$S_{ads,CO2/N2}{}^{ads} = \frac{{N_{CO2}}^{ads}/{N_{N2}}^{ads}}{y_{CO2}/y_{N2}}$
$S_{SP,CO2/N2}$	Sorbent selection parameter	$S_{SP,CO2/N2} = \frac{({S_{ads,CO2/N2}}^{ads})^2}{({S_{ads,CO2/N2}}^{des})} \frac{\Delta N_{CO2}}{\Delta N_{N2}}$
$APS_{CO2/N2}$ (mol/kg)	Adsorbent performance score	$APS_{CO2/N2} = {S_{ads,CO2/N2}}^{ads} \Delta N_{CO2}$
R (%)	Regenerability	$R = \frac{\Delta N_{CO2}}{{N_{CO2}}^{ads}} \times 100$

4.2.3 Idealized PSA Process Model

Adsorbent evaluation metrics do not necessarily translate into process-level insights. Several simplified adsorption process models have been proposed to overcome this limitation.[24-27] Such models impose multiple assumptions on adsorbents and cycle configurations but are analogous to cyclic adsorption processes. We adapted an idealized PSA process model proposed by Ga et al.[27] This model provides two process performance indicators for an idealized ad-/desorption cycles, namely product purity (Pu_{CO2}) and specific energy consumption (En_{CO2}). The latter quantity provides insight in the separation cost. In addition, swing capacity (ΔN_{CO2} and/or ΔN_{N2}) can be obtained separately. In this idealized model the composition of the gas products is found by numerically solving a series of non-linear equations of mixture adsorption capacities. The major assumptions underlying this idealized description of PSA are that the process operates isothermally without dispersion or kinetic effects with a two-step cycle configurations for ad-/desorption, and that adsorption is described as a binary mixture of a strongly and a weakly adsorbing species. The model assumes the use of a compressor and vacuum, and also

assumes 100% product recovery is achieved. The idealized PSA process is illustrated in Figure 4.1.

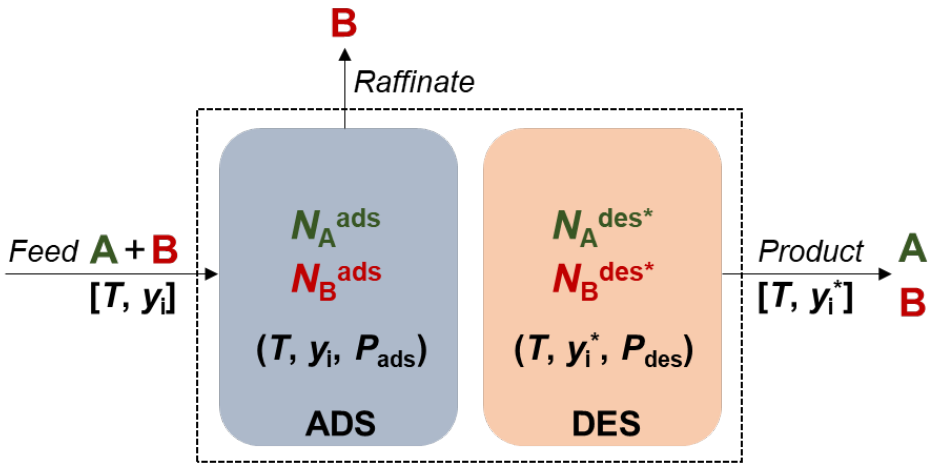

Figure 4.1. Schematic illustration of the idealized PSA process model. The model imposes idealized cycle of adsorption (ADS) and desorption (DES) with feed binary mixture of CO_2/N_2 in molar fraction of 0.14/0.86 (y_i). Components A and B refer to strongly and weakly adsorbing species, respectively. The model numerically solves for the composition of the produced gas or molar composition of gas components in the desorption step (y_i^*). Adsorption amounts at given desorption conditions can be obtained (N_i^{des*}). Isothermal operation is assumed at T = 243 K.

A fundamental piece of information to perform process modeling is the mixture adsorption equilibrium. The model outlined above requires an analytical expression or other methods to estimate the mixture adsorption equilibrium at different pressures, temperatures, and mole fractions in gas phase.[12,54] We employed ideal adsorbed solution theory (IAST)[54-56] to predict mixture adsorption. IAST estimates the mixture equilibrium from single component adsorption isotherms by assuming an ideal solution is formed by the adsorbed phase.[55] We simulated single component adsorption isotherms for CO_2 and N_2 at temperatures of 213, 228, 243, 258, and 273 K via GCMC. More details of the idealized PSA process model and IAST are given in Appendix 4.A (Section 4.A.4).

4.2.4 Rigorous Process Model

Due to the inherent complexity of cyclic adsorption processes, detailed process optimization modeling is needed to achieve the highest fidelity regarding the evaluation of adsorbent materials. We used a rigorous process model with multi-objective optimization[57,58] to assess the cyclic performance of each MOF considered. Table 4.2 summarizes the definitions used for our process-level objectives.

Table 4.2. Definitions of process-level objectives from multi-objective optimization used to assess adsorbent materials for post-combustion CO_2 separation with a sub-ambient PSA process.

Objectives	**Objective Formula**
Purity, Pu_{CO2} (%)	$Pu_{CO2} = \frac{Total\ CO_2\ moles\ in\ the\ extract\ product}{Total\ gas\ moles\ in\ the\ extract\ product} \times 100$
Recovery, Re_{CO2} (%)	$Re_{CO2} = \frac{Total\ CO_2\ moles\ in\ the\ extract\ product}{Total\ CO_2\ moles\ fed\ into\ the\ cycle} \times 100$
Productivity, Pr_{CO2} (mol/kg·s)	$Pr_{CO2} = \frac{Total\ CO_2\ moles\ in\ the\ extract\ product}{Total\ adsorbent\ mass \times Cycle\ time}$
Energy, En_{CO2} (kWh/t)	$En_{CO2} = \frac{\sum_{i=cycle\ configuration} E_i}{CO_2\ mass\ in\ the\ extract\ product\ per\ cycle}$

We considered a PSA process model based on a four-step Skarstrom cycle.[5,59-61] Figure 4.2a illustrates this cycle, which includes light product pressurization[4,58] with N_2, adsorption of CO_2 and production of N_2, co-current blowdown, and counter-current evacuation with production of CO_2. Our model implemented mathematical expressions to describe packed-bed operation of a PSA under non-isobaric conditions. This includes transient balance equations which are a set of non-linear partial differential equations (PDEs) coupled with molecular diffusion and adsorption properties. The linear driving force model[4,62] and the mixture adsorption isotherms predicted by IAST are used for molecular diffusion and adsorption properties, respectively. A finite volume method was applied to discretize the PDE system in space by taking account flux function

approximations.[63,64] This results in a set of ordinary differential equations (ODEs) that were solved using MATLAB with the *ode15s* function at default tolerances until the system reaches the cyclic steady state. Details of PSA modeling are provided in the Section 4.A.5 of Appendix 4.A.

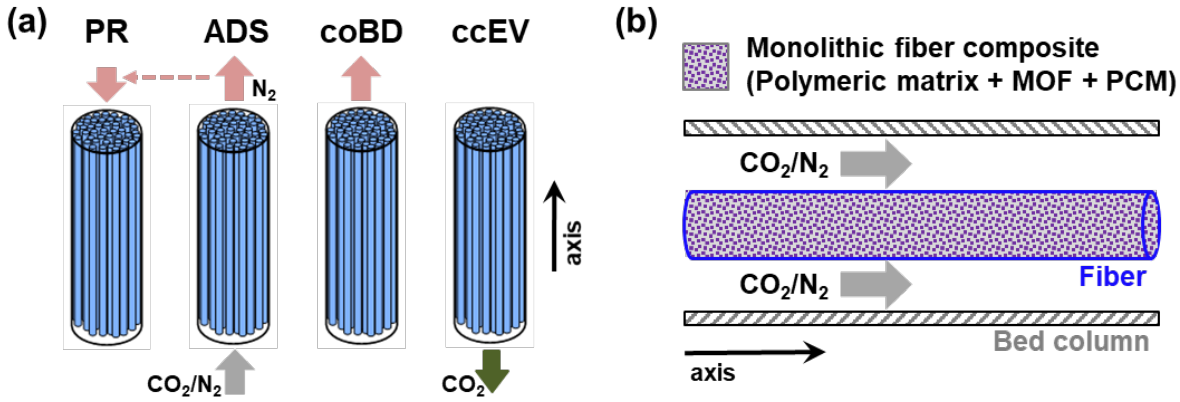

Figure 4.2. (a) Schematic illustration of the four-step PSA cycle for the rigorous process modeling of a hollow fiber bed contactor. The cycle includes counter-current light product pressurization (PR), adsorption (ADS), co-current blowdown (coBD), and counter-current evacuation (ccEV). (b) Schematic illustration of the PCM-based thermally modulated fiber adsorbent and flow of bulk CO_2/N_2 mixture in the bed column.

Our rigorous process model focused on thermally modulated hollow fiber adsorbents as illustrated in Figure 4.2b.[65-70] Incorporation of fiber adsorbents as structured contactors in cyclic adsorption processes allows for efficient mass and heat transfer, and reduced pressure drop relative to packed beds.[71-74] We modeled a fiber adsorbent contactor comprised of a non-adsorbing polymeric matrix, MOF particles, and microencapsulated phase change materials (PCM).[65-67] Judicious use of PCM can enable near-isothermal operation of a PSA by its melting and freezing upon CO_2 adsorption (exothermic reaction) and desorption (endothermic reaction).[74] By assuming this approach for heat management, we modeled the process as allowing temperature variation modulated with PCM. Details of the modeling of fiber adsorbent are available in Appendix 4.A (Section 4.A.5). Only the

PSA unit is considered in this chapter without assessing other details of the flowsheet that would be required to completely describe an integration of this unit with a power plant.

Sub-ambient PSA process modeling above was coupled with multi-objective optimization. Optimization was carried out in MATLAB using the *gamultiobj* function for which a variant of the NSGA-II genetic algorithm[58,75] was applied. We consider the rigorous process modeling as a black-box function with a set of available decision variables as inputs and process-level objectives at cyclic steady state as outputs. Further details of the optimization procedures are provided in Appendix 4.A (Section 4.A.5). This optimization leads to maximizing purity, recovery, and productivity while minimizing energy consumption under each process condition that is determined by decision variables.

4.3 RESULTS AND DISCUSSION

4.3.1 Adsorbent Evaluation by Approximate Models

It is typically impractical to conduct rigorous process modeling or to perform detailed experimental testing for hundreds of potential adsorbent materials. We therefore used approximate models to reduce the number of MOFs to examine with our detailed process model. We began by examining 143 MOFs using the adsorbent evaluation metrics in Table 4.1 and then studied 30 of these adsorbents using the idealized PSA process model described in Section 4.2.3. The goal of this work was not to identify individual "winning" materials but to reveal a spectrum of materials performance that could then be compared for selected materials to our more rigorous process model.

4.3.1.1 Material Selection by Adsorbent Evaluation Metrics

143 MOFs were characterized with the adsorbent evaluation metrics in Table 4.1. In order to discover high performing materials, previous studies commonly used one or two of the metrics in Table 4.1.[7,13-21,38] Top-ranked materials for a single metric[7,13,21,38] or those judged to have a good combination of each metric[17-19] were then labeled as potential adsorbents. We employ the latter screening strategy for the filtering of MOF candidates. Our strategy is illustrated in Figure 4.3a.

We first set constraints for each metric. A key advantage of sub-ambient gas processing is that the swing capacity for small molecules can be large.[38] On this basis the lower bound for swing capacity was set to 10 mol/kg. Adsorption selectivity has long been viewed as controlling the achievable product purity.[4,20] We set a lower bound on the mole fraction of CO_2 in adsorbed phase (x_{CO2}) of 0.9 when considering selectivity. The sorbent selection parameter includes information from the swing capacities for both CO_2 and N_2. Increasing or suppressing the adsorption of strongly or weakly adsorbing molecules, respectively, is a route for efficient separation of gas mixtures.[13,20,24,33] We therefore set a constraint to have CO_2 swing capacity more than ten times the N_2 swing capacity. The adsorbent performance score is calculated by the product of swing capacity and adsorption selectivity. We use same constraints of swing capacity and adsorption selectivity when setting the constraint for this quantity. Having a highly selective adsorbent does not guarantee high regenerability. We adopted a target regenerability of 75% from previous work.[18] The “best” adsorbents at this stage would be candidates that meet all of these constraints (cluster I in Figure 4.3a). To ensure we are considering a spectrum of materials, we also considered materials that satisfy some, but not all, of these constraints. Figure 4.3a

indicates clusters of materials that have extremely high selectivity but relatively low swing capacity (cluster II) or vice versa (cluster III in Figure 4.3a).

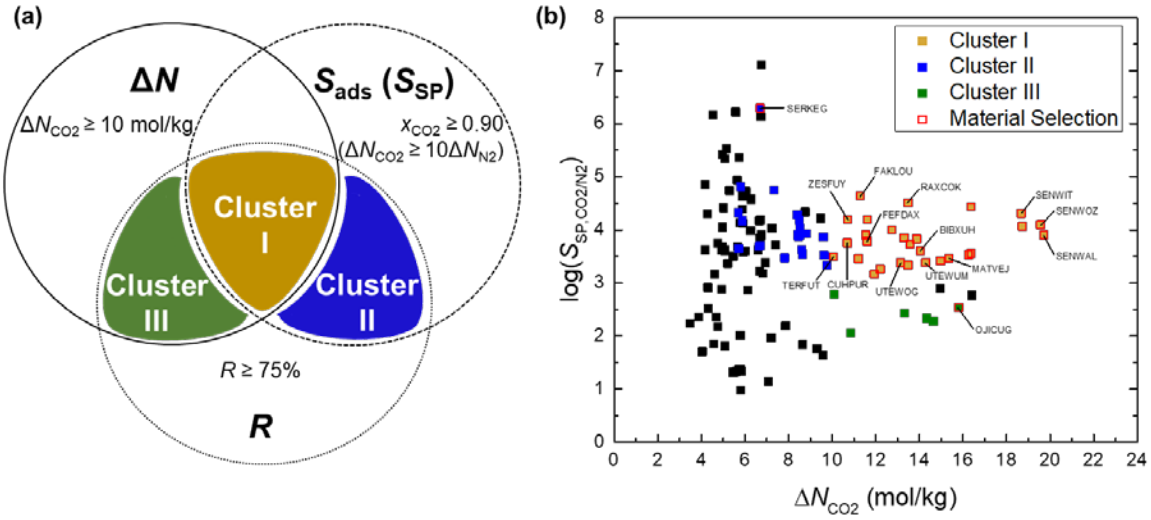

Figure 4.3. (a) Material selection strategy employed in this chapter to filter 143 MOFs by forming clusters. The constraints on each metrics and definitions of each cluster are described in the text. (b) Adsorbent evaluation metrics calculated for a CO_2/N_2 0.14/0.86 mixture at bulk pressures of 0.7 bar and 14.3 bar at 243 K. The horizontal and vertical axes are the swing capacity and the sorbent selection parameter, respectively. Data in black squares correspond to MOFs that do not belong to any of the clusters we defined.

Figure 4.3b shows the adsorbent evaluation metric data for 143 MOFs and clustering of this information as defined in Figure 4.3a. 28 MOFs were found from cluster I. We then selected additional MOFs from clusters II and III. The swing capacity for CO_2 in MOFs from cluster II ranges between 6-9 mol/kg, values considerably higher than typical materials for CO_2 capture via PSA at ambient temperatures.[76,77] The MOF from cluster II (CSD reference code SERKEG) with the highest sorbent selection parameter was chosen for further consideration. Similarly, the MOF from cluster III (OJICUG) with the largest swing capacity was chosen. This defined a set of 30 MOFs that were used in our more detailed models. These materials are indicated with highlighted borders in Figure

4.3b. Information about selected physical properties of 28 MOFs from cluster I is given in Figure 4.A.2 (Section 4.A.3 of Appendix 4.A).

4.3.1.2 Material Selection by an Idealized PSA Process Model

We next used the idealized PSA process model defined above[27] to obtain process-level performance descriptors of 30 MOFs. This approach allows us to incorporate a range of adsorption and desorption conditions.[24,27] The results obtained from this model were used to further reduce the number of MOFs to which we applied a rigorous process model.

Our process modeling uses IAST to predict mixture adsorption.[54] Although there are indications that applying IAST in MOFs may be viable[7,55,56], IAST may be inaccurate at high pressure and for weakly adsorbing molecules[20,56]. We therefore directly tested IAST in the 30 MOFs we considered by comparison with mixture GCMC calculations as shown in Figure 4.4. Both CO_2 (Figure 4.4a) and N_2 (Figure 4.4b) show good agreement between direct simulation of mixture adsorption with GCMC and simulation using IAST within the pressure range of our process. We calculated the fractional IAST error, defined as the ratio of the difference between IAST and GCMC results to the GCMC result.[20] For all 30 materials the fractional error in the CO_2 and N_2 uptakes were less than 10% and 15%, respectively. The fractional error for selectivity was also smaller than 15% for every material (Figure 4.4c). We took this as an indication that using IAST within our process models was an acceptable approximation.[20,56]

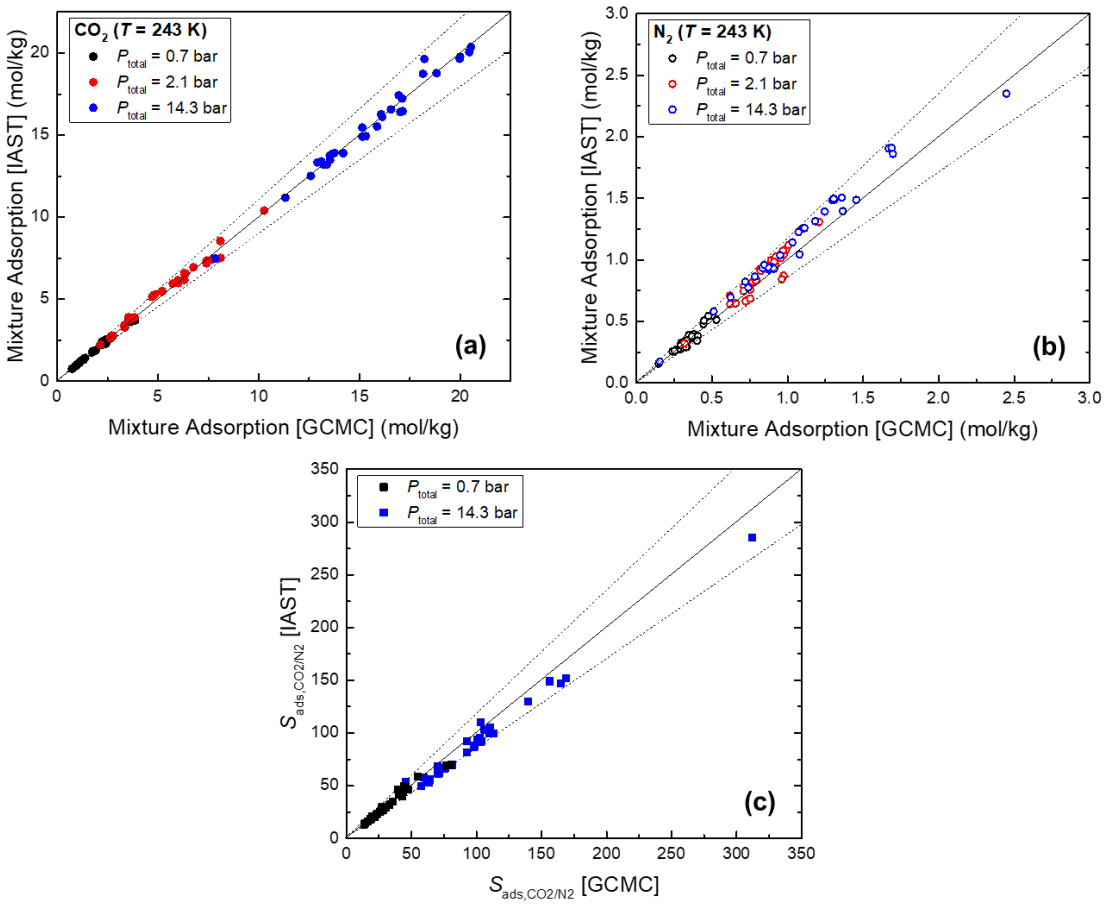

Figure 4.4. Comparison between mixture adsorption amounts in 30 MOFs computed from GCMC (horizontal axes) and IAST (vertical axes) for (a) CO_2 and (b) N_2 at low, intermediate, and high total pressures at 243 K and (c) adsorption selectivities in 30 MOFs computed from GCMC (horizontal axis) and IAST (vertical axis). In all cases the gas phase CO_2/N_2 composition is 0.14/0.86. The diagonal lines have slopes of 1.1, 1, and 0.9 from top to bottom, respectively, in (a). Similar lines are drawn for slopes of 1.15, 1, and 0.85 from top to bottom, respectively, in (b) and (c).

We used the idealized PSA model to select materials for use in our detailed process model as indicated in Table 4.A.1. We first chose MOFs that do not have open-metal sites (OMS) based on previous reports that examined the crystal structures via connectivity analysis for each metal center.[78,79] This choice avoids complications associated with the limited accuracy of generic force fields for molecular simulations of MOFs with OMS.[11,78-81] Among the 20 non-OMS MOFs, we sampled MOFs based on the CO_2 purity predicted

by the idealized model, Pu_{CO2}. We set 90% purity as the benchmark for this quantity.[82] All MOFs that exceed this benchmark for some combination of process conditions, i.e. adsorption and desorption pressures, were selected. In addition, four MOFs that did not exceed this standard were randomly chosen to ensure our final selection included a spectrum of materials performance. This gave the list of 15 MOFs shown in Figure 4.5. The process performance indicators for all 30 MOFs are shown in Figure 4.A.3.

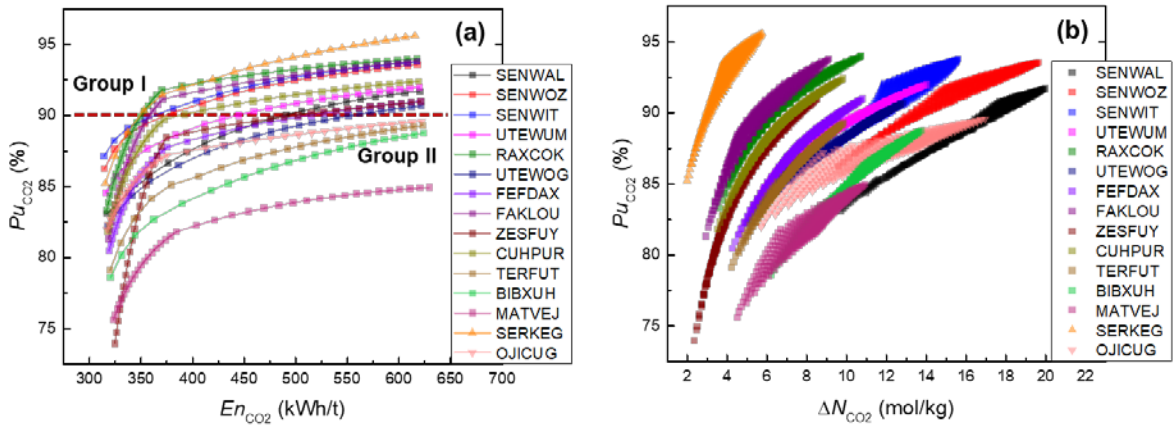

Figure 4.5. Performance indicators derived from the idealized PSA process model for 15 MOFs. The indicators were calculated for a CO_2/N_2 0.14/0.86 mixture at 243 K for 400 combinations of ad-/desorption pressures. Squares, triangles, and downward-pointing triangles indicate MOFs collected from cluster I, cluster II, and cluster III, respectively, from the pre-selection stage. (a) En_{CO2}-Pu_{CO2} shown by Pareto fronts across operating pressures in each material. MOFs in group I are the ones that meet the Pu_{CO2} benchmark while those in group II do not. (b) ΔN_{CO2}-Pu_{CO2} shown with each data points calculated from all combinations of ad-/desorption pressures.

Figure 4.5 shows ΔN_{CO2}, Pu_{CO2}, and En_{CO2} for each of the 15 MOFs we considered further. It is important to note that the metrics from Table 4.1 cannot provide any information about the two latter quantities. These indicators were calculated with the idealized process model at 20 adsorption pressures equally spaced from 5.0 to 15.0 bar and 20 desorption pressures equally spaced from 0.15 to 0.35 bar. Figure 4.5a shows Pareto fronts of En_{CO2}-Pu_{CO2} across this range of operating conditions. As might be expected,

there is a trade-off between Pu_{CO2} and En_{CO2}. Figure 4.5b shows ΔN_{CO2} and Pu_{CO2} at each of the 400 process conditions we considered. The sensitivity of ΔN_{CO2}-Pu_{CO2} as a function of process pressures is heavily material dependent.

4.3.2 Adsorbent Evaluation by a Detailed Process Model

The steps above defined a shortlist of 15 MOFs with a spectrum of performance for sub-ambient CO_2 capture as predicted from a series of approximate models. We used rigorous multi-objective process optimization to develop processes based on each of these MOFs. This optimization allows each adsorbent to be coupled with process conditions that maximize their potential.[83]

Figure 4.6 shows the Pareto fronts for pairs of process-level objectives. Figure 4.6a shows minimization of En_{CO2} and maximization of Pu_{CO2}. En_{CO2} is a useful proxy for operating process cost.[84] This pair of objectives enables a direct comparison of the similarity of material evaluation made between the rigorous and idealized process model described in Section 4.3.1.2. Figures 4.6b and 4.6c show other common approaches to evaluating the capability of adsorbents and the viability of chosen adsorption system. Figure 4.6b assesses maximization of Pu_{CO2} and Re_{CO2}. We find the presence of MOFs in this sub-ambient system approaching 90% and 95% for both Pu_{CO2} and Re_{CO2}, respectively, a suggested target[82] for these objectives. Figure 4.6c assesses maximization of Pr_{CO2} and minimization of En_{CO2}. This is useful because it identifies process in which energy consumption is low while the maximum productivity for a given mass (or volume) of adsorbent can be reached. We find MOF candidates capable with Pr_{CO2} up to ~ 0.1 mol/kg·s with ~ 250 kWh/t of En_{CO2}.

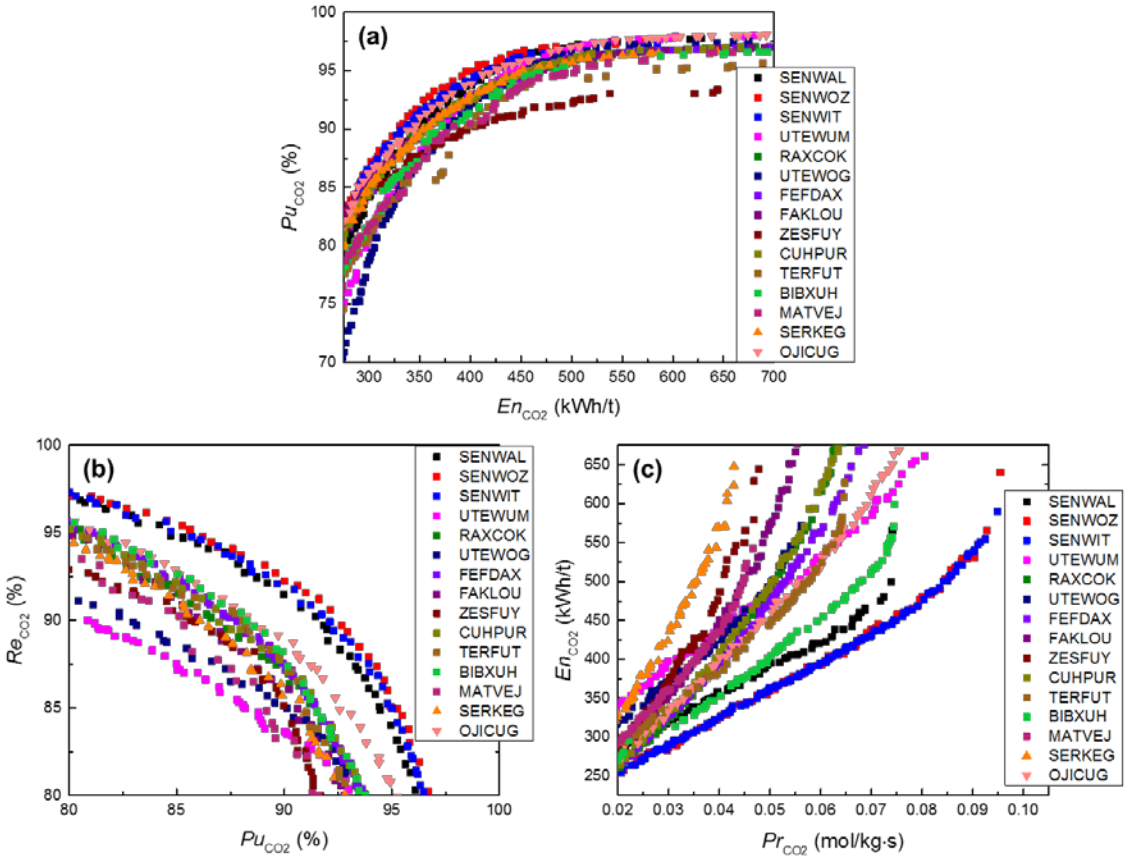

Figure 4.6. Multi-objective optimization for 15 MOFs in a sub-ambient PSA using a hollow fiber adsorbent module at 243 K. Pareto fronts are shown for optimized objectives of (a) En_{CO2} and Pu_{CO2}, (b) Pu_{CO2} and Re_{CO2}, and (c) Pr_{CO2} and En_{CO2}.

The results from Figure 4.6 allow us to revisit the evaluation of each MOF. When considering En_{CO2}-Pu_{CO2}, we ranked MOFs using Pu_{CO2} at a fixed En_{CO2} of 400 kWh/t. For Pu_{CO2}-Re_{CO2}, a ranking was made by the product of Pu_{CO2} and Re_{CO2}. For Pr_{CO2}-En_{CO2}, we ranked MOFs using Pr_{CO2} at a fixed En_{CO2} of 400 kWh/t. These three rankings are summarized in Table 4.3. We give three separate rankings to emphasize that focusing on different aspects of process performance favors different materials. For instance, a material that is a good candidate when the focus is on product purity may be less attractive when process economics are the dominant concern, and vice versa. The MOF with structure code SERKEG is an example; it is ranked in the top 5 materials when considering En_{CO2}-Pu_{CO2},

11 of 15 with respect to Pu_{CO2}-Re_{CO2}, and the last among the 15 materials with respect to Pr_{CO2}-En_{CO2}. Some materials, however, are ranked quite consistently in each list. The MOFs with structure codes SENWOZ and SENWIT, for example, are ranked 1 and 2 in every list, and SENWAL is ranked either third or fourth in each list.

Table 4.3. Three rankings of MOFs based on multi-objective process optimization. Definitions of each ranking are given in the text. MOFs whose ranking varies by five or more places among two rankings are shown in italic.

Ranking	**MOFs Ranked by**		
	(a) En_{CO2}-Pu_{CO2}	(b) Pu_{CO2}-Re_{CO2}	(c) Pr_{CO2}-En_{CO2}
1	SENWOZ	SENWOZ	SENWOZ
2	SENWIT	SENWIT	SENWIT
3	OJICUG	SENWAL	SENWAL
4	SENWAL	OJICUG	*BIBXUH*
5	*SERKEG*	*BIBXUH*	*TERFUT*
6	*FAKLOU*	*TERFUT*	FEFDAX
7	FEFDAX	FEFDAX	RAXCOK
8	RAXCOK	CUHPUR	OJICUG
9	CUHPUR	RAXCOK	CUHPUR
10	UTEWUM	ZESFUY	UTEWOG
11	UTEWOG	*SERKEG*	*FAKLOU*
12	*BIBXUH*	*FAKLOU*	MATVEJ
13	MATVEJ	MATVEJ	ZESFUY
14	*TERFUT*	UTEWOG	UTEWUM
15	ZESFUY	UTEWUM	*SERKEG*

4.3.3 Comparing Approximate and Detailed Models of Adsorption-based Carbon Capture Process

Having introduced the results from each level of modeling, we now turn to comparing results among these models. We first quantify the similarity of results between our rigorous process model and adsorbent evaluation metrics. We then conduct the same analysis comparing from rigorous and simplified process models.

4.3.3.1 Rigorous Process Model and Adsorbent Evaluation Metrics

For the group of 15 MOFs ranked by our rigorous process model (Table 4.3) we also developed rankings based on each simplified adsorbent ranking listed in Table 4.1. The latter rankings are listed in Table 4.A.4. Spearman's rank-order correlation was used to compare the results from these two very different levels of modeling. Spearman's rank-order correlation is a non-parametric measure of statistical dependence between the rankings of two variables that assesses how well the relationship between two variables can be described.[85,86] A rank order correlation of 1 indicates perfect correlation between two rankings, a value of 0 indicates no correlation between the two rankings, and a value of -1 occurs if two rankings are perfectly anti-correlated. Spearman's rank-order correlations between each process-level ranking and adsorbent evaluation metrics are shown in Figure 4.7. There is considerable variation between the various ranking methods. This is consistent with previous findings[30-33] that suggested caution must be used in using adsorbent evaluation metrics.

Rigorous Process Model	Adsorbent Evaluation Metrics				
	ΔN_{CO2}	$S_{ads,CO2/N2}^{ads}$	$S_{SP,CO2/N2}$	$APS_{CO2/N2}$	R
En_{CO2}-Pu_{CO2}	0.50	0.31	0.34	0.54	0.37
Pu_{CO2}-Re_{CO2}	0.46	-0.16	0.14	0.05	0.79
Pr_{CO2}-En_{CO2}	0.54	-0.19	0.03	0.11	0.69

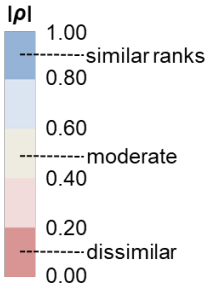

Figure 4.7. Spearman's rank-order correlation (ρ) between rankings of 15 MOFs from rigorous process modeling (vertical axis) and adsorbent evaluation metrics (horizontal axis). A general guideline for correlation strength and data interpretation associated with the color coding is provided in detail in Table 4.A.3 in Appendix 4.A.

Among the five adsorbent evaluation metrics, ΔN_{CO2} and R appear to be the most useful proxies for process scale performance in our particular process. ΔN_{CO2} showed a

comparable moderately similar rank correlation for each of the three process-level rankings. Regenerability, *R*, was the most successful adsorbent evaluation metric when process performance was characterized using purity and recovery or productivity and energy. *R* was only moderately successful, however, if the process-level ranking was made based on energy and purity. Other separation processes that are highly driven by product purity (e.g. direct air capture of CO_2) might results in different correlations. The other three adsorbent evaluation metrics performed quite poorly. It might be expected that $S_{SP,CO2/N2}$ and $APS_{CO2/N2}$ would be useful because they use a combination of inputs. We found, however, that these metrics were dominated by $S_{ads,CO2/N2}^{ads}$ for the CO_2 capture process we considered. As a result, the rank correlations of $S_{SP,CO2/N2}$, $APS_{CO2/N2}$ and $S_{ads,CO2/N2}^{ads}$ were quite similar.

As an aside, a possible reason that some metrics make poor predictions in terms of process-level ranking is that individual metrics only reflect specific features of the cyclic process.[15] To this end, we formulated a combined adsorbent evaluation metric (CAEM) that incorporates linear combinations of the adsorbent evaluation metrics to balance the contribution of each metric. We analyzed the rank correlations between each process-level ranking and the CAEM ranking. We found that the rank correlation can be improved by using CAEM in the absence of a winning single metric as for the case of En_{CO2}-Pu_{CO2}. On the other hand, the effect of CAEM on rank correlation was negligible when a single metric was already successful, as for the cases of Pu_{CO2}-Re_{CO2} and Pr_{CO2}-En_{CO2}. Details of this approach are provided in Section 4.A.6.

4.3.3.2 Rigorous and Idealized PSA Process Models

Following the above analysis, we also quantified the similarity in rankings of materials provided from the rigorous and idealized PSA process models. The rankings derived from the idealized PSA model are listed in Table 4.A.7. Unlike the situation for adsorbent evaluation metrics, the predicted process performance from each level of modeling can be compared. Because the idealized model only gives En_{CO2} and Pu_{CO2} but not Re_{CO2} or Pr_{CO2}, it is only possible to directly compare these predictions to the detailed process model for the information in Figure 4.6a.

Figure 4.8 compares the process objectives in terms of En_{CO2}-Pu_{CO2} from the rigorous and idealized process models. The full process optimization (Figure 4.6a) gives a narrower range of achievable Pu_{CO2} than the idealized PSA model results (Figure 4.5a). Since we are primarily interested in the relative performance of different materials, Figure 4.8 shows a normalized achievable Pu_{CO2} at a fixed En_{CO2} of 400 kWh/t for each level of modeling. The Spearman's rank-order correlation for these two levels of modeling was 0.54. When ranking MOFs with respect to En_{CO2}-Pu_{CO2} using the idealized and detailed process models, we compared Pu_{CO2} at a constraint of En_{CO2}. Because the Pareto fronts are not always on top of each other as a function of En_{CO2}, the MOF rankings can vary at different choice of En_{CO2}. We tested the sensitivity of Spearman's rank-order correlation to the choice of En_{CO2} as summarized in Table 4.A.8.

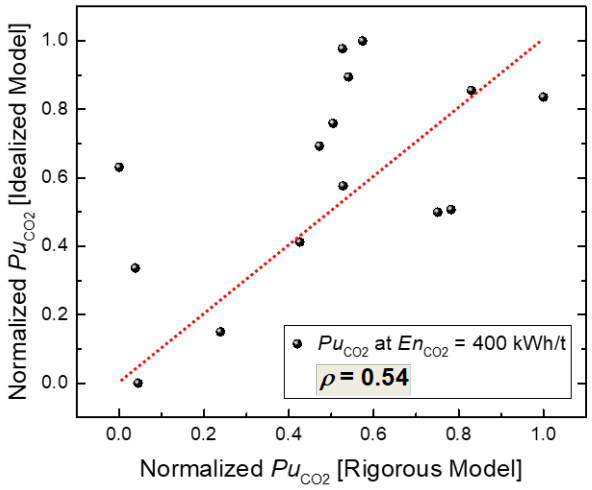

Figure 4.8. The normalized Pu_{CO2} at a fixed En_{CO2} using results from our rigorous process model (horizontal axis) and an idealized process model (vertical axis). Normalization was performed using the range of values from each data set. The red dashed line is a parity line.

It is also possible to compare the results of the adsorbent evaluation metrics with the idealized PSA process model. A comparison of MOF rankings from these approaches is shown in Figure 4.A.5 (Section 4.A.6 of Appendix 4.A). The metrics of adsorption selectivity, sorbent selection parameter, and the adsorbent performance score are strongly correlated with the predictions of the idealized PSA model. Somewhat surprisingly, these are not the same adsorbent evaluation metrics that were best correlated with the predictions from our rigorous process model. At one level, our data suggests that in terms of the ability to rank materials according to their performance as defined by the rigorous process model the idealized PSA model adds little to the information available from the simpler adsorbent evaluation metrics. This characterization is too simplistic, however, because the idealized model provides information that is not available from the simple metrics (see Figure 4.5) and the predictive power of the simple metrics is only available when the right metric among multiple possible choices is used.

4.4 CONCLUSIONS

In this chapter we have examined the value of using approximate models of a sub-ambient PSA process to evaluate a large number of candidate adsorbents for a CO_2 capture process. This chapter integrates molecular modeling, idealized process model and rigorous multi-objective process models to consider a spectrum of materials performance indicators. We examined MOF rankings derived from multiple modeling levels that allow quantitative measurements on the ranking similarity between approximate and detailed models.

We compared a group of MOFs ranked by rigorous process modeling and adsorbent evaluation metrics. Our findings showed CO_2 swing capacity and the regenerability of MOFs are successful proxies to predict process-level rankings, while other simple metrics were not strongly correlated with the detailed results. Our analysis only considered a specific separation process, a PSA process for CO_2 capture from dry flue gas at sub-ambient temperatures, so we cannot conclude that the same two adsorbent evaluation metrics will be the best suited to all possible chemical separations. Nevertheless, the observation that two of the metrics we tested performed far better than the others indicates that future efforts to use adsorbent evaluation metrics in screening libraries of materials should carefully consider which metric(s) are best suited for the process of interest. Our results are an example of the risks that exist if choices about materials selection are made by relying exclusively on a single metric.[87] Moreover, our models considered the performance of a separations process without regard for many of the practical issues that can limit scale up and implementation of new separations technologies.[88] The challenges that almost inevitably arise during this kind of process development mean that making well justified choices at the earliest stages of materials selection and process design are critical.

It is hoped that the multi-level modeling approach we have illustrated here can make these choices more reliable and efficient in similar efforts in the future.

4.5 REFERENCES

(1) Mikkelsen, M.; Jorgensen, M.; Krebs, F. C. The teraton challenge. A review of fixation and transformation of carbon dioxide. *Energy Environ. Sci.* **2010**, *3*, 43-81.

(2) Choi, S.; Drese, J. H.; Jones, C. W. Adsorbent Materials for Carbon Dioxide Capture from Large Anthropogenic Point Sources. *ChemSusChem* **2009**, *2*, 796-854.

(3) Sholl, D. S.; Lively, R. P. Seven Chemical Separations to Change the World, *Nature* **2016**, *532*, 435-437.

(4) Yang, R. T. *Gas Separation by Adsorption Processes*; Imperial College Press: London, 1987.

(5) Webley, P. A. Adsorption technology for CO_2 separation and capture: a perspective. *Adsorption* **2014**, *20*, 225-231.

(6) Hedin, N.; Andersson, L.; Bergstrom, L.; Yan, J. Adsorbents for the post-combustion capture of CO_2 using rapid temperature swing or vacuum swing adsorption. *Appl. Energ.* **2013**, *104*, 418-433.

(7) Bae, Y. S.; Snurr, R. Q. Development and Evaluation of Porous Materials for Carbon Dioxide Separation and Capture. *Angew. Chem. Int. Ed.* **2011**, *50*, 11586-11596.

(8) Ferey, G.; Mellot-Draznieks, C.; Serre, C.; Millange, F. Crystallized Frameworks with Giant Pores: Are There Limits to the Possible? *Acc. Chem. Res.* **2005**, *38*, 217-225.

(9) Meek, S. T.; Greathouse, J. A.; Allendorf, M. D. Metal-Organic Frameworks: A Rapidly Growing Class of Versatile Nanoporous Materials. *Adv. Mater.* **2011**, *23*, 249-267.

(10) Keskin, S.; van Heest, T. M.; Sholl, D. S. Can Metal-Organic Framework Materials Play a Useful Role in Large-Scale Carbon Dioxide Separations? *ChemSusChem* **2010**, *3*, 879-891.

(11) Park, J.; Howe, J. D.; Sholl, D. S. How Reproducible Are Isotherm Measurement in Metal-Organic Frameworks? *Chem. Mater.* **2017**, *29*, 10487-10495.

(12) Leperi, K. T.; Chung, Y. G.; You, F.; Snurr, R. Q. Development of a General Evaluation Metric for Rapid Screening of Adsorbent Materials for Postcombustion CO_2 Capture. *ACS Sustain. Chem. Eng.* **2019**, *7*, 11529-11539.

(13) Wilmer, C. E.; Farha, O. K.; Bae, Y. S.; Hupp, J. T.; Snurr, R. Q. Structure-property relationships of porous materials for carbon dioxide separation and capture. *Energy Environ. Sci.* **2012**, *5*, 9849-9856.

(14) Tong, M.; Lan, Y.; Yang, Q.; Zhong, C. High-throughput computational screening and design of nanoporous materials for methane storage and carbon dioxide capture. *Green Energy Environ.* **2018**, *3*, 107-119.

(15) Wiersum, A. D.; Chang, J. S.; Serre, C.; Llewellyn, P. L. An Adsorbent Performance Indicator as a First Step Evaluation of Novel Sorbents for Gas Separations: Application to Metal-Organic Frameworks. *Langmuir* **2013**, *29*, 3301-3309.

(16) Chung, Y. G.; Gomez-Gualdron, D. A.; Li, P.; Leperi, K. T.; Deria, P.; Zhang, H.; Vermeulen, N. A.; Stoddart, J. F.; You, F.; Hupp, J. T.; Farha, O. K.; Snurr, R. Q. *In silico* discovery of metal-organic frameworks for precombustion CO_2 capture using a genetic algorithm. *Sci. Adv.* **2016**, *2*, e1600909.

(17) Altintas, C.; Erucar, I.; Keskin, S. High-Throughput Computational Screening of the Metal Organic Framework Database for CH_4/H_2 Separations. *ACS Appl. Mater. Interfaces* **2018**, *10*, 3668-3679.

(18) Sumer, Z.; Keskin, S. Ranking of MOF Adsorbents for CO_2 Separations: A Molecular Simulation Study. *Ind. Eng. Chem. Res.* **2016**, *55*, 10404-10419.

(19) Altintas, C.; Avci, G.; Daglar, H.; Azar, A. N. V.; Velioglu, S.; Erucar, I.; Keskin, S. Database for CO_2 Separation Performances of MOFs Based on Computational Materials Screening. *ACS Appl. Mater. Interfaces* **2018**, *10*, 17257-17268.

(20) Braun, E.; Zurhelle, A. F.; Thijssen, W.; Schnell, S. K.; Lin, L. C.; Kim, J.; Thompson, J. A.; Smit, B. High-throughput computational screening of nanoporous adsorbents for CO_2 capture from natural gas. *Mol. Syst. Des. Eng.* **2016**, *1*, 175-188.

(21) Wu, D.; Yang, Q.; Zhong, C.; Liu, D.; Huang, H.; Zhang, W.; Maurin, G. Revealing the Structure-Property Relationships of Metal-Organic Frameworks for CO_2 Capture from Flue Gas. *Langmuir* **2012**, *28*, 12094-12099.

(22) Keskin, S.; Liu, J.; Rankin, R. B.; Johnson, J. K.; Sholl, D. S. Progress, Opportunities, and Challenges for Applying Atomically Detailed Modeling to Molecular Adsorption and Transport in Metal-Organic Framework Materials. *Ind. Eng. Chem. Res.* **2009**, *48*, 2355-2371.

(23) Watanabe, T.; Sholl, D. S. Accelerating Applications of Metal-Organic Frameworks for Gas Adsorption and Separation by Computational Screening of Materials. *Langmuir* **2012**, *28*, 14114-14128.

(24) Maring, B. J.; Webley, P. A. A new simplified pressure/vacuum swing adsorption model for rapid adsorbent screening for CO_2 capture applications. *Int. J. Greenhouse Gas Control* **2013**, *15*, 16-31.

(25) Khurana, M.; Farooq, S. Adsorbent Screening for Postcombustion CO_2 Capture: A Method Relating Equilibrium Isotherm Characteristics to an Optimum Vacuum Swing Adsorption Process Performance. *Ind. Eng. Chem. Res.* **2016**, *55*, 2447-2460.

(26) Balashankar, V. S.; Rajagopalan, A. K.; de Pauw, R.; Avila, A. M.; Rajendran, A. Analysis of a Batch Adsorber Analogue for Rapid Screening of Adsorbents for Postcombustion CO_2 Capture. *Ind. Eng. Chem. Res.* **2019**, *58*, 3314-3328.

(27) Ga, S.; Jang, H.; Lee, J. H. New performance indicators for adsorbent evaluation derived from a reduced order model of an idealized PSA process for CO_2 capture. *Comput. Chem. Eng.* **2017**, *102*, 188-212.

(28) Budhathoki, S.; Ajayi, O.; Steckel, J. A.; Wilmer, C. E. High-throughput computational prediction of the cost of carbon capture using mixed matrix membranes. *Energy Environ. Sci.* **2019**, *12*, 1255-1264.

(29) Bahamon, D.; Diaz-Marquez, A.; Gamallo, P.; Vega, L. F. Energetic evaluation of swing adsorption processes for CO_2 capture in selected MOFs and zeolites: Effect of impurities. *Chem. Eng. J.* **2018**, *342*, 458-473.

(30) Nalaparaju, A.; Khurana, M.; Farooq, S.; Karimi, I. A.; Jiang, J. W. CO_2 capture in cation-exchanged metal-organic frameworks: Holistic modeling from molecular simulation to process optimization. *Chem. Eng. Sci.* **2015**, *124*, 70-78.

(31) Faruque Hasan, M. M.; First, E. L.; Floudas, C. A. Cost-effective CO_2 capture based on *in silico* screening of zeolites and process optimization. *Phys. Chem. Chem. Phys.* **2013**, *15*, 17601-17618.

(32) Farmahini, A. H.; Krishnamurthy, S.; Friedrich, D.; Brandani, S.; Sarkisov, L. From Crystal to Adsorption Column: Challenges in Multiscale Computational Screening of Materials for Adsorption Separation Processes. *Ind. Eng. Chem. Res.* **2018**, *57*, 15491-15511.

(33) Rajagopalan, A. K.; Avila, A. M.; Rajendran, A. Do adsorbent screening metrics predict process performance? A process optimization based study for post-combustion capture of CO_2. *Int. J. Greenhouse Gas Control* **2016**, *46*, 76-85.

(34) Pullumbi, P.; Brandani, F.; Brandani, S. Gas separation by adsorption: technological drivers and opportunities for improvement. *Curr. Opin. Chem. Eng.* **2019**. *24*. 131-142.

(35) Hasse, D.; Kulkarni, S.; Sanders, E.; Corson, E.; Tranier, J. P. CO_2 capture by sub-ambient membrane operation. *Energy Procedia* **2013**, *37*, 993-1003.

(36) Hasse, D.; Ma, J.; Kulkarni, S.; Terrien, P.; Tranier, J. P.; Sanders, E.; Chaubey, T.; Brumback, J. CO_2 Capture by Cold Membrane Operation. *Energy Procedia* **2014**, *63*, 186-193.

(37) Liu, L.; Sanders, E. S.; Kulkarni, S. S.; Hasse, D. J.; Koros, W. J. Sub-ambient temperature flue gas carbon dioxide capture *via* Matrimid® hollow fiber membranes. *J. Membrane Sci.* **2014**, *465*, 49-55.

(38) Park, J.; Lively, R. P.; Sholl, D. S. Establishing upper bounds on CO_2 swing capacity in sub-ambient pressure swing adsorption *via* molecular simulation of metal-organic frameworks. *J. Mater. Chem. A* **2017**, *5*, 12258-12265.

(39) Agrawal, M.; Sholl, D. S. Effects of Intrinsic Flexibility on Adsorption Properties of Metal-Organic Frameworks at Dilute and Nondilute Loadings. *ACS Appl. Mater. Interfaces* **2019**, *11*, 31060-31068.

(40) Mason, J. A.; Sumida, K.; Herm, Z. R.; Krishna, R.; Long, J. R. Evaluating metal-organic frameworks for post-combustion carbon dioxide capture *via* temperature swing adsorption. *Energy Environ. Sci.* **2011**, *4*, 3030-3040.

(41) Chow, J. C.; Watson, J. G.; Herzog, A.; Benson, S. M.; Hidy, G. M.; Gunter, W. D.; Penkala, S. J.; White, C. M. Separation and Capture of CO_2 from Large Stationary Sources and Sequestration in Geological Formations. *J. Air Waste Manage.* **2003**, *53*, 1172-1182.

(42) Granite, E. J.; Pennline, H. W. Photochemical Removal of Mercury from Flue Gas. *Ind. Eng. Chem. Res.* **2002**, *41*, 5470-5476.

(43) Lee, K. B.; Sircar, S. Removal and recovery of compressed CO_2 from flue gas by a novel thermal swing chemisorption process. *AIChE J.* **2008**, *54*, 2293-2302.

(44) Sun, W.; Lin, L. C.; Peng, X.; Smit, B. Computational screening of porous metal-organic frameworks and zeolites for the removal of SO_2 and NO_x from flue gases. *AIChE J.* **2014**, *60*, 2314-2323.

(45) Burtch, N. C.; Jasuja, H.; Walton, K. S. Water Stability and Adsorption in Metal-Organic Frameworks. *Chem. Rev.* **2014**, *114*, 10575-10612.

(46) Tang, H.; Fang, H.; Duan, Y.; Sholl, D. S. Predictions of Hg^0 and $HgCl_2$ Adsorption Properties in UiO-66 from Flue Gas Using Molecular Simulations. *J. Phys. Chem. C* **2019**, *123*, 5972-2979.

(47) Hasse, D. J.; Kulkarni, S. S.; Sanders Jr., E. S.; Tranier, J. P.; Terrien, P. Method of Obtaining Carbon Dioxide From a Carbon Dioxide-Containing Gas Mixture. EP Patent 2,512,634. 2012.

(48) Garcia, E. J.; Perez-Pellitero, J.; Pirngruber, G. D.; Jallut, C.; Palomino, M.; Rey, F.; Valencia, S. Tuning the Adsorption Properties of Zeolites as Adsorbents for CO_2 Separation: Best Compromise between the Working Capacity and Selectivity. *Ind. Eng. Chem. Res.* **2014**, *53*, 9860-9874.

(49) Garcia, E. J.; Perez-Pellitero, J.; Pirngruber, G. D.; Jallut, C. Sketching a Portrait of the Optimal Adsorbent for CO_2 Separation by Pressure Swing Adsorption. *Ind. Eng. Chem. Res.* **2017**, *56*, 4818-4829.

(50) Anderson, R.; Rodgers, J.; Argueta, E.; Biong, A.; Gomez-Gualdron, D. A. Role of Pore Chemistry and Topology in the CO_2 Capture Capabilities of MOFs: From Molecular Simulation to Machine Learning. *Chem. Mater*. **2018**, *30*, 6325-6337.

(51) Chung, Y. G.; Camp, J.; Haranczyk, M.; Sikora, B. J.; Bury, W.; Krungleviciute, V.; Yildirim, T.; Farha, O. K.; Sholl, D. S.; Snurr, R. Q. Computation-Ready, Experimental Metal-Organic Frameworks: A Tool To Enable High-Throughput Screening of Nanoporous Crystals. *Chem. Mater.* **2014**, *26*, 6185-6192.

(52) Nazarian, D.; Camp, J. S.; Chung, Y. G.; Snurr, R. Q.; Sholl, D. S. Large-Scale Refinement of Metal-Organic Framework Structures Using Density Functional Theory. *Chem. Mater.* **2017**, *29*, 2521-2528.

(53) Nazarian, D.; Camp, J. S.; Sholl, D. S. A Comprehensive Set of High-Quality Point Charges for Simulations of Metal-Organic Frameworks. *Chem. Mater.* **2016**, *28*, 785-793.

(54) Rubiera Landa, H. O.; Flockerzi, D.; Seidel-Morgenstern, A. A method for efficiently solving the IAST equations with an application to adsorber dynamics. *AIChE J.* **2013**, *59*, 1263-1277.

(55) Walton, K. S.; Sholl, D. S. Predicting multicomponent adsorption: 50 years of the ideal adsorbed solution theory. *AIChE J.* **2015**, *61*, 2757-2762.

(56) Dickey, A. N.; Ozgur Yazaydin, A.; Willis, R. R.; Snurr, R. Q. Screening CO_2/N_2 selectivity in metal-organic frameworks using Monte Carlo simulations and ideal adsorbed solution theory. *Can. J. Chem. Eng.* **2012**, *90*, 825-832.

(57) Sircar, S. Pressure Swing Adsorption. *Ind. Eng. Chem. Res.* **2002**, *41*, 1389-1392.

(58) Haghpanah, R.; Majumder, A.; Nilam, R.; Rajendran, A.; Farooq, S.; Karimi, I. A.; Amanullah, M. Multiobjective Optimization of a Four-Step Adsorption Process for Postcombustion CO_2 Capture *via* Finite Volume Simulation. *Ind. Eng. Chem. Res.* **2013**, *52*, 4249-4265.

(59) Ebner, A. D.; Ritter, J. A. State-of-the-art Adsorption and Membrane Separation Processes for Carbon Dioxide Production from Carbon Dioxide Emitting Industries. *Sep. Sci. Technol.* **2009**, *44*, 1273-1421.

(60) Haghpanah, R.; Nilam, R.; Rajendran, A.; Farooq, S.; Karimi, I. A. Cycle synthesis and optimization of a VSA process for postcombustion CO_2 capture. *AIChE J.* **2013**, *59*, 4735-4748.

(61) Wang, L.; Yang, Y.; Shen, W.; Kong, X.; Li, P.; Yu, J.; Rodrigues, A. E. CO_2 Capture from Flue Gas in an Existing Coal-Fired Power Plant by Two Successive Pilot-Scale VPSA Units. *Ind. Eng. Chem. Res.* **2013**, *52*, 7947-7955.

(62) Sircar, S.; Hufton, J. R. Why Does the Linear Driving Force Model for Adsorption Kinetics Work? *Adsorption* **2000**, *6*, 137-147.

(63) Schiesser, W. E. *The Numerical Method of Lines: Integration of Partial Differential Equations*; Academic Press: San Diego, 1991.

(64) Vreugdenhil, C. B.; Koren, B. *Numerical Methods for Advection-Diffusion Problems: Notes on Numerical Fluid Mechanics*; Vieweg: Berlin, 1993.

(65) Rezaei, F.; Subramanian, S.; Kalyanaraman, J.; Lively, R. P.; Kawajiri, Y.; Realff, M. J. Modeling of rapid temperature swing adsorption using hollow fiber sorbents. *Chem. Eng. Sci.* **2014**, *113*, 62-76.

(66) Kalyanaraman, J.; Fan, Y.; Lively, R. P.; Koros, W. J.; Jones, C. W.; Realff, M. J.; Kawajiri, Y. Modeling and experimental validation of carbon dioxide sorption on hollow fibers loaded with silica-supported poly(ethylenimine). *Chem. Eng. J.* **2015**, *259*, 737-751.

(67) Fan, Y.; Kalyanaraman, J.; Labreche, Y.; Rezaei, F.; Lively, R. P.; Realff, M. J.; Koros, W. J.; Jones, C. W.; Kawajiri, Y. CO_2 Sorption Performance of Composite Polymer/Aminosilica Hollow Fiber Sorbents: An Experimental and Modeling Study. *Ind. Eng. Chem. Res.* **2015**, *54*, 1783-1795.

(68) Lively, R. P.; Chance, R. R.; Kelley, B. T.; Deckman, H. W.; Drese, J. H.; Jones, C. W.; Koros, W. J. Hollow Fiber Adsorbents for CO_2 Removal from Flue Gas. *Ind. Eng. Chem. Res.* **2009**, *48*, 7314-7324.

(69) Lively, R. P.; Chance, R. R.; Mysona, J. A.; Babu, V. P.; Deckman, H. W.; Leta, D. P.; Thomann, H.; Koros, W. J. CO_2 sorption and desorption performance of thermally cycled hollow fiber sorbents. *Int. J. Greenhouse Gas Control* **2012**, *10*, 285-294.

(70) Lively, R. P.; Bessho, N.; Bhandari, D. A.; Kawajiri, Y.; Koros, W. J. Thermally moderated hollow fiber sorbent modules in rapidly cycled pressure swing adsorption mode for hydrogen purification. *Int. J. Hydrog. Energy* **2012**, *37*, 15227-15240.

(71) DeWitt, S. J. A.; Sinha A.; Kalyanaraman, J.; Zhang, F.; Realff, M. J.; Lively, R. P. Critical Comparison of Structured Contactors for Adsorption-Based Gas Separations. *Annu. Rev. Chem. Biomol. Eng.* **2018**, *9*, 129-152.

(72) Pimentel, B. R.; Fultz, A. W.; Presnell, K. V.; Lively, R. P. Synthesis of Water-Sensitive Metal-Organic Frameworks within Fiber Sorbent Modules. *Ind. Eng. Chem. Res.* **2017**, *56*, 5070-5077.

(73) Sujan, A. R.; Koh, D. Y.; Zhu, G.; Babu, V. P.; Stephenson, N.; Rosinski, A.; Du, H.; Luo, Y.; Koros, W. J.; Lively, R. P. High-Temperature Activation of Zeolite-Loaded Fiber Sorbents. *Ind. Eng. Chem. Res.* **2018**, *57*, 11757-11766.

(74) DeWitt, S. J. A.; Rubiera Landa, H. O.; Kawajiri, Y.; Realff, M.; Lively, R. P. Development of Phase-Change-Based Thermally Modulated Fiber Sorbents. *Ind. Eng. Chem. Res.* **2019**, *58*, 5768-5776.

(75) Deb, K.; Pratap, A.; Agarwal, S.; Meyarivan, T. A Fast and Elitist Multiobjective Genetic Algorithm: NSGA-II. *IEEE Trans. Evol. Comput.* **2002**, *6*, 182-197.

(76) Fang, H.; Kulkarni, A.; Kamakoti, P.; Awati, R.; Ravikovitch, P. I.; Sholl, D. S. Identification of High-CO_2-Capacity Cationic Zeolites by Accurate Computational Screening. *Chem. Mater.* **2016**, *28*, 3887-3896.

(77) McDonald, T. M.; Mason, J. A.; Kong, X.; Bloch, E. D.; Gygi, D.; Dani, A.; Crocella, V.; Giordanino, F.; Odoh, S. O.; Drisdell, W. S.; Vlaisavljevich, B.; Dzubak, A. L.; Poloni, R.; Schnell, S. K.; Planas, N.; Lee, K.; Pascal, T.; Wan, L. F.; Prendergast, D.; Neaton, J. B.; Smit, B.; Kortright, J. B.; Gagliardi, L.; Bordiga, S.; Reimer, J. A.; Long, J. R. Cooperative insertion of CO_2 in diamine-appended metal-organic frameworks. *Nature* **2015**, *519*, 303-308.

(78) Tang, D.; Wu, Y.; Verploegh, R. J.; Sholl, D. S. Efficiently Exploring Adsorption Space to Identify Privileged Adsorbents for Chemical Separations of a Diverse Set of Molecules. *ChemSusChem* **2018**, *11*, 1567-1575.

(79) Kulkarni, A. R.; Sholl, D. S. Screening of Copper Open Metal Site MOFs for Olefin/Paraffin Separations Using DFT-Derived Force Fields. *J. Phys. Chem. C* **2016**, *120*, 23044-23054.

(80) Dzubak, A. L.; Lin, L. C.; Kim, J.; Swisher, J. A.; Poloni, R.; Maximoff, S. N.; Smit, B.; Gagliardi, L. *Ab initio* carbon capture in open-site metal-organic frameworks. *Nat. Chem.* **2012**, *4*, 810-816.

(81) Poloni, R.; Lee, K.; Berger, R. F.; Smit, B.; Neaton, J. B. Understanding Trends in CO_2 Adsorption in Metal-Organic Frameworks with Open-Metal Sites. *J. Phys. Chem. Lett.* **2014**, *5*, 861-865.

(82) Woods, M.; Matuszewski, M.; Summers, W. Quality Guidelines for Energy System Studies: CO_2 Impurity Design Parameters. Tech. Rep. DOE/NETL-341/011212, US Department of Energy. 2012.

(83) Agarwal, A.; Biegler, L. T.; Zitney, S. E. A superstructure-based optimal synthesis of PSA cycles for post-combustion CO_2 capture. *AIChE J.* **2010**, *56*, 1813-1828.

(84) Susarla, N.; Haghpanah, R.; Karimi, I. A.; Farooq, S.; Rajendran, A.; Tan, L. S. C.; Lim, J. S. T. Energy and cost estimates for capturing CO_2 from a dry flue gas using pressure/vacuum swing adsorption. *Chem. Eng. Res. Des.* **2015**, *102*, 354-367.

(85) Piantadosi, J.; Howlett, P.; Boland, J. Matching the grade correlation coefficient using a copula with maximum disorder. *J. Ind. Manag. Optim.* **2007**, *3*, 305-312.

(86) Fieller, E. C.; Hartley, H. O.; Pearson, E. S. Tests for Rank Correlation Coefficients. I. *Biometrika* **1957**, *44*, 470-481.

(87) Realff, M. J. The logic of efficiency and other metrics. *J. Adv. Manuf. Process.* **2019**, *1*, e10022.

(88) Walton, K. S.; Sholl, D. S. Research Challenges in Avoiding ″Showstoppers″ in Developing Materials for Large-Scale Energy Applications. *Joule* **2017**, *1*, 208-211.

APPENDIX 4.A. SUPPORTING INFORMATION – CHAPTER 4

4.A.1 Molecular Modeling Details

Molecular modeling of adsorption of a bulk CO_2/N_2 0.14/0.86 mixture and single component CO_2 and N_2 adsorption were conducted by Grand Canonical Monte Carlo (GCMC) simulations[1,2-5] using the RASPA software[4,5]. To perform GCMC appropriate force fields are needed to describe non-bonding interactions such as van der Waals and electrostatic interactions for adsorbate/adsorbent and adsorbate/adsorbate interactions.[6] Classical force fields were used to compute van der Waals interaction, namely the universal force field (UFF)[7] and the TraPPE[8] force field. Lennard-Jones parameters for MOF atoms and quadrupolar CO_2, N_2 molecules were taken from UFF and TraPPE force field, respectively. Adsorbate/adsorbent interactions were defined with Lorentz-Berthelot mixing rule.[9] Truncated potentials with tail corrections are applied where Lennard-Jones interactions are truncated at 12 Å. Simulation boxes are expanded to at least 26 Å along *x*, *y*, and *z* dimensions. Periodic boundary conditions were defined in all dimensions, and adsorbents and adsorbates were approximated as rigid. Electrostatic interactions were modeled pairwise with a long-range Ewald summation scheme.[10] These interactions are computed via the density derived electrostatic and chemical (DDEC) point charges for MOF atoms[11-13] and TraPPE charges for CO_2 and N_2 molecules[4,5]. The DDEC method assigns high-quality electrostatic point charges on framework atoms which is based on the electron density partitioning in periodic structures.[11-13] GCMC simulations included 5,000 initialization cycles followed by 50,000 production cycles for which initial tests indicated good convergence. Attempted Monte Carlo moves include translation, rotation, regrowth,

reinsertion, deletion and insertion of adsorbates with identical probabilities. For mixture GCMC, a Monte Carlo move that swapped the identity of existing molecules of which takes account for the competitive adsorption of each species was imposed in addition to above random moves.

Pore volumes of computation-ready MOF structures were calculated from the void fractions of each structure using a Widom particle insertion method with a He probe molecule (ε/k_B = 10.9 K, σ = 2.64 Å) at 298 K.[5] Pore limiting diameters (PLD) were calculated with Zeo++[14,15] applying the high-accuracy setting with a N_2 probe molecule using a radius of 1.86 Å.[14] Isosteric heats of adsorption at zero loading (Q_{ads}^0) for CO_2 and N_2 were computed in the canonical ensemble.[16,17] Monte Carlo moves in this simulation allowed translation, rotation, regrowth, and reinsertion moves of each CO_2 and N_2 at the identical probabilities.

4.A.2 MOF Material Set

Figure 4.A.1a illustrates the origin of 143 MOF structures from the energy optimized CoRE MOF DDEC charge database.[18-20] Such a database enables high-throughput computational screening of MOFs for modeling of gas adsorption and diffusion in those materials.[18] DFT optimization and assignment of atomic point charges for computation-ready structures allow reliable adsorption modeling.[19,20] In our earlier work of Chapter 3, PSA CO_2 swing capacities were calculated for 477 structures of the energy optimized CoRE MOF DDEC charge database at sub-ambient temperatures. 143 of these structures had single component CO_2 swing capacities from ~ 4 mol/kg to ~ 23 mol/kg at 243 K over

a pressure range from 0.1 bar to 2.0 bar.[21] A list of 143 MOFs and swing capacities estimated from single component adsorption data are tabulated in Section 4.A.7.

Competitive adsorption during treatment of multicomponent gas mixtures almost always reduce capacities relative to single component adsorption.[22,23] Figure 4.A.1b compares swing capacities of 143 MOFs that are calculated for the difference between capacities of CO_2 at adsorption pressure ($P_{CO2,ads}$ = 2.0 bar) and desorption pressure ($P_{CO2,des}$ = 0.1 bar) from single component adsorption in our earlier study (Chapter 3)[21] and from CO_2/N_2 bulk mixture adsorption in this chapter. The results show that swing capacity is reduced by mixture adsorption, although this is not a dramatic effect at the pressures and temperatures we considered.

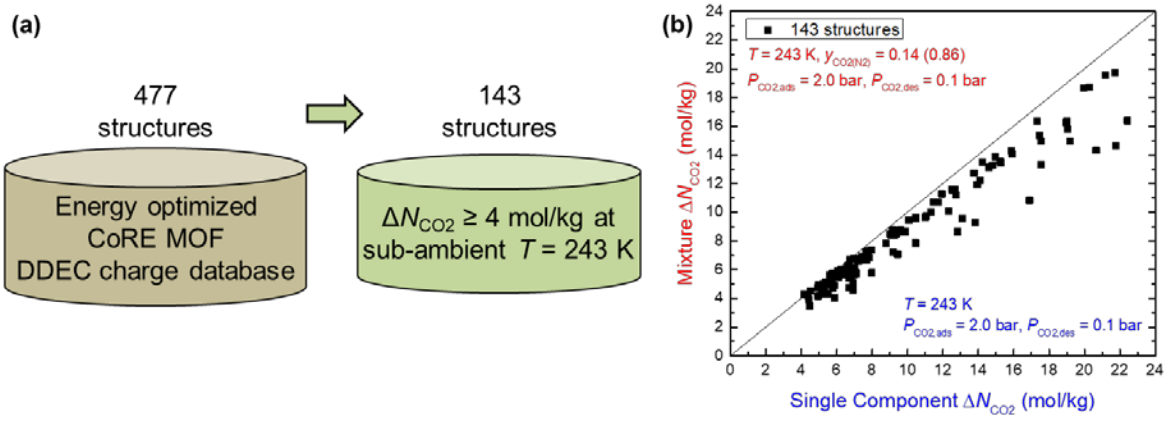

Figure 4.A.1. (a) Schematic illustration of the origin of a MOF material set used in this chapter. (b) Comparison of CO_2 swing capacities in 143 structures computed by single component adsorption data (horizontal axis) and by CO_2/N_2 0.14/0.86 bulk mixture adsorption data (vertical axis) at 243 K over adsorption pressure ($P_{CO2,ads}$ = 2.0 bar) and desorption pressure ($P_{CO2,des}$ = 0.1 bar).

4.A.3 Structure-Property Relationships for Adsorbent Evaluation Metrics

Revealing the structure-property relationships between physical properties of adsorbent materials and their gas capture performances in various separation systems helps in selecting adsorbents.[23-26] We examined such relationships with respect to swing capacity and adsorption selectivity for CO_2 from a CO_2/N_2 0.14/0.86 bulk mixture adsorption data in 143 MOFs at a sub-ambient PSA process. The adsorbent evaluation metrics are tabulated in Section 4.A.7. The chosen physical properties include geometric features of MOFs, i.e. pore volume and pore size (adopted from the original CoRE MOF database resource[18]), and an energetic feature of MOFs, i.e. the difference of heats of adsorption at zero loading for CO_2 and N_2, $\Delta Q_{ads}^0 = Q_{ads,CO2}^0 - Q_{ads,N2}^0$ (data not tabulated).

Figure 4.A.2a shows the structure-property relationship for swing capacity as a function of MOF properties. Like the observation for CO_2 swing capacity calculated from single component adsorption data in our previous study, large pore volume (V_P) and pore limiting diameter (PLD) along with the difference in heats of adsorption at zero loading for competing species (ΔQ_{ads}^0) within a narrow range enable high swing capacity.[21,23]

Figure 4.A.2b shows the structure-property relationship for adsorption selectivity as a function of MOF properties. Unlike the swing capacity, smaller V_P and narrower PLD along with optimal range of ΔQ_{ads}^0 are correlated with large adsorption selectivity, i.e. x_{CO2} over 0.9.[25,26] The optimal ranges of the ΔQ_{ads}^0 leading to large swing capacity and adsorption selectivity were observed for similar values. The desirable features of V_P and PLD, however, were different between swing capacity and adsorption selectivity. This

illustrates a trade-off relationship that generally exist between swing capacity and adsorption selectivity.[27]

We have identified the desirable V_P, PLD, and ΔQ_{ads}^0 for 28 MOFs that were classified as the cluster I in Chapter 4, i.e. the "best" adsorbents at the stage of using adsorbent evaluation metrics. These 28 MOFs (shown in red symbols in Figures 4.A.2a and 4.A.2b) have $0.7 \leq V_P \leq 1.15$ cm^3/g, $5 \leq$ PLD ≤ 10 Å, and $7.5 \leq \Delta Q_{ads}^0 \leq 15$ kJ/mol.

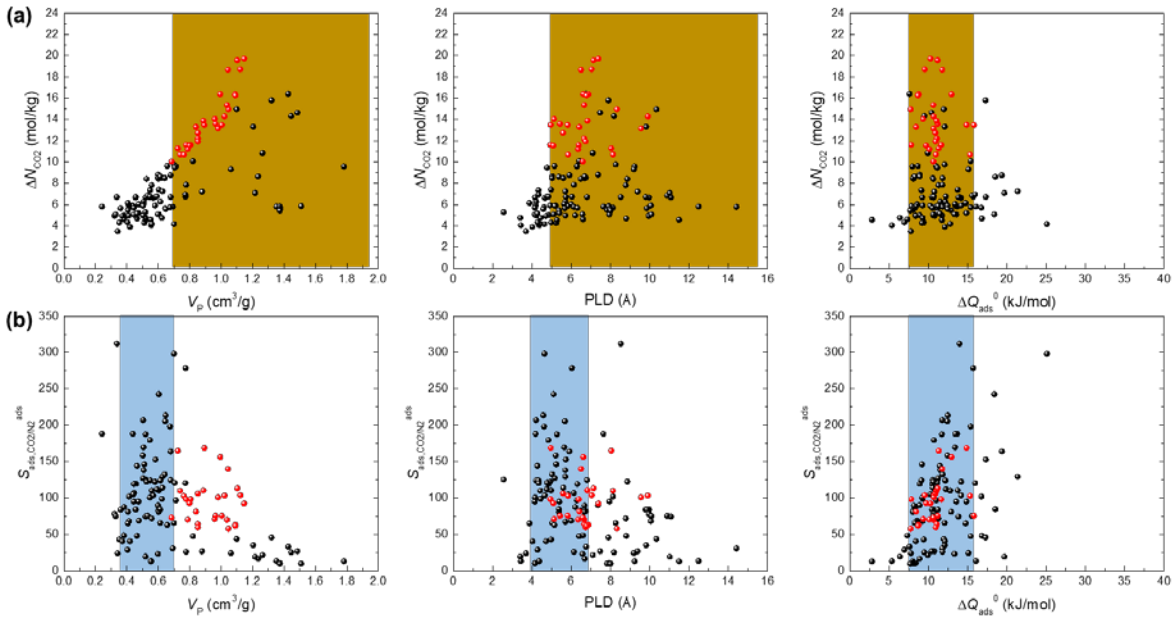

Figure 4.A.2. (a) CO_2 swing capacities of 143 MOFs at 243 K as a function of pore volume (V_P), pore limiting diameter (PLD), and the difference of heats of adsorption at zero loading for CO_2 and N_2 (ΔQ_{ads}^0). (b) Adsorption selectivities for CO_2 in 143 MOFs at bulk adsorption pressure and at 243 K as a function of V_P, PLD, and ΔQ_{ads}^0. Each box in (a) and (b) show desirable ranges of V_P, PLD, and of ΔQ_{ads}^0. Data in red symbols in (a) and (b) refer to 28 MOFs in cluster I which is defined in Chapter 4.

4.A.4 Idealized PSA Model Details and IAST Implementation

We adapted an idealized PSA process model from the prior work of Ga et al.[28] Details of the performance indicators derived from this model and settings used in the model are

provided. In addition, the details of ideal adsorbed solution theory (IAST) that we used for prediction of mixture adsorption equilibrium in a series of process modeling are described.

4.A.4.1 Idealized PSA Model Details

The idealized PSA model calculates two performance indicators: product purity (Pu_{CO2}, written as y^{E}_{CO2} here) and energy efficiency indicator (η_{VPSA}). The specific energy consumption we used in this chapter (En_{CO2}) is the reciprocal of the energy efficiency indicator. These quantities are derived in the form of explicit formulas as below. Swing capacities for each species can also be obtained separately which are the components in calculating product purity (ΔN_i, written as Δq_i here).

Product purity	$y^{E}_{CO_2} = \dfrac{\Delta q_{CO_2}}{\Delta q_{N_2} + \Delta q_{CO_2}}$. with $\Delta q_i = q_i^{I} - q_i^{II}, \quad i = 1, 2.$ where $q_i^{I} = f\left(p_{high}, T, y_{N_2,fg}, y_{CO_2,fg}\right)$. $q_i^{II} = f\left(p_{Ev}, T, y^{E}_{N_2}, y^{E}_{CO_2}\right)$. $y^{E}_{N_2} + y^{E}_{CO_2} = 1.$
Energy efficiency indicator	$\eta_{VPSA} = \dfrac{(\gamma - 1) y_{CO_2,fg}}{\gamma \Re T \left[\dfrac{1}{\eta_{compr.}} \left[\left(\dfrac{p_{high}}{p_{fg}} \right)^{\frac{\gamma-1}{\gamma}} - 1 \right] + \dfrac{y_{CO_2,fg}}{y^{E}_{CO_2}} \dfrac{1}{\eta_{vac.}} \left[\left(\dfrac{p_{ej.,out}}{p_{Ev}} \right)^{\frac{\gamma-1}{\gamma}} - 1 \right] \right]}$.

The idealized PSA model considers a two-step cycle process that occurs isothermally. In the adsorption step, the model assumes the adsorbent is saturated when exposed to flue gas of known composition (y_i) at a specified high-pressure level and temperature, thus establishing equilibrium at these operating conditions. In the desorption step, the model assumes equilibrium at the evacuation conditions, thus the adsorption loadings under these conditions can be described in terms of the unknown purity of the gas product. The latter calculation is then combined with a separate mass balance that expresses the gas product composition in terms of the differences between the adsorption loadings at

equilibrium. The gas product compositions correspond to the molar amounts of the components left in the bulk gas phase of the extract product stream. Figure 4.1 in Chapter 4 shows a schematic illustration of the model.

The derivations above yield a non-linear algebraic equation in terms of the unknown purity of the extract product, y^{E}_{CO2}. The adsorption loadings are calculated by IAST. We solve this task numerically by applying the function *fsolve* in MATLAB, with default settings and tolerances. The *optimset* module was used as an optimization option to solve the equations. Energy efficiency indicator, η_{VPSA}, can be calculated directly once y^{E}_{CO2} is obtained. The required energies in each of the operating steps are described by the isentropic work of compression and evacuation. The efficiency of the compressor (η_{compr}) and vacuum (η_{vac}) were set for 75% and 30%, respectively. The feed pressure (P_{fg}) and ejection pressure (P_{ej}) were set at 1.0 bar.

Performance indicators above were calculated for 30 MOFs that were selected on the basis of adsorbent evaluation metrics (Figure 4.A.3). We apply the idealized PSA process model, along with examining the physical properties of MOFs, to select a small number of MOFs as possible to impose the rigorous PSA process optimization.

We first chose non-open-metal site (OMS) MOFs to avoid the limited accuracy in molecular modeling of OMS MOFs, and possible uncertainty propagation in further process modeling. These OMS MOFs are discarded regardless of the results of performance indicators of the idealized model. The final selection of MOFs relied on Pu_{CO2} predicted by the idealized PSA process model. All MOFs of $Pu_{CO2} \geq 90\%$ were selected (MOFs in group I among cluster I). Among eight MOFs that belonged to cluster I but did

not exceed this standard, three MOFs were randomly chosen (MOFs in group II among cluster I). MOFs from clusters II and III are kept irrelevant to Pu_{CO2} predicted by the idealized model. The entire procedure is described in Table 4.A.1 with lists of MOFs in each category.

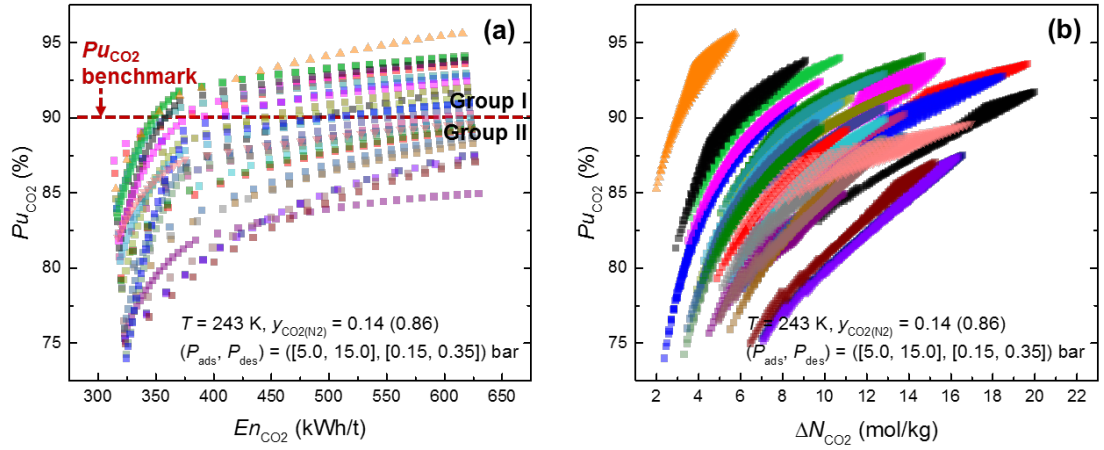

Figure 4.A.3. Performance indicators derived from the idealized PSA process model for 30 MOFs. The indicators were calculated for a CO_2/N_2 0.14/0.86 mixture at 243 K at 400 combinations of ad-/desorption pressures. Square, triangle, and downward-pointing triangle symbols stand for MOFs collected from clusters I, II, and III, respectively, from the pre-selection stage. (a) En_{CO2}-Pu_{CO2} shown by Pareto fronts across operating pressures in each material. (b) ΔN_{CO2}-Pu_{CO2} shown with data from all combinations of ad-/desorption pressures.

Table 4.A.1. Material selection at the idealized PSA process modeling stage. MOFs are listed with CSD reference codes reported in the CoRE MOF database with a number of MOFs in each category in brackets. 15 MOFs that were selected to conduct rigorous process modeling are shown in bold.

MOFs from Section 4.3.1.1.	**Non-open-metal site MOFs**	**MOFs from Section 4.3.1.2.**
Cluster I	Cluster I	Cluster I
BIBXUH, **CUHPUR**, **FAKLOU**, FEFCUQ, **FEFDAX**, FIQCEN, KEFBEE, LASYOU, **MATVEJ**, MOCKEV, NUTQAV, NUTQEZ, QUQFIS, **RAXCOK**, RIFDUG01, **SENWAL**, **SENWIT**, **SENWOZ**, **TERFUT**, UBUMAH, **UTEWOG**, **UTEWUM**, XAMDUM07, XINFUW, XUGSEY, YUGLES, **ZESFUY**, ZIKJIO (# = 28)	**BIBXUH**, **CUHPUR**, **FAKLOU**, FEFCUQ, **FEFDAX**, **MATVEJ**, QUQFIS, **RAXCOK**, **SENWAL**, **SENWIT**, **SENWOZ**, **TERFUT**, UBUMAH, **UTEWOG**, **UTEWUM**, XINFUW, XUGSEY, **ZESFUY** (# = 18)	Group I ($Pu_{CO2} \geq 90\%$) **CUHPUR**, **FAKLOU**, **FEFDAX**, **RAXCOK**, **SENWAL**, **SENWIT**, **SENWOZ**, **UTEWOG**, **UTEWUM**, **ZESFUY** (# = 10) Group II ($Pu_{CO2} < 90\%$) **BIBXUH**, **MATVEJ**, **TERFUT** (# = 3)
Cluster II	Cluster II	Cluster II
SERKEG (# = 1)	**SERKEG** (# = 1)	**SERKEG** (# = 1)
Cluster III	Cluster III	Cluster III
OJICUG (# = 1)	**OJICUG** (# = 1)	**OJICUG** (# = 1)

* Note OJICUG resulted in $Pu_{CO2} < 90\%$ from prediction of the idealized PSA process model.

4.A.4.2 IAST Implementation

In our idealized and rigorous process models IAST was used to define mixture adsorption equilibrium.[29-32] The constitutive equations[29] for IAST are listed below.

Descriptions	**Equations**
Raoult's law	$c_i = c_{\text{tot}}\, y_i = c_i^0(T,\pi)\, x_i$
Equilibrium condition	$\Pi \equiv \Pi_1 \stackrel{!}{=} \cdots \stackrel{!}{=} \Pi_N$
Spreading pressure	$\Pi_i = f(c_i^0) \equiv \frac{\mathcal{A}}{\Re\, T}\pi_i(c_i^0) = \int_0^{c_i^0} \frac{q_i^0}{s}\, \mathrm{d}s$
Closure	$\sum_{i=1}^{N} x_i = \sum_{i=1}^{N} \frac{c_i}{c_i^0} = 1$
Total adsorbed phase concentration	$q_{\text{tot}} = \left[\sum_{i=1}^{N} \frac{x_i}{q_i^0}\right]^{-1} = \left[\sum_{i=1}^{N} \frac{1}{q_i^0}\, \frac{c_i}{c_i^0}\right]^{-1}$
Adsorbed phase concentration for component i	$q_i = q_{\text{tot}}\, x_i, \quad i = 1, \ldots, N$

Accurate characterization of single component adsorption isotherms, i.e. fitting the single component adsorption data to an analytical adsorption model that can best describe the adsorption behavior, is necessary for reliable mixture adsorption prediction via IAST.[29-32] Using the chosen isotherm equation and corresponding parameters enables an analytical formulation of the spreading pressure which is a key component for IAST calculations.[29,30]

Single component adsorption isotherms for CO_2 and N_2 were estimated by molecular simulations (see Section 4.A.1). The process models require temperature-dependent adsorption equilibrium. Therefore we estimated adsorption equilibrium of both CO_2 and N_2 at temperatures of 213, 228, 243, 258, and 273 K. We provide the analytical adsorption models used in this chapter and a summary of isotherm equations applied for 15 chosen MOFs below. Note that fitting for CO_2 adsorption is much more complicated than that for N_2 adsorption at low temperatures. This is highly related with the accuracy

and robustness in rigorous process modeling. Due to this reason, we revisit the parameter estimation for CO_2 isotherms in chosen MOFs we proceed with the rigorous process modeling (see Section 4.A.4.2.1).

Analytical Models	Model Equations and Parameters
Dual-site Langmuir (dsL)	$q_i^0 = q_{i1}^{sat}\frac{b_{i1}c_i^0}{1+b_{i1}c_i^0} + q_{i2}^{sat}\frac{b_{i2}c_i^0}{1+b_{i2}c_i^0}, \quad i = 1, \ldots, N.$
	$b_{i1} = b_{i10}\exp\left[\frac{B_{i1}}{T}\right], \quad b_{i2} = b_{i20}\exp\left[\frac{B_{i2}}{T}\right],$
dual-site Langmuir-Freundlich (dsLF)	$q_i^0 = q_{i1}^{sat}\frac{b_{i1}c_i^{0\vartheta_{i1}}}{1+b_{i1}c_i^{0\vartheta_{i1}}} + q_{i2}^{sat}\frac{b_{i2}c_i^{0\vartheta_{i2}}}{1+b_{i2}c_i^{0\vartheta_{i2}}} + q_{i3}^{sat}\frac{b_{i3}c_i^{0\vartheta_{i3}}}{1+b_{i3}c_i^{0\vartheta_{i3}}}, \quad i = 1, \ldots, N.$
	$b_{i1} = b_{i10}\exp\left[\frac{B_{i1}}{T}\right], \quad b_{i2} = b_{i20}\exp\left[\frac{B_{i2}}{T}\right],$ $\vartheta_{i1} = \theta_{i10}\exp\left[\frac{\Theta_{i1}}{T}\right], \quad \vartheta_{i2} = \theta_{i20}\exp\left[\frac{\Theta_{i2}}{T}\right],$
triple-site Langmuir-Freundlich (tsLF)	$q_i^0 = q_{i1}^{sat}\frac{b_{i1}c_i^{0\vartheta_{i1}}}{1+b_{i1}c_i^{0\vartheta_{i1}}} + q_{i2}^{sat}\frac{b_{i2}c_i^{0\vartheta_{i2}}}{1+b_{i2}c_i^{0\vartheta_{i2}}} + q_{i3}^{sat}\frac{b_{i3}c_i^{0\vartheta_{i3}}}{1+b_{i3}c_i^{0\vartheta_{i3}}}, \quad i = 1, \ldots, N.$
	$b_{i1} = b_{i10}\exp\left[\frac{B_{i1}}{T}\right], \quad b_{i2} = b_{i20}\exp\left[\frac{B_{i2}}{T}\right], \quad b_{i3} = b_{i30}\exp\left[\frac{B_{i3}}{T}\right],$ $\vartheta_{i1} = \theta_{i10}\exp\left[\frac{\Theta_{i1}}{T}\right], \quad \vartheta_{i2} = \theta_{i20}\exp\left[\frac{\Theta_{i2}}{T}\right], \quad \vartheta_{i3} = \theta_{i30}\exp\left[\frac{\Theta_{i3}}{T}\right],$
quadratic plus Langmuir (quadL)	$q_i^0 = q_{i1}^{sat}\frac{c_i^0[b_{i1}+2b_{i2}c_i^0]}{1+b_{i1}c_i^0+b_{i2}c_i^{0^2}} + q_{i2}^{sat}\frac{b_{i3}c_i^0}{1+b_{i3}c_i^0}, \quad i = 1, \ldots, N.$
	$b_{i1} = b_{i10}\exp\left[\frac{B_{i1}}{T}\right], \quad b_{i2} = b_{i20}\exp\left[\frac{B_{i2}}{T}\right], \quad b_{i3} = b_{i30}\exp\left[\frac{B_{i3}}{T}\right],$

Summary of Isotherm Equations							
MOFs	**CO_2**	**N_2**	**CO_2 (*)**	**MOFs**	**CO_2**	**N_2**	**CO_2 (*)**
SENWAL	dsLF	dsL	tsLF	ZESFUY	dsLF	dsL	quadL
SENWOZ	dsLF	dsL	tsLF	CUHPUR	dsLF	dsL	quadL
SENWIT	tsLF	dsL	tsLF	TERFUT	dsLF	dsL	tsLF
UTEWUM	tsLF	dsL	tsLF	BIBXUH	tsLF	dsL	tsLF
RAXCOK	dsLF	dsL	quadL	MATVEJ	dsLF	dsL	quadL
UTEWOG	dsLF	dsL	tsLF	SERKEG	dsLF	dsL	quadL
FEFDAX	dsLF	dsL	quadL	OJICUG	dsLF	dsL	dsL
FAKLOU	dsLF	dsL	quadL				

* Analytical models applied to CO_2 isotherms after re-parameterization (Section 4.A.4.2.1).

Figure 4.A.4 shows the fitting results for CO_2 and N_2 adsorption isotherms at 243 K via non-linear parameter estimation[31,32] for 15 MOFs. All cases show good agreements between the fits and isotherm data. The choice of isotherm models is material and component dependent on giving the best fits on isotherms. Models parameters for each MOF are summarized in Table 4.A.2.

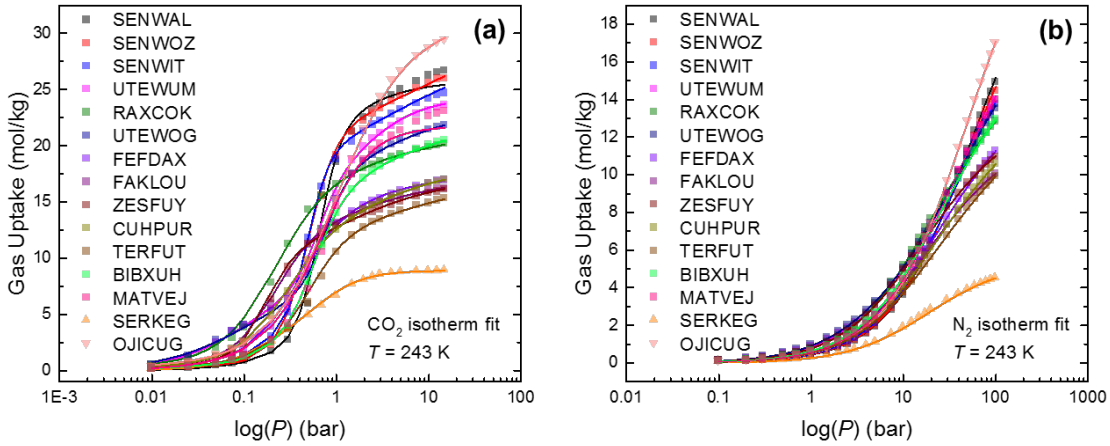

Figure 4.A.4. Analytical model fits (solid curves) for (a) CO_2 and (b) N_2 single component isotherms predicted by GCMC simulations (symbols) at 243 K for 15 MOFs. More information about the analytical model fits is given in Tables 4.A.2 and 4.A.2.1.

Table 4.A.2. Analytical adsorption model parameters for 15 MOFs: CO_2 isotherms.

Model Parameters for CO_2 (component i = 2 in model equations)															
	q_{21}^{sat}	q_{22}^{sat}	q_{23}^{sat}	b_{210}	b_{220}	b_{230}	B_{21}	B_{22}	B_{23}	θ_{210}	θ_{220}	θ_{230}	Θ_{21}	Θ_{22}	Θ_{23}
SENWAL	7.9	17.9	-	2.4e-6	3.3e-6	-	2.2e3	1.7e-3	-	9.0e-1	1.0e-1	-	45.4	8.4e2	-
SENWOZ	19.9	11.4	-	1.3e-4	1.4e-6	-	1.7	2.4e3	-	1.1e-1	5.9e-1	-	8.0e2	1.6e-5	-
SENWIT	13.8	4.6	9.8	4.3e-6	6.2e-6	6.8e-8	0.7e-3	1.9e3	3.0e3	9.9e-2	5.4e-1	7.4e-1	8.9e2	2.7e2	6.5e-9
UTEWUM	8.4	8.8	7.1	4.9e-9	3.1e-8	4.6e-8	3.2e3	1.5e3	3.7e3	4.9e-1	2.7e-1	9.3e-1	2.3e2	6.0e2	42.8
RAXCOK	6.8	15.0	-	5.2e-6	3.0e-8	-	2.4e3	3.3e3	-	5.0e-1	7.0e-1	-	24.6	1.8e2	-
UTEWOG	5.0	9.4	-	3.5e-3	2.0e-6	-	3.8e2	2.0e2	-	9.9e-3	3.5e-1	-	1.1e3	5.5e2	-
FEFDAX	6.2	11.4	-	1.1e-6	2.9e-8	-	2.7e3	3.0e3	-	5.2e-1	4.3e-1	-	82.4	3.4e2	-
FAKLOU	9.9	7.2	-	2.2e-7	5.3e-7	-	2.6e3	2.9e3	-	2.1e-1	6.9e-1	-	5.5e2	2.5e-7	-
ZESFUY	8.5	8.7	-	1.9e-8	4.1e-7	-	2.9e3	2.9e3	-	2.0e-1	7.3e-1	-	6.4e2	9.8	-
CUHPUR	8.7	9.8	-	6.5e-7	4.1e-8	-	2.8e3	3.0e3	-	6.7e-1	7.1e-1	-	3.6e-6	2.2e2	-
TERFUT	10.5	7.0	-	2.3e-7	3.2e-6	-	2.2e3	2.4e3	-	3.8e-1	5.5e-1	-	4.0e2	9.5e-7	-
BIBXUH	1.5	13.5	7.0	4.2e-2	1.3e-5	3.9e-8	2.2e2	8.3e2	3.3e3	5.2e-1	2.5e-1	7.1e-1	20.2	5.5e2	20.8
MATVEJ	12.3	4.5	-	2.8e-8	2.4e-6	-	2.7e3	2.5e3	-	3.3e-1	8.9e-1	-	4.1e2	25.8	-
SERKEG	2.9	6.0	-	7.3e-4	6.5e-8	-	50.0	3.2e3	-	1.3e-2	8.1e-1	-	1.2e3	1.2e2	-
OJICUG	26.8	6.6	-	1.9e-7	1.9e-5	-	2.6e3	2.0e3	-	1.2	6.2e-2	-	14.2	4.6e2	-

* Parameter units: q_i^0 [=] mol/kg, c_i^0 [=] mol/m^3, T [=] K, R = 8.314 x 10^{-5} m^3·bar/mol·K and/or = 8.314 J/mol·K
q_{ij}^{sat} [=] mol/kg, b_{ij0} [=] m^3/mol, B_{ij} [=] J/mol, θ_{ij0} [=] -, Θ_{ij} [=] J/mol (where j refers to adsorption sites)

Table 4.A.2. Continued: N_2 isotherms.

Model Parameters for N_2 (component i = 1 in model equations)						
	q_{11}^{sat}	q_{12}^{sat}	b_{110}	b_{120}	B_{11}	B_{12}
SENWAL	22.9	2.4e-2	9.9e-6	6.8e-3	8.9e2	1.4e-2
SENWOZ	1.7	20.1	2.5e-8	1.3e-5	2.1e3	8.6e2
SENWIT	2.0	17.8	3.5e-8	1.3e-5	2.0e3	9.1e2
UTEWUM	16.1	4.3	3.4e-6	3.3e-5	1.1e3	1.1e3
RAXCOK	3.5	13.6	4.3e-8	1.1e-5	1.9e3	1.1e3
UTEWOG	4.1	14.7	3.6e-5	3.5e-6	1.1e3	1.2e3
FEFDAX	12.3	2.8	1.0e-5	2.5e-8	1.1e3	2.1e3
FAKLOU	11.3	1.3	9.7e-6	6.6e-9	1.2e3	2.3e3
ZESFUY	2.0	11.2	1.2e-8	1.1e-5	2.4e3	1.2e3
CUHPUR	11.6	3.6	1.2e-5	2.0e-8	1.1e3	2.0e3
TERFUT	3.7	9.9	1.3e-7	1.1e-5	1.7e3	1.1e3
BIBXUH	3.4	14.6	2.3e-8	1.4e-5	2.0e3	1.0e3
MATVEJ	2.9	16.7	3.1e-8	1.4e-5	2.0e3	9.5e2
SERKEG	5.4	2.3e-14	6.9e-6	1.8e-3	1.2e3	2.2e-5
OJICUG	4.4	21.5	1.5e-7	1.5e-5	1.7e3	8.3e2

* Parameter units: q_i^0 [=] mol/kg, c_i^0 [=] mol/m^3, T [=] K, R = 8.314 x 10^{-5} m^3·bar/mol·K and/or = 8.314 J/mol·K
q_{ij}^{sat} [=] mol/kg, b_{ij0} [=] m^3/mol, B_{ij} [=] J/mol (where j refers to adsorption sites)

4.A.4.2.1 Re-parameterization of CO_2 Isotherms for Rigorous Modeling

The characterization of single component adsorption data requires more cautious efforts in process optimization where IAST is highly coupled with other complex iterative calculations.[33] Potential numerical challenges in IAST can affect the accuracy and robustness in rigorous process modeling. The origin of numerical difficulties arises from the fact that dual-site Langmuir-Freundlich models do not have finite Henry coefficients at infinite dilution. This limit is, however, an important quantity to accurately predict mixture equilibrium via IAST at dilute concentrations. Corrections to this deficiency have been presented in the literature.[34]

In order to avoid potential numerical difficulties with IAST in the dynamic simulation and multi-objective optimization, we conducted re-parameterization of CO_2 single component adsorption isotherms of chosen MOFs. We employed a Type IV equilibrium equation, i.e. quadratic plus Langmuir equation, which is able to precisely describe inflection points along isotherm courses. The structure codes of MOFs for which CO_2 isotherms were re-parameterized to the quadratic plus Langmuir equation are RAXCOK, FEFDAX, FAKLOU, ZESFUY, CUHPUR, MATVEJ, and SERKEG. Triple-site Langmuir-Freundlich model also helps to avoid numerical difficulties discussed above by introducing an additional adsorption site.[34] MOFs for which re-parameterization was achieved by triple-site Langmuir-Freundlich model were SENWAL, SENWOZ, SENWIT, UTEWUM, UTEWOG, TERFUT, and BIBXUH. For OJICUG, the dual-site Langmuir equation was used that allows simple calculation of Henry coefficient.

We found this re-parameterization step significantly reduced the computational cost and improved robustness of our simulations, without affecting the results of IAST (data not shown). Table 4.A.2.1 lists the model parameters obtained after the re-parameterization. Comparison of GCMC simulated adsorption data and model fits using re-parameterized parameters for CO_2 in Table 4.A.2.1 and using parameters in Table 4.A.2 for N_2 at five temperatures (213, 228, 243, 258, and 273 K) in 15 MOFs are provided below.

Table 4.A.2.1. Analytical adsorption model parameters for 15 MOFs after re-parameterization of CO_2 isotherms.

Model Parameters for CO_2 (component i = 2 in model equations)															
	q_{21}^{sat}	q_{22}^{sat}	q_{23}^{sat}	b_{210}	b_{220}	b_{230}	B_{21}	B_{22}	B_{23}	θ_{210}	θ_{220}	θ_{230}	Θ_{21}	Θ_{22}	Θ_{23}
SENWAL	16.8	3.8	13.0	4.8e-7	8.8e-6	2.5e-8	1.9e-5	1.8e3	3.0e3	1.7e-1	6.5e-1	7.2e-1	7.9e2	2.1e2	26.5
SENWOZ	15.1	3.5	11.7	3.7e-6	6.0e-6	4.9e-8	6.4e-4	1.9e3	3.0e3	9.5e-2	5.3e-1	7.4e-1	9.0e2	2.7e2	7.4
SENWIT	13.8	4.6	9.8	4.3e-6	6.2e-6	6.8e-8	0.7e-3	1.9e3	3.0e3	9.9e-2	5.4e-1	7.4e-1	8.9e2	2.7e2	6.5e-9
UTEWUM	8.4	8.8	7.1	4.9e-9	3.1e-8	4.6e-8	3.2e3	1.5e3	3.7e3	4.9e-1	2.7e-1	9.3e-1	2.3e2	6.0e2	42.8
RAXCOK	3.4	13.4	-	4.3e-2	8.0e-10	2.3e-8	1.2e-2	4.0e3	3.6e3	-	-	-	-	-	-
UTEWOG	14.3	9.4	2.4	8.5e-6	3.2e-8	1.8e-8	2.1e3	1.7e3	4.0e3	6.1e-1	4.0e-1	5.3e-1	7.2e-8	4.8e2	2.9e2
FEFDAX	3.7	9.7	-	7.7e-3	1.0e-8	2.5e-8	2.7e2	3.1e3	3.5e3	-	-	-	-	-	-
FAKLOU	2.7	10.9	-	2.3e-2	6.2e-9	2.5e-8	23.1	3.5e3	3.5e3	-	-	-	-	-	-
ZESFUY	3.0	10.8	-	2.9e-5	7.5e-9	2.4e-8	8.0e-7	3.5e3	3.4e3	-	-	-	-	-	-
CUHPUR	3.3	10.8	-	2.5e-2	4.2e-9	8.1e-9	4.7e-2	3.5e3	3.7e3	-	-	-	-	-	-
TERFUT	4.9	9.9	1.9	4.5e-8	1.0e-7	7.1e-3	1.1e3	3.0e3	3.1e2	2.4e-1	6.2e-1	1.7e-1	6.8e2	95.5	5.5e2
BIBXUH	7.6	1.5	12.2	1.4e-8	2.7e-2	3.8e-8	3.4e3	2.2e3	2.1e3	6.4e-1	2.6e-1	5.1e-1	93.0	3.8e2	3.9e2
MATVEJ	2.8	14.7	-	2.9e-2	1.3e-8	6.4e-8	25.7	2.9e3	3.0e3	-	-	-	-	-	-
SERKEG	1.0	7.9	-	6.6e-4	2.9e-8	1.5e-8	32.6	3.0e3	3.5e3	-	-	-	-	-	-
OJICUG	15.9	16.3	-	4.3e-6	1.1e-7	-	2.1e3	2.9e3	-	-	-	-	-	-	-

* Parameter units: q_i^0 [=] mol/kg, c_i^0 [=] mol/m^3, T [=] K, R = 8.314 x 10^{-5} m^3·bar/mol·K and/or = 8.314 J/mol·K
q_{ij}^{sat} [=] mol/kg, b_{ij0} [=] m^3/mol, B_{ij} [=] J/mol, θ_{ij0} [=] -, Θ_{ij} [=] J/mol (where j refers to adsorption sites)

MOFs	Adsorption Data and Model Fits
SENWAL	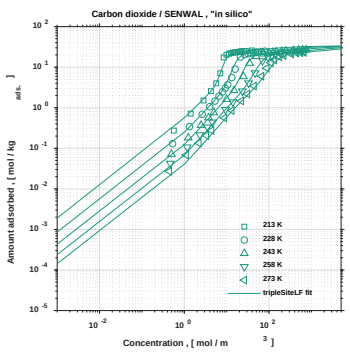 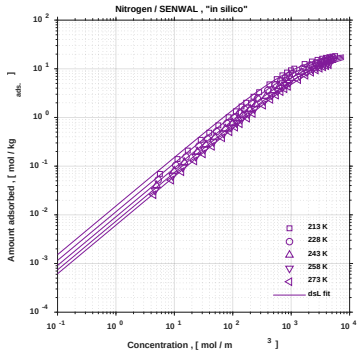
SENWOZ	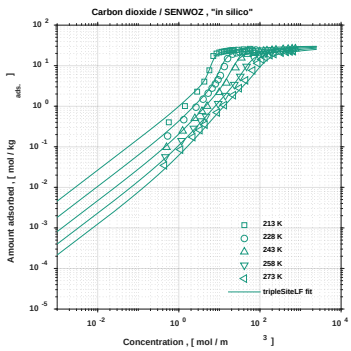 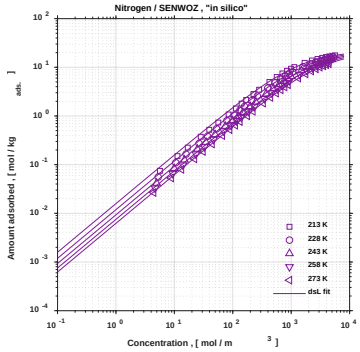
SENWIT	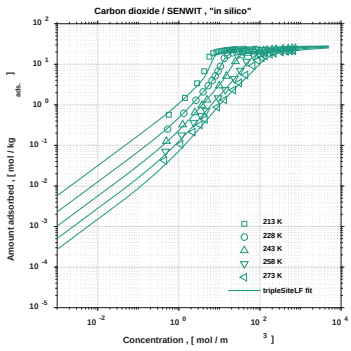 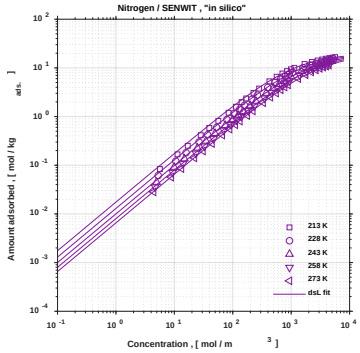
UTEWUM	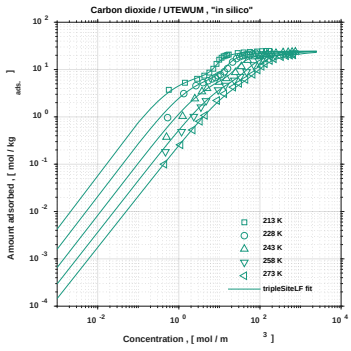 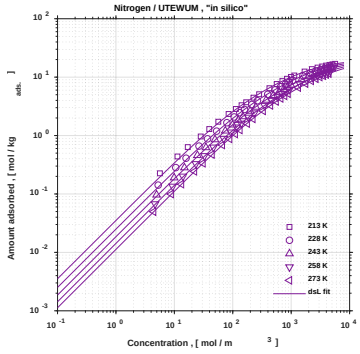

MOFs	Adsorption Data and Model Fits
RAXCOK	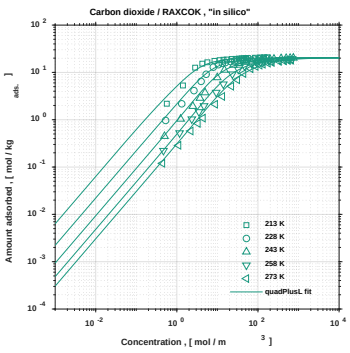 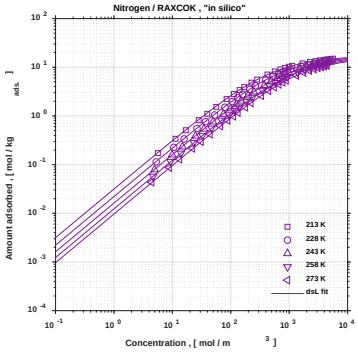
UTEWOG	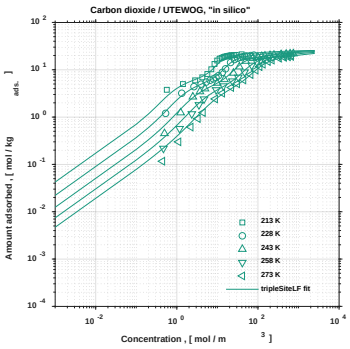 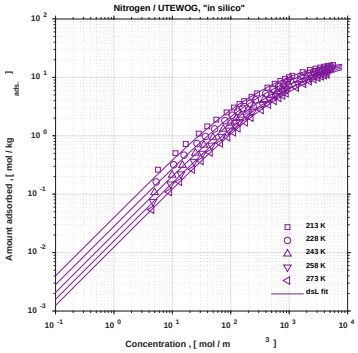
FEFDAX	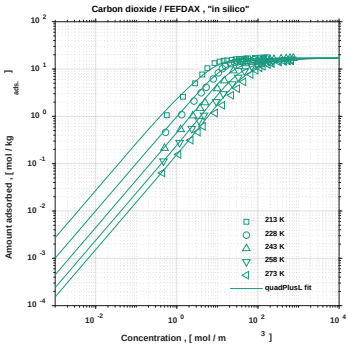 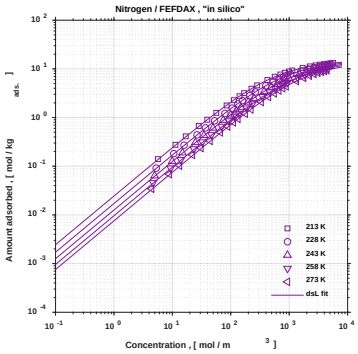
FAKLOU	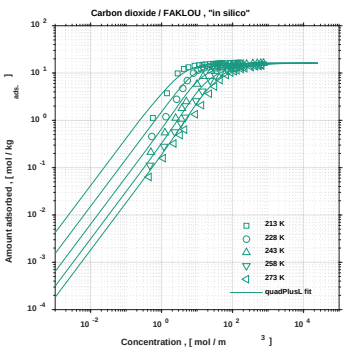 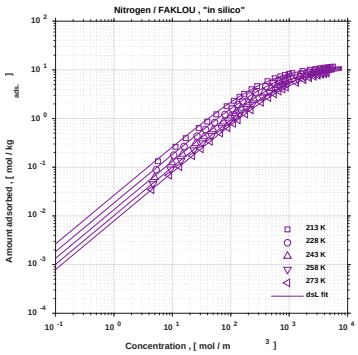

MOFs	Adsorption Data and Model Fits
ZESFUY	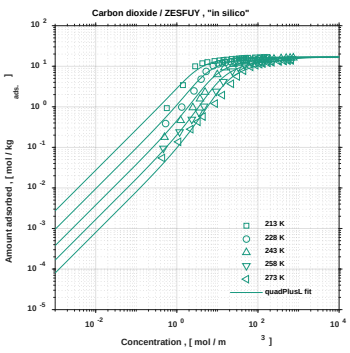 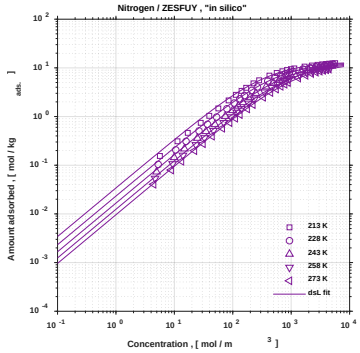
CUHPUR	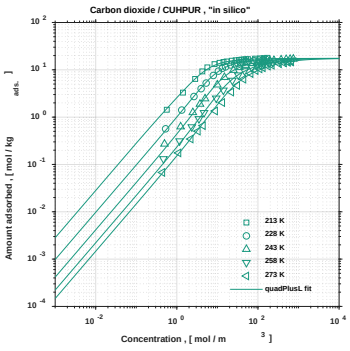 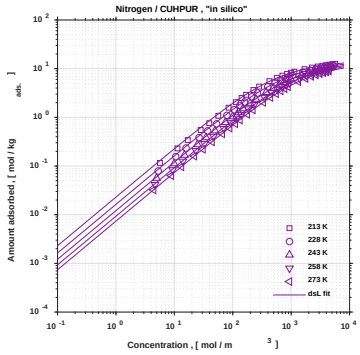
TERFUT	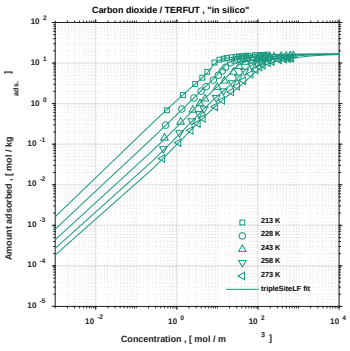 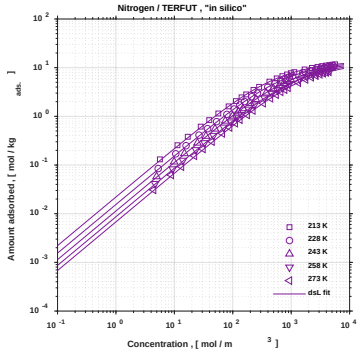
BIBXUH	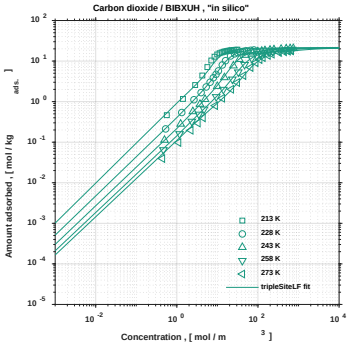 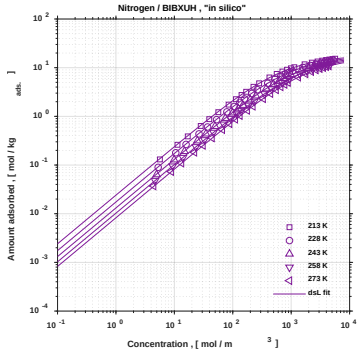

MOFs	Adsorption Data and Model Fits
MATVEJ	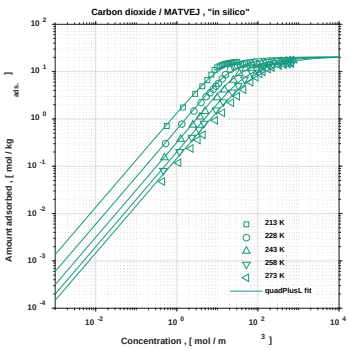 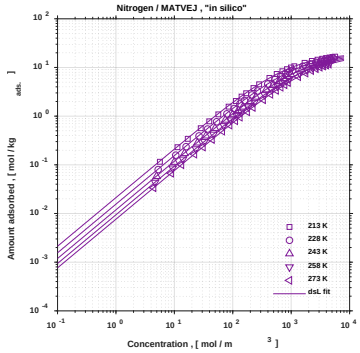
SERKEG	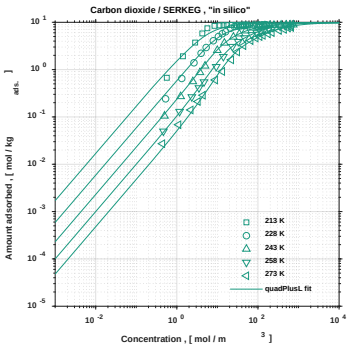 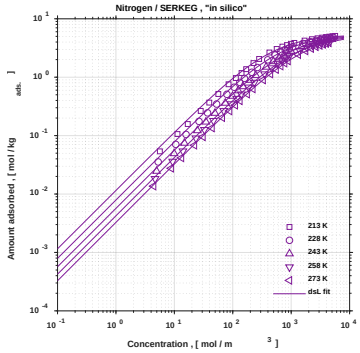
OJICUG	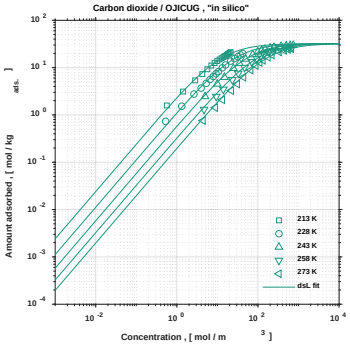 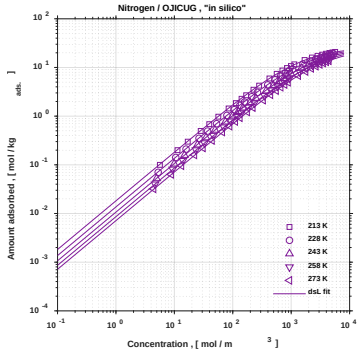

Isosteric heats of adsorption ($\Delta H_{ads,i}$) for each gas species is needed for temperature-dependent adsorption isotherm fitting. Below summarizes $\Delta H_{ads,CO2}$ and $\Delta H_{ads,N2}$ in 15 MOFs that were calculated using Clausius-Clapeyron equation.

MOFs	**$\Delta H_{ads,CO2}$ (kJ/mol)**	**$\Delta H_{ads,N2}$ (kJ/mol)**
SENWAL	-24.9	-9.4
SENWOZ	-30.0	-9.5
SENWIT	-30.3	-9.9
UTEWUM	-28.8	-11.3
RAXCOK	-24.8	-11.6
UTEWOG	-30.9	-11.5
FEFDAX	-25.5	-11.5
FAKLOU	-25.6	-11.9
ZESFUY	-29.4	-12.3
CUHPUR	-23.2	-11.2
TERFUT	-37.9	-11.6
BIBXUH	-30.8	-10.7
MATVEJ	-18.4	-10.3
SERKEG	-27.1	-12.2
OJICUG	-22.3	-9.6

4.A.5 Rigorous Process Modeling Details

4.A.5.1 PSA Modeling and Thermally Modulated Fiber Adsorbent Modeling Details

A PSA process model that incorporates thermally modulated fiber adsorbents was developed in a recent study by Rubiera Landa et al.[35] The following assumptions were made in developing the transient balance equations that describe the cyclic adsorption process using thermally modulated fiber adsorbents. We also refer interested readers to the original source of Rubiera Landa et al.[35] for more details.

- The process is modeled in one spatial dimension (1D) in the direction of fluid flow.
- The ideal-gas law holds.
- The process operates adiabatically.
- A linear driving-force (LDF) approximation[36,37] is used to describe mass transfer between gas phase and fiber composite.
- Fibers are distributed evenly within the module, allowing a uniform gas flow.
- Radial distributions within a fiber and a module, including dispersion and heat conduction, are negligible.
- Mass transfer resistance occurs at the macropores of the fiber adsorbent with negligible micropore resistance in the MOF crystals and negligible gas-film resistance surrounding the fibers.
- Pressure drop along the direction of fluid flow is represented by the Happel equation[38] along solid cylinders arranged in parallel.
- Gas viscosity is constant within the temperature range considered.
- Heat transfer between fiber composite and gas phase occurs instantaneously.
- Heat transfer between all solid elements of the fiber composite (i.e. polymeric matrix, MOF crystals, and PCM) occurs instantaneously. This assumption simplifies the energy balance, which accommodates a simplified melting/solidification of PCM, i.e. a smooth-interface model.
- Changes in the PCM density are included in the model equations. However, volumetric expansion and contraction within the microencapsulated PCMs are neglected.
- Temperature dependency of the PCM is taken account.
- Melting and solidification kinetics of the PCM are neglected.
- Heat capacities and densities for the solid materials that constitute the fiber composite, i.e. polymeric matrix and MOF, are constant.

Below are the transient balances equations with corresponding boundary conditions, valve behavior expressions for the pressurization boundary condition, and initial conditions used in our rigorous PSA modeling applying fiber composite adsorbents.

Transient Balance Equations

Total mass balance

$$\frac{\partial}{\partial t}\left(\frac{p}{\Re T}\right) = -\frac{\partial}{\partial z}\left(u\frac{p}{\Re T}\right) - \frac{v_f}{v_{\text{fs}}}(1-\epsilon_f)\,(1-\psi)\,\varphi\,\rho_{\text{MOF}}\sum_i \frac{\partial q_i}{\partial t}.$$

Mass balance for component *i*

$$\frac{\partial c_i}{\partial t} + \frac{v_f}{v_{\text{fs}}}(1-\epsilon_f)\,(1-\psi)\,\varphi\,\rho_{\text{MOF}}\frac{\partial q_i}{\partial t} = -\frac{\partial}{\partial z}\,(uc_i) + \frac{\partial}{\partial z}\left(D_{\text{ax.},i}\frac{\partial c_i}{\partial z}\right), \quad i = 1, \ldots, N.$$

$$c_i = \frac{p}{\Re T}y_i$$

$$\frac{\partial q_i}{\partial t} = k_i^{\text{ldf}}\,(q_i^{\star} - q_i)$$

Energy balance

$$\begin{aligned}\frac{v_f}{v_{\text{fs}}}\Xi_f\frac{\partial T}{\partial t} + \hat{\rho}_g\hat{C}_g\frac{\partial T}{\partial t} - \frac{\partial p}{\partial t} = &-\frac{\partial}{\partial z}\left(u\hat{\rho}_g\hat{C}_g\right) + \frac{\partial}{\partial z}\left(k_g\frac{\partial T}{\partial z}\right)\\ &- \frac{v_f}{v_{\text{fs}}}(1-\epsilon_f)(1-\psi)\,\varphi\,\rho_{\text{MOF}}\,\hat{C}_{\text{ads.}}T\sum_i\frac{\partial q_i}{\partial t}\\ &+ \frac{v_f}{v_{\text{fs}}}(1-\epsilon_f)\frac{\partial}{\partial z}\left(k_{\text{eff.},f}\frac{\partial T}{\partial z}\right)\\ &+ \frac{v_f}{v_{\text{fs}}}(1-\epsilon_f)(1-\psi)\,\varphi\,\rho_{\text{MOF}}\sum_i(-\Delta H_{\text{ads.},i})\frac{\partial q_i}{\partial t}\end{aligned}$$

where,

$$\begin{aligned}\Xi_f \equiv\ &(1-\epsilon_f)\psi\left[\rho_{\text{PCM}}C_{\text{PCM}} + \rho_{\text{PCM}}\frac{\mathrm{d}}{\mathrm{d}T}\lambda_{\text{PCM}}\right]\\ &+ (1-\epsilon_f)(1-\psi)(1-\varphi)\,\rho_{\text{poly.}}C_{\text{poly.}} + (1-\epsilon_f)(1-\psi)\,\varphi\,\rho_{\text{MOF}}\,C_{\text{MOF}}\\ &+ (1-\epsilon_f)(1-\psi)\,\varphi\,\rho_{\text{MOF}}\,\hat{C}_{\text{ads.}}\sum_i q_i\end{aligned}$$

Momentum balance

$$u = -\beta_{\text{bed}}\frac{\partial p}{\partial z}$$

$$\beta_{\text{bed}} \equiv \frac{1}{\mu_g}\left[\frac{r_f^2 - 3r_{\text{fs}}^2}{8} + \frac{1}{2}\frac{r_{\text{fs}}^4}{r_{\text{fs}}^2 - r_f^2}\ln\left[\frac{r_{\text{fs}}}{r_f}\right]\right]$$

Boundary Conditions	
at $z = 0$	at $z = L$
Counter-current pressurization	
$\frac{\partial}{\partial z} y_i(t, z = 0) = 0,\ i = 1, \ldots, N$;	$y_i(t, z = L) = y_{i,\mathrm{Pr}},\ i = 1, \ldots, N$;
$u(t, z = 0) = 0$;	$u(t, z = L) = f_{\mathrm{valve}}(\Delta p, T, \cdots)$;
$\frac{\partial}{\partial z} p(t, z = 0) = 0$;	$\frac{\partial}{\partial z} p(t, z = L) = -\frac{1}{\beta_{\mathrm{bed}}} u(t, z = L)$;
$\frac{\partial}{\partial z} T(t, z = 0) = 0.$	$T(t, z = L) = T_{\mathrm{Pr}}.$
Adsorption	
$y_i(t, z = 0) = y_{i,\mathrm{feed}},\ i = 1, \ldots, N$;	$\frac{\partial}{\partial z} y_i(t, z = L) = 0,\ i = 1, \ldots, N$;
$u(t, z = 0) = u_{\mathrm{feed}}$;	
$\frac{\partial}{\partial z} p(t, z = 0) = -\frac{1}{\beta_{\mathrm{bed}}} u(t, z = 0)$;	$u(t, z = L) = -\beta_{\mathrm{bed}} \frac{\partial}{\partial z} p(t, z = L)$;
$T(t, z = 0) = T_{\mathrm{feed}}.$	$p(t, z = L) = p_{\mathrm{Ad}} = p_{\mathrm{high}}$
	$\frac{\partial}{\partial z} T(t, z = L) = 0.$
Co-current blowdown	
$\frac{\partial}{\partial z} y_i(t, z = 0) = 0,\ i = 1, \ldots, N$;	$\frac{\partial}{\partial z} y_i(t, z = L) = 0,\ i = 1, \ldots, N$;
$u(t, z = 0) = 0$;	$u(t, z = L) = u_{\mathrm{Bd}}$;
$\frac{\partial}{\partial z} p(t, z = 0) = 0$;	$\frac{\partial}{\partial z} p(t, z = L) = -\frac{1}{\beta_{\mathrm{bed}}} u(t, z = L)$;
$\frac{\partial}{\partial z} T(t, z = 0) = 0.$	$\frac{\partial}{\partial z} T(t, z = L) = 0.$
Counter-current evacuation	
$\frac{\partial}{\partial z} y_i(t, z = 0) = 0,\ i = 1, \ldots, N$;	$\frac{\partial}{\partial z} y_i(t, z = L) = 0,\ i = 1, \ldots, N$;
$u(t, z = 0) = u_{\mathrm{Ev}}$;	
$\frac{\partial}{\partial z} p(t, z = 0) = -\frac{1}{\beta_{\mathrm{bed}}} u(t, z = 0)$;	$u(t, z = L) = 0$;
	$\frac{\partial}{\partial z} p(t, z = L) = 0$;
$\frac{\partial}{\partial z} T(t, z = 0) = 0.$	$\frac{\partial}{\partial z} T(t, z = L) = 0.$

Valve Behavior Expressions for the Pressurization Boundary Condition
$u = \min[u_1, u_2] = f_{\text{valve}}(\Delta p, T, \cdots)$
$u_1 = k_V p_{\text{high}} \sqrt{\text{abs}\left[\frac{1}{\bar{M}_g}\left[1 - \left(\frac{p}{p_{\text{high}}}\right)^2\right]\right]} \quad u_2 = k_V p_{\text{high}} \sqrt{\text{abs}\left[\frac{1}{\bar{M}_g}\left[1 - \left(\frac{1}{p_{\text{crit.}}}\right)^2\right]\right]}$
$p_{\text{crit.}} = \left[\frac{2}{1+\gamma}\right]^{\frac{\gamma}{1-\gamma}}$
$\bar{M}_g = y_{N_2} M_{N_2} + y_{CO_2} M_{CO_2}$

Initial Conditions
$y_i(t = 0, z) = y_{i0}, \quad i = 1, \ldots, N$
$q_i(t = 0, z) = q_{i0} = q_{i0}^{\star}$
$p(t = 0, z) = p_0$
$T(t = 0, z) = T_0$
$x(t = 0, z) = x_0$
$x_0 = [y_{10}, \ldots, y_{N0}, q_{10}, \ldots, q_{N0}, p_0, T_0]^T$

Cyclic operation was implemented by initializing the time integration for each step of cycle configuration in k^{th} cycle as follows.

Cycle Configuration	Time Integration in k^{th} cycle
Counter-current pressurization	$x_k(t_{\text{Pr,start}}, z) = \begin{cases} x_0 & \text{for } k = 1, \\ x_{k-1}(t_{\text{Ev,end}}, z) & \text{otherwise.} \end{cases}$
Adsorption	$x_k(t_{\text{Ad,start}}, z) = x_k(t_{\text{Pr,end}}, z).$
Co-current blowdown	$x_k(t_{\text{Bd,start}}, z) = x_k(t_{\text{Ad,end}}, z).$
Counter-current evacuation	$x_k(t_{\text{Ev,start}}, z) = x_k(t_{\text{Bd,end}}, z).$

The linear driving-force approximation[36,37] for mass transfer calculation is carried out with the following mathematical descriptions.

Mass transfer

$$k_i = k_i^{\text{macro}} \frac{c_i}{q_i^\star}, \quad q_i^\star = f(c,T), \quad i = 1, \ldots, N.$$

$$k_i^{\text{macro}} = \frac{8}{r_f^2} D_{fp,i} \left[\frac{\epsilon_f}{1-\epsilon_f} \right] \frac{1}{(1-\psi)\,\varphi\,\rho_{\text{MOF}}}$$

$$D_{fp,i} = D_{g,i} \frac{\epsilon_f}{\tau_f^2}, \quad i = 1, \ldots, N. \qquad D_{g,i} = 0.0018583 \sqrt{T^3 \left[\frac{1}{M_{\text{N}_2}} + \frac{1}{M_{\text{CO}_2}} \right]} \left[\frac{1}{p \left[\sigma_{12}^{\text{LJ}}\right]^2 \Omega^{\text{LJ}}} \right]$$

Estimation of fiber tortuosity

$$\tau_f = 1.0 - \ln\left[\epsilon_f\right].$$

The following auxiliary expressions and parameters necessary to describe the fiber composites complete the mathematical description of the rigorous process model. The following smooth-interface model[39] approximates the PCM melting/freezing processes.

Auxiliary Expressions and Parameters

Volumetric ratio of PCM to solids in fiber composite

$$\psi := \frac{V_{\text{PCM}}}{V_{\text{PCM}} + V_{\text{MOF}} + V_{\text{poly.}}} = \frac{\omega_{\text{PCM}}/\rho_{\text{PCM},s}}{\omega_{\text{PCM}}/\rho_{\text{PCM},s} + \omega_{\text{MOF}}/\rho_{\text{MOF}} + \omega_{\text{poly.}}/\rho_{\text{poly.}}}.$$

Volumetric ratio of MOF to combined volume of polymer and MOF

$$\varphi := \frac{V_{\text{MOF}}}{V_{\text{MOF}} + V_{\text{poly.}}} = \frac{\omega_{\text{MOF}}/\rho_{\text{MOF}}}{\omega_{\text{MOF}}/\rho_{\text{MOF}} + \omega_{\text{poly.}}/\rho_{\text{poly.}}}$$

Weight fractions of fiber components

$$\omega_{\text{PCM}} = f(\omega_{\text{MOF}}) = 1.0 - \omega_{\text{MOF}} - \omega_{\text{poly.}}$$

Smooth-Interface Model[39] for Phase-Transitions of PCM

$$\lambda_{\text{PCM}} = f(T) = \frac{\Delta H_{\text{fus.}}}{1 + \exp\left[-\dfrac{T - T_{\text{fus.}}}{\varsigma_{\text{tr.}}} \right]} \qquad \frac{\mathrm{d}}{\mathrm{d}T}\lambda_{\text{PCM}} = \frac{\Delta H_{\text{fus.}} \exp\left[\dfrac{T_{\text{fus.}} - T}{\varsigma_{\text{tr.}}} \right]}{\varsigma_{\text{tr.}} \left[1 + \exp\left[\dfrac{T_{\text{fus.}} - T}{\varsigma_{\text{tr.}}} \right] \right]^2}$$

$$\rho_{\text{PCM},s} - \frac{\rho_{\text{PCM},s} - \rho_{\text{PCM},l}}{1 + \exp\left[-\dfrac{T - T_{\text{ph.}}}{\varsigma_{\text{ph.}}} \right]} \qquad C_{\text{PCM}} = f(T) = C_{\text{PCM},s} - \frac{C_{\text{PCM},l} - C_{\text{PCM},s}}{1 + \exp\left[-\dfrac{T - T_{\text{ph.}}}{\varsigma_{\text{ph.}}} \right]}$$

Process-level objectives (Table 4.2 of Chapter 4) evaluated at cyclic steady state are derived as the following equations.

Objectives	**Objective Formula**
Purity	$\mathrm{Pur}_i^{\mathrm{E}} = \dfrac{n_i^{\mathrm{E}}}{n_{\mathrm{tot}}} = \dfrac{n_i^{\mathrm{E}}}{\sum_{i=1}^{N} n_i^{\mathrm{E}}}.$
Recovery	$\mathrm{Rec}_i^{\mathrm{E}} = \dfrac{n_i^{\mathrm{E}}}{n_{i,\mathsf{Pr}} + n_{i,\mathrm{feed}}}.$
Productivity	$\mathrm{Prod}_i = \dfrac{n_i^{\mathrm{E}}}{m_{\mathrm{MOF}}\, t_{\mathrm{cycle}}}.$
Specific energy consumption	$\mathrm{En}_i = \dfrac{W_{\mathsf{Pr}} + W_{\mathsf{Ad}} + W_{\mathsf{Bd}} + W_{\mathsf{Ev}}}{n_i^{\mathrm{E}}\, t_{\mathrm{cycle}}}.$
where,	
$n_i^{\mathrm{E}} = \int_{t_{\mathsf{Ev,start}}}^{t_{\mathsf{Ev,end}}} Q_{\mathsf{Ev}}(t,0)\, \dfrac{p(t,0)}{\Re T(t,0)} y_i(t,0)\, \mathrm{d}t.$	$n_{i,\mathrm{feed}} = \int_{t_{\mathsf{Ad,start}}}^{t_{\mathsf{Ad,end}}} Q_{\mathsf{Ad}}(t,0)\, \dfrac{p(t,0)}{\Re T(t,0)} y_i(t,0)\, \mathrm{d}t = \int_{t_{\mathsf{Ad,start}}}^{t_{\mathsf{Ad,end}}} Q_{\mathrm{feed}}\, \dfrac{p_{\mathrm{feed}}}{\Re T_{\mathrm{feed}}} y_{i,\mathrm{feed}}\, \mathrm{d}t.$
$n_{i,\mathsf{Pr}} = \int_{t_{\mathsf{Pr,start}}}^{t_{\mathsf{Pr,end}}} Q_{\mathsf{Pr}}(t,L)\, \dfrac{p(t,L)}{\Re T(t,L)} y_i(t,L)\, \mathrm{d}t.$	$t_{\mathrm{cycle}} = t_{\mathsf{Pr}} + t_{\mathsf{Ad}} + t_{\mathsf{Bd}} + t_{\mathsf{Ev}} = \int_{t_{\mathsf{Pr,start}}}^{t_{\mathsf{Pr,end}}} t\, \mathrm{d}t + \int_{t_{\mathsf{Ad,start}}}^{t_{\mathsf{Ad,end}}} t\, \mathrm{d}t + \int_{t_{\mathsf{Bd,start}}}^{t_{\mathsf{Bd,end}}} t\, \mathrm{d}t + \int_{t_{\mathsf{Ev,start}}}^{t_{\mathsf{Ev,end}}} t\, \mathrm{d}t.$

Work terms (W) required for each step of the cycles in calculating the specific energy consumption are given as the following equations.

Cycle Configuration	**Work Calculation**
Counter-current pressurization	$W_{\mathsf{Pr}} = 0.$
Adsorption	$W_{\mathsf{Ad}} = \int_{t_{\mathsf{Ad,start}}}^{t_{\mathsf{Ad,end}}} \dfrac{1}{\eta_{\mathrm{compr.}}} \dfrac{\gamma}{\gamma - 1}\, p(t, z = L)\, Q(t, z = L) \left[\left(\dfrac{p(t, z = L)}{p_{\mathrm{fg}}} \right)^{\frac{\gamma - 1}{\gamma}} - 1 \right] \mathrm{d}t.$
Co-current blowdown	$W_{\mathsf{Bd}} = 0.$
Counter-current evacuation	$W_{\mathsf{Ev}} = \int_{t_{\mathsf{Ev,start}}}^{t_{\mathsf{Ev,end}}} \dfrac{1}{\eta_{\mathrm{vac.}}} \dfrac{\gamma}{\gamma - 1}\, p(t, z = 0)\, Q(t, z = 0) \left[\left(\dfrac{p(t, z = 0)}{p_{\mathsf{Ev}}} \right)^{\frac{\gamma - 1}{\gamma}} - 1 \right] \mathrm{d}t.$

We proceed with a numerical approximation to obtain solutions of the rigorous process model described above. We applied the finite volume method (FVM) in order to discretize the partial differential equation (PDE) system in space and obtain an ordinary differential equation (ODE) system, which can then be integrated in time. This discretization is commonly referred to as "method of lines" approach.[40] The required flux function approximations applied in the FVM are obtained with the third order upwind-biased scheme, applying the flux monitor function given by Koren *et al.*[41] Finally, the ODE system is integrated in time with the backward differentiation formulas.[42] We implemented these numerical schemes in MATLAB.[43]

Below we provide a collection of material properties describing the thermally modulated fiber adsorbents and a set of parameters applied in our PSA process modeling.

Solid and Liquid Properties in Smooth-Interface Model

Properties	**Symbols**	**Values**	**Units**
PCM heat capacity (liquid)	$C_{\mathrm{PCM},l}$	2140	J/kg·K
PCM heat capacity (solid)	$C_{\mathrm{PCM},s}$	2900	J/kg·K
PCM heat of transition	$\Delta H_{\mathrm{fus.}}$	150.0e3	J/kg
PCM heat conductivity (liquid)	$k_{\mathrm{PCM},l}$	0.15	W/m·K
PCM heat conductivity (solid)	$k_{\mathrm{PCM},s}$	0.17	W/m·K
PCM density (liquid)	$\rho_{\mathrm{PCM},l}$	760	kg/m^3
PCM density (solid)	$\rho_{\mathrm{PCM},s}$	880	kg/m^3
Smoothing parameter	$\varsigma_{\mathrm{tr.}}$	1.5	-
Temperature of transition	$T_{\mathrm{fus.}}$	243.15	K

Set of Parameters in Rigorous Process Model			
Parameters	**Symbols**	**Values**	**Units**
Molar heat capacity (gas phase)	$\hat{C}_g$	30.5	J/mol·K
Molar heat capacity (adsorbed phase)	$\hat{C}_{\text{ads.}}$	30.5	J/mol·K
Heat capacity (MOF)	C_{MOF}	750	J/kg·K
Heat capacity (polymer)	$C_{\text{poly.}}$	1465	J/kg·K
Axial dispersion coefficient	$D_{\text{ax},i}$	0.5e-3	m^2/s
Compression efficiency	$\eta_{\text{compr.}}$	0.7	-
Evacuation efficiency	$\eta_{\text{evac.}}$	0.3	-
Fiber porosity	ϵ_f	0.6	-
Packing fraction of fiber bed	ϕ_p	0.7	-
Ratio of gas heat capacities	γ	1.4	-
Gas heat conductivity	k_g	2.5e-2	W/m·K
Polymer heat conductivity	$k_{\text{poly.}}$	1.9e-1	W/m·K
Valve coefficient	k_V	0.1e-3	$m \cdot g^{1/2}/s \cdot Pa \cdot mol^{1/2}$
Bed length	L	1.0	m
Molecular weight (N_2)	M_{N_2}	28.0	g/mol
Molecular weight (CO_2)	M_{CO_2}	44.0	g/mol
Gas viscosity	μ_g	1.5e-5	Pa·s
Ideal gas constant	$\Re$	8.314	J/mol·K
Single fiber radius	r_f	25.0e-5	m
Free-surface radius	r_{fs}	30.0e-5	m
Density (MOF)	ρ_{MOF}	1.1e3	kg/m^3
Density (polymer)	$\rho_{\text{poly.}}$	1.2e3	kg/m^3
Lennard-Jones collision diameter (N_2)	$\sigma_{\text{N}_2}^{\text{LJ}}$	3.7	Å
Lennard-Jones collision diameter (CO_2)	$\sigma_{\text{CO}_2}^{\text{LJ}}$	3.8	Å
Lennard-Jones collision diameter (CO_2/N_2 pair)	σ_{12}^{LJ}	1.5	Å
Temperature of operation	$T_{\text{op.}}$	243.15	K
Blow-down gas velocity	u_{Bd}	0.2	m/s
Evacuation gas velocity	u_{Ev}	3.2	m/s
Single fiber volume	v_f	2.0e-7	m^3
Free-surface volume	v_{fs}	8.6e-8	m^3
Collision integral value, Lennard-Jones (LJ)	Ω^{LJ}	1.3	-
Weight fraction of polymer in fiber composite	$\omega_{\text{poly.}}$	0.3	-

4.A.5.2 Process Optimization Details

We treat the rigorous process modeling as a black-box function with a set of available decision variables for the PSA cycle as inputs. Five decision variables were considered: adsorption pressure, velocity of the feed gas, adsorption step time, evacuation pressure, and weight fraction of MOF in the fiber composite. The outputs are given by the process-level objectives at cyclic steady state described in detail above. The table below lists the decision variables considered with their lower and upper bounds.

Set of Decision Variables and Bounds				
Decision Variables	**Symbols**	**Lower Bounds**	**Upper Bounds**	**Units**
Adsorption pressure	p_{high}	3.0	7.5	atm
Gas velocity of feed	u_{feed}	0.15	1.0	m/s
Adsorption step time	t_{Ad}	15.0	120.0	s
Evacuation pressure	p_{Ev}	0.15	0.35	atm
MOF weight fraction in fiber	ω_{MOF}	0.15	0.40	-

Three bi-objective optimization tasks were conducted by formulating pairs of process-level objectives. Pareto fronts of below pairs of process objectives were obtained.

- Specific energy consumption and product purity.
- Product purity and product recovery.
- Productivity and specific energy consumption.

We applied the multi-objective optimization function *gamultiobj* included in the Global Optimization Toolbox available in MATLAB.[43] The algorithm of this function is a variant of the NSGA-II genetic algorithm.[44] Optimization variables and additional information used in our process optimization is summarized below.

Settings in NSGA-II Optimizer to Compute Pareto fronts	
Optimizer Parameters	**Values**
Number of decision variables	5
Population size	80
Cross-over fraction	0.95
Maximum number generations	30
Function tolerance	7.5e-3
Number of workers (parallelization option)	4

4.A.6 Comparing Approximate and Detailed Models of Adsorption-based Carbon Capture Process

4.A.6.1 Spearman's Rank-Order Correlation

Spearman's rank-order correlation (ρ) is defined as below where d_i and n refer to the difference between two paired ranks and the number of observations, respectively. Note all n ranks should be distinct integers without data having tied ranks within each data set. A general guideline for interpreting Spearman's rank-order correlation is provided in Table 4.A.3. The sign of the rank order correlation indicates the direction of association between two variables. Interpretation on the strength of the rank order correlation is adopted from previous discussions.[45,46]

$$\rho = 1 - \frac{6\sum d_i^2}{n(n^2-1)}$$

Table 4.A.3. Spearman's rank-order correlation (ρ) for a quantitative comparison between rankings provided by different variables. A general guideline to assess the measure of ranking dis-/similarity associated with the color coding is adopted from the literature.[45,46]

Direction	Range	Strength	Interpretation
$\lvert\rho\rvert$	0.80 – 1.00	very strong	observations have similar ranks between two variables
	0.60 – 0.79	strong	
	0.40 – 0.59	moderate	
	0.20 – 0.39	weak	observations have dissimilar ranks between two variables
	0.00 – 0.19	very weak	

Spearman's rank-order correlation reaches to values of 1 and/or -1 when two rankings are monotonically related. Note that ranks are defined as relative position label of the observations within the variables so the rank order correlation does not capture differences in magnitudes of the variables of interest.[45,46]

4.A.6.2 Rigorous Process Model and Adsorbent Evaluation Metrics

A quantitative comparison of MOF rankings between rigorous process model and adsorbent evaluation metrics were measured via Spearman's rank-order correlation in Figure 4.7. Table 4.A.4 lists 15 MOFs and their detailed performance rankings given by each descriptor.

Table 4.A.4. Spearman's rank-order correlation (ρ) between rankings of 15 MOFs from rigorous process modeling and adsorbent evaluation metrics. Standard deviation (SD) is calculated for normalized performance descriptors derived from each level of modeling to reflect the dispersion of each descriptor. Detailed MOF rankings (1-15) are given for each performance descriptor.

	Rigorous Process Model			**Adsorbent Evaluation Metrics**				
	En_{CO2}-Pu_{CO2}	Pu_{CO2}-Re_{CO2}	Pr_{CO2}-En_{CO2}	ΔN_{CO2}	$S_{ads,CO2/N2}^{ads}$	$S_{SP,CO2/N2}$	$APS_{CO2/N2}$	R
	Ref/0.29	-	-	0.50/0.29	0.31/0.24	0.34/0.22	0.54/0.32	0.37/0.34
ρ/SD	-	Ref/0.28	-	0.46/0.29	-0.16/0.24	0.14/0.22	0.05/0.32	0.79/0.34
	-	-	Ref/0.29	0.54/0.29	-0.19/0.24	0.03/0.22	0.11/0.32	0.69/0.34
SENWOZ	1	1	1	2	5	6	3	2
SENWIT	2	2	2	3	4	4	1	3
OJICUG	3	4	8	4	15	15	15	7
SENWAL	4	3	3	1	11	7	6	1
SERKEG	5	11	15	15	1	1	4	9
FAKLOU	6	12	11	11	3	2	5	11
FEFDAX	7	7	6	10	10	8	10	8
RAXCOK	8	9	7	8	2	3	2	13
CUHPUR	9	8	9	13	8	9	11	12
UTEWUM	10	15	14	6	7	13	7	14
UTEWOG	11	14	10	9	9	14	8	15
BIBXUH	12	5	4	7	13	10	13	4
MATVEJ	13	13	12	5	14	12	12	5
TERFUT	14	6	5	14	12	11	14	6
ZESFUY	15	10	13	12	6	5	9	10

We formulated a Combined Adsorbent Evaluation Metric (CAEM) defined as the following equation. CAEM considers all five adsorbent evaluation metrics to balance the contribution of each metric. Here D_i refers to adsorbent evaluation metric and f_i is a power for each metric D_i.

$$CAEM = \sum_i {D_i}^{f_i}$$

CAEM is formed for each pair of process objectives that we examined. This is possible by tuning f_i where $0 \leq f_i \leq 1$. f_i are empirical parameters that are meant to best improve the rank order correlation between process-level rankings (Table 4.A.4) and CAEM rankings (rankings not tabulated). Case dependent parameters of f_i that were found to work best are summarized in Table 4.A.5.

Table 4.A.5. Summary of the f_i parameters in CAEM for each pair of process-level objectives from rigorous process model. D_i refers to adsorbent evaluation metrics of ΔN_{CO2}, $S_{ads,CO2/N2}{}^{ads}$, $S_{SP,CO2/N2}$, $APS_{CO2/N2}$, and R from i = 1 to i = 5. f_i stands for a power on corresponding metrics of i.

Rigorous Process Model		**Adsorbent Evaluation Metrics**				
		D_1	D_2	D_3	D_4	D_5
En_{CO2}-Pu_{CO2}	f_i	0.78	0.20	0.11	0.40	0.17
Pu_{CO2}-Re_{CO2}	f_i	0.30	0.07	0.05	0.01	0.98
Pr_{CO2}-En_{CO2}	f_i	0.30	0.07	0.01	0.05	0.98

Table 4.A.6 summarizes the same analysis of ranking comparison between rigorous process modeling and CAEM as in Figure 4.7. Spearman's rank-order correlation for single adsorbent evaluation metrics is reproduced from Figure 4.7 to allow clear comparison with the correlation for CAEM.

For En_{CO2}-Pu_{CO2}, CAEM improved the rank correlation relative to using single metrics. All single metrics had $\rho < 0.60$ in predicting the materials ranking. This indicates a fine tuning of f_i in CAEM helps to provide better similarity to process-level ranking of materials when there was no winning single metric. Nevertheless, CAEM did not have positive impact on rank correlation for Pu_{CO2}-Re_{CO2} and Pr_{CO2}-En_{CO2}. These pairs of process objectives already had a successful metric in predicting the materials ranking, i.e. R with $\rho \geq 0.60$. In such cases, adjusting f_i is biased to the winning metric, i.e. f_5 (a power on R) approaches to 1 as shown in Table 4.A.5. It showed having a balance between single metrics can be destructive relative to relying on single metrics in these cases.

Table 4.A.6. Spearman's rank-order correlation (ρ) between rankings of 15 MOFs from rigorous process modeling and adsorbent evaluation metrics along with rankings from CAEMs.

	Rigorous Process Model	**Adsorbent Evaluation Metrics**					**CAEM**
		ΔN_{CO2}	$S_{ads,CO2/N2}{}^{ads}$	$S_{SP,CO2/N2}$	$APS_{CO2/N2}$	R	
ρ	En_{CO2}-Pu_{CO2}	0.50	0.31	0.34	0.54	0.37	0.66
	Pu_{CO2}-Re_{CO2}	0.46	-0.16	0.14	0.05	0.79	0.79
	Pr_{CO2}-En_{CO2}	0.54	-0.19	0.03	0.11	0.69	0.69

4.A.6.3 Rigorous and Idealized PSA Process Models

A quantitative comparison of MOF rankings between rigorous process model and idealized PSA process model were measured via Spearman's rank-order correlation in Figure 4.8. Table 4.A.7 lists 15 MOFs and their detailed performance rankings given by each level of process model.

Table 4.A.7. Spearman's rank-order correlation (ρ) between rankings of 15 MOFs from rigorous process modeling and idealized PSA process modeling. MOF rankings are provided from objectives of En_{CO2}-Pu_{CO2} using achievable Pu_{CO2} at a fixed En_{CO2} of 400 kWh/t. Standard deviation (SD) is calculated for normalized Pu_{CO2} at En_{CO2} constraint for each level of modeling to reflect the dispersion of each normalized Pu_{CO2}. Detailed MOF rankings (1-15) are given for each level of process model.

	Rigorous Process Model	**Idealized PSA Process Model**
	En_{CO2}-Pu_{CO2}	En_{CO2}-Pu_{CO2}
ρ/SD	Ref/0.29	0.54/0.29
SENWOZ	1	5
SENWIT	2	4
OJICUG	3	10
SENWAL	4	11
SERKEG	5	1
FAKLOU	6	3
FEFDAX	7	9
RAXCOK	8	2
CUHPUR	9	6
UTEWUM	10	7
UTEWOG	11	12
BIBXUH	12	14
MATVEJ	13	15
TERFUT	14	13
ZESFUY	15	8

Table 4.A.8 summarizes the sensitivity of rank order correlation between two process models as a function of different choice of En_{CO2} constraints. The choice of En_{CO2} constraints were made within En_{CO2} range where En_{CO2}-Pu_{CO2} Pareto fronts were likely to cross over each other.

Table 4.A.8. Spearman's rank-order correlation (ρ) between rankings of 15 MOFs from rigorous process modeling and idealized PSA process modeling. MOF rankings are provided from objectives of En_{CO2}-Pu_{CO2} using achievable Pu_{CO2} as a function of choice of En_{CO2}. Spearman's rank-order correlation for rankings made at corresponding En_{CO2} constraints are shown.

Rigorous Process Model	**Idealized PSA Process Model**		
	En_{CO2} = 350 kWh/t	En_{CO2} = 400 kWh/t	En_{CO2} = 450 kWh/t
En_{CO2} = 350 kWh/t	ρ = 0.71	-	-
En_{CO2} = 400 kWh/t	-	ρ = 0.54	-
En_{CO2} = 450 kWh/t	-	-	ρ = 0.41

As for the last comparison of the rankings of MOFs in terms of their performance derived from models of multiple levels of complexity and fidelity, Figure 4.A.5 summarizes Spearman's rank-order correlation between rankings of 15 MOFs from from idealized PSA process model and adsorbent evaluation metrics. This is a similar analysis that was made in Figure 4.7 but with "pseudo"-process scale performance derived from a simplified process model. Unlike the observations for the rigorous process modeling, $S_{ads,CO2/N2}^{ads}$, $S_{SP,CO2/N2}$, and $APS_{CO2/N2}$ appeared to be highly successful metrics for predicting pseudo-process scale performance. On the other hand, ΔN_{CO2} and R were found as relatively poor proxies for predicting pseudo-process scale performance. It may imply the importance of process optimization for each material that can cause considerable variation in process-level evaluation of those materials.

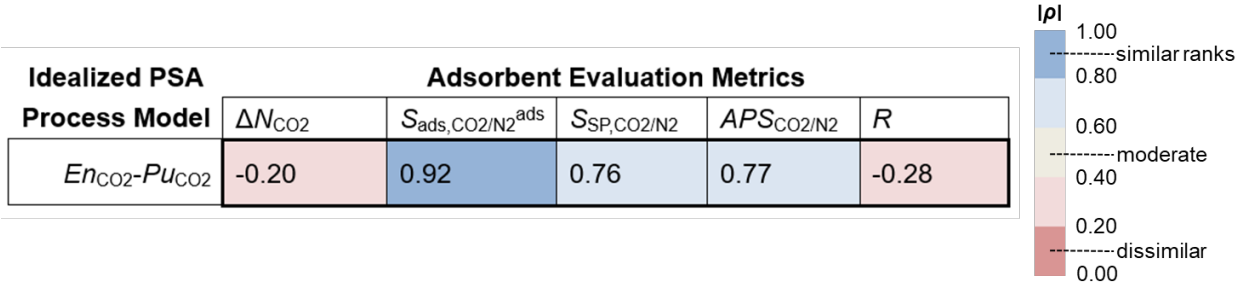

Figure 4.A.5. Spearman's rank-order correlation (ρ) between rankings of 15 MOFs from idealized PSA process modeling (vertical axis) and adsorbent evaluation metrics (horizontal axis). MOFs ranked by idealized process model are based on Pu_{CO2} at a fixed En_{CO2} of 400 kWh/t (Table 4.A.7). MOFs ranked by adsorbent evaluation metrics are based on the relative performance of materials using each metric (Table 4.A.4).

4.A.7 Numerical Data for Analysis

Table 4.A.9. List of 143 MOFs and swing capacities (ΔN_{CO2} in mol/kg) estimated from CO_2 single component adsorption data.

CSD code	ΔN_{CO2}	CSD code	ΔN_{CO2}	CSD code	ΔN_{CO2}	CSD code	ΔN_{CO2}	CSD code	ΔN_{CO2}
BETGAK	6.67	ZIKJIO	13.75	VACFOV01	7.10	FAPTOH	7.18	HIHGOW	7.18
NUVWIL	6.17	CANRUG	6.34	WONZOP	19.17	FECZAQ	9.56	IBICAZ	6.28
OTAVOV	5.15	KAYBUJ	4.16	WONZUV	17.55	FEFCUQ	12.73	IBICED	5.58
QOCRUW	6.10	NALWOO	5.79	XIBZUF	4.96	FEFDAX	12.67	IBICON	5.53
ANUGIA	22.41	NOCKUM	5.59	ZESFUY	11.49	FERHAN	12.31	IBIDAA	5.73
FIQCEN	14.10	XENKIM	6.77	AFITIT	6.08	FIJCUX	6.23	IGOCOX	5.66
FUSWIA	7.22	BIBXUH	15.90	AMILUE	7.71	FIJCUX01	6.28	ISOHEE	10.47
JAVNIE	7.97	DUXZIG01	5.87	AMIMEP	7.85	FUNBEW	13.83	JIVFUQ	4.52
LAGCED	5.30	EBEMEF	5.88	BEPMIU	7.47	FUNBIA	6.05	KEFBEE	20.26
LASYOU	12.52	IXODUV	9.25	BEPPAP	7.51	FUNBOG	9.45	KEWZOD	10.08
MOCKEV	17.31	IXOFAD	9.35	BICDAU	12.82	FUNCAT	8.80	LAWGEW	7.04
MOYYEF	9.61	IXOFEH	9.28	COGWEB	7.66	FUNCEX	6.81	LAWGIA	7.07
MOYYIJ	9.19	IXOFIL	9.34	CUHPUR	11.73	FUTKEL	5.73	LAWGOG	6.92
NUTQAV	18.99	LAGNUE	5.22	DEYVUA	4.93	GACQAE	11.07	LAWGUM	7.10
NUTQEZ	17.55	LOQLEJ	7.98	DIDDOK	20.65	GIMSIG	5.53	LUVTEC	6.73
RAZYIC	5.62	ODIXEG	21.78	ECAHAT	6.92	GUYLOC	6.23	MATTUX	6.21
RAZYOI	6.75	OJICUG	19.03	EDUSIF	6.85	GUYMAP	6.05	MATVAF	9.18
SUKYIH	16.89	RABHAZ	5.88	EMITUQ	7.14	HAMJOW	5.61	MATVEJ	17.47
UTEWUM	15.87	SEHTEF	5.77	EXEWAG	6.62	HIFTOG	5.51	MIBQAR	7.02
XAMDUM07	13.94	SERJUV	6.31	EZUCIM	4.38	HIFTOG01	7.04	MIBQAR16	7.08
XAWVUN	13.11	SERKEG	6.90	FAKLOU	11.94	HIFTOG02	5.51	MIBQAR18	6.99
YUGLES	18.97	UTEWOG	14.60	FAPTIB	7.79	HIFVOI	6.91	MODNIC	4.47

Table 4.A.9. Continued.

CSD code	ΔN_{CO2}	CSD code	ΔN_{CO2}	CSD code	ΔN_{CO2}	CSD code	ΔN_{CO2}	CSD code	ΔN_{CO2}
OFERUN02	6.71	RELLAW	9.12	SENWAL	21.72	UWELIS	5.67	XINFUW	12.57
OFUYUL	4.96	RIFDUG01	14.96	SENWIT	19.95	VAZTOG	6.98	XINWUO	5.53
PEVPUD	6.90	SAHYOQ03	7.10	SENWOZ	21.18	VUSKAW	6.73	XUGSEY	15.27
PIFPIE	5.37	SAHYOQ04	7.07	TASXIW	6.96	VUSKEA	6.72	YARYEV	4.44
QUQFIS	15.22	SAHYOQ05	6.81	TERFUT	11.32	WIYFAM	10.45	YEKXET	9.02
QUQPOI	7.43	SAKRED	9.87	UBUMAH	14.80	XEXMEU	9.07	YEZFIU	7.00
RAXCOK	14.22	SEFBOV	10.99	UNIGEE	6.72				

Table 4.A.10. Adsorbent evaluation metric data (Figure 4.3b) calculated from CO_2/N_2 0.14/0.86 mixture adsorption data in 143 MOFs.

CSD code	ΔN_{CO2} (mol/kg)	S_{ads}^{ads}	S_{SP}	*APS* (mol/kg)	*R* (%)	CSD code	ΔN_{CO2} (mol/kg)	S_{ads}^{ads}	S_{SP}	*APS* (mol/kg)	*R* (%)
BETGAK	6.3	124.1	9.7e3	777.2	60.7	ZIKJIO	12.7	106.3	1.0e4	1.4e3	84.2
NUVWIL	5.8	188.1	6.6e4	1.1e3	96.5	CANRUG	5.9	122.3	1.3e4	723.1	54.9
OTAVOV	4.3	42.9	823.9	184.8	89.9	KAYBUJ	4.3	146.2	2.0e4	625.4	46.4
QOCRUW	5.9	188.1	4.3e4	1.1e3	64.1	NALWOO	4.7	48.0	227.7	224.9	69.1
ANUGIA	16.4	32.9	586.2	540.0	96.5	NOCKUM	5.1	242.6	2.2e5	1.2e3	42.3
FIQCEN	12.2	64.2	1.8e3	782.9	90.2	XENKIM	6.7	278.5	1.4e6	1.9e3	45.5
FUSWIA	6.6	103.5	4.2e3	684.1	69.1	BIBXUH	14.0	71.1	4.0e3	997.9	92.8
JAVNIE	7.4	110.5	5.2e3	817.5	69.7	DUXZIG01	4.0	13.2	49.7	53.3	94.2
LAGCED	4.6	48.6	1.4e3	223.6	88.0	EBEMEF	4.0	13.3	50.9	53.7	94.3
LASYOU	11.6	98.3	1.6e4	1.1e3	86.8	IXODUV	8.4	82.6	8.0e3	695.0	83.1
MOCKEV	16.4	156.3	2.7e4	2.6e3	87.0	IXOFAD	8.5	81.9	7.9e3	697.8	83.4
MOYYEF	8.8	90.0	8.4e3	792.7	87.5	IXOFEH	8.5	89.5	1.1e4	763.5	83.0
MOYYIJ	7.2	26.8	93.8	193.2	81.8	IXOFIL	8.5	80.8	7.4e3	683.9	83.4
NUTQAV	16.4	63.1	3.6e3	1.0e3	95.5	LAGNUE	5.0	119.5	2.6e4	599.1	64.4
NUTQEZ	15.0	57.8	2.6e3	864.3	94.3	LOQLEJ	5.8	30.7	103.9	177.4	77.3
RAZYIC	5.0	87.4	1.1e4	435.1	79.8	ODIXEG	14.7	26.9	192.4	393.6	94.0
RAZYOI	6.0	68.8	3.9e3	414.8	79.2	OJICUG	15.8	45.7	344.6	722.6	86.7
SUKYIH	10.8	21.5	113.7	233.3	92.2	RABHAZ	4.9	40.5	764.8	199.5	94.0
UTEWUM	14.3	103.3	2.4e3	1.5e3	78.7	SEHTEF	5.7	198.2	2.3e5	1.1e3	46.1
XAMDUM07	11.9	59.4	1.5e3	709.1	90.3	SERJUV	5.7	102.1	4.4e3	583.3	79.1
XAWVUN	9.6	13.1	43.3	125.2	95.9	SERKEG	6.7	312.1	1.9e6	2.1e3	85.4
YUGLES	16.3	61.6	3.4e3	1.0e3	95.5	UTEWOG	13.1	100.8	2.4e3	1.3e3	77.5

Table 4.A.10. Continued.

CSD code	ΔN_{CO2} (mol/kg)	S_{ads}^{ads}	S_{SP}	*APS* (mol/kg)	*R* (%)	CSD code	ΔN_{CO2} (mol/kg)	S_{ads}^{ads}	S_{SP}	*APS* (mol/kg)	*R* (%)
VACFOV01	6.7	124.6	7.0e3	834.9	56.8	FAPTOH	6.7	100.6	1.5e4	670.3	73.4
WONZOP	15.0	43.7	778.2	653.5	94.8	FECZAQ	8.6	84.5	4.2e3	727.4	84.3
WONZUV	13.3	35.0	267.9	465.9	89.5	FEFCUQ	11.2	70.4	2.8e3	788.6	89.0
XIBZUF	4.2	298.4	7.1e4	1.2e3	30.3	FEFDAX	11.6	98.1	6.1e3	1.1e3	85.8
ZESFUY	10.7	110.1	1.5e4	1.2e3	82.9	FERHAN	10.1	47.4	620.7	478.1	88.6
AFITIT	5.5	81.0	3.2e3	442.6	79.9	FIJCUX	5.8	107.0	1.4e4	619.2	74.1
AMILUE	6.7	74.6	1.7e3	497.3	83.6	FIJCUX01	5.9	105.1	1.5e4	617.9	76.5
AMIMEP	6.8	75.4	1.5e3	515.0	82.6	FUNBEW	9.3	24.3	57.1	226.6	84.9
BEPMIU	6.7	84.0	4.9e3	558.7	93.4	FUNBIA	5.7	119.3	2.1e4	678.6	76.0
BEPPAP	6.7	84.0	5.1e3	563.1	93.6	FUNBOG	7.1	19.4	14.0	137.3	73.9
BICDAU	8.7	16.5	69.0	143.0	94.3	FUNCAT	7.8	71.9	2.9e3	562.6	85.7
COGWEB	7.2	129.4	1.1e4	937.6	66.2	FUNCEX	5.8	13.5	9.6	78.5	79.3
CUHPUR	10.7	102.8	5.6e3	1.1e3	81.6	FUTKEL	5.2	95.1	2.e3	494.9	63.8
DEYVUA	4.8	98.6	5.6e3	468.1	48.3	GACQAE	9.8	65.7	2.1e3	641.4	87.5
DIDDOK	14.3	25.3	216.7	362.8	95.2	GIMSIG	5.0	67.3	4.9e3	333.4	80.7
ECAHAT	4.6	13.0	71.1	59.2	90.8	GUYLOC	6.0	169.7	5.3e4	1.0e3	64.5
EDUSIF	5.6	10.0	21.6	56.2	95.5	GUYMAP	5.9	158.4	4.4e4	934.2	63.5
EMITUQ	6.7	152.8	1.5e4	1.0e3	65.5	HAMJOW	5.7	205.6	8.6e4	1.2e3	45.1
EXEWAG	6.3	138.0	3.8e4	865.4	70.8	HIFTOG	5.1	95.1	4.2e3	481.6	67.7
EZUCIM	4.2	110.1	4.1e3	460.0	46.5	HIFTOG01	5.7	10.3	22.6	58.7	95.4
FAKLOU	11.3	164.9	4.4e4	1.9e3	82.4	HIFTOG02	5.1	95.0	4.1e3	480.5	67.5
FAPTIB	7.3	124.2	5.5e4	911.5	75.0	HIFVOI	5.1	23.3	64.7	118.4	81.5

Table 4.A.10. Continued.

CSD code	ΔN_{CO2} (mol/kg)	S_{ads}^{ads}	S_{SP}	*APS* (mol/kg)	*R* (%)	CSD code	ΔN_{CO2} (mol/kg)	S_{ads}^{ads}	S_{SP}	*APS* (mol/kg)	*R* (%)
HIHGOW	6.8	111.9	8.0e3	755.9	65.8	OFERUN02	4.8	19.6	150.6	93.0	95.0
IBICAZ	5.7	83.9	4.9e3	474.1	91.6	OFUYUL	5.0	207.1	2.6e5	1.0e3	49.5
IBICED	5.0	78.6	4.4e3	390.4	92.3	PEVPUD	5.9	9.9	21.8	57.9	96.0
IBICON	4.9	78.1	4.2e3	384.9	92.0	PIFPIE	5.2	144.0	3.3e5	743.7	61.2
IBIDAA	5.1	75.1	4.0e3	380.6	92.9	QUQFIS	13.6	75.5	5.4e3	1.0e3	88.7
IGOCOX	5.3	125.5	5.5e4	663.0	63.6	QUQPOI	6.9	120.5	2.4e3	836.7	51.7
ISOHEE	9.6	96.8	7.3e3	929.4	82.6	RAXCOK	13.5	168.8	3.2e4	2.3e3	78.8
JIVFUQ	4.5	187.4	1.5e6	849.5	46.3	RELLAW	8.5	114.1	1.5e4	968.7	80.4
KEFBEE	18.7	103.7	1.2e4	1.9e3	93.7	RIFDUG01	13.9	110.6	6.7e3	1.5e3	86.0
KEWZOD	9.5	120.9	1.6e4	1.1e3	73.7	SAHYOQ03	5.7	10.3	22.4	58.6	95.4
LAWGEW	5.7	10.3	22.6	58.5	95.4	SAHYOQ04	5.8	10.5	23.4	60.9	95.4
LAWGIA	5.7	10.2	22.2	58.3	95.4	SAHYOQ05	5.6	10.0	21.3	55.6	95.4
LAWGOG	5.7	10.3	22.5	58.6	95.4	SAKRED	8.7	65.8	3.5e3	568.6	90.6
LAWGUM	5.7	10.3	23.1	59.3	95.4	SEFBOV	9.6	62.9	3.3e3	605.6	92.8
LUVTEC	5.9	68.2	3.8e3	403.2	92.0	SENWAL	19.7	92.4	8.0e3	1.8e3	96.4
MATTUX	5.9	127.3	2.5e4	748.4	68.3	SENWIT	18.7	139.9	2.0e4	2.6e3	93.4
MATVAF	8.8	164.0	2.2e4	1.4e3	70.1	SENWOZ	19.6	113.4	1.2e4	2.2e3	95.3
MATVEJ	15.4	67.0	2.9e3	1.1e3	92.7	TASXIW	6.8	179.4	1.3e7	1.2e3	65.3
MIBQAR	5.7	10.3	22.9	58.7	95.5	TERFUT	10.1	73.1	3.1e3	734.8	88.8
MIBQAR16	5.7	10.2	22.5	58.3	95.5	UBUMAH	13.3	81.3	7.1e3	1.1e3	93.7
MIBQAR18	5.7	10.2	22.4	58.2	95.5	UNIGEE	5.5	9.8	20.8	53.9	95.5
MODNIC	3.5	24.1	172.9	83.7	94.0	UWELIS	5.6	213.7	1.6e6	1.2e3	44.8

Table 4.A.10. Continued.

CSD code	ΔN_{CO2} (mol/kg)	S_{ads}^{ads}	S_{SP}	*APS* (mol/kg)	*R* (%)	CSD code	ΔN_{CO2} (mol/kg)	S_{ads}^{ads}	S_{SP}	*APS* (mol/kg)	*R* (%)
VAZTOG	5.6	10.1	21.8	57.0	95.4	XINWUO	4.3	28.8	331.9	124.5	93.8
VUSKAW	5.6	9.9	21.4	55.2	95.5	XUGSEY	13.5	75.7	2.2e3	1.0e3	83.9
VUSKEA	5.4	9.7	20.7	52.7	95.6	YARYEV	3.9	40.5	227.3	157.6	85.0
WIYFAM	7.9	26.0	154.7	204.3	90.1	YEKXET	8.5	132.3	1.7e4	1.1e3	74.3
XEXMEU	8.4	122.5	1.9e4	1.0e3	88.1	YEZFIU	6.1	65.1	733.3	400.1	80.3
XINFUW	11.5	92.8	8.0e3	1.1e3	83.9						

Table 4.A.11. Mixture adsorption amounts and adsorption selectivities (Figure 4.4) computed from GCMC and IAST at 243 K in 30 MOFs.

MOFs	N_{CO2} (mol/kg)						N_{N2} (mol/kg)						$S_{ads,CO2/N2}$			
	P_{total} = 0.7 bar		P_{total} = 2.1 bar		P_{total} = 14.3 bar		P_{total} = 0.7 bar		P_{total} = 2.1 bar		P_{total} = 14.3 bar		P_{total} = 0.7 bar		P_{total} = 14.3 bar	
	GCMC	IAST	GCMC	IAST	GCMC	IAST	GCMC	IAST	GCMC	IAST	GCMC	IAST	GCMC	IAST	GCMC	IAST
FIQCEN	1.33	1.35	2.77	2.77	13.54	13.50	0.29	0.28	0.72	0.67	1.30	1.49	27.75	30.04	64.15	55.82
LASYOU	1.76	1.83	6.76	6.94	13.38	13.21	0.50	0.55	0.99	1.09	0.84	0.93	21.53	20.56	98.32	86.94
MOCKEV	2.45	2.48	8.10	8.54	18.82	18.78	0.37	0.36	0.89	0.99	0.74	0.77	40.32	41.79	156.31	149.06
NUTQAV	0.77	0.78	2.15	2.22	17.14	16.45	0.35	0.36	0.92	0.96	1.67	1.91	13.67	13.44	63.12	53.02
NUTQEZ	0.91	0.91	2.68	2.74	15.87	15.52	0.38	0.40	0.98	1.04	1.69	1.91	14.62	14.13	57.76	49.93
UTEWUM	3.86	3.70	6.30	6.17	18.15	18.74	0.30	0.33	0.62	0.64	1.08	1.04	80.28	69.78	103.3	110.23
XAMDUM07	1.28	1.31	2.67	2.67	13.21	13.20	0.29	0.28	0.72	0.66	1.37	1.40	27.01	29.28	59.44	58.09
YUGLES	0.77	0.77	2.13	2.20	17.02	16.41	0.35	0.36	0.92	0.96	1.70	1.86	13.55	13.26	61.63	54.15
ZIKJIO	2.40	2.50	7.42	7.34	15.13	15.47	0.44	0.48	0.92	1.03	0.87	0.92	33.20	32.11	106.26	103.08
BIBXUH	1.10	1.11	3.66	3.86	15.14	14.90	0.36	0.37	0.97	1.08	1.31	1.49	18.66	18.67	71.05	61.51
UTEWOG	3.81	3.68	6.00	5.97	16.95	17.43	0.31	0.33	0.66	0.65	1.03	1.14	76.52	69.00	100.84	93.81
ZESFUY	2.21	2.40	8.10	7.51	12.91	13.33	0.45	0.51	0.82	0.92	0.72	0.82	30.46	29.20	110.08	99.64
CUHPUR	2.42	2.37	6.36	6.56	13.10	13.39	0.33	0.29	0.75	0.69	0.78	0.86	44.46	49.84	102.76	95.27
FAKLOU	2.41	2.54	7.72	7.42	13.69	13.88	0.35	0.39	0.62	0.71	0.51	0.58	42.70	40.12	164.86	146.87
FEFCUQ	1.38	1.41	3.77	3.83	12.58	12.51	0.33	0.34	0.79	0.84	1.10	1.25	25.50	25.14	70.39	61.32
FEFDAX	1.92	1.87	5.21	5.48	13.52	13.75	0.33	0.33	0.77	0.82	0.85	0.96	35.59	34.90	98.12	88.15
KEFBEE	1.26	1.27	4.71	5.14	19.97	19.66	0.37	0.38	1.01	1.12	1.18	1.31	21.04	20.49	103.74	91.87
MATVEJ	1.21	1.25	3.83	3.89	16.56	16.56	0.32	0.34	0.88	0.92	1.45	1.49	22.98	22.92	69.96	68.41
QUQFIS	1.73	1.76	4.84	5.27	15.31	14.93	0.53	0.51	1.21	1.31	1.25	1.39	20.12	21.02	75.53	65.87
RAXCOK	3.64	3.62	10.27	10.40	17.12	17.23	0.41	0.38	0.71	0.78	0.62	0.69	54.92	58.63	168.84	152.02

Table 4.A.11. Continued.

MOFs	N_{CO2} (mol/kg)						N_{N2} (mol/kg)						$S_{ads,CO2/N2}$			
	P_{total} = 0.7 bar		P_{total} = 2.1 bar		P_{total} = 14.3 bar		P_{total} = 0.7 bar		P_{total} = 2.1 bar		P_{total} = 14.3 bar		P_{total} = 0.7 bar		P_{total} = 14.3 bar	
	GCMC	IAST	GCMC	IAST	GCMC	IAST	GCMC	IAST	GCMC	IAST	GCMC	IAST	GCMC	IAST	GCMC	IAST
RIFDUG01	2.25	2.22	6.30	6.58	16.12	16.11	0.32	0.31	0.78	0.84	0.90	0.94	43.78	43.81	110.57	105.09
SENWAL	0.73	0.76	2.62	2.61	20.44	20.06	0.24	0.26	0.75	0.76	1.36	1.51	18.85	18.19	92.39	81.84
SENWIT	1.32	1.30	4.79	5.24	19.99	19.77	0.27	0.27	0.82	0.91	0.88	0.94	29.56	29.23	139.88	129.85
SENWOZ	0.97	1.00	3.55	3.75	20.53	20.37	0.25	0.26	0.79	0.83	1.11	1.26	23.62	23.62	113.37	99.39
TERFUT	1.27	1.28	3.33	3.41	11.32	11.19	0.29	0.30	0.71	0.75	0.95	1.04	26.54	25.77	73.13	66.27
UBUMAH	0.90	0.91	3.54	3.89	14.19	13.90	0.33	0.35	0.91	0.98	1.07	1.22	16.58	16.22	81.25	69.65
XINFUW	2.22	2.35	7.41	7.18	13.76	13.91	0.48	0.54	0.96	1.01	0.91	0.93	28.57	26.56	92.8	92.15
XUGSEY	2.58	2.58	5.73	5.94	16.06	16.27	0.40	0.34	0.97	0.87	1.30	1.49	39.45	46.23	75.65	66.8
SERKEG	1.14	1.19	3.35	3.29	7.84	7.47	0.15	0.16	0.32	0.32	0.15	0.17	47.65	46.37	312.13	285.02
OJICUG	2.42	2.28	5.98	6.15	18.22	19.64	0.33	0.29	0.96	0.84	2.45	2.35	45.26	48.45	45.73	53.79

4.A.8 References for Appendix 4.A

(1) Duren, T.; Bae, Y. S.; Snurr, R. Q. Using molecular simulation to characterise metal-organic frameworks for adsorption applications. *Chem. Soc. Rev.* **2009,** *38*, 1237-1247.

(2) Coudert, F. X.; Fuchs, A. H. Computational characterization and prediction of metal-organic framework properties. *Coord. Chem. Rev.* **2016,** *307*, 211-236.

(3) Li, J. R.; Ma, Y. G.; McCarthy, M. C.; Sculley, J.; Yu, J. M.; Jeong, H. K.; Balbuena, P. B.; Zhou, H. C. Carbon dioxide capture-related gas adsorption and separation in metal-organic frameworks. *Coord. Chem. Rev.* **2011,** *255*, 1791-1823.

(4) Dubbeldam, D.; Calero, S.; Ellis, D. E.; Snurr, R. Q. RASPA: molecular simulation software for adsorption and diffusion in flexible nanoporous materials. *Mol. Simulat.* **2016,** *42*, 81-101.

(5) Dubbeldam, D.; Torres-Knoop, A.; Walton, K. S. On the inner workings of Monte Carlo codes. *Mol. Simulat.* **2013,** *39*, 1253-1292.

(6) Addicoat, M. A.; Vankova, N.; Akter, I. F.; Heine, T. Extension of the Universal Force Field to Metal-Organic Frameworks. *J. Chem. Theory Comput.* **2014,** *10*, 880-891.

(7) Rappe, A. K.; Casewit, C. J.; Colwell, K. S.; Goddard, W. A.; Skiff, W. M. UFF, A Full Periodic-Table Force-Field for Molecular Mechanics and Molecular Dynamics Simulations. *J. Am. Chem. Soc.* **1992,** *114*, 10024-10035.

(8) Martin, M. G.; Siepmann, J. I. Transferable potentials for phase equilibria. 1. United-atom description of n-alkanes. *J. Phys. Chem. B* **1998,** *102*, 2569-2577.

(9) Allen, M. P.; Tildesley, D. J. *Computer Simulation of Liquids*; Oxford University Press: New York, 1987.

(10) Wells, B. A.; Chaffee, A. L. Ewald Summation for Molecular Simulations. *J. Chem. Theory Comput.* **2015**, *11*, 3684-3695.

(11) Manz, T. A.; Sholl, D. S. Chemically Meaningful Atomic Charges That Reproduce the Electrostatic Potential in Periodic and Nonperiodic Materials. *J. Chem. Theory Comput.* **2010**, *6*, 2455-2468.

(12) Manz, T. A.; Sholl, D. S. Improved Atoms-in-Molecule Charge Partitioning Functional for Simultaneously Reproducing the Electrostatic Potential and Chemical States in Periodic and Nonperiodic Materials. *J. Chem. Theory Comput.* **2012**, *8*, 2844-2867.

(13) Watanabe, T.; Manz, T. A.; Sholl, D. S. Accurate Treatment of Electrostatics during Molecular Adsorption in Nanoporous Crystals without Assigning Point Charges to Framework Atoms. *J. Phys. Chem. C* **2011**, *115*, 4824-4836.

(14) Willems, T. F.; Rycroft, C. H.; Kazi, M.; Meza, J. C.; Haranczyk, M. Algorithms and tools for high-throughput geometry-based analysis of crystalline porous materials. *Micropor. Mesopor. Mat.* **2012**, *149*, 134-141.

(15) Pinheiro, M.; Martin, R. L.; Rycroft, C. H.; Haranczyk, M. High accuracy geometric analysis of crystalline porous materials. *CrystEngComm* **2013**, *15*, 7531-7538.

(16) Do, D. D.; Nicholson, D.; Do, H.D. On the Henry constant and isosteric heat at zero loading in gas phase adsorption. *J. Colloid Interface Sci.* **2008**, *324*, 15-24.

(17) Dickey, A. N.; Ozgur Yazaydin, A.; Willis, R. R.; Snurr, R. Q. Screening CO_2/N_2 selectivity in metal-organic frameworks using Monte Carlo simulations and ideal adsorbed solution theory. *Can. J. Chem. Eng.* **2012**, *90*, 825-832.

(18) Chung, Y. G.; Camp, J. S.; Haranczyk, M.; Sikora, B. J.; Bury, W.; Krungleviciute, V.; Yildirim, T.; Farha, O. K.; Sholl, D. S.; Snurr, R. Q. Computation-Ready, Experimental Metal-Organic Frameworks: A Tool To Enable High-Throughput Screening of Nanoporous Crystals. *Chem. Mater.* **2014,** *26*, 6185-6192.

(19) Nazarian, D.; Camp, J. S.; Sholl, D. S. A Comprehensive Set of High-Quality Point Charges for Simulations of Metal-Organic Frameworks. *Chem. Mater.* **2016,** *28*, 785-793.

(20) Nazarian, D.; Camp, J. S.; Chung, Y. G.; Snurr, R. Q.; Sholl, D. S. Large-Scale Refinement of Metal-Organic Framework Structures Using Density Functional Theory. *Chem. Mater.* **2017,** *29*, 2521-2528.

(21) Park, J.; Lively, R. P.; Sholl, D. S. Establishing upper bounds on CO_2 swing capacity in sub-ambient pressure swing adsorption *via* molecular simulation of metal-organic frameworks. *J. Mater. Chem. A* **2017**, *5*, 12258-12265.

(22) Yang, R. T. *Gas Separation by Adsorption Processes*; Imperical College Press: London, 1987.

(23) Braun, E.; Zurhelle, A. F.; Thijssen, W.; Schnell, S. K.; Lin, L. C.; Kim, J.; Thompson, J. A.; Smit, B. High-throughput computational screening of nanoporous adsorbents for CO_2 capture from natural gas. *Mol. Syst. Des. Eng.* **2016**, *1*, 175-188.

(24) Bae, Y. S.; Snurr, R. Q. Development and Evaluation of Porous Materials for Carbon Dioxide Separation and Capture. *Angew. Chem. Int. Ed.* **2011**, *50*, 11586-11596.

(25) Wilmer, C. E.; Farha, O. K.; Bae, Y. S.; Hupp, J. T.; Snurr, R. Q. Structure-property relationships of porous materials for carbon dioxide separation and capture. *Energy Environ. Sci.* **2012**, *5*, 9849-9856.

(26) Wu, D.; Yang, Q.; Zhong, C.; Liu, D.; Huang, H.; Zhang, W.; Maurin, G. Revealing the Structure-Property Relationships of Metal-Organic Frameworks for CO_2 Capture from Flue Gas. *Langmuir* **2012**, *28*, 12094-12099.

(27) Garcia, E. J.; Perez-Pellitero, J.; Pirngruber, G. D.; Jallut, C. Sketching a Portrait of

the Optimal Adsorbent for CO_2 Separation by Pressure Swing Adsorption. *Ind. Eng. Chem. Res.* **2017**, *56*, 4818-4829.

(28) Ga, S.; Jang, H.; Lee, J. H. New performance indicators for adsorbent evaluation derived from a reduced order model of an idealized PSA process for CO_2 capture. *Comput. Chem. Eng.* **2017**, *102*, 188-212.

(29) Myers, A. L.; Prausnitz, J. M. Thermodymanics of mixed-gas adsorption. *AIChE J.* **1965**, *11*, 121-127.

(30) Walton, K. S.; Sholl, D. S. Predicting Multicomponent Adsorption: 50 Years of the Ideal Adsorbed Solution Theory. *AIChE J.* **2015**, *61*, 2757-2762.

(31) Rubiera Landa, H. O.; Flockerzi, D.; Seidel-Morgenstern, A. A Method for Efficiently Solving the IAST Equations with an Application to Adsorber Dynamics. *AIChE J.* **2013**, *59*, 1263-1277.

(32) Do, D. D. *Adsorption Analysis: Equilibria and Kinetics*; Imperical College Press: London, 1998.

(33) Kawajiri, Y.; Biegler, L. T. Nonlinear Programming Superstructure for Optimal Dynamic Operations of Simulated Moving Bed Processes. *Ind. Eng. Chem. Res.* **2006**, *45*, 8503-8513.

(34) Linders, M. J. G.; van den Broeke, L. J. P.; Kapteijn, F.; Moulijn, J. A.; van Bokhoven, J. J. G. M. Binary Adsorption Equilibrium of Organics and Water on Activated Carbon. *AIChE J.* **2001**, *47*, 1885-1892.

(35) Rubiera Landa, H. O.; Lively, R. P.; Kawajiri, Y.; Realff, M. J. *Theoretical investigation of vacuum pressure-swing adsorption process applying thermally-modulated fiber composite adsorbents*. Unpublished manuscript.

(36) Glueckauf, E. Theory of chromatography. Part 10.–Fomulae for diffusion into spheres and their application to chromatography. *Trans. Faraday Soc.* **1955,** *51*, 1540-1551.

(37) Sircar, S. Adsorbate mass transfer into porous adsorbents – A practical viewpoint. *Sep. Purif. Technol.* **2018,** *192*, 383-400.

(38) Happel, J. Viscous Flow Relative to Arrays of Cylinders. *AIChE J.* **1959**, *5*, 174-177.

(39) Surana, K. S.; Joy, A. D.; Quiros Fonseca, L. A.; Reddy, J. N. Mathematical Models and Numerical Solutions of Liquid-Solid and Solid-Liquid Phase Change. *J. Therm. Eng.* **2015**, *1*, 61-98.

(40) Schiesser, W. E. *The Numerical Method of Lines: Integration of Partial Differential Equations*; Academic Press: San Diego, 1991.

(41) Vreugdenhil, C. B.; Koren, B. *Numerical Methods for Advection-Diffusion Problems: Notes on Numerical Fluid Mechanics*; Vieweg: Berlin, 1993.

(42) Gear, C. W. *Numerical Initial Value Problems in Ordinary Differential Equations*; Prentice-Hall: Upper Saddle River, 1971.

(43) MATLAB, *Version 9.5.0. (R2018b)*; The MathWorks Inc.: Natick, Massachusetts, 2018.

(44) Deb, K.; Pratap, A.; Agarwal, S.; Meyarivan, T. A Fast and Elitist Multiobjective Genetic Algorithm: NSGA-II. *IEEE Trans. Evol. Comput.* **2002**, *6*, 182-197.

(45) Piantadosi, J.; Howlett, P.; Boland, J. Matching the grade correlation coefficient using a copula with maximum disorder. *J. Ind. Manag. Optim.* **2007**, *3*, 305-312.

(46) Fieller, E. C.; Hartley, H. O.; Pearson, E. S. Tests for Rank Correlation Coefficients. I. *Biometrika* **1957**, *44*, 470-481.

CHAPTER 5. IMPACT OF INTRINSIC FRAMEWORK FLEXIBILITY FOR SELECTIVE ADSORPTION OF SARIN IN NON-AQUEOUS SOLVENTS USING METAL-ORGANIC FRAMEWORKS

Molecular modeling of mixture adsorption in nanoporous materials can provide insight into the molecular-level details that underlie adsorptive separations. Modeling of adsorption often employs a rigid framework approximation for computational convenience. All real materials, however, have intrinsic flexibility due to thermal vibrations. In this chapter, we examine quantitative predictions of the adsorption selectivity for a dilute concentration of a chemical warfare agent, sarin, from bulk mixtures with aqueous and non-aqueous (methanol, isopropyl alcohol) solvents using metal-organic frameworks (MOFs). These predictions were made in MOFs approximated as rigid and also in MOFs allowed to have intrinsic flexibility. Including framework flexibility appears to be important for making quantitative predictions of adsorption selectivity, particularly for sarin/water mixtures. Our observations suggest the intrinsic flexibility of MOFs can have a nontrivial impact on adsorption modeling of molecular mixtures, particularly for mixtures containing polar species and molecules of different sizes.

* Contents of this chapter are part of a manuscript in preparation

Jongwoo Park, Mayank Agrawal, Dorina F. Sava Gallis, Jacob A. Harvey, Jeffery A. Greathouse, David S. Sholl, ″Impact of Intrinsic Framework Flexibility for Selective Adsorption of Sarin in Non-Aqueous Solvents using Metal-Organic Frameworks″, *in preparation*.

5.1 INTRODUCTION

Due to the extremely toxic properties of chemical warfare agents (CWAs)[1,2], efforts have been made to develop methods and materials for the detection and destruction of CWAs[3-5]. Sarin, for instance, is an organophosphate nerve agent, one of the major categories of CWAs.[6,7] Catalytic degradation of CWAs into less toxic compounds using porous materials is a viable method of decontaminating these agents. Activated carbon and metal oxides have been widely investigated for this purpose, but finding alternative types of protective materials is of significant interest.[2,3] Metal-organic frameworks (MOFs) have emerged as promising candidates due to their large pores that enable easy access of CWAs to internal catalytic sites.[4-10] Nonetheless, an efficient detoxification procedure for CWAs in porous materials can be possible only if CWAs are selectively captured in those materials.[11,12] It is therefore useful to consider adsorption properties of CWAs before their catalytic activity is examined.

The majority of studies of catalytic degradation of CWAs to date have focused on hydrolysis.[13-19] Nucleophilic water substitutes at the phosphorus atom of the agent via hydrolysis that leads to elimination of the toxic leaving group.[17-20] Nevertheless, situations exist where hydrolysis reactions are not appropriate. The damage-free decontamination of electronics after exposure to CWAs, for example, is incompatible with hydrolysis.[21] This motivates interest in the detection and detoxification of CWAs in non-aqueous solvents.[21-24] In the context of considering adsorption of CWAs in the nanopores of MOFs, these observations motivated us to examine the adsorption selectivity for CWAs in the presence of a range of solvents using MOFs.

Molecular modeling has been used to predict the adsorption properties of a variety of adsorbing molecules in a wide range of MOFs.[25-29] Adsorption modeling of this kind, often referred to high-throughput materials screening, almost always assumes that the MOF structure can be held rigid during simulation of adsorption, an assumption that leads to very significant computational efficiencies. This approximation assumes that the relaxation of the framework atoms due to the presence of adsorbed molecules can be neglected.[30-33] Although there are classes of MOFs that undergo significant adsorption-induced deformations, including swelling and transitions between bistable states,[34] there are also many MOFs for which assuming that the change in volume in response to adsorption, ΔV, is zero is well justified. In all MOFs, however, and indeed in all materials, thermal vibrations cause atoms to move with small displacements.[35-37] We refer to these movements as the intrinsic flexibility of the adsorbent. Several recent studies have shown that this intrinsic flexibility can in some cases have a nontrivial impact on the predictions of molecular modeling of adsorption in MOFs.[38-41]

In this chapter, we examine the adsorption of sarin in MOFs in the presence of water, methanol, and isopropyl alcohol via molecular simulations for a collection of 23 sarin-selective hydrophobic MOFs. In each material, we examined the impact of intrinsic flexibility with $\Delta V = 0$ on adsorption selectivity. Our findings provide insight on the impact of this kind of flexibility on mixture adsorption when molecular mixtures consist of adsorbates of different polarities and sizes which, to our best knowledge, has not been examined before.

5.2 COMPUTATIONAL METHODS

5.2.1 MOF Selection Criteria and Bulk Mixture Conditions

We selected a set of adsorbent materials from a large collection of experimentally known MOFs. A subset of the CoRE MOF database[42] for which high-quality atomic point charges have been assigned[43] contains 2932 crystal structures. It has been reported that Zr-based UiO-66 and its derivatives are effective catalysts for sarin degradation.[14-19,44,45] We therefore also considered UiO-66 and 36 UiO-66 derivatives with distinctive functional groups.[46] The same type of atomic point charges as for the CoRE MOF database have been assigned previously to these frameworks.[46] This gave an initial set of 2969 MOFs.

Because it is computationally intensive to carry out molecular simulations for adsorption of bulky molecules in MOFs with intrinsic flexibility, we needed to reduce the number of materials. The material selection criteria used in this chapter is illustrated in Figure 5.1. We aimed to find CWA-selective, hydrophobic MOFs with sufficient pore size to admit sarin. 2469 structures were first chosen from the initial set that have largest cavity diameters larger than 4 Å, indicating a sufficient pore size to admit sarin. We then selected CWA-selective hydrophobic MOFs in order to find materials that would be suitable for CWA capture under humid conditions. To do so, we used the constraints of Henry constants (K_H) as suggested in similar earlier work by Matito-Martos et al.[11,47] We calculated room temperature Henry constants for sarin and soman, another extensively studied nerve agent[1-3], ($K_{H,CWA}$) and that for water ($K_{H,H2O}$) using methods defined further below. Including information about the adsorption affinity of soman gives a more general perspective on finding CWA-selective materials candidates, although below we

exclusively examine the adsorption of sarin. We retained only those MOFs for which $K_{H,CWA}$ was larger than 10^{-3} mol/kg·Pa for both sarin and soman and also had $K_{H,H2O}$ less than 10^{-5} mol/kg·Pa. This selection procedure resulted in 23 MOFs. More information about these 23 materials is given in Appendix 5.A (Table 5.A.1).

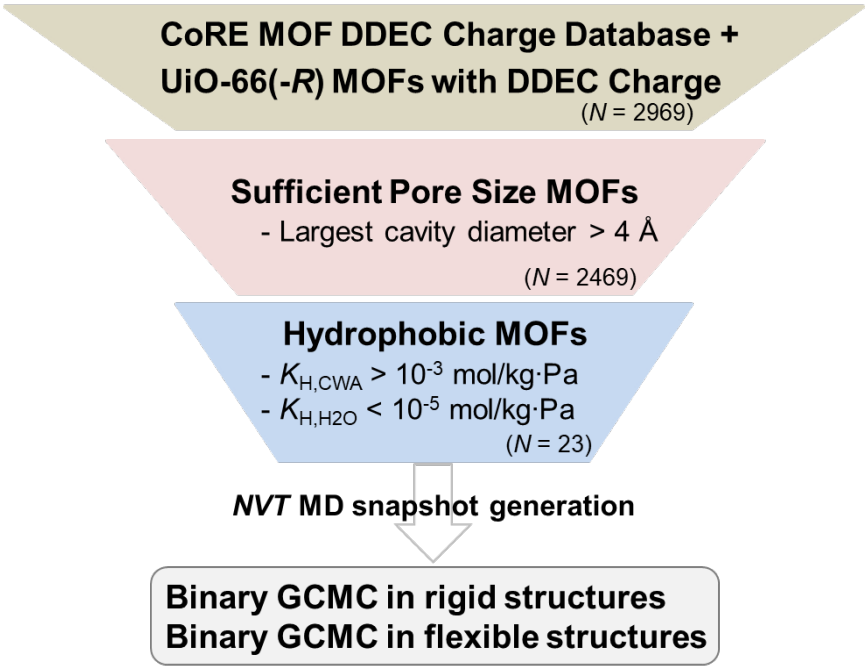

Figure 5.1. Schematic illustration of the MOF selection strategy. The number of MOFs at each stage are shown in brackets (*N*).

We explored the adsorption of sarin in the presence of three solvents at 298 K, sarin/water (H_2O), sarin/methanol (MeOH), and sarin/isopropyl alcohol (IPA). The mixture compositions in the bulk phase were defined by the partial pressures of sarin (P_{sarin}) and each solvent *i* (P_i). To represent a dilute concentration of sarin in solvent saturated environments, we set P_{sarin} = 0.001 bar in mixtures with P_i set to the saturation pressure of each solvent (P^0_i). The adsorption selectivity for sarin at was then calculated at total pressures of each mixture.[48] Figure 5.2 shows atomic representations of sarin and the solvent molecules.

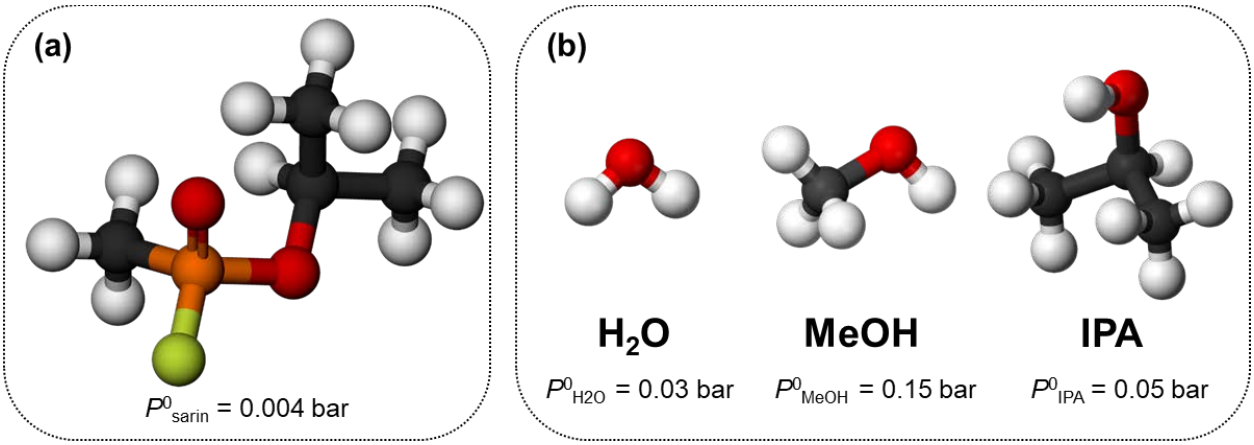

Figure 5.2. Atomic representations of (a) sarin and (b) solvent molecules. Carbon, oxygen, hydrogen, phosphorus, and fluorine are shown in black, red, white, orange, and yellow, respectively. Room temperature saturation pressures for each molecule that were used to determine the bulk mixture compositions are also shown. P^0_{sarin} is taken from the literature[2] and $P^0_{solvent}$ were defined using the Antoine equation[49] at 298 K.

5.2.2 Flexible Snapshot Method

We performed simulations allowing intrinsic flexibility for the 23 MOFs chosen above. The flexible snapshot method first introduced by Gee et al.[40] was used to generate an ensemble of empty MOF frameworks by simulating the dynamics of each MOF.[41] *NVT* molecular dynamics (MD) simulations were conducted after structure relaxation using classical force fields[50] in LAMMPS[51] at 300 K with a time step of 1.0 fs. Each MOF was described using the UFF4MOF force field of Coupry et al.[50] The temperature was controlled via a Nosé-Hoover thermostat with a 0.1 ps decay period. As a result, *NVT* MD snapshots are generated that represent intrinsically flexible empty MOFs. This method cannot capture aspects of flexibility that might arise due to coupling with adsorbate degrees of freedom.[41] Adsorption in the flexible material was characterized by averaging independent Grand Canonical Monte Carlo (GCMC) simulations of each snapshot.

The computational cost of the flexible snapshot method is proportional to the number of *NVT* MD snapshots employed for GCMC calculations. To this end, selecting uncorrelated MD snapshots from each structure is important.[41] In this chapter, MD snapshots were taken every 100 ps from a production period of 1 ns, which is consistent with the recent work of Agrawal et al.[41] In principle it would also be possible to use *ab initio* MD as an alternative method to generate framework snapshots.[52,53] This method, however, is even more computationally demanding than classical simulations we have used here.

5.2.3 Adsorption Modeling of Rigid and Intrinsically Flexible MOFs

Molecular modeling of adsorption of binary molecular mixtures in MOFs was conducted with GCMC simulations using RASPA.[54,55] MOF structures reported by the CoRE MOF database and a set of UiO-66 derivatives were first relaxed using the UFF4MOF force field[50] in LAMMPS[51] followed by fixing the atoms in the relaxed structures. We refer to these structures as rigid MOFs while carrying out GCMC simulations. GCMC simulations were also performed independently in the snapshots generated for each structure as described above; we refer to these results below as coming from flexible MOFs. To perform GCMC appropriate force fields are needed to describe non-bonding interactions such as van der Waals and Coulombic interactions for adsorbate/adsorbent and adsorbate/adsorbate interactions. Standard force fields were used to compute van der Waals interaction, namely the universal force field (UFF)[56] and the TraPPE[57] force field. Lennard-Jones parameters for MOF atoms and sarin, solvent molecules were taken from UFF and TraPPE force field, respectively. Adsorbate/adsorbent interactions were defined with Lorentz-Berthelot mixing rules.[58] Periodic boundary

conditions were defined in all dimensions and adsorbates were approximated as rigid. Coulombic interactions were modeled pairwise with a long-range Ewald summation scheme.[59] These interactions are computed via the DDEC point charges for MOF atoms[60-62] and TraPPE charges for sarin and solvent molecules[54,55]. Attempted Monte Carlo moves include translation, rotation, regrowth, reinsertion, deletion and insertion of adsorbates with identical probabilities. In addition, a Monte Carlo move that swapped the identity of adsorbed molecules was used.

Henry constants, K_H, for sarin, soman, and water used as a material selection criteria as discussed in Section 5.2.1 were computed via a Widom particle insertion method[63] with the force fields just discussed. All K_H calculations were performed at 298 K in rigid MOFs only. K_H data for all MOFs considered in Figure 5.1 are provided in Table 5.A.2.

Using the flexible snapshot method, the adsorption properties of intrinsically flexible MOFs are approximated by performing independent GCMC simulations in distinct MOF structures taken from MD snapshots. The adsorption data were then averaged over GCMC results from each MD snapshot. We used 10 snapshots for each material. Preliminary tests indicated that this was sufficient to achieve converged results.

5.3 RESULTS AND DISCUSSION

5.3.1 Selective Adsorption of Sarin in Non-/Aqueous Environments

Our discussion focuses on adsorption selectivity for sarin at conditions corresponding to the liquid state for each solvent. This means that the MOFs were typically highly loaded with solvent molecules (see Figure 5.A.1). The computed adsorption

selectivity for sarin in the 23 MOFs at 298 K by employing the rigid framework approximation, S_{Rigid}, is shown in Figure 5.3. As might be expected, chosen MOFs were selective for sarin in every co-adsorbed solvents. This suggests they could be effective for catalytic degradation of sarin, assuming of course that catalytically active sites can be created in each material.

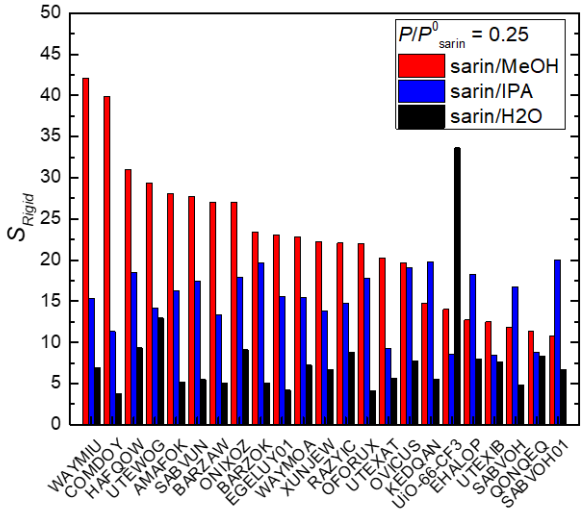

Figure 5.3. Adsorption selectivity for sarin calculated via binary mixture GCMC in rigid approximations of 23 MOFs for each molecular mixture at bulk pressure of $P_{total} = P_{sarin} + P_{solvents}$ at 298 K. Mixture compositions in the bulk phase were defined to give a partial pressure of sarin of $P/P^0_{sarin} = 0.25$ and a solvent partial pressure of $P/P^0_{solvent} = 1$. MOFs are listed in order of decreasing sarin selectivity in the sarin/MeOH mixture.

In almost every MOF, the sarin adsorption selectivity was larger for the non-aqueous solvents than for H_2O. This trend is reasonable because the non-aqueous molecules are larger than water and also typically have weaker adsorption affinity as characterized by K_H (see Table 5.A.2). Based on size alone the sarin/IPA mixture might be expected to show the highest selectivity among the mixtures we examined. IPA, however, has a weaker degree of interaction with polar solutes than MeOH[64] (see also Table 5.A.3). This appears to result in lower adsorption selectivity from sarin/IPA mixtures than from

sarin/MeOH mixtures in most MOFs, although we observed a small number of materials where this trend was reversed.

5.3.2 Impact of Intrinsic MOF Flexibility on Mixture Adsorption Modeling

We repeated the GCMC simulations of adsorption of sarin-containing binary mixtures allowing intrinsic flexibility of the MOFs with $\Delta V = 0$ using the flexible snapshot method. Figure 5.4 compares the computed selectivities from rigid and flexible representations of the MOFs. An immediate observation is that for many of the MOFs there is a clear quantitative discrepancy between the two calculations for all three sarin-containing mixtures. Modeling the MOFs as rigid tends to underestimates the adsorption selectivity, although there are exceptions to this description. In most cases, the increased selectivity in the flexible MOFs was associated with higher adsorbed amounts of sarin and lower adsorbed amounts of the solvent than in the rigid MOF. In examples where the selectivity in the flexible material was smaller than in the rigid material, this typically arose because sarin adsorption was reduced in the flexible materials without as much change in the number of solvent molecules. The observation made above from Figure 5.3 that sarin is more selectively adsorbed from non-aqueous solvents than water is also seen in our simulations of flexible MOFs (see also Figure 5.A.2).

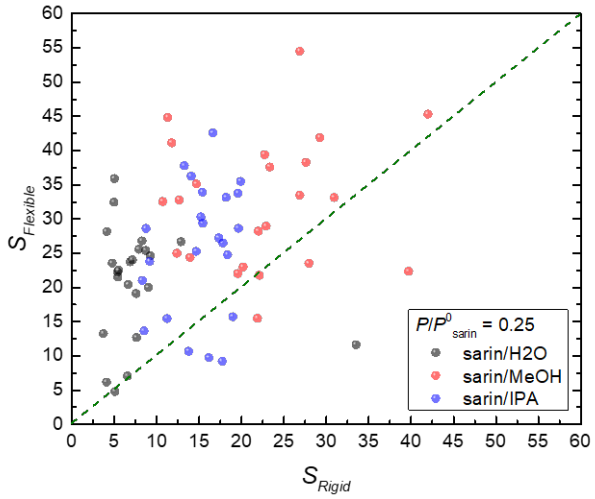

Figure 5.4. Parity plot of adsorption selectivities predicted at 298 K in 23 MOFs approximated as rigid (horizontal axis) and allowed to have intrinsic flexibility (vertical axis) for each molecular mixture. The parity line indicates the result that would be obtained if there was no effect of intrinsic flexibility.

As noted above, high-throughput screening of MOFs or other porous adsorbents essentially always relies on rigid framework calculations because of their computational efficiency. One common goal of material screening is to rank a large number of materials. It is therefore useful to ask whether rankings of MOFs based on rigid and flexible calculations are similar for the sarin mixtures we studied. We approached this by calculating Spearman's rank-order correlation, ρ, to the rankings for sarin/H_2O, sarin/MeOH and sarin/IPA selectivities from rigid and flexible calculations.[65,66] This ranking can vary between -1 and 1, with values of -1, 0 and 1 corresponding to rankings that are anti-correlated, uncorrelated and completely correlated, respectively. For the 23 materials we studied, ρ for sarin/H_2O was 0.08, for sarin/MeOH was 0.15 and for sarin/IPA was 0.23. These values show there is little correlation between the two rankings.[65] To illustrate this another way, the three most selective MOFs from our set of 23 for sarin/MeOH as predicted using rigid structures have CSD reference codes WAYMIU,

COMDOY and HAFQOW (see Figure 5.3). With our calculations for intrinsically flexible structures, these three MOFs are ranked 2nd, 20th and 11th for sarin/MeOH selectivity. This suggests that attempting to accurately select a handful of the "best" MOFs for this separation based on rigid structure calculations may be difficult. It is important to note, however, that the rigid calculations do correctly describe key trends in CWA adsorption. For example, both the rigid and flexible structure calculations predict that sarin selectivity as a function of solvent follows the general trend sarin/MeOH > sarin/IPA > sarin/H_2O mixtures.

Figure 5.5 shows the number of MOF seen as a function of $S_{Flexible}/S_{Rigid}$ for each mixture. For sarin/MeOH and sarin/IPA, the rigid MOF calculations underestimate the result from the flexible materials by 60-70%, on average and the rigid MOFs only overpredict the selectivity in 17% of materials. For sarin/H_2O, however, the rigid MOFs underestimate the selectivity by an average of 322%. The variability in the difference between the rigid and flexible calculations is more marked for aqueous mixtures than non-aqueous mixtures. Three of the 23 MOFs we examined showed more than 600% higher selectivity for sarin/H_2O in the flexible calculations, while for two MOFs the selectivity for the same mixture was overestimated by the rigid MOF calculation.

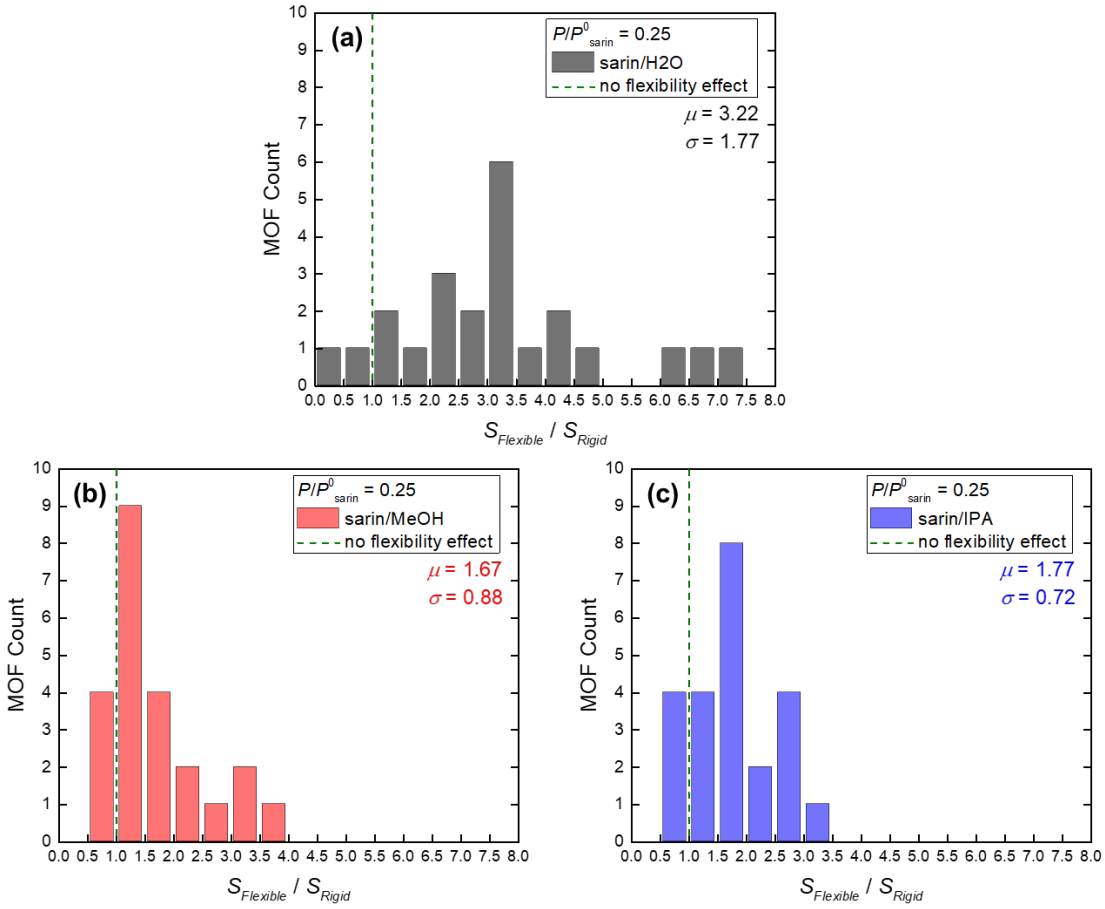

Figure 5.5. The number of MOFs observed as a function of $S_{Flexible}/S_{Rigid}$ in each mixture of (a) sarin/H_2O, (b) sarin/MeOH, and (c) sarin/IPA. Green dashed lines show $S_{Flexible}/S_{Rigid}$ = 1, indicating the situation with no effect of intrinsic flexibility. For each histogram the mean (μ) and standard deviation (σ) on $S_{Flexible}/S_{Rigid}$ are given.

Agrawal et al.[41] recently conducted similar studies for four different bulk mixtures containing equimolar mixtures of nonpolar adsorbates with similar sizes in 100 randomly chosen MOFs. At conditions were the pores were filled with many molecules, the mean and standard deviation of log($S_{Flexible}/S_{Rigid}$) from their simulations were -0.01 and 0.57, respectively. This means that on average the selectivities predicted with rigid structures were quite accurate, although there is considerable variation in this statement from case to case. Describing our data in the same logarithmic terms gives a mean (standard deviation)

of 0.43 (0.30), 0.17 (0.22), and 0.20 (0.21) for sarin/H_2O, sarin/MeOH, and sarin/IPA mixtures, respectively. This indicates that unlike the results of Agrawal et al. the mixtures of polar molecules of disparate sizes that we examined show systematic deviations between rigid and flexible structures, even on average.

5.3.3 Effect of Coulombic Interactions of Molecular Mixtures

It is worthwhile trying to understand what aspects of the adsorbing molecules contribute the most to lack of quantitative agreement between simulations with rigid and flexible MOFs. The bulk mixtures we considered contain solvents that have distinct polarities and molecular sizes, but the results above cannot indicate whether one of these two factors plays a dominant role. To probe this issue, we performed simulations with unphysical nonpolar versions of each solvent by removing the point charges from each solvent molecule. The same binary GCMC simulations as above were carried with these unphysical solvent models for rigid and flexible MOFs. These simulations used the same partial pressures for each component as were used above; we did not attempt to determine the effective vapor pressure of the unphysical solvents.

In Figure 5.6, we repeated the same analysis as in Figure 5.4 but using the unphysical nonpolar solvents in the GCMC simulations. Much, although not all, of the difference between the rigid and flexible results seen in Figure 5.4 disappears when using the nonpolar solvents. This indicates that the polarity of adsorbing species was more responsible for the influence of framework flexibility than solvent size. The decreased sarin selectivity in intrinsically flexible MOFs when using nonpolar solvents occurs primarily because of lower sarin uptakes rather than changes in loadings of solvent molecules relative

to the rigid MOFs. We note that Coulombic interactions in these molecular mixtures are not totally eliminated because the atomic point charges for sarin remained non-zero in these simulations.

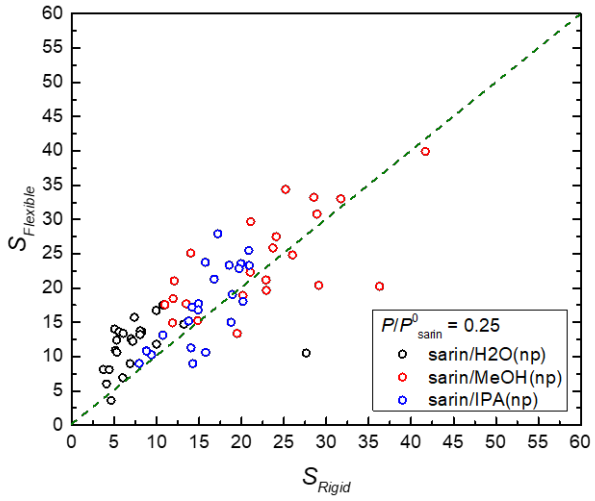

Figure 5.6. Parity plot of adsorption selectivities predicted at 298 K in 23 MOFs approximated as rigid (horizontal axis) and allowed to have intrinsic flexibility (vertical axis) for each molecular mixture using unphysical nonpolar (np) solvents. The parity line indicates the result that would be obtained if there was no effect of intrinsic flexibility.

We revisit in Figure 5.7 the histograms of $S_{Flexible}/S_{Rigid}$ after omitting the point charges on solvent molecules. Both μ and σ were significantly reduced in each binary mixture compared to those shown in Figure 5.5. In agreement with Figure 5.6, this indicates that solvent polarity is more important than solvent size in determining the impact of framework flexibility on selective adsorption of sarin. The selectivity in the sarin/H_2O mixture, however, is still more affected by intrinsic flexibility than other two mixtures. The difference in molecular sizes of sarin and the solvents is largest for sarin/H_2O. This implies that the impact of framework flexibility on adsorption can also be affected by the disparity in molecular size between adsorbing species.

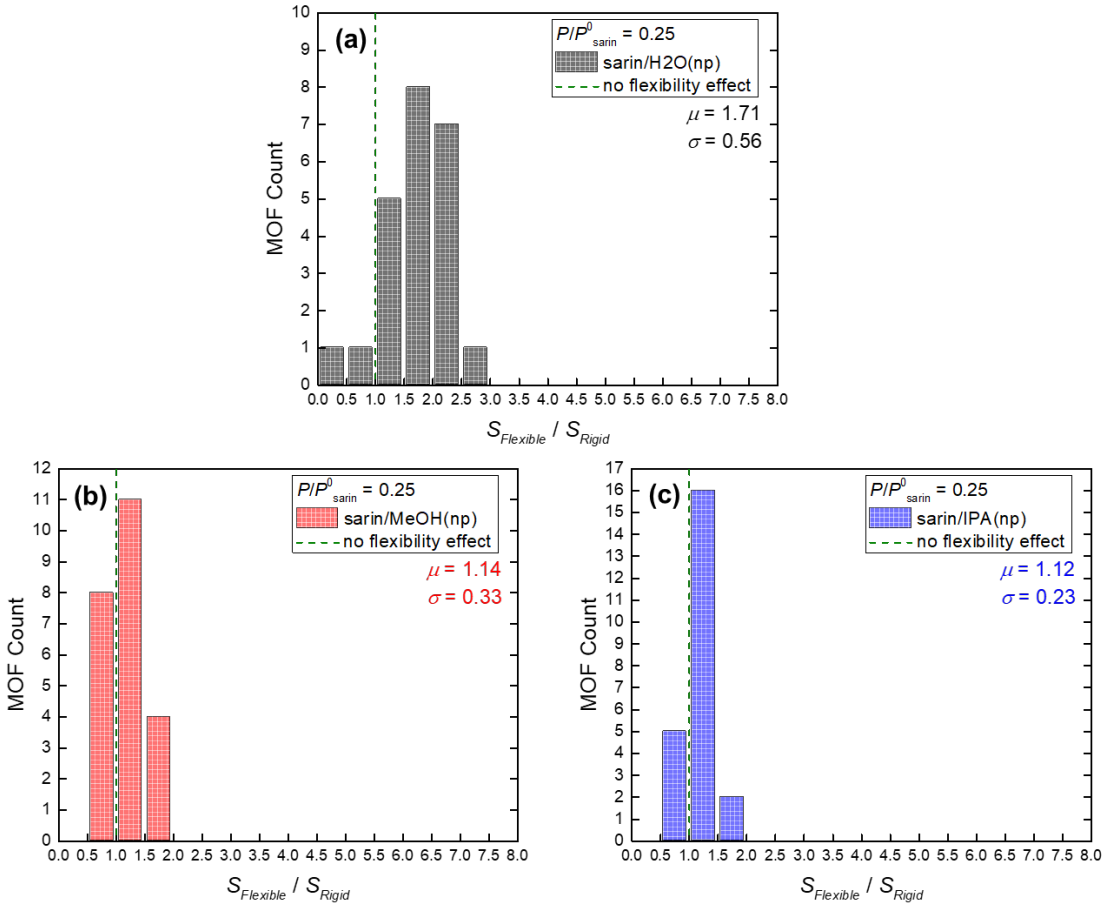

Figure 5.7. The number of MOFs observed as a function of $S_{Flexible}/S_{Rigid}$ in each mixture of (a) sarin/H_2O, (b) sarin/MeOH, and (c) sarin/IPA using unphysical nonpolar (np) solvents. Green dashed lines show $S_{Flexible}/S_{Rigid}$ = 1, indicating the situation with no effect of intrinsic flexibility. For each histogram the mean (μ) and standard deviation (σ) on $S_{Flexible}/S_{Rigid}$ are given.

5.4 SUMMARY

In this chapter, we examined the adsorptive capture of sarin under bulk mixture adsorption conditions with aqueous and non-aqueous solvents in a collection of sarin-selective hydrophobic MOFs that were approximated as rigid and intrinsically flexible. Efficient catalytic degradation of sarin in MOFs under any of non-/aqueous environments can be feasible only if sarin is selectively adsorbed in the frameworks in advance. Quantitative molecular modeling of adsorption, however, can be affected by taking account

of intrinsic flexibility that all porous materials indeed have by nature. Higher adsorption selectivity for sarin in non-aqueous solvents was predicted, both in rigid and intrinsically flexible MOFs, for which indicating the sarin detoxification using those solvents may be viable in properly chosen MOFs when hydrolysis is incompatible. More importantly we assessed the nontrivial deviation in adsorption properties predicted via rigid and intrinsically flexible MOFs. Our observations implied the impact of flexibility of this kind upon mixture adsorption is not negligible for mixtures containing polar adsorbates and adsorbates of disparate sizes.

We exclusively focused on adsorption of sarin in a limited number of materials. Although our observations do not represent the wide spectrum of materials, we were able to make an immediate alert that caution must be used in adsorption modeling of complex molecules combined with including the details in the molecular modeling of adsorption. In addition, we cannot simply expand our findings with respect to adsorption property into catalytic activity of sarin in the same mixtures. However, our assessment suggests that computational explorations on sarin hydrolysis or other catalytic reactions in MOFs also have to be conducted with caution considering the approximations used in their calculations.

5.5 REFERENCES

(1) Sidell, F. R. Soman and Sarin: Clinical Manifestations and Treatment of Accident of Accidental Poisoning by Organophosphates. *Clin. Toxicol.* **1974,** *7*, 1-17.

(2) Delfino, R. T.; Ribeiro, T. S.; Figueroa-Villar, J. D. Organophosphorus Compounds as Chemical Warfare Agents: A Review. *J. Braz. Chem. Soc.* **2009,** *20*, 407-428.

(3) Kim, K.; Tsay, O. G.; Atwood, D. A.; Churchill, D. G. Destruction and Detection of Chemical Warfare Agents. *Chem. Rev.* **2011,** *111*, 5345-5403.

(4) Vellingiri, K.; Philip, L.; Kim, K. H. Metal-organic frameworks as media for the catalytic degradation of chemical warfare agents. *Coord. Chem. Rev.* **2017,** *353*, 159-179.

(5) Liu, Y.; Howarth, A. J.; Vermeulen, N. A.; Moon, S. Y.; Hupp, J. T.; Farha, O. K. Catalytic degradation of chemical warfare agents and their simulants by metal-organic frameworks. *Coord. Chem. Rev.* **2017,** *346*, 101-111.

(6) Peterson, G. W.; Wagner, G. W. Detoxification of chemical warfare agents by CuBTC. *J. Porous Mater.* **2014,** *21*, 121-126.

(7) Mondloch, J. E.; Katz, M. J.; Isley III, W. C.; Ghosh, P.; Liao, P.; Bury, W.; Wagner, G. W.; Hall, M. G.; DeCoste, J. B.; Peterson, G. W.; Snurr, R. Q.; Cramer, C. J.; Hupp, J. T.; Farha, O. K. Destruction of chemical warfare agents using metal-organic frameworks. *Nat. Mater.* **2015,** *14*, 512-516.

(8) Montoro, C.; Linares, F.; Quartapelle Procopio, E.; Senkovska, I.; Kaskel, S.; Galli, S.; Masciocchi, N.; Barea, E.; Navarro, J. A. R. Capture of Nerve Agents and Mustard Gas Analogues by Hydrophobic Robust MOF-5 Type Metal-Organic Frameworks. *J. Am. Chem. Soc.* **2011,** *133*, 11888-11891.

(9) Liu, Y.; Moon, S. Y.; Hupp, J. T.; Farha, O. K. Dual-Function Metal-Organic Framework as a Versatile Catalyst for Detoxifying Chemical Warfare Agent Simulants. *ACS Nano* **2015,** *9*, 12358-12364.

(10) Soares, C. V.; Maurin, G.; Leitao, A. A. Computational Exploration of the Catalytic Degradation of Sarin and Its Simulants by a Titanium Metal-Organic Framework. *J. Phys. Chem. C* **2019,** *123*, 19077-19086.

(11) Matito-Martos, I.; Moghadam, P. Z.; Li, A.; Colombo, V.; Navarro, J. A. R.; Calero, S.; Fairen-Jimenez, D. Discovery of an Optimal Porous Crystalline Material for the Capture of Chemical Warfare Agents. *Chem. Mater.* **2018,** *30*, 4571-4579.

(12) Agrawal, M.; Sava Gallis, D. F.; Greathouse, J. A.; Sholl, D. S. How Useful Are Common Simulants of Chemical Warfare Agents at Predicting Adsorption Behavior? *J. Phys. Chem. C* **2018,** *122*, 26061-26069.

(13) Jang, Y. J.; Kim, K.; Tsay, O. G.; Atwood, D. A.; Churchill, D. G. Update 1 of: Destruction and Detection of Chemical Warfare Agents. *Chem. Rev.* **2015,** *115*, PR1-PR76.

(14) Katz, M. J.; Moon, S. Y.; Mondloch, J. E.; Beyzavi, M. H.; Stephenson, C. J.; Hupp, J. T.; Farha, O. K. Exploiting parameter space in MOFs: a 20-fold enhancement of phosphate-ester hydrolysis with UiO-66-NH_2. *Chem. Sci.* **2015,** *6*, 2286-2291.

(15) Moon, S. Y.; Liu, Y.; Hupp, J. T.; Farha, O. K. Instantaneous Hydrolysis of Nerve-Agent Simulants with a Six-Connected Zirconium-Based Metal-Organic Framework. *Angew. Chem., Int. Ed.* **2015,** *54*, 6795-6799.

(16) Moon, S. Y.; Wagner, G. W.; Mondloch, J. E.; Peterson, G. W.; DeCoste, J. B.; Hupp, J. T.; Farha, O. K. Effective, Facile, and Selective Hydrolysis of the Chemical Warfare Agent VX Using Zr_6-Based Metal-Organic Frameworks. *Inorg. Chem.* **2015,** *54*, 10829-10833.

(17) Momeni, M. R.; Cramer, C. J. Dual Role of Water in Heterogeneous Catalytic Hydrolysis of Sarin by Zirconium-Based Metal-Organic Frameworks. *ACS Appl. Mater. Interfaces* **2018,** *10*, 18435-18439.

(18) Momeni, M. R.; Cramer, C. J. Structure Characterization of Pristine and Defective $[Zr_{12}(\mu_3\text{-}O)_8(\mu_3\text{-}OH)_8(\mu_2\text{-}OH)_6]^{18+}$ Double-Node Metal-Organic Framework and Predicted Applications for Single0Site Catalytic Hydrolysis of Sarin. *Chem. Mater.* **2018,** *30*, 4432-4439.

(19) Momeni, M. R.; Cramer, C. J. Computational Screening of Roles of Defects and Metal Substitution on Reactivity of Different Single- vs Double-Node Metal-Organic Frameworks for Sarin Decomposition. *J. Phys. Chem. C* **2019,** *123*, 15157-15165.

(20) Mendonca, M. L.; Snurr, R. Q. Screening for Improved Nerve Agent Simulants and Insights into Organophosphate Hydrolysis Reactions from DFT and QSAR Modeling. *Chem. Eur. J.* **2019,** *25*, 9217-9229.

(21) Sava Gallis, D. F.; Harvey, J. A.; Pearce, C. J.; Hall, M. G.; DeCoste, J. B.; Kinnan, M. K.; Greathouse, J. A. Efficient MOF-Based Degradation of Organophosphorus Compounds in Non-Aqueous Environments. *J. Mater. Chem. A* **2018,** *6*, 3038-3045.

(22) Mandal, D.; Sen, K.; Das, A. K. Aminolysis of a Model Nerve Agent: A Computational Reaction Mechanism Study of *O,S*-Dimethyl Methylphosphonothiolate. *J. Phys. Chem. A* **2012,** *116*, 8382-8396.

(23) Katz, M. J.; Mondloch, J. E.; Totten, R. K.; Park, J. K.; Nguyen, S. T.; Farha, O. K.; Hupp, J. T. Simple and compelling biomimetic metal-organic framework catalyst for the degradation of nerve agent simulants. *Angew. Chem. Int. Ed.* **2014,** *53*, 497-501.

(24) Wang, S.; Bromberg, L.; Schreuder-Gibson, H.; Hatton, T. A. Organophophorous Ester Degradation by Chromium(III) Terephthalate Metal-Organic Framework (MIL-101) Chelated to *N,N*-Dimethylaminopyridine and Related Aminopyridines. *ACS Appl. Mater. Interfaces* **2013,** *5*, 1269-1278.

(25) Park, J.; Lively, R. P.; Sholl, D. S. Establishing upper bounds on CO_2 swing capacity in sub-ambient pressure swing adsorption *via* molecular simulation of metal-organic frameworks. *J. Mater. Chem. A* **2017**, *5*, 12258-12265.

(26) Park, J.; Howe, J. D.; Sholl, D. S. How Reproducible Are Isotherm Measurement in Metal-Organic Frameworks? *Chem. Mater.* **2017**, *29*, 10487-10495.

(27) Tang, D.; Wu, Y.; Verploegh, R. J.; Sholl, D. S. Efficiently Exploring Adsorption Space to Identify Privileged Adsorbents for Chemical Separations of a Diverse Set of Molecules. *ChemSusChem* **2018,** *11*, 1567-1575.

(28) Keskin, S.; Sholl, D. S. Screening Metal-Organic Framework Materials for Membrane-based Methane/Carbon Dioxide Separations. *J. Phys. Chem. C* **2007,** *111*, 14055-14059.

(29) Altintas, C.; Avci, G.; Daglar, H.; Nemati Vesali Azar, A.; Velioglu, S.; Erucar, I.; Keskin, S. Database for CO_2 Separation Performances of MOFs Based on Computational Materials Screening. *ACS Appl. Mater. Interfaces* **2018,** *10*, 17257-17268.

(30) Duren, T.; Bae, Y. S.; Snurr, R. Q. Using molecular simulation to characterise metal-organic frameworks for adsorption applications. *Chem. Soc. Rev.* **2009,** *38*, 1237-1247.

(31) Coudert, F. X.; Fuchs, A. H. Computational characterization and prediction of metal-organic framework properties. *Coord. Chem. Rev.* **2016,** *307*, 211-236.

(32) Li, J. R.; Ma, Y. G.; McCarthy, M. C.; Sculley, J.; Yu, J. M.; Jeong, H. K.; Balbuena, P. B.; Zhou, H. C. Carbon dioxide capture-related gas adsorption and separation in metal-organic frameworks. *Coord. Chem. Rev.* **2011,** *255*, 1791-1823.

(33) Keskin, S.; Liu, J.; Rankin, R. B.; Johnson, J. K.; Sholl, D. S. Progress, Opportunities, and Challenges for Applying Atomically Detailed Modeling to Molecular Adsorption and Transport in Metal-Organic Framework Materials. *Ind. Eng. Chem. Res.* **2009,** *48*, 2355-2371.

(34) Ferey, G.; Serre, C. Large breathing effects in three-dimensional porous hybrid matter: facts, analyses, rules and consequences. *Chem. Soc. Rev.* **2009,** *38*, 1380-1399.

(35) Lee, J. H.; Jeoung, S.; Chung, Y. G.; Moon, H. R. Elucidation of flexible metal-organic frameworks: Research progresses and recent developments. *Coord. Chem. Rev.* **2019,** *389*, 161-188.

(36) Pimentel, B. R.; Jue, M. L.; Zhou, E. K.; Verploegh, R. J.; Leisen, J.; Sholl, D. S.; Lively, R. P. Sorption and Transport of Vapors in ZIF-11: Adsorption, Diffusion, and Linker Flexibility. *J. Phys. Chem. C* **2019,** *123*, 12862-12870.

(37) Gladysiak, A.; Deeg, K. S.; Dovgaliuk, I.; Chidambaram, A.; Ordiz, K.; Boyd, P. G.; Moosavi, S. M.; Ongari, D.; Navarro, J. A. R.; Smit, B.; Stylianou, K. C. Biporous Metal-Organic Framework with Tunable CO_2/CH_4 Separation Performance Facilitated by Intrinsic Flexibility. *ACS Appl. Mater. Interfaces* **2018,** *10*, 36144-36156.

(38) Witman, M.; Ling, S.; Jawahery, S.; Boyd, P. G.; Haranczyk, M.; Slater, B.; Smit, B. The Influence of Intrinsic Framework Flexibility on Adsorption in Nanoporous Materials. *J. Am. Chem. Soc.* **2017,** *139*, 5547-5557.

(39) Witman, M.; Wright, B.; Smit, B. Simulating Enhanced Methane Deliverable Capacity of Guest Responsive Pores in Intrinsically Flexible MOFs. *J. Phys. Chem. Lett.* **2019,** *10*, 5929-5934.

(40) Gee, J. A.; Sholl, D. S. Effect of Framework Flexibility on C_8 Aromatic Adsorption at High Loadings in Metal-Organic Frameworks. *J. Phys. Chem. C* **2016,** *120*, 370-376.

(41) Agrawal, M.; Sholl, D. S. Effects of Intrinsic Flexibility on Adsorption Properties of Metal-Organic Frameworks at Dilute and Nondilute Loadings. *ACS Appl. Mater. Interfaces* **2019**, *11*, 31060-31068.

(42) Chung, Y. G.; Camp, J.; Haranczyk, M.; Sikora, B. J.; Bury, W.; Krungleviciute, V.; Yildirim, T.; Farha, O. K.; Sholl, D. S.; Snurr, R. Q. Computation-Ready, Experimental Metal-Organic Frameworks: A Tool To Enable High-Throughput Screening of Nanoporous Crystals. *Chem. Mater.* **2014**, *26*, 6185-6192.

(43) Nazarian, D.; Camp, J. S.; Sholl, D. S. A Comprehensive Set of High-Quality Point Charges for Simulations of Metal-Organic Frameworks. *Chem. Mater.* **2016**, *28*, 785-793.

(44) Harvey, J. A.; McEntee, M. L.; Garibay, S. J.; Durke, E. M.; DeCoste, J. B.; Greathouse, J. A.; Sava Gallis, D. F. Spectroscopically Resolved Binding Sites for the Adsorption of Sarin Gas in a Metal-Organic Framework: Insights beyond Lewis Acidity. *J. Phys. Chem. Lett.* **2019,** *10*, 5142-5147.

(45) Harvey, J. A.; Greathouse, J. A.; Sava Gallis, D. F. Defect and Linker Effects on the Binding of Organophosphorous Compounds in UiO-66 and Rare-Earth MOFs. *J. Phys. Chem. C* **2018,** *122*, 26889-26896.

(46) Demir, H.; Walton, K. S.; Sholl, D. S. Computational Screening of Functionalized UiO-66 Materials for Selective Contaminant Removal from Air. *J. Phys. Chem. C* **2017,** *121*, 20396-20406.

(47) Moghadam, P. Z.; Fairen-Jimenez, D.; Snurr, R. Q. Efficient Identification of Hydrophobic MOFs: Application in the Capture of Toxic Industrial Chemicals. *J. Mater. Chem. A* **2015,** *4*, 529-536.

(48) Yang, R. T. *Gas Separation by Adsorption Processes*; Imperial College Press: London, 1987.

(49) Reid, Robert C.; Prausnitz, J. M.; Sherwood, T. K. *Properties of Gases and Liquids*; McGraw-Hill: New York, 1977.

(50) Coupry, D. E.; Addicoat, M. A.; Heine, T. Extension of the Universal Force Field for Metal-Organic Frameworks. *J. Chem. Theory Comput.* **2016,** *12*, 5215-5225.

(51) Plimpton, S. Fast Parallel Algorithms for Short-Range Molecular Dynamics. *J. Comput. Phys.* **1995,** *117*, 1-19.

(52) Watanabe, T.; Sholl, D. S. Accelerating Applications of Metal-Organic Frameworks for Gas Adsorption and Separation by Computational Screening of Materials. *Langmuir* **2012,** *28*, 14114-14128.

(53) Haldoupis, E.; Watanabe, T.; Nair, S.; Sholl, D. S. Quantifying Large Effects of Framework Flexibility on Diffusion in MOFs: CH_4 and CO_2 in ZIF-8. *ChemPhysChem* **2012,** *13*, 3449-3452.

(54) Dubbeldam, D.; Calero, S.; Ellis, D. E.; Snurr, R. Q. RASPA: molecular simulation software for adsorption and diffusion in flexible nanoporous materials. *Mol. Simulat.* **2016,** *42*, 81-101.

(55) Dubbeldam, D.; Torres-Knoop, A.; Walton, K. S. On the inner workings of Monte Carlo codes. *Mol. Simulat.* **2013,** *39*, 1253-1292.

(56) Rappe, A. K.; Casewit, C. J.; Colwell, K. S.; Goddard, W. A.; Skiff, W. M. UFF, A Full Periodic-Table Force-Field for Molecular Mechanics and Molecular Dynamics Simulations. *J. Am. Chem. Soc.* **1992,** *114*, 10024-10035.

(57) Martin, M. G.; Siepmann, J. I. Transferable potentials for phase equilibria. 1. United-atom description of n-alkanes. *J. Phys. Chem. B* **1998,** *102*, 2569-2577.

(58) Allen, M. P.; Tildesley, D. J. *Computer Simulation of Liquids*; Oxford University Press: New York, 1987.

(59) Wells, B. A.; Chaffee, A. L. Ewald Summation for Molecular Simulations. *J. Chem. Theory Comput.* **2015,** *11*, 3684-3695.

(60) Manz, T. A.; Sholl, D. S. Chemically Meaningful Atomic Charges That Reproduce the Electrostatic Potential in Periodic and Nonperiodic Materials. *J. Chem. Theory Comput.* **2010,** *6*, 2455-2468.

(61) Manz, T. A.; Sholl, D. S. Improved Atoms-in-Molecule Charge Partitioning Functional for Simultaneously Reproducing the Electrostatic Potential and Chemical States in Periodic and Nonperiodic Materials. *J. Chem. Theory Comput.* **2012,** *8*, 2844-2867.

(62) Watanabe, T.; Manz, T. A.; Sholl, D. S. Accurate Treatment of Electrostatics during Molecular Adsorption in Nanoporous Crystals without Assigning Point Charges to Framework Atoms. *J. Phys. Chem. C* **2011,** *115*, 4824-4836.

(63) Widom, B. Some Topics in the Theory of Fluids. *J. Chem. Phys.* **1963,** *39*, 2808-2812.

(64) Harvey, J. A.; Pearce, C. J.; Hall, M. G.; Bruni, E. J.; DeCoste, J. B.; Sava Gallis, D. F. *Insights into the solvent-assisted degradation of organophosphorus compounds by a Zr-based metal-organic framework.* Manuscript under revision.

(65) Piantadosi, J.; Howlett, P.; Boland, J. Matching the grade correlation coefficient using a copula with maximum disorder. *J. Ind. Manag. Optim.* **2007**, *3*, 305-312.

(66) Park, J.; Rubiera Landa, H. O.; Kawajiri, Y.; Realff, M. J.; Lively, R. P.; Sholl, D. S. *How Well Do Approximate Models of Adsorption-based CO_2 Capture Processes Predict Results of Detailed Process Models?* Manuscript under review.

APPENDIX 5.A. SUPPORTING INFORMATION – CHAPTER 5

5.A.1 MOF Material Set

Table 5.A.1 curates a list of 23 MOFs chosen via MOF selection criteria illustrated in Figure 5.1 in Chapter 5.

Table 5.A.1. List of 23 MOFs chosen via MOF selection criteria. MOFs are listed with CSD reference codes reported in the CoRE MOF database[1], except UiO-66-CF_3[2], in alphabetical order. The physical properties of MOFs are adapted from the CoRE MOF database and calculated for UiO-66-CF_3 in this work.

MOFs	Metal Type	V_P (cm^3/g)	SA_{acc} (m^2/g)	LCD (Å)	PLD (Å)
AMAFOK	Cu	0.30	513.32	6.60	5.66
BARZAW	Zn	0.26	337.15	7.74	2.56
BZRZOK	Cu	0.28	340.18	7.66	2.74
COMDOY	Ga	0.48	971.33	6.12	5.54
EGELUY01	Al	0.67	1555.22	7.46	7.05
EHALOP	Al	0.65	1632.09	7.57	7.12
HAFQOW	Al	0.65	1593.41	7.39	6.93
KEDQAN	Zn	0.39	551.92	6.47	4.70
OFORUX	Cd, Cu	0.26	264.75	5.54	5.06
ONIXOZ	Cu	0.74	1971.77	9.94	9.19
OVICUS	Zn	0.29	409.62	5.88	5.25
QONQEQ	Al	0.67	1519.12	7.41	7.01
RAZYIC	Cu	0.43	1033.43	7.88	6.21
SABVOH	Al	0.59	1333.73	6.27	5.98
SABVOH01	Al	0.59	1377.25	6.49	6.20
SABVUN	Al	0.61	1439.47	7.02	6.76
UiO-66-CF_3	Zn	0.36	554.21	7.20	3.20
UTEWOG	Ni	0.95	1702.39	14.60	9.55
UTEXAT	Zn	0.61	1068.81	6.27	4.01
UTEXIB	Co	0.60	1082.64	6.30	3.96
WAYMIU	Al	0.60	1412.09	7.35	6.91
WAYMOA	Al	0.65	1471.49	7.08	6.89
XUNJEW	Zn	0.40	778.07	7.72	4.21

* Abbreviations stand for V_P: pore volume; SA_{acc}: accessible surface area; LCD: largest cavity diameter; and PLD: pore limiting diameter.

5.A.2 Adsorption Conditions for Solvents and Mixtures

Table 5.A.2 summarizes Henry constants (K_H) computed via a Widom particle insertion method[3] for sarin, soman, and H_2O in 23 MOFs at 298 K as a part of the material selection criteria. K_H calculated for non-aqueous solvents of MeOH and IPA at 298 K are also summarized.

Table 5.A.2. Henry constants (K_H) computed for CWAs of sarin, soman, and solvents of H_2O, MeOH, IPA in 23 MOFs at 298 K.

MOFs	$K_{H,sarin}$	$K_{H,soman}$	$K_{H,H2O}$	$K_{H,MeOH}$	$K_{H,IPA}$
AMAFOK	1.60E-01	1.75E+01	3.90E-06	5.31E-08	1.27E-08
BARZAW	4.47E-01	2.06E-01	1.55E-06	4.43E-08	1.06E-08
BZRZOK	3.75E-01	1.02E-03	2.06E-06	4.61E-08	1.10E-08
COMDOY	6.10E-02	2.52E+02	5.88E-06	6.28E-08	1.50E-08
EGELUY01	6.47E-03	4.73E+01	7.45E-06	1.75E-07	4.18E-08
EHALOP	5.12E-03	5.04E+01	8.36E-06	1.76E-07	4.19E-08
HAFQOW	5.78E-03	4.29E+02	8.11E-06	1.74E-07	4.17E-08
KEDQAN	6.76E-02	8.94E-03	4.41E-06	5.06E-08	1.21E-08
OFORUX	1.48E-01	2.37E-03	2.11E-06	2.68E-08	6.41E-09
ONIXOZ	2.99E-03	1.18E-03	9.09E-06	9.29E-08	2.22E-08
OVICUS	6.34E-01	1.83E-01	8.57E-06	5.59E-08	1.34E-08
QONQEQ	6.06E-03	2.62E+01	6.88E-06	1.75E-07	4.18E-08
RAZYIC	1.20E-02	5.62E+01	9.39E-06	6.88E-08	1.64E-08
SABVOH	7.91E-02	2.47E+03	6.67E-06	1.65E-07	3.94E-08
SABVOH01	1.14E-01	2.60E+02	6.91E-06	1.64E-07	3.92E-08
SABVUN	2.40E-02	1.53E+02	6.92E-06	1.69E-07	4.03E-08
UiO-66-CF_3	9.49E-03	1.20E-02	2.03E-06	3.74E-07	1.90E-07
UTEWOG	4.21E-02	7.69E+00	8.90E-06	1.05E-07	2.52E-08
UTEXAT	4.98E-03	1.54E-01	8.36E-06	7.20E-08	1.72E-08
UTEXIB	5.45E-03	5.30E+02	8.32E-06	7.90E-08	1.89E-08
WAYMIU	2.14E-02	2.99E+03	7.62E-06	1.69E-07	4.03E-08
WAYMOA	9.25E-03	9.69E+01	6.29E-06	1.73E-07	4.13E-08
XUNJEW	2.31E-03	3.22E+00	3.53E-06	5.61E-08	1.34E-08

For the bulk mixture adsorption condition, the partial pressure of each solvent was set to represent MOFs being exposed to liquid solvents. It is useful to understand whether the pores of the MOFs would be filled by solvent molecules under these conditions. We examined this by performing single component GCMC simulations of each solvent in the rigid MOF structure. Figure 5.A.1 shows the resulting adsorption loading from GCMC at P^0_{solvent} as well as a simple approximate of the saturation loading of each solvent ($N_{sat,approx}$) as calculated with Eq. (5.A.1) using the room temperature liquid density of each solvent ($\rho_{liq,solvent}$)[4]. It is clear that under these conditions the pore of each MOF are essentially completely filled with solvent molecules.

$$N_{sat,approx} \approx V_P \cdot \rho_{liq,solvent} \cdot \frac{1}{MW_{solvent}} \quad (5.A.1)$$

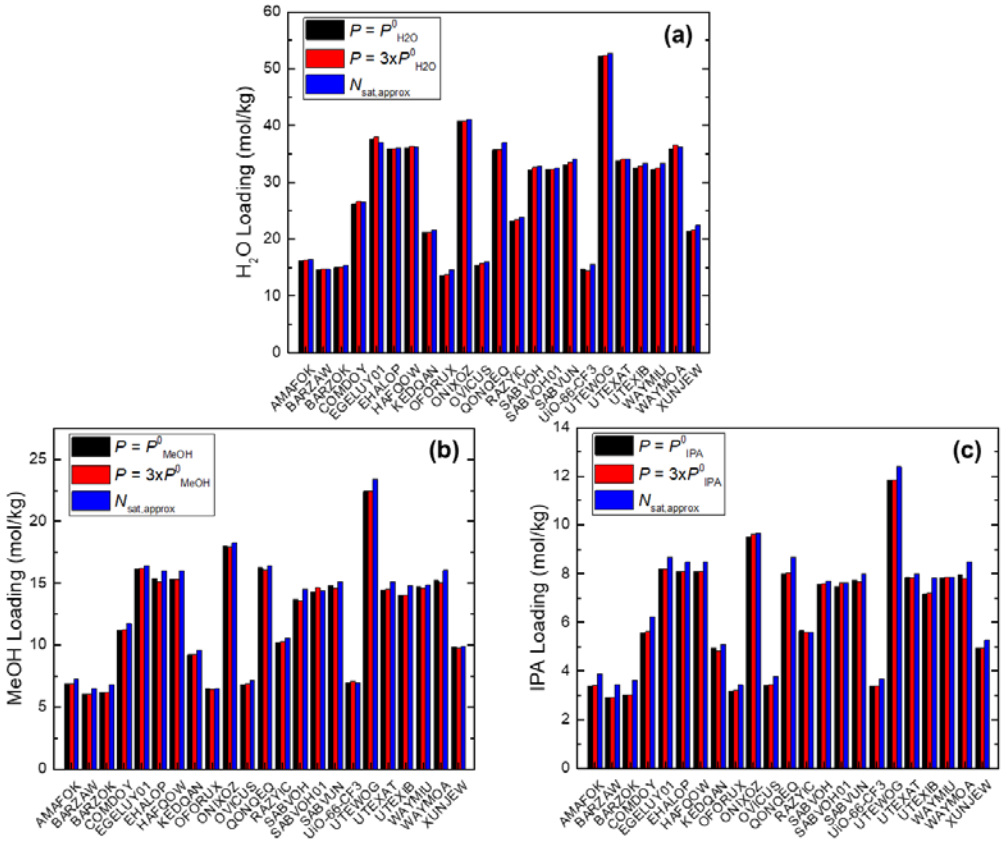

Figure 5.A.1. Comparison of solvent loadings estimated via single component GCMC simulations at $P = P^0_{\text{solvent}}$ and $3 \cdot P^0_{\text{solvent}}$[5] and $N_{sat,approx}$ for (a) H_2O, (b) MeOH, and (c) IPA. GCMC at $P = P^0_{\text{solvent}}$ is in good agreement with $N_{sat,approx}$.

5.A.3 Adsorption Selectivity in Rigid and Intrinsically Flexible MOFs

Figure 5.A.2 shows adsorption selectivity calculations at 298 K at fixed P/P^0_{sarin} = 0.25, and their ratio to allow direct comparisons between two approximations (reproduced from Figures 5.3 to 5.5 in Chapter 5). The conclusions of what types of mixture and MOFs could give higher sarin adsorption selectivity, i.e. sarin/H_2O vs. sarin/MeOH, can be similarly drawn between two approximations, though their numerical deviation is nontrivial.

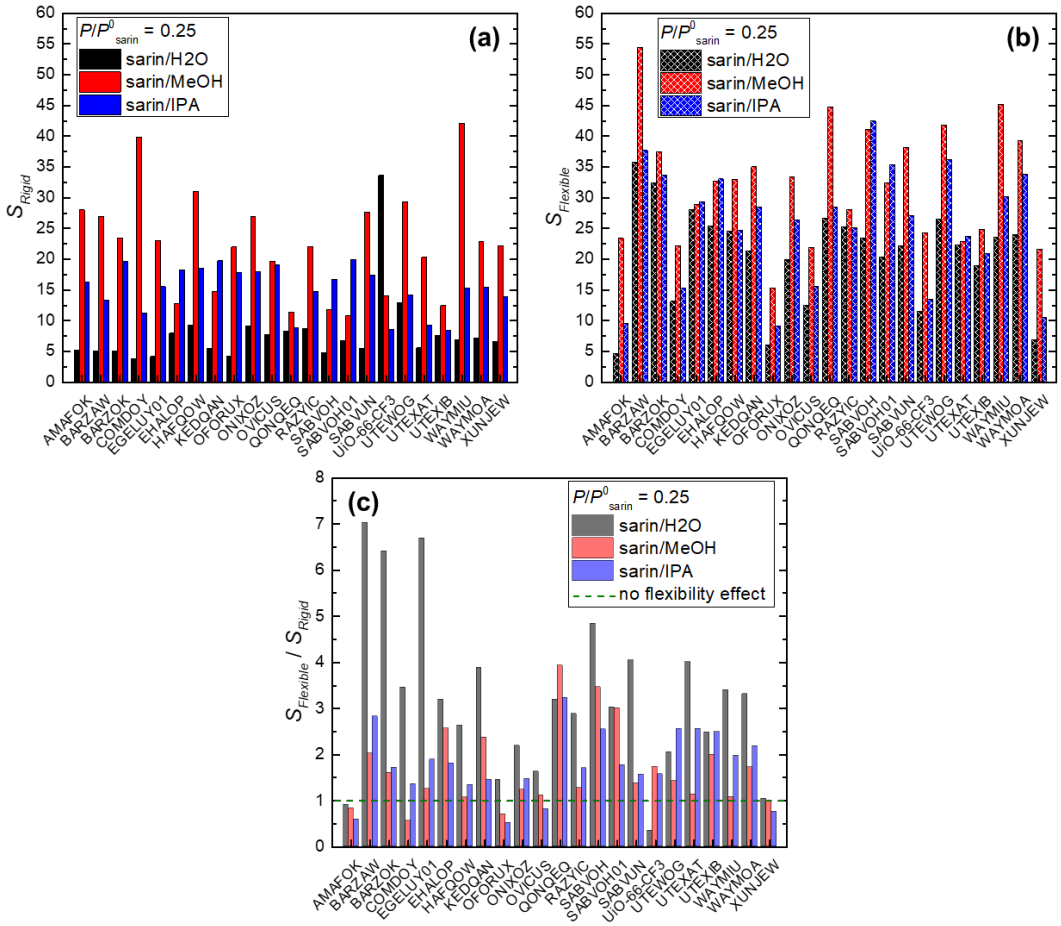

Figure 5.A.2. Adsorption selectivities for sarin at 298 K in 23 MOFs (a) approximated as rigid (S_{Rigid}) and (b) allowed to have intrinsic flexibility ($S_{Flexible}$) for each molecular mixture. (c) Ratio of $S_{Flexible}$ to S_{Rigid} in 23 MOFs for each molecular mixture. A green dashed line shows $S_{Flexible}/S_{Rigid}$ = 1 indicating no effect of intrinsic flexibility on adsorption modeling.

5.A.4 Effect of MOF Properties on Quantitative Predictions of Selectivity

Figure 5.A.3a compares LCD and PLD in rigid MOFs against those in flexible MOFs. Pore sizes in flexible MOFs were averaged over those from each MD snapshot. There were only marginal structural changes in MOFs by including intrinsic flexibility.

Figures 5.A.3b and 5.A.3c show the ratio of adsorption selectivity in rigid and flexible MOFs as a function of LCD of each MOF using polar and nonpolar solvent molecules, respectively. MOFs that have small LCDs are more affected by intrinsic flexibility. However, we find insufficient correlation considering LCDs to identify the underlying reasons for the sensitivity of flexibility as a function of molecular mixtures.

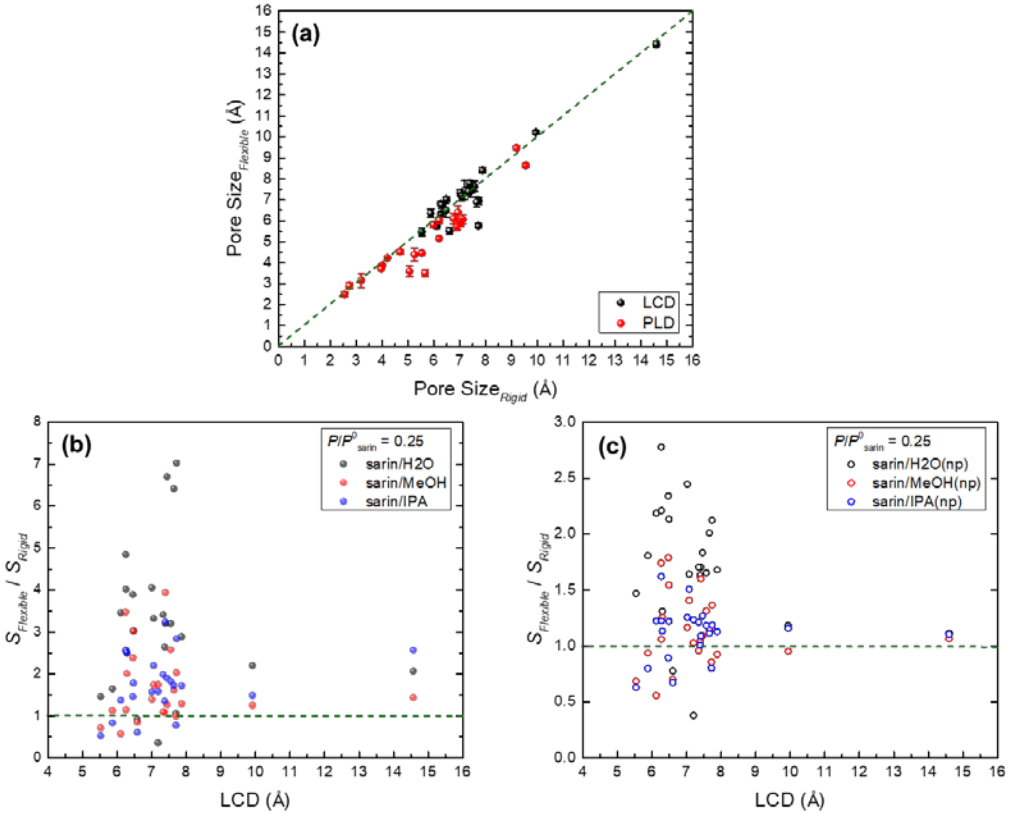

Figure 5.A.3. (a) Parity plot of pore sizes, i.e. LCD and PLD, of 23 MOFs calculated in rigid approximation (horizontal axis) and in intrinsically flexible approximation (vertical axis). Error bars for Pore Size$_{Flexible}$ show variation over ten distinct MD snapshots. $S_{Flexible}/S_{Rigid}$ as a function of LCD with simulations of using (b) realistic polar solvents and (c) unphysical nonpolar (np) solvents. LCD in (b) and (c) are that for rigid MOFs.

5.A.5 Molecular Modeling Details

For GCMC simulations[6,7], truncated potentials with tail corrections are applied where Lennard-Jones interactions are truncated at 12 Å. Simulation boxes are expanded to at least 26 Å along *x*, *y*, and *z* dimensions. GCMC simulations included 5,000 initialization cycles followed by 50,000 production cycles. Henry constants were computed using 200,000 production cycles while including an identical Widom probability.

Pore volumes of computation-ready MOF structures were calculated from the void fractions of each structure using a Widom particle insertion method with a He probe molecule (ε/k_B = 10.9 K, σ = 2.64 Å) at 298 K.[7] Accessible surface areas were calculated by using N_2 as probe molecule with overlap distance criteria set to a size parameter σ of 3.31 Å.[7] Largest cavity diameters and pore limiting diameters were calculated with Zeo++[8,9] applying the high-accuracy setting with a N_2 probe molecule using a radius of 1.86 Å.[8]

For binary GCMC simulations using "unphysical" nonpolar solvent molecules we omitted Coulombic adsorbate/adsorbate interactions[10]. Point charges were retained on sarin in these calculations.

Table 5.A.3 summarizes two molecular descriptors for the solvents examined in this work. It shows that molecular mixtures consist of adsorbates of different sizes and polarities.

Table 5.A.3. Molecular descriptors for the solvents. Kinetic diameter[11] and polarity index[12,13] of H_2O, MeOH, and IPA are listed. Polarity index is a relative measure of the degree of interaction of the solvent with various polar test solutes.

	H_2O	**MeOH**	**IPA**
Kinetic diameter, *d* (Å)	2.6	4.3	4.7
Polarity index	10.2	5.1	3.9

* Sarin[14] has a molecular shape of ~ 5 Å x ~ 12 Å.

5.A.6 Numerical Data for Analysis

Table 5.A.4. Numerical data in Figures 5.3, 5.4, and 5.5. Adsorption selectivities for sarin over solvents predicted in rigid MOFs (S_{Rigid}) and intrinsically flexible MOFs ($S_{Flexible}$), and their ratio ($S_{Flexible}/S_{Rigid}$): sarin/H_2O mixture.

MOFs	S_{Rigid}	$S_{Flexible}$	$S_{Flexible}/S_{Rigid}$
AMAFOK	5.16	4.66	0.90
BARZAW	5.10	35.82	7.02
BZRZOK	5.05	32.36	6.40
COMDOY	3.81	13.14	3.45
EGELUY01	4.19	28.07	6.69
EHALOP	7.99	25.46	3.19
HAFQOW	9.36	24.56	2.62
KEDQAN	5.52	21.40	3.88
OFORUX	4.18	6.04	1.44
ONIXOZ	9.10	19.88	2.19
OVICUS	7.72	12.56	1.63
QONQEQ	8.36	26.69	3.19
RAZYIC	8.80	25.29	2.88
SABVOH	4.85	23.45	4.84
SABVOH01	6.74	20.32	3.03
SABVUN	5.48	22.16	4.04
UiO-66-CF_3	33.62	11.52	0.34
UTEWOG	12.97	26.57	2.05
UTEXAT	5.59	22.39	4.01
UTEXIB	7.66	18.99	2.48
WAYMIU	6.95	23.62	3.40
WAYMOA	7.23	23.94	3.31
XUNJEW	6.65	6.93	1.04

Table 5.A.4. Continued: sarin/MeOH mixture.

MOFs	S_{Rigid}	$S_{Flexible}$	$S_{Flexible}/S_{Rigid}$
AMAFOK	28.06	23.41	0.83
BARZAW	26.99	54.44	2.02
BZRZOK	23.44	37.51	1.60
COMDOY	39.83	22.25	0.56
EGELUY01	23.02	28.86	1.25
EHALOP	12.75	32.71	2.56
HAFQOW	31.04	33.03	1.06
KEDQAN	14.78	35.03	2.37
OFORUX	21.99	15.38	0.70
ONIXOZ	26.99	33.38	1.24
OVICUS	19.67	21.92	1.11
QONQEQ	11.40	44.77	3.93
RAZYIC	22.09	28.11	1.27
SABVOH	11.86	41.04	3.46
SABVOH01	10.81	32.46	3.00
SABVUN	27.71	38.20	1.38
UiO-66-CF_3	14.04	24.26	1.73
UTEWOG	29.37	41.82	1.42
UTEXAT	20.30	22.89	1.13
UTEXIB	12.48	24.89	1.99
WAYMIU	42.12	45.23	1.07
WAYMOA	22.83	39.33	1.72
XUNJEW	22.20	21.66	0.98

Table 5.A.4. Continued: sarin/IPA mixture.

MOFs	S_{Rigid}	$S_{Flexible}$	$S_{Flexible}/S_{Rigid}$
AMAFOK	16.26	9.61	0.59
BARZAW	13.36	37.70	2.82
BZRZOK	19.70	33.66	1.71
COMDOY	11.32	15.34	1.36
EGELUY01	15.54	29.30	1.89
EHALOP	18.29	33.06	1.81
HAFQOW	18.47	24.67	1.34
KEDQAN	19.74	28.53	1.45
OFORUX	17.83	9.09	0.51
ONIXOZ	17.92	26.38	1.47
OVICUS	19.08	15.60	0.82
QONQEQ	8.84	28.51	3.23
RAZYIC	14.76	25.17	1.70
SABVOH	16.72	42.49	2.54
SABVOH01	20.01	35.40	1.77
SABVUN	17.42	27.13	1.56
UiO-66-CF_3	8.61	13.53	1.57
UTEWOG	14.17	36.17	2.55
UTEXAT	9.28	23.70	2.55
UTEXIB	8.39	20.92	2.49
WAYMIU	15.32	30.21	1.97
WAYMOA	15.50	33.84	2.18
XUNJEW	13.87	10.55	0.76

Table 5.A.5. Numerical data in Figures 5.6 and 5.7. Adsorption selectivities for sarin over solvents in rigid MOFs (S_{Rigid}) and intrinsically flexible MOFs ($S_{Flexible}$), and their ratio ($S_{Flexible}/S_{Rigid}$) calculated by using unphysical nonpolar (np) solvents: sarin/H_2O(np) mixture.

MOFs	S_{Rigid}	$S_{Flexible}$	$S_{Flexible}/S_{Rigid}$
AMAFOK	4.64	3.61	0.78
BARZAW	5.13	10.91	2.12
BZRZOK	5.29	10.64	2.01
COMDOY	3.71	8.11	2.19
EGELUY01	4.42	8.10	1.83
EHALOP	8.25	13.64	1.65
HAFQOW	10.74	17.51	1.63
KEDQAN	5.30	12.41	2.34
OFORUX	4.10	6.02	1.47
ONIXOZ	9.98	11.82	1.18
OVICUS	6.97	12.61	1.81
QONQEQ	8.07	13.74	1.70
RAZYIC	9.95	16.73	1.68
SABVOH	5.05	14.04	2.78
SABVOH01	7.37	15.72	2.13
SABVUN	5.57	13.61	2.45
UiO-66-CF_3	27.62	10.53	0.38
UTEWOG	13.21	14.72	1.11
UTEXAT	6.06	13.40	2.21
UTEXIB	6.87	8.99	1.31
WAYMIU	7.18	12.25	1.70
WAYMOA	8.04	13.21	1.64
XUNJEW	6.02	6.93	1.15

Table 5.A.5. Continued: sarin/MeOH(np) mixture.

MOFs	S_{Rigid}	$S_{Flexible}$	$S_{Flexible}/S_{Rigid}$
AMAFOK	29.11	20.40	0.70
BARZAW	25.20	34.41	1.37
BZRZOK	24.09	27.51	1.14
COMDOY	36.28	20.25	0.56
EGELUY01	23.72	25.86	1.09
EHALOP	13.48	17.71	1.31
HAFQOW	31.70	33.03	1.04
KEDQAN	14.02	25.10	1.79
OFORUX	19.49	13.38	0.69
ONIXOZ	26.02	24.83	0.95
OVICUS	20.17	18.91	0.94
QONQEQ	10.97	17.58	1.60
RAZYIC	22.90	21.17	0.92
SABVOH	12.08	21.04	1.74
SABVOH01	11.95	18.46	1.55
SABVUN	28.52	33.23	1.16
UiO-66-CF_3	14.84	15.26	1.03
UTEWOG	28.90	30.80	1.07
UTEXAT	21.03	22.32	1.06
UTEXIB	11.88	14.94	1.26
WAYMIU	41.67	39.92	0.96
WAYMOA	21.08	29.68	1.41
XUNJEW	22.92	19.66	0.86

Table 5.A.5. Continued: sarin/IPA(np) mixture.

MOFs	S_{Rigid}	$S_{Flexible}$	$S_{Flexible}/S_{Rigid}$
AMAFOK	15.77	10.62	0.67
BARZAW	14.94	17.72	1.19
BZRZOK	20.92	23.31	1.11
COMDOY	10.73	13.13	1.22
EGELUY01	16.79	21.30	1.27
EHALOP	19.94	23.56	1.18
HAFQOW	18.91	19.05	1.01
KEDQAN	20.17	18.03	0.89
OFORUX	14.26	8.99	0.63
ONIXOZ	19.72	22.84	1.16
OVICUS	18.77	15.02	0.80
QONQEQ	9.40	10.25	1.09
RAZYIC	14.90	16.82	1.13
SABVOH	17.22	27.92	1.62
SABVOH01	20.86	25.47	1.22
SABVUN	18.56	23.33	1.26
UiO-66-CF_3	8.80	10.85	1.23
UTEWOG	13.77	15.20	1.10
UTEXAT	8.81	10.79	1.22
UTEXIB	7.93	8.99	1.13
WAYMIU	14.18	17.22	1.21
WAYMOA	15.74	23.76	1.51
XUNJEW	14.05	11.29	0.80

5.A.7 References for Appendix 5.A

(1) Chung, Y. G.; Camp, J. S.; Haranczyk, M.; Sikora, B. J.; Bury, W.; Krungleviciute, V.; Yildirim, T.; Farha, O. K.; Sholl, D. S.; Snurr, R. Q. Computation-Ready, Experimental Metal-Organic Frameworks: A Tool To Enable High-Throughput Screening of Nanoporous Crystals. *Chem. Mater.* **2014,** *26*, 6185-6192.

(2) Demir, H.; Walton, K. S.; Sholl, D. S. Computational Screening of Functionalized UiO-66 Materials for Selective Contaminant Removal from Air. *J. Phys. Chem. C* **2017,** *121*, 20396-20406.

(3) Widom, B. Some Topics in the Theory of Fluids. *J. Chem. Phys.* **1963,** *39*, 2808-2812.

(4) Furniss, B. S.; Hannaford, A. J.; Smith, P. W. G.; Tatchell, A. R. *Practical Organic Chemistry (5th Edition)*; John Wiley & Sons, Inc.: New York, 1989.

(5) Tang, D.; Kupgan, G.; Colina, C. M.; Sholl, D. S. Rapid Prediction of Adsorption Isotherms of a Diverse Range of Molecules in Hyper-Cross-Linked Polymers. *J. Phys. Chem. C* **2019,** *123*, 17884-17893.

(6) Dubbeldam, D.; Calero, S.; Ellis, D. E.; Snurr, R. Q. RASPA: molecular simulation software for adsorption and diffusion in flexible nanoporous materials. *Mol. Simulat.* **2016,** *42*, 81-101.

(7) Dubbeldam, D.; Torres-Knoop, A.; Walton, K. S. On the inner workings of Monte Carlo codes. *Mol. Simulat.* **2013,** *39*, 1253-1292.

(8) Willems, T. F.; Rycroft, C. H.; Kazi, M.; Meza, J. C.; Haranczyk, M. Algorithms and tools for high-throughput geometry-based analysis of crystalline porous materials. *Micropor. Mesopor. Mat.* **2012**, *149*, 134-141.

(9) Pinheiro, M.; Martin, R. L.; Rycroft, C. H.; Haranczyk, M. High accuracy geometric analysis of crystalline porous materials. *CrystEngComm* **2013**, *15*, 7531-7538.

(10) Martin, M. G.; Siepmann, J. I. Transferable potentials for phase equilibria. 1. United-atom description of n-alkanes. *J. Phys. Chem. B* **1998,** *102*, 2569-2577.

(11) van Leeuwen, M. E. Derivation of Stockmayer potential parameters for polar fluids. *Fluid Phase Equilib.* **1994,** *99*, 1-18.

(12) Harris, D. C. *Quantitative Chemical Analysis (9th Edition)*; Freeman: New York, 2015.

(13) Katz, E.; Eksteen, R.; Schoenmakers, P.; Miller, N. *Handbook of HPLC*; Marcel Dekker: New York, 1998.

(14) Delfino, R. T.; Ribeiro, T. S.; Figueroa-Villar, J. D. Organophosphorus Compounds as Chemical Warfare Agents: A Review. *J. Braz. Chem. Soc.* **2009,** *20*, 407-428.

CHAPTER 6. SUMMARY AND OUTLOOK

6.1 SUMMARY OF DISSERTATION IMPACT

This dissertation used atomistic simulations to examine a sub-ambient PSA process employing MOF adsorbents as a potential route towards post-combustion CO_2 capture. This filled a critical gap in knowledge about this kind of sub-ambient gas processing. We also provided fundamental insights into a standard approximation of adsorption modeling as exemplified by CWA adsorption in MOFs.

Reproducibility of experiments in psychology and biomedical science has received enormous attention in recent years, but similar efforts have not been made in materials chemistry. Chapter 2 addressed this issue using a meta-analysis of results from a specific area of materials chemistry, adsorption properties of MOFs.[1] This represented an innovative approach to tackling an important general problem in materials chemistry, and the methods we introduced could be applied widely in materials chemistry and related disciplines. This also gave us useful information on the viability of applying molecular modeling to CO_2 adsorption in MOFs.

Recent process developments have indicated that sub-ambient temperature processes may be made economically viable for large-scale CO_2 capture. Chapter 3 tackled the important question of how whether this choice can substantially increase the CO_2 capacity possible in structured adsorbents.[2] We showed by molecular simulation that CO_2 swing capacities as high as 40 mol/kg were possible with appropriately chosen MOFs. This

improves upon commonly accepted limits of CO_2 swing capacity in a similar class of materials by an order of magnitude.

Appropriate selection of adsorbent materials is essential in developing adsorption-based processes such as CO_2 capture. Approximate methods such as adsorbent evaluation metrics do not completely describe the performance of adsorbents in real separation processes. Chapter 4 assessed the correlation between approximate predictions and detailed process model predictions of MOFs in a sub-ambient PSA. We illustrated the opportunities and challenges in bridging approximate and detailed methods for evaluating adsorbents for cyclic separation processes.

Molecular modeling of adsorption of CO_2 and similar species in a wide range of MOFs typically employ a rigid framework approximation. Nevertheless, all real frameworks have intrinsic flexibility due to thermal vibrations. Chapter 5 demonstrated the adsorptive separation of CWAs under bulk mixture adsorption conditions with solvents of different polarities and sizes in MOFs. Our observations implied the intrinsic flexibility can have significant effects on quantitative analysis of adsorbed molecules when electrostatic interactions between those molecules are non-trivial.

6.2 SUGGESTIONS FOR FUTURE WORK

6.2.1 Reproducibility Analysis of Porous Material Intrinsic Properties

In Chapter 2, we examined the reproducibility of CO_2 isotherm measurements in MOF materials where ~ 20% of measurements were labeled outliers on the basis of our metrics. We pointed out that the meta-analysis described does not provide direct physical

insight into why a particular measurement is an outlier or why a material may have a smaller or larger fraction of outliers. Because the measurements of simple gas adsorption are relatively routine[1,3], it is reasonable to assume that most outliers occur because of variations in the intrinsic properties of porous materials. Identification of reproducibility on those properties of MOFs, therefore, merits further examination in terms of understanding isotherm reproducibility. A challenge in this regard would be collecting simple quantities that can imply the intrinsic properties of materials from hundreds and thousands of existing literatures. The recent development of a simple text mining algorithm[4] enabled identification of surface area and pore volumes of MOFs from hundreds and thousands of reported literatures with high accuracy. This kind of approach may be a useful tool to facilitate the collection of a large set of reference data of those properties and additional material information. It may then be possible to conduct similar reproducibility analysis as in Chapter 2 on various intrinsic materials properties.

6.2.2 Engineering the Inflection in Adsorption Isotherms

Chapters 3 and 4 identified high performing MOF candidates estimated at the approximate molecular level (i.e. adsorbent evaluation metrics) and detailed process level (i.e. industry-relevant process objectives) in terms of CO_2 capture in a sub-ambient PSA. A common feature, although perhaps not a necessary condition, that underlies for high performance is these MOFs have inflections in their CO_2 adsorption isotherms that are bracketed within the operating pressure range at temperatures we examined. Such adsorption behavior in several rigid MOFs (i.e. materials with no structural volume change upon gas adsorption) at low temperatures was studied in the literature.[5] Nonetheless, the origin of the inflection in isotherms for rigid frameworks that compromise the majority of

existing MOFs is still relatively unexamined. Understanding the inflection mechanism of the sub-ambient CO_2 adsorption isotherms in rigid MOFs would, therefore, enable utilizing many existing MOFs in a process. This would also lead to exploiting the inflection point induced into the pressure swing range by material engineering to achieve larger swing capacity (and/or other performance metrics) in a cyclic adsorption process. Simon et al.[6] have posed a statistical mechanical model of gas adsorption dictating the condition for the inflection point in isotherm is related to the chemical potential of the adsorbate. Similar efforts could pave a way to derive thermodynamic principle that induces inflections in isotherms.

6.2.3 Sub-Ambient CO_2 Adsorption Modeling in Intrinsically Flexible MOFs

CO_2 adsorption modeling in the presence of N_2 throughout this thesis was conducted employing a rigid framework approximation of MOFs. In Chapter 5, however, we observed considerable discrepancies of adsorption selectivity for CWA over various solvents between calculations in rigid and intrinsically flexible frameworks. Such impact was dominantly attributed to the fact that bulk mixtures we examined were consisted of molecules of having strong interactions between adsorbing molecules. This is consistent with previous observations indicating electrostatic interactions are a contributing factor in under-/overestimation of adsorption properties by including the flexibility effect, even for large pore MOFs.[7] Gee et al. showed flexibility in adsorption modeling can also be significant in MOFs at high loadings of adsorbing molecules.[8] CO_2 in post-combustion flue gas is a quadrupolar molecule that can induce non-trivial electrostatic interactions with N_2 or with other species in a flue gas mixture. In addition, the results in Chapters 3 and 4 pointed large CO_2 adsorbed amounts at sub-ambient temperatures were attained in large

open pore MOFs. These observations, thereby, make it interesting to consider sub-ambient CO_2 adsorption behavior under a bulk flue gas mixture condition in large pore MOFs by taking account of their intrinsic flexibility.

6.3 REFERENCES

(1) Park, J.; Howe, J. D.; Sholl, D. S. How reproducible are isotherm measurements in metal-organic frameworks? *Chem. Mater.* **2017,** *29,* 10487-10495.

(2) Park, J.; Lively, R. P.; Sholl, D. S. Establishing upper bounds on CO_2 swing capacity in sub-ambient pressure swing adsorption *via* molecular simulation of metal-organic frameworks. *J. Mater. Chem. A* **2017,** *5*, 12258-12265.

(3) Nguyen, H. G. T.; Espinal, L.; van Zee R. D.; Thommes, M.; Toman, B.; Hudson, M. S. L.; Mangano, E.; Brandani, S.; Broom, D. P.; Benham, M. J.; Cychosz, K.; Bertier, P.; Yang, F.; Krooss, B. M.; Siegelman, R. L.; Hakuman, M.; Nakai, K.; Ebner, A. D.; Erden, L.; Ritter, J. A.; Moran, A.; Talu, O.; Huang, Y.; Walton, K. S.; Billemont, P.; De Weireld, G. A reference high-pressure CO_2 adsorption isotherm for ammonium ZSM-5 zeolite: results of an interlaboratory study. *Adsorption* **2018,** *24*, 531-539.

(4) Park, S.; Kim, B.; Choi, S.; Boyd, P. G.; Smit, B.; Kim, J. Text Mining Metal-Organic Framework Papers. *J. Chem. Inf. Model.* **2018,** *58*, 244-251.

(5) Walton, K. S.; Millward, A. R.; Dubbeldam, D.; Frost, H.; Low, J. J.; Yaghi, O. M.; Snurr, R. Q. Understanding inflections and steps in carbon dioxide adsorption isotherms in metal-organic frameworks. *J. Am. Chem. Soc.* **2008,** *130*, 406-407.

(6) Simon, C. M.; Braun, E.; Carraro, C.; Smit, B. Statistical mechanical model of gas adsorption in porous crystals with dynamic moieties. *Proc. Natl. Acad. Sci. U.S.A.* **2017,** *114*, E287-E296.

(7) Agrawal, M.; Sholl, D. S. Effects of Intrinsic Flexibility on Adsorption Properties of Metal-Organic Frameworks at Dilute and Nondilute Loadings. *ACS Appl. Mater. Interfaces* **2019,** *11,* 31060-31068.

(8) Gee, J. A.; Sholl, D. S. Effect of Framework Flexibility on C_8 Aromatic Adsorption at High Loadings in Metal-Organic Frameworks. *J. Phys. Chem. C* **2016,** *120*, 370-376.